National Technical University of Athens
School of Naval Architecture and Marine Engineering
Division of Marine Hydrodynamics

Sofia Peppa
Dipl. Naval Architect & Marine Engineer, MSc

COMPUTATIONAL STUDY OF FLOW-STRUCTURE INTERACTION

**Submitted to the School of Naval Architecture and Marine Engineering
for the degree of Doctor of Philosophy
at the National Technical University of Athens**

George S. Triantafyllou
Professor, Division of Marine Hydrodynamics
Thesis Supervisor

Lambros Kaiktsis
Assistant Professor, Division of Marine Engineering

George D. Tzabiras
Professor, Division of Marine Hydrodynamics

MAY 2012

Advisory Committee:

George S. Triantafyllou
Professor NTUA
Thesis Supervisor

Lambros Kaiktsis
Assistant Professor NTUA

George D. Tzabiras
Professor NTUA

Examination Committee:

George S. Triantafyllou
Professor NTUA
Thesis Supervisor

Kostas A. Belibassakis
Associate Professor NTUA

John A. Ekaterinaris
Professor University of Patras

Lambros Kaiktsis
Assistant Professor NTUA

Efstathios Konstantinidis
Assistant Professor University of Western Macedonia

Sokrates Tsangaris
Professor NTUA

George D. Tzabiras
Professor NTUA

MAY 2012

Abstract

A wide variety of engineering structures exhibit Vortex-induced Vibration (VIV) problems arising from the flow dynamics. Vortex-induced vibrations commonly involve excitation of the structure in both the in-line and transverse directions; thus they are characterized by complex trajectories, which often take the form of a figure *eight*. This thesis reports the results of a computational study of flow past a cylinder forced to oscillate in both the in-line and transverse directions with respect to a uniform stream, at a Reynolds number equal to 400. The in-line vibration occurs at twice the frequency of the transverse oscillation, resulting in a figure *eigh*t motion of the cylinder, emulating vortex-induced vibration.

For a flow stream from left to right, we have distinguished between two oscillation modes of the cylinder, depending on the direction of the cylinder motion in the upper half plane: a counter-clockwise mode (if the upper part of the trajectory is traversed counter-clockwise), and a clockwise mode (if the upper part of the trajectory is traversed clockwise). Both two- and three-dimensional simulations of the flow were performed, using Direct Numerical Simulation (DNS) based on a Spectral Element Method (SEM). A spectral element based parallel code was used to enable efficient computations; the code has been evaluated for its performance and scalability in parallel computer clusters. This thesis reports on the results of both two- and three-dimensional simulations, quantifying the forces acting on the moving cylinder, and characterizing the wake dynamics.

We have performed two-dimensional flow simulations of the two oscillation modes (counter-clockwise and clockwise), using a range of frequencies close to the natural frequency of the Kármán vortex street, and several oscillation amplitudes. We have calculated the non-dimensional values of the power transfer from the fluid to the body, the forces acting upon the cylinder, and have correlated the results to the structure of the wake. We have found that the results are greatly influenced by the direction in which the figure *eight* is traversed (counter-clockwise and clockwise). In general, the counter-clockwise motion maintains positive power transfer at higher oscillation amplitudes, and is also characterized by higher force levels. Flow field visualizations have shown that wakes are characterized by 2S structure (two single vortices) at low amplitudes, and more complicated wake structures at higher amplitudes. It is found that the presence of in-line oscillation affects the forces acting on the cylinder and the wake structures.

Three-dimensional simulations have been performed for the counter-clockwise mode, for the case of resonant forcing. The results demonstrate a much smoother variation of force coefficients in comparison to the two-dimensional flow. In accordance with two-dimensional flow, the lift signal is characterized by the presence of the strong third harmonic component. The flow visualization has demonstrated the formation of 2S type mode in the wake, with the wake structure becoming very complex at high oscillation amplitudes. Three-dimensionality in the wake has been identified indicating the development of streamwise vortices interacting with Kármán vortices.

Acknowledgements

I would like to sincerely express my gratitude to my supervisor, Prof. George Triantafyllou, for his encouragement, guidance and confidence in me over the last five years. Prof. Triantafyllou has always been very approachable and willing to share his vast knowledge of fluid mechanics. He was very understanding and supportive both on a professional and a personal level and I would I like to thank him, above all, for providing me with the opportunity to fulfill my research.

I am also extremely grateful to Assist. Prof. Lambros Kaiktsis for his continuous support and assistance. His friendly personality and his knowledge on CFD, creates an inspiring environment for academic research. I thank him not only for being an excellent mentor by encouraging and driving me, but also for always being available for informal discussions.

I also want to thank Prof. George Tzabiras for serving in my thesis committee and for his cooperation. He gave me the original inspiration to deal with CFD as my MSc degree supervisor. I want to thank him for his support, his friendly conversations and his critical comments that have helped me to improve my dissertation.

Furthermore, I would like to thank Assoc. Prof. Kostas Belibassakis, Prof. John Ekaterinaris, Assist. Prof. Efstathios Konstantinidis and Prof. Sokrates Tsangaris for kindly serving in my committee.

Part of this work would not have been possible without the help of Dr. Christos Frouzakis from ETH Zurich, who kindly provided us with the computing resources necessary for hosting some of the computations in the present work. I would like to thank him for his assistance and his kind support.

I would like to acknowledge Assos. Professor Nectarios Koziris and Dr. George Goumas for their kind support and providing us with the computing resources at CSLab in the School of Electrical and Computer Engineering of NTUA in which part of the computations of this work was performed.

I would also like to extend a big thank-you to my co-workers and friends; particularly Dr. John Galionis for his help whilst at NTUA, Andreas Skoufis for his hardware expertise and Babis Papadopoulos for his supportive friendship.

Most importantly I would like to thank my family. My husband George and my son Nickolas, for their unconditional understanding and support. They have kept me constantly focused and motivated to keep on trying and I apologize for the time I didn't spend with them. My sister Dimitra, for being so caring and supportive throughout my whole life. Nick, for his assistance with the intricacies of the English language. And finally, I would like to express my deepest gratitude to my parents Constantinos and Evaggelia for all they have done for me. I dedicate this thesis to all my family.

Layout of Thesis

The thesis is organized as follows:

The Introduction (*Chapter 1*) describes the motivation and objectives of the dissertation. A brief overview of the phenomena of vortex shedding and Vortex-induced Vibration (VIV) is provided. A number of literature studies involving forced vibrations of a circular cylinder in the transverse direction, in-line direction and both transverse and in-line direction, with respect to an incoming flow, are reported. Reference is also made to two degrees of freedom VIV studies.

Chapter 2 presents the numerical method employed in the Navier-Stokes solver. In particular, an outline of the spatial discretization and the time-splitting scheme that was used for two- and three-dimensional simulations is given.

Chapter 3 refers to the implementation of the Navier-Stokes solver on parallel computer clusters as well as on the code validation. The code scalability and performance is characterized, based on tests with different parallel clusters.

Chapter 4 presents the computational results of two-dimensional flow past a cylinder oscillating both transversely and in-line with respect to a uniform stream, at Reynolds number of 400. The dependence of motion direction, oscillation frequency and amplitude on the flow structure and forces acting on the cylinder is discussed in detail.

Chapter 5 presents corresponding computational results of three-dimensional flow for resonant forcing. Effects of flow three-dimensionality on wake structure and forces are analyzed.

Finally, *Chapter 6* summarizes the main findings of the present study and suggests further research.

Contents

Chapter 4

Chapter 5

List of Figures

List of Tables

Nomenclature

Roman Symbols

A_x	in-line oscillation amplitude
A_y	transverse oscillation amplitude
C_D	drag coefficient
$C_{D\alpha}$	inertia force (added mass) coefficient in the in-line direction
C_{Dv}	excitation force coefficient in the in-line direction
$\langle C_D \rangle$	time-averaged drag coefficient
$C_{D,RMS}$	root mean square of drag coefficient
C_L	lift coefficient
$C_{L\alpha}$	inertia force (added mass) coefficient in the transverse direction
C_{Lv}	excitation force coefficient in the transverse direction
$\langle C_L \rangle$	time-averaged lift coefficient
$C_{L,RMS}$	root mean square of lift coefficient
C_M	inertia force (added mass) coefficient in the transverse direction
C_{Mx}	inertia force (added mass) coefficient in the in-line direction
D	cylinder diameter
F_y	hydrodynamic force in the transverse direction
F_x	hydrodynamic force in the in-line direction
F_{Hydro}	total hydrodynamic force
f_s	Strouhal frequency
f_x	in-line oscillation frequency
f_y	transverse oscillation frequency
$F = \frac{f_y}{f_s}$	reduced oscillation frequency
L_z	the domain length in the spanwise dimension (z direction)
N	polynomial order
p	fluid pressure
P	total power transfer
$\langle P_d \rangle$	mean power dissipation
P_x	power transfer in the in-line direction
P_y	power transfer in transverse direction
Q	number of quadrature points
$Re = \frac{U_\infty D}{\nu}$	Reynolds number
$S_t = \frac{f_s D}{U_\infty}$	Strouhal number
$T = \frac{1}{f_y}$	oscillation period
t	time
U_∞	free stream velocity
x	variable of physical space

Greek Symbols

Δt	time-step
$\varepsilon = \frac{A_x}{A_y}$	excitation amplitude ratio
η	instantaneous cylinder displacement from the mean position
ν	fluid kinematic viscosity
ρ	fluid density
ω_x	streamwise vorticity component
ω_y	vertical vorticity component
ω_z	spanwise vorticity component

List of Common Abbreviations

2D	two-dimensional
3D	three-dimensional
CFD	Computational Fluid Dynamics
DNS	Direct Numerical Simulation
Eq.	equation
FDM	Finite Difference Method
FEM	Finite Element Method
FVM	Finite Volume Method
GLL	Gauss-Lobatto-Legendre
RMS	Root Mean Square
VIV	Vortex-induced Vibration
SEM	Spectal Element Method

Chapter 1

Introduction

1.1 Wake flows

The study of the flow past non-aerodynamic (bluff) bodies is an area of considerable interest in fluid dynamics. The dynamics of flow past a bluff body depend on the Reynolds number, commonly defined as $Re=\frac{U_\infty D}{\nu}$, where U_∞ is the free-stream velocity, D a characteristic length of a cylinder diameter and ν the kinematic viscosity of the fluid.

The flow past a bluff body, such as a circular cylinder, usually experiences boundary layer separation and flow instabilities in the wake region. Ludwig Prandtl, in the early twentieth century, was the first to describe the phenomenon of boundary layer separation, Prandtl (1928). As the boundary layer separates from the body surface it forms a discrete vortex. The vortex grows and it sheds in the near wake region. At a low Reynolds number, the vortex shedding is periodic with two staggered counter-rotating vortices shed within a period (**Figure 1-1**).

Figure 1-1: Von Kármán vortex street at *Re=140* by S. Taneda, Van Dyke (1982).

The non-dimensional frequency of the vortex shedding is the Strouhal number, $S_t=\frac{f_s D}{U_\infty}$, where f_S is the shedding frequency, D the diameter of the cylinder and U_∞ the velocity of the incoming uniform flow. The Strouhal number is almost constant at a value of 0.2 for a wide range of Reynolds numbers (approximately $300 \leq Re \leq 100.000$), see (**Figure 1-2**). The formation and shedding of vortices results in time-dependent lift and drag forces, which in turn can initiate oscillation and in some cases fatigue damage.

The phenomenon of *lock-in* or synchronisation occurs when the vortex shedding frequency is synchronized with the natural frequency of the structure.

The wake flows of bluff bodies in certain range of Reynolds numbers exhibit a variety of flow phenomena. At very low Reynolds number, the flow is steady involving a region of two counter-rotating standing vortices placed symmetrically in the wake. Bifurcation to oscillatory flow (Kármán street) occurs at *Re≈49*. Up to Reynolds, *Re≈190,* the oscillatory flow remains two-dimensional and forms a dynamical system described by Stuart–Landau equation, see Provansal et al. (1987).

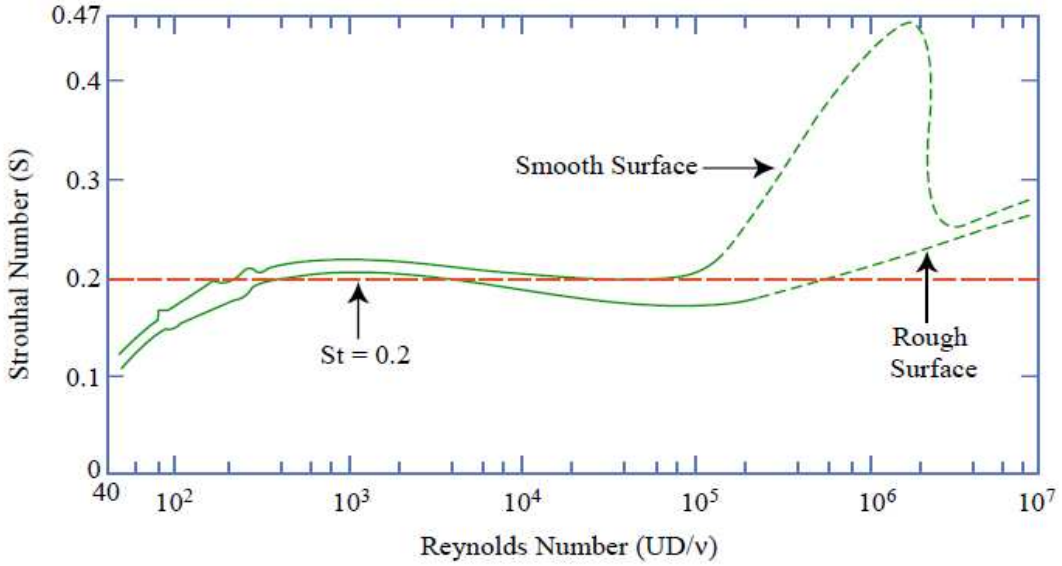

Figure 1-2: Strouhal number versus Reynolds number in a flow past a stationary circular cylinder. Techet (2005)

Three-dimensional wake transition of the flow past a circular cylinder was originally described by Roshko (1954) based on velocity fluctuation measurements, in the range of Reynolds number 150 to 300. Flow visualizations of the wake presented by Hama (1957), at Reynolds numbers between 80 to 300, showed that the wake transition is characterized by irregular spanwise waviness of the Kármán vortices, introducing three-dimensionality in the near wake. The flow visualization study by Gerrard (1978) showed the presence of dye "fingers", associated with streamwise vortices. The dye "fingers" were connecting the successive Kármán rolls. The distance between the streamwise vortex structures in the spanwise direction was shown to vary along the cylinder span.

Transition to three-dimensionality in the wake is characterized by two discontinuous changes in the Strouhal – Reynolds curve as shown in **Figure 1-3**, Williamson (1989; 1996). The curve of Strouhal frequency illustrates a region of laminar vortex shedding up to a Reynolds number of 190 which is characterized by two types of vortex shedding (parallel or oblique). The first discontinuity in the Strouhal frequency occurs at a Reynolds number around 190 corresponding to the Mode-A three-dimensional instability. The second discontinuity corresponds to the Mode-B vortex shedding, occurring at Reynolds number in the range of 230 - 260, Williamson (1996a). Barkley and Henderson (1996) used Floquet stability analysis to identify the critical spanwise wavelengths for both Mode A and Mode B. They reported that the critical Reynolds numbers were 188.5 and 259 for Mode A and Mode B respectively, in accordance with the experimental results presented in Williamson (1996). A sketch of vortex shedding with the corresponding wake modes, as well as experimental flow visualizations of the streamwise vortices, are presented in **Figure 1-4** and **Figure 1-5** respectively.

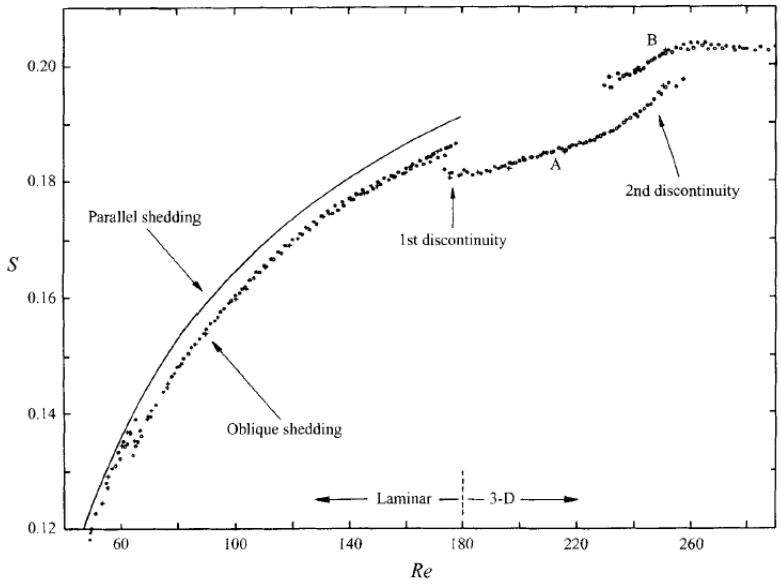

Figure 1-3: Strouhal-Reynolds number relationship, based on experimental data. Results correspond to parallel shedding as well as oblique shedding induced by end (spanwise) boundary conditions. Williamson (1989; 1996a)

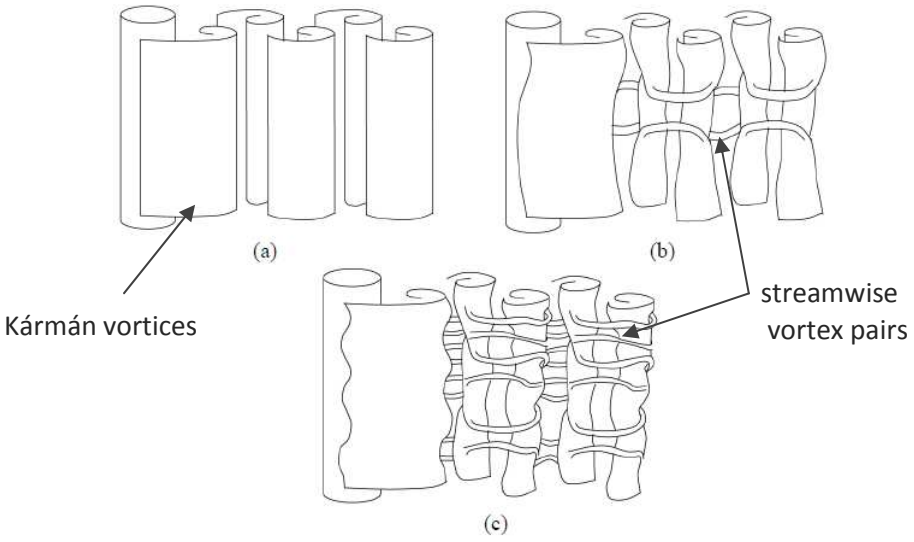

Figure 1-4: Sketch of vortex shedding process in the wake of a circular cylinder: (a) Laminar vortex shedding (b) Mode A vortex shedding (c) Mode B vortex shedding. Morton (2010)

Three-dimensional wakes are characterized by the presence of spanwise vortex Kármán rolls and streamwise vortex pairs. Mode-A instability is associated with a spanwise wavelength 3-4 cylinder diameters, see Williamson (1996a). In contrast, Mode-B instability is characterized by a shorter wavelength (approximately one cylinder diameter). The presence of Mode A and Mode B in the wake of a circular cylinder observed by Williamson (1989; 1996) have been confirmed in various other experimental studies, Zhang et al. (1995), Henderson (1997), Brede et al. (1996). Numerical studies of the three-dimensional flow past a circular cylinder performed by Thompson et al. (1996; 2001) also demonstrated the presence of Mode A and Mode B type of vortex shedding (see **Figure 1-6**).

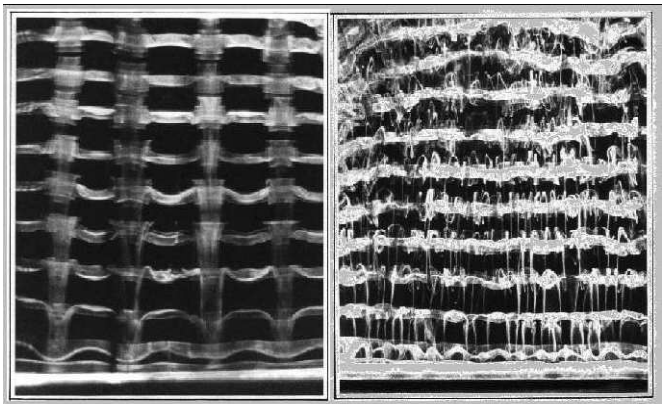

Figure 1-5: Top-view of the three-dimensional wake vortex structures in flow past a circular cylinder at *Re= 200* and *Re=270*, corresponding to Mode A and Mode B. Both photographs are to the same scale, and the flow is upwards. Williamson (1996a)

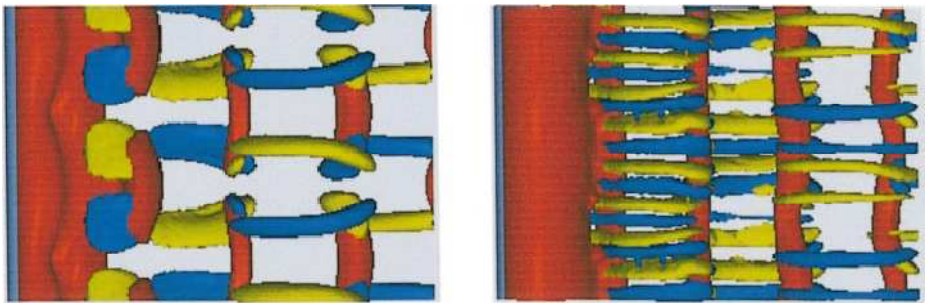

Figure 1-6: Three-dimensional wake vortex structures in flow past a circular cylinder at *Re=210* (Mode A) and *Re=250* (Mode B), based on computational results. The yellow and blue isosurfaces represent positive and negative streamwise vorticity. The flow is from left to right. The front of the circular cylinder is shown at the left of each plot. Thompson et al. (2001)

A third mode of wake instability was discovered by Blackburn and Lopez (2003) using Floquet stability analysis; the mode is referred to as quasi-periodic (QP) mode. Blackburn and Lopez (2003) suggested that the QP mode resulted from a centrifugal type of instability in the wake. The critical wavelength of the QP mode was approximately 2.5 cylinder diameters, i.e. in-between that of Mode A and Mode B.

For Reynolds number higher than approximately 10^3, the shear layers separating from the upper and lower surface of the cylinder develop unstable flow structures due to the Kelvin-Helmholtz mode of instability (Williamson (1996)). The Kelvin-Helmholtz instability mode was first observed by Bloor (1964) and is characterized by the formation of small scale vortices in the separated shear layers in contrast to large scale Kármán vortices. Braza et al. (1986) observed that the presence of Kelvin-Helmholtz vortices in the wake results in a primarily two-dimensional instability. At $Re \approx 3.5 \cdot 10^5$ the laminar boundary layer becomes unstable and undergoes a transition to turbulence. Thus the mean separation points move downstream, resulting in a substantial decrease of drag coefficient (drag crisis).

In the Reynolds number region of $3.5 \times 10^5 < Re < 1.5 \times 10^6$, known as the supercritical regime, the flow is symmetric in mean, characterized by a laminar-turbulent boundary layer and turbulent boundary layer separation; the mean drag coefficient is extremely low. For a Reynolds number higher than 10^6, the drag begins to increase at increasing Reynolds number, see **Figure 1-7**. The boundary layer is now turbulent upstream of the separation point.

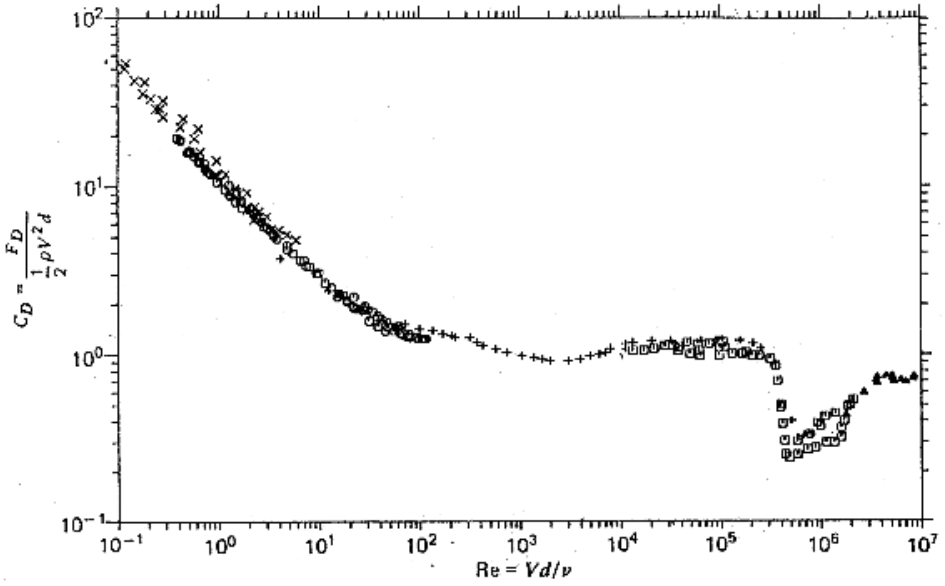

Figure 1-7: Variation of drag coefficient versus Reynolds number in flow past a stationary cylinder based on experimental results. Panton (2005)

1.2 Vortex-induced vibrations

The phenomenon of flow induced vibration is a major issue in the design and operation of various marine, mechanical and civil engineering structures, such as deep sea risers, underwater and hanging cables, offshore platforms, bridges, buildings, heat exchanger tubes, cooling towers, etc. (see **Figure 1-8**). Most of the practically used bluff structures tend to experience vibrations due to the formation of Kármán vortex street, which results in time-dependent forces. These forces can induce an oscillatory motion of the body, known as Vortex-induced Vibration (VIV). VIV may cause fatigue damage and catastrophic failure of engineering structures. Thus, understanding and mitigating VIV is essential for the safe design of structures exposed to fluid streams.

It was Leonardo da Vinci that first dealt with VIV, in particular “Aeolian Tones”. Since then, a lot of research has been carried in the field of flow-structure interaction; nonetheless, many fundamental questions remain unanswered. Furthermore, the failure of engineering structures, as the collapse of the Tacoma Narrows bridge in 1940, has been a substantial motivation to VIV research. Although the failure was originally attributed to VIV, it was proved that it was a complicated fluid-structure interaction between the gusting winds and

the bridge that caused the Tacoma Narrows bridge to undergo complex vibrations that eventually reached a severe enough magnitude to cause collapse.

Several structural failures due to VIV involve risers, platform mooring cables and other construction parts that are employed in an offshore oil exploration and production. One of the first reported failures is related to the severe construction difficulties encountered during the installation of an offshore oil terminal in a tidal flow, at Immingham, UK in 1969. A wide range test program was conducted both at the field site and at various laboratories, in order to determine the causes of the vibrations and to devise means of preventing similar ones. In 1979, the jack-up rig "Offshore Mercury" was drilling for the British Gas Corporation in 61 m of water in the English Channel near the Isle of Wight. Problems were encountered with vibrations of a drill pipe due to vortex shedding. This rig was operating in a 1.5 m/s current; the pipe, 610 mm in diameter, was oscillating with a displacement amplitude of 0.5 diameters transversely to the current direction. The drilling machinery on the deck of the rig was vibrating in unison with the pipe. These resonant vibrations resulted in the fatigue failure of the drill pipe inducing losses over five million U.S. dollars for the company, Griffin (1985).

Numerous cases of marine structure failures were attributed to VIV. For this reason the prediction of force distributions is extremely important for estimating the lifetime of such structures. The potential VIV problems are investigated prior to installation, in order to prevent fatigue failure. For example, the vibrations of long foundation piles (130 m) for a Shell Oil production platform in the Cognac field of Mexico Gulf due to underwater currents were measured during installation. The anticipated difficulties involved the "stabbing" of oscillating pipes into the sleeves of the platform base, as well as the vibrations of the stabbed pipes during the driving procedure. When the foundation pipes were excited by the currents at a velocity magnitude of 0.45 m/s, the prediction for the fatigue failure of the foundation piles was four days, Griffin (1985).

The design goal of engineering structures subjected to fluid flow is to mitigate VIV, thus avoiding fatigue damage. Recently, energy harvesting from structures undergoing VIV has attracted considerable attention. In such applications, VIV enhancement is used to maximize energy extraction from the fluid. Among others, the Vortex Induced Vibration Aquatic Clean Energy (VIVACE) converter, invented by Prof. M. Bernitsas of the University of Michigan, is a VIV-based energy harvesting device. Generation of energy by the VIVACE Converter is based on extracting kinetic energy from a fluid flow by VIV excitation of a rigid cylinder, and converting the motion energy to useful forms of energy as electrical energy. The device has been proven to extract energy even at current velocities as low as 0.25 m/s, Raghavan (2007). Although the topic of the present study bears several similarities with the above problem, due to the high values of Reynolds number, its study would require another approach than the DNS one utilized here, as the Large Eddy Simulation (LES).

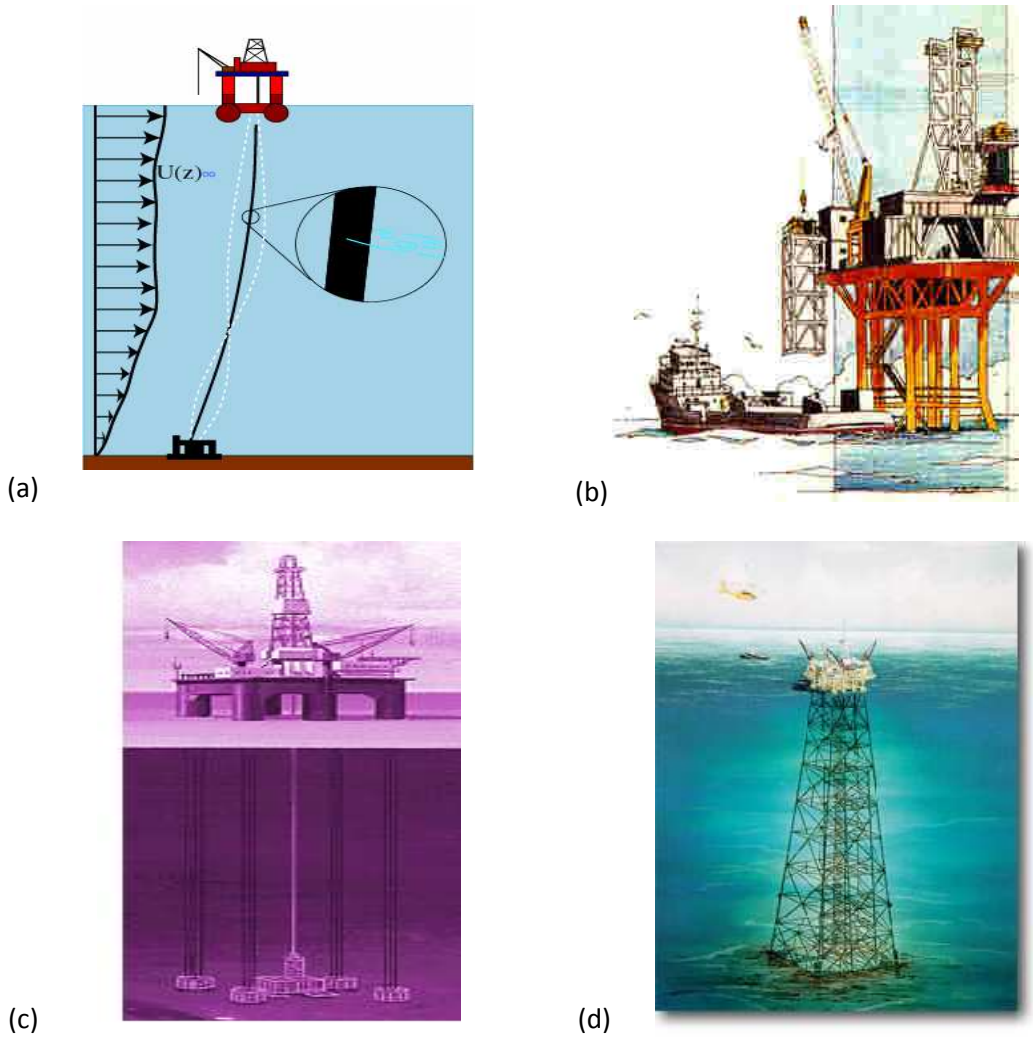

(a) (b)

(c) (d)

Figure 1-8: Marine structures: (a) Deep-sea risers (b) Offshore platforms (c) Tensor leg platforms (d) Fixed rigs. Techet (2005)

1.3 A review of forced and free vibration studies

The problem of a flow past a cylinder has been the subject of many experimental and numerical investigations; see the review articles by: Sarpkaya (2004), Sarpkaya and Shoaff (1979), Bearman (1984; 2011), Williamson and Govardhan (2004; 2008) and relevant textbooks by Zdravkovich (1997; 2003) and Blevins (1990).

Flows past circular cylinders undergoing prescribed motions are important for vortex-induced vibration studies. Due to the periodic vortex shedding the cylinder experiences time-dependent forces at the frequency of vortex shedding. Under certain conditions, the cylinder can be excited to oscillate by the flow at a frequency close to its natural frequency. Large amplitude vibrations can occur predominantly in the transverse direction with respect to the incoming flow whether lower amplitude vibrations have been observed in the in-line direction. While the transverse vibration occurs at or near the vortex shedding frequency,

the in-line vibration occurs at twice the transverse frequency associating with figure eight motions, Vandiver (1983).

Studies of vortex-induced vibration of cylinders generally consider either forced or free oscillations (see **Figure 1-9**). Cylinders may be forced to oscillate transversely to the direction of the incoming flow, in-line with the direction of the flow, or both in the transverse and in-line directions. Experimental studies have mainly focused on forced rigid cylinder oscillation, especially oscillation transversely to the incoming flow. Experimental studies of free oscillation have involved both rigid and flexible cylinders, oscillating either in the transverse-only or both in the transverse and inline direction with respect to a free stream. Computational studies also concern both forced and free cylinder oscillation. A large portion of these studies involves Direct Numerical Simulation (DNS), and is thus limited to low Reynolds numbers due to the requirement for extensive computational resources. For higher Reynolds numbers alternative numerical methods have been used as the Large Eddy Simulation (LES) and Reynolds Averaged Navier Stokes (RANS) simulations.

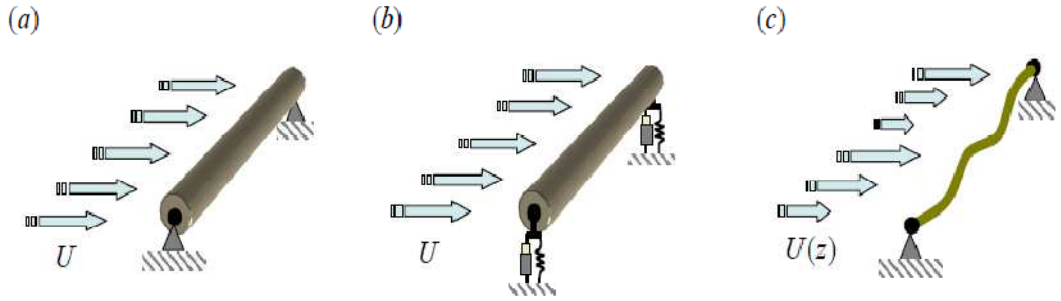

Figure 1-9: Three representative configurations of cylinder undergoing VIV: (a) flow of a uniform stream past a fixed rigid cylinder (b) flow of a uniform stream past an elastically mounted rigid cylinder (c) flow of a non-uniform stream past a flexible cylinder. Mukundan (2008).

Below, representative works are reviewed, involving free and forced oscillation in one direction only (mainly in the transverse-only direction) or both in the transverse and in-line direction.

Firstly, studies of flow past a cylinder oscillating transversely to a free stream include the experiments of Bishop and Hassan (1964). These experiments, performed for Reynolds numbers of a few thousand (order 6000 to 11000), showed that the system undergoes a transition as the oscillation frequency is increased, at constant amplitude, resulting in abrupt changes in the amplitude and phase of the lift force. The transition was characterized by hysteresis, and was always observed at frequencies lower than the Strouhal frequency.

In early experiments of forced oscillations by Protos et al. (1968), Toebes (1969), Stansby (1976) and Sarpkaya (1977; 1978), the lift force and its phase angle were measured. More specifically, Protos et al. (1968) and Toebes (1969) indicated the correspondence of phase angle and power transfer between the fluid and the cylinder. Stansby (1976) observed a switch in phase angle of the lift force in certain values of frequency and amplitude of oscillation, resulting in changes in the wake width. Sarpkaya (1977; 1978) expressed the harmonic part of the lift force in terms of two components: the inertial component, in-phase with the cylinder acceleration, and the excitation component, in-phase with the cylinder velocity. These measurements are in agreement with the subsequent experimental results by Moe and Wu (1990). Similar experiments with a transversely oscillating cylinder were performed by Staubli (1983). He used his measurements to predict the response of a freely vibrating cylinder in crossflow. His measurements were compared with previous data of freely oscillating cylinder provided by Feng (1968). He also demonstrated the hysteresis effect in experiments with elastically mounted cylinders due to the nonlinearities between the amplitude of oscillation and fluid force.

Williamson and Roshko (1988) performed a reference experimental study for the case of the cylinder forced to vibrate transversely to a steady stream, in a low Reynolds number range of 300 to 1000. Based on flow visualization, they produced a detailed map of wake modes at $Re \cong 400$, over a wide range of normalized amplitudes and frequencies of the cylinder motion. These wake modes correspond to different vortex shedding patterns, including two single vortices (2S), two vortex pairs (2P), a combination of a pair and a single vortex (P+S), as well as more complex patterns. In this study, the transitions reported in Bishop and Hassan (1964) were attributed to a switch in the wake mode from 2P to 2S, at increasing oscillation frequency, at values lower than the Strouhal frequency. Many studies have further addressed the issues related to the mode transitions in a flow past a cylinder forced to oscillate transversely with respect to a uniform stream, see Carberry, Sheridan et al. (2001; 2005). Similar wake transitions that characterized the flow past a forced oscillating cylinder were also found in studies of a freely vibrating cylinder as in the early experiments by Feng (1968), Brika and Laneville (1993) and later by Govardhan and Williamson (2000; 2001).

The P+S type of vortex shedding has also been found in earlier studies in which the cylinder was forced to oscillate in-line with the incoming flow by Griffin and Ramberg (1974) and Ongoren and Rockwell (1988). More specifically, the smoke visualizations of Griffin and Ramberg (1974) showed an asymmetric wake structure with two counter-rotating vortices and a single vortex. Using flow visualization, Ongoren and Rockwell (1988) found a symmetrical vortex pair and anti-symmetrical modes correspond to 2S, S+P and 2P in the wake. For these two modes of vortex shedding it is possible either to synchronize with the motion of the cylinder or to compete with each other.

Gopalkrishnan (1993) conducted detailed experimental studies of turbulent flow past cylinders undergoing transverse oscillation, in which he identified the excitation regime versus the non-dimensional amplitude and frequency of the cylinder oscillation. His results

confirmed the transition and corresponding phase shift in the lift signal reported in Bishop and Hassan (1964) at frequencies lower than the Strouhal frequency.

Blackburn and Henderson (1999) performed a computational study of the same problem at *Re=500*, at a constant oscillation amplitude of 0.25 cylinder diameters, and oscillation frequencies between 0.75 and 1.05 times the Strouhal frequency. They also observed the phase angle switch reported in the higher Reynolds number experiments of Bishop and Hassan (1964), and attempted to interpret it, based on vorticity dynamics. In addition, their results demonstrated that the flow dynamics is characterized by hysteresis, as well as that the flow structure can be rather complex.

Anagnostopoulos (2000) studied numerically the flow past a circular cylinder oscillating transversely to a steady stream, at Reynolds number equal to 106, a band of frequencies ranging from 0.8 to 1.2 times the Strouhal frequency, and oscillation amplitudes up to half the cylinder diameter. His results illustrate that, while the flow is periodic for oscillation frequencies less than or equal to the Strouhal frequency, it is qualitatively different for higher oscillation frequencies, with the wake becoming quasi-periodic.

Carberry et al. (2001) conducted experiments of a cylinder oscillating transversely to a free stream, at a Reynolds number of 2300. They concluded that the interaction between the natural instability of the wake and the forced oscillation of the cylinder leads to a transition between the 2S and 2P wake modes. This interaction depends strongly on the ratio of the excitation frequency to the natural shedding frequency. Within the lock-in regime an abrupt change in the magnitude and phase of lift force was observed. Carberry et al. (2005) extended their previous experimental study to Reynolds numbers up to 9300. They found similarities in the timing and mode of vortex shedding between their experiments of forced oscillating cylinder and the experiments of freely oscillating cylinder by Govardhan and Williamson (2000). They also underlined the difference between flow past forced and freely oscillating cylinder regarding the direction of energy transfer from the fluid to the cylinder. The excitation in free vibration evidently exhibits positive power transfer, whereas for forced vibration the energy transfer can be either positive or negative. Thus, they concluded that a forced strictly sinusoidal vibration characterized by a negative energy transfer from the fluid to the cylinder does not exclude free oscillation at comparable oscillation amplitude.

DNS studies were performed by Dong and Karniadakis (2005) to compute the three-dimensional flow past a stationary cylinder as well as past a cylinder forced to oscillate in the transverse direction, at a Reynolds number of 10,000. They used a Spectral Element Fourier method, with 300 million degrees of freedom and polynomial orders ranging, from 5 to 8. The calculated values of drag and lift coefficients were in good agreement with the previous experimental data (Bishop and Hassan (1964), Gopalkrishnan (1993), Norberg (2003)).

Recently, Willden et al. (2008) reported both two-dimensional (at *Re=100*) and three-dimensional (at *Re=300*) numerical simulations of flow past a cylinder undergoing transverse oscillation with respect to a uniform flow. The two-dimensional simulations corresponded to a detailed variation of both the normalized oscillation frequency and amplitude, and

identified the limiting curve of zero energy transfer from the flow to the structure. On the other hand, the three-dimensional simulations, performed for frequency values equal to or lower than the Strouhal frequency, reported transitions from 2S to P+S and finally to 2P wake modes, at increasing oscillation amplitudes.

Kaiktsis et al. (2007) studied numerically the forces exerted on a cylinder forced to oscillate harmonically in the transverse direction, at a Reynolds number of 400. They solved the two-dimensional Navier-Stokes equations in a coordinate system fixed to the cylinder. Three cases of motion were studied corresponding to frequencies below, at, and above the resonant forcing. The lift force was decomposed into a component in phase with the velocity and a component 180^{o} out of phase with the acceleration. The variations of these components, along with other flow parameters were examined over a range of non-dimensional oscillation amplitudes. Smooth variations of the force coefficients and regular vortex patterns were found below resonance oscillation frequency. Two sharp transitions in the force coefficients were found for resonant forcing, whereas changes of the hydrodynamic coefficients appeared in a sharp but continuous manner for above resonant forcing.

Atluri et al. (2009) used a two-dimensional Large Eddy Simulation (LES) to study the flow past a cylinder forced to transverse oscillation, for Reynolds number in the range of 500 to 8000. They concluded that the nature of the wake patterns is more complicated than that suggested by the Williamson - Roshko map (derived for $Re \approx 400$).

Recently Morse and Williamson (2006; 2009) performed experiments with a cylinder undergoing transverse controlled vibration, at Reynolds number of 2400-6800, 4000 and 12000. They demonstrated that under carefully controlled experimental conditions there exists close correspondence between the forced cylinder and the freely vibrating cylinder; thus experiments with forced cylinder vibrations can be used to predict vortex-induced vibrations.

In contrast to the large body of literature studies on the flow past a cylinder oscillating transversely to a free stream, few studies have examined the more realistic case of the flow past a cylinder vibrating both transversely and in-line with respect to the free steam. Among these Moe and Wu (1990) performed experiments in which the cylinder was allowed to vibrate both in the transverse and the in-line direction with respect to the incoming flow, thus following a figure *eight* motion; the cylinder was also clamped and/or forced to vibrate transversely. Moe and Wu found that when the cylinder followed a figure *eight* motion the responses were different than those of the transversely oscillating cylinder. Sarpkaya (1995) performed similar experiments to study the behavior of a cylinder allowed to oscillate in both the transverse and in-line direction with respect to incoming stream. He found that, in certain cases, the amplitudes of transverse oscillation were also quite different from those of a freely vibrating cylinder.

The flow past of a circular cylinder allowed to freely vibrate both in the transverse and in-line direction with respect to a free stream at a Reynolds number of 325 was investigated in

the two-dimensional simulations of Mittal and Kumar (1999). In most of the considered cases, the cylinder followed a figure *eight* trajectory (Lissajou figure of 8). Mittal and Kumar observed that the vortex shedding frequency of the oscillating cylinder does not match exactly the structural frequency but is slightly modified ("soft lock-in"). The flow structure was related to the variation of forces, as well as to the appearance of additional frequencies in their power spectra. Higher Reynolds number simulations (in the range 10^3-10^4) demonstrated the presence of disorganized wakes, Mittal and Kumar (2001).

Experimental studies for a cylinder motion with two degrees of freedom include the one of Jeon and Gharib (2001), who conducted experiments by forcing a cylinder to move both in the in-line and transverse directions. In their work, the frequency of the in-line motion was twice that of the transverse motion; thus the cylinder followed a trajectory resembling a figure *eight*. The transverse and in-line cylinder instantaneous displacements were thus, $y(t)=A_Y sin(\omega t)$ and $x(t)=A_X sin(2\omega t+\varphi)$. They considered an amplitude ratio, A_X/A_Y of 0.2, and phase angles equal to 0^o and -45^o. Their results indicate that, while the frequency of vortex shedding is still determined by the transverse motion, the in-line motion controls the phase of shedding, and thus the phase of the instantaneous lift force, determining the energy transfer to the cylinder. Another interesting result is that the presence of in-line motion, even at small amplitude, can inhibit the formation of the 2P mode in the wake.

Several published studies have addressed the problem of VIV in prototype experiments with elastically-mounted cylinders. Jauvtis and Williamson (2003; 2004) conducted experiments with an elastically mounted cylinder, free to oscillate both in-line and transversely with respect to the free stream, at Reynolds numbers ranged from 1000 to 15000. They found complex wake structures with two triplets of vortices known as 2T mode. They also found that the in-line oscillation affects surprisingly little the forces and wake structures. Thus, they concluded that the study of transverse-only VIV can be used to characterize more complex VIV motions. This observation contradicts the experiments of Marcollo and Hinwood (2006) of long flexible cylinder free to oscillate at several vibration modes to a uniform flow, at Reynolds number varied from 8000 to 40000. Marcollo and Hinwood (2006) found that there is a strong interaction between transverse and in-line oscillations at low Reynolds numbers.

Didier and Borges (2007) performed a two-dimensional computational study of the flow past a cylinder oscillating in the in-line, transverse or both the in-line and transverse directions, resulting in a circular motion, at a Reynolds number of 300. The frequency lock-in band of the circular motion was found to be different than those obtained for in-line or transverse oscillation. For transverse and circular oscillation, the time mean and RMS values of the drag and lift coefficients present an abrupt jump in a narrow band of oscillation frequencies that can be caused by a critical change in vortex structure.

Dahl et al. (2007; 2010) have published experimental results of a rigid circular cylinder free to oscillate in the in-line and transverse direction at subcritical ($1.1 - 6 \times 10^4$) and supercritical ($32\text{-}71 \times 10^4$) regions of Reynolds number as well as computational results at a Reynolds number 1×10^4. They found that the phase difference between the in-line and transverse

motion can have a strong influence on the regularity of the cylinder trajectory as well as on the possible occurrence of strong harmonic components in the lift force.

Although VIV refers to the free oscillation of the bluff body, recent studies emphasize the importance of forced oscillation studies for understanding VIV, e.g. Bearman (2009), Morse and Williamson (2006; 2009).

Forced vibration studies involve the excitation of the cylinder at several combinations of oscillation frequency and amplitude (for a given Reynolds number); thus, the cylinder motion affects the wake, while the inverse is obviously not possible. Free vibrations are excited internally by the wake at an average excitation frequency depending on the past and present state of the motion; as a consequence, there is a coupling between the cylinder motion and the wake, so any change to the cylinder motion will affect the wake, which in turn can affect the cylinder motion. Thus, using force data from forced oscillation studies may or may not be adequate for predicting the response of a freely oscillating cylinder. State of the art codes use such data to do the predictions.

In forced oscillations, the cylinder is commonly prescribed a harmonic motion at a constant amplitude and frequency. Experiments of free vibration of rigid cylinders have indicated that the response can be harmonic. Thus, forced oscillation experiments, performed using a harmonic cylinder motion are of relevance for VIV. Forced oscillation studies can yield the time-dependent forces acting on the cylinder. This information is useful for understanding the corresponding trends in forces on freely oscillating cylinders.

As suggested by Sarpkaya (2004), forced oscillations can be used in order to “regularize VIV leading to nearly sinusoidal oscillations, and forces, as well as approximately repeatable wake states”. Thus, the interaction between the fluid and the structure is simplified and the study mainly concerns the investigation of the wake response to a prescribed motion.

1.4 Motivation and objectives of the present study

As demonstrated in the previous sections, several engineering structures exhibit vortex-induced vibration problems, arising from the flow dynamics. In particular, it was shown that in several engineering structures, excitation is due to the formation of Kármán vortex street, which results in time-dependent loads. To understand the dynamics of the coupled flow-structure system, it is customary to study prototype flows around bluff bodies, whose motion is prescribed externally, and is characterized by the non-dimensional values of the oscillation amplitude and frequency.

The present work concerns the study of flow past an oscillating circular cylinder. As outlined in this chapter, the flow past a circular cylinder, despite the simple shape of the bluff body, is characterized by rich wake dynamics depending on the Reynolds number. Despite extensive research efforts for several decades a complete understanding of flow past stationary and oscillating cylinders is still missing.

Freely oscillating cylindrical structures commonly follow a trajectory of a figure *eight*. Thus, the present thesis concerns the computational study of flow past an oscillating cylinder following a figure *eight* motion, using Direct Numerical Simulation (DNS) based on a Spectral Element Method (SEM). Here, the cylinder is forced to oscillate both transversely and in-line with respect to a uniform flow. The frequency of the in-line motion is twice that of the transverse motion; thus the cylinder follows a trajectory resembling a figure *eight*, emulating the motion of a free vortex-induced vibration. The Reynolds number is held constant to a value of 400, falling into the regime of three-dimensional flow. Both two- and three-dimensional simulations are performed to characterize the flow dynamics and compute the forces acting on the cylinder.

The main objectives of the present study are:

- To utilize the current capabilities of parallel clusters for the efficient computation of two- and three-dimensional flow past an oscillating cylinder following a figure *eight* motion. For the simulations we have implemented a spectral element based parallel code. Here, a Direct Numerical Simulation (DNS) approach is followed. The thesis objectives were accomplished by developing the computational tools necessary for the geometry input and subsequent mesh generation, as well as proper routines for problem definition and post-processing simulation results and extracting statistical quantities related to forces.

- To characterize the flow past an oscillating cylinder, in particular :

  a) To characterize the wake dynamics, in a wide range of oscillation amplitude and frequency, for two- and three-dimensional flow.
  b) To compute the non-dimensional power transferred to the body, and thus assess on the parameter range corresponding to excitation and VIV.
  c) To compute the non-dimensional forces on the body, and relate the trends to the flow dynamics.
  d) To assess on the importance of three-dimensionality effects.

- To assess the scalability and performance of a parallel spectral element code in parallel computer clusters.

Chapter 2

Numerical Method

2.1. Background

In this thesis we have studied numerically the flow past a forced oscillating cylinder. Both two- and three-dimensional simulations have been performed by means of Direct Numerical Simulation (DNS). A Spectral Element Method (SEM) is used for the spatial discretization. SEM combines the advantages of spectral methods and finite element methods. The main advantage of spectral methods is their high accuracy, which is demonstrated by the *exponential convergence* to the correct solution at increasing resolution. Spectral methods are fitting for simple geometry problems. Finite element methods are suitable for problems in complex geometries. The spectral element method combines the good convergence properties of spectral methods with the flexibility of finite element methods in treating complex geometries. Here, high order polynomial expansions are applied within each element, in order to achieve high accuracy. Detailed information and foundations of the method can be found in Patera (1984), Maday and Patera (1989), Karniadakis (1989), Maday et al. (1990), Fischer and Patera (1991), Karniadakis and Sherwin (2005) and Deville et al. (2004). SEM is applicable to large simulations with parallel codes, Fischer (1994), Fischer and Rønquist (1994), Lee et al. (1996). In the present study, the parallel spectral element code *Nek5000* has been utilized (see *http://nek5000.mcs.anl.gov*).

2.2. Spectral element method

The numerical solution of the Navier–Stokes equations has been a challenging issue for the research community. The complex phenomena and dynamics, that are simultaneously present at several different scales in fluid flow problems, call for demanding resolution requirements but also for accurate numerical methods. The methods available to solve the incompressible fluid flow equations are classified according to the formulation of the differential equations. Thus, we distinguish between the “strong” formulation that involves methods such as the Finite Difference Method (FDM) and the Finite Volume Method (FVM) and the “weak” formulation, involving Finite Element Methods (FEM) and spectral methods. The methods using the equations in the “strong” form are of great interest in applications of aerospace science, where there is a need for high speed simulations to capture the discontinuities (bow shocks) in the front of bluff bodies, Fletcher (1988). On the other hand, FEM is popular for its geometric flexibility. In FEM, the computational domain is divided into many small elements and a trial function (usually a linear or quadratic shape function) is specified into each element. Therefore, the method is employed to solve problems with complex geometries; a low-order (linear or quadratic) convergence rate is expected.

FEM and spectral methods are based on the method of weighted residuals. Spectral methods involve in general two main categories, the collocation or pseudo-spectral methods and the Galerkin or modal methods. The former uses a set of nodes representing a grid, where the unknown velocity coefficients are taken by the requirement of zero residual at a set of nodes. The second approach utilizes the weighted residuals technique where the residual function is weighted with test functions and is set to zero after integration. The trial functions and the test functions are similar. Both the pseudo-spectral method and the

Galerkin method attain exponential convergence at increasing spatial resolution. This follows directly from the fact that the test functions are infinitely differentiable global functions (such as Chebyshev or Legendre polynomials), and have the advantage of exponential convergence. The order of the convergence is not fixed as in the finite element and finite difference methods, but depends on the solution regularity. Exponential convergence for a very smooth solution, in practice, implies that for an increase in the number of collocation points or the number of modes the numerical error decreases by at least the same order. Among the disadvantages of the spectral methods is that it is not easily applicable to complex geometries of engineering application since domain discretization is not involved, Canuto et al. (1988). A detail reference on the subject of spectral methods can be found in the monograph by Gottlieb and Orszag (1977) and the book by Canuto et al. (1988).

The Spectral Element Method (SEM) introduced by Patera (1984) is a method capable of combining the accuracy of spectral methods and the geometric flexibility of FEM. It employs a technique of high-order weighted residuals for the solution of partial differential equations, similar to FEM, but based on orthogonal polynomials and highly accurate numerical quadrature. For this reason, the rate of convergence is exponential for the smooth solutions (such as incompressible fluid flow) instead of quadratic (or linear) as in FEM.

In the following sections we will refer to implementation of flow-structure interaction problem in particular the formulation of Navier-Stokes equation, the imposition of boundary conditions, the spatial and temporal discretizations for two- and three-dimensional flow.

2.3. Numerical formulation

In this thesis we have considered the incompressible fluid flow, which is governed by the Navier–Stokes and incompressibility equations. For convenience, we non-dimensionalize all lengths with respect to cylinder's diameter *D*, all velocities with respect to the free stream velocity U_∞, time with respect to D/U_∞, and pressure with respect to ρU_∞^2. Then the incompressibility and Navier–Stokes equations can be written as:

$$\nabla \cdot \mathbf{u} = 0 \text{ in } \Omega \tag{2.1}$$

$$\frac{\partial \mathbf{u}}{\partial t} + \mathbf{u} \cdot \nabla \mathbf{u} = -\nabla p + \frac{1}{Re} \nabla^2 \mathbf{u} \text{ in } \Omega \tag{2.2}$$

where the fluid velocity $\mathbf{u}$ and the pressure p are functions of space x and time t in a computational domain $\Omega \subset \mathbb{R}$. The Reynolds number of the flow, $Re = \frac{U_\infty D}{\nu}$ is based on the free stream velocity U_∞, a characteristic length *D* as the cylinder diameter and the kinematic viscosity of the fluid, ν.

Eq. (2.1) and (2.2) are subject to proper initial and boundary conditions. The initial condition specifies the velocity field at time *t=0* such as, $\mathbf{u}=\mathbf{u}^0$. On the cylinder surface, the

instantaneous fluid velocity is equal to the cylinder velocity, $\mathbf{u} = \mathbf{u}(x,t)$. In the present problem of flow past a cylinder, we will consider Dirichlet boundary conditions on the inflow and lateral boundaries of the flow domain.

A serious difficulty to overcome when solving numerically Eq. (2.1) and (2.2) is the coupling between the incompressibility condition and calculation of the pressure field. The incompressibility condition represents a constraint for the velocity filed whereas the pressure variable derived from the momentum equation provides the extra degrees of freedom to satisfy that constraint. For this reason, we calculate the pressure field by an implicit time scheme instead of an explicit one. The pressure equation is derived by taking the gradient of Eq. (2.2) and considering the incompressibility requirement Eq. (2.1), yielding the pressure Poisson equation:

$$\Delta p = \nabla(-\mathbf{u}\cdot\nabla\mathbf{u}) \tag{2.3}$$

For the spatial descritization of Eq. (2.1) and (2.2) a spectral element method is used, whereas a discrete splitting scheme is used for the temporal descritization.

2.4. Spatial discretization

The SEM spatial discretization is based on a weak formulation of Eq. (2.1) and (2.2) and implementation of a Galerkin method. In contrast to the strong formulation of the problem, the weak formulation provides a lower solution regularity for velocity and pressure, along with proper natural boundary conditions.

We assume that Eq. (2.1) and (2.2) are multiplied by a test function (**v**, *q*) and integrated over a computational reference domain *Ω.* Here, the functional spaces for the velocity **v** and pressure *q* are denoted as $X:=H_0^1(\Omega)^d$ and $Z:=L_0^2(\Omega)$ respectively, where *d* refers to the space dimension (*d=2* or *3*). The integration of pressure and viscous term is done by parts. Then the problem in the weak formulation reads:

*Find a solution (***u***(t), p(t))* $\in X\times Z$ *such that, for almost every t* $\in (0,T)$:

$$(\nabla\cdot\mathbf{u},q) = 0 \qquad \forall\, q \in Z \tag{2.4}$$

$$\frac{d}{dt}(\mathbf{v},\mathbf{u}) + (\mathbf{v},\mathbf{u}\cdot\nabla\mathbf{u}) = (p,\nabla\cdot\mathbf{v}) - \frac{1}{Re}(\nabla\mathbf{v},\nabla\mathbf{u}) \qquad \forall\, \mathbf{v} \in X \tag{2.5}$$

$$\mathbf{u}(0) = \mathbf{u}^0 \tag{2.6}$$

where the inner comma (,) in the above equations is defined as:

$$(v,u) := \int_\Omega vu\,dx \tag{2.7}$$

In SEM spatial descritization, the first step is to split the domain $\bar{\Omega} = \Omega \cup \partial\Omega$ into *E* quadrilateral (in $\mathbb{R}^2$) or hexahedral (in $\mathbb{R}^3$) spectral elements, Ω^e, with non-overlapping sides, where *e* = 1, . . . , *E*. The common sides between the elements will create an edge, a face or a vertex. Each element will involve a separate discretization mesh with the same number of collocation points in each direction. The dependant variables in each element are expanded in terms of Lagrange polynomials using Gauss-Lobatto-Legendre (GLL) collocation points. In each spatial direction, the number of collocation points in each element corresponds to the order of the polynomials plus one *(N+1)*. To obtain convergence it can be increased either the number of elements or the number of collocation points.

By applying the Galerkin approximation we define the sub-spaces $X_N \subset X$ *and* $Z_N \subset Z$ for the velocity and pressure respectively, in which we calculate the approximation for the velocity and pressure. To reduce the spurious modes in pressure, a staggered grid approach for discretization, introduced by Maday and Patera (1989), can be used where the interpolants for pressure are polynomials of two degrees lower than for velocities.

The representation of a single element $\mathbf{u} \in X_N$, where X_N is a space of N^{th}-order Lagrange polynomial interpolants, in two-dimensions is:

$$\mathbf{u}(x^e(r,s))\Big|_{\Omega^e} = \sum_{i=0}^{N}\sum_{j=0}^{N} \mathbf{u}_{ij}^e h_i^N(r) h_j^N(s) \qquad \forall\, r,s \in \hat{\Omega} := [-1,1]^2 \tag{2.8}$$

where the indices *i, j* refer to the Lagrangian GLL grid nodes, $x^e(r, s)$ is the mapping coordinate of the reference domain element $\hat{\Omega}$ to the physical domain element Ω^e (see **Figure 2-1**) and $\mathbf{u}_{ij}^e$ is the basis coefficient corresponding to *e* element. Also $h_i^N(r)$ and $h_j^N(s)$ are the basis functions of Lagrangian interpolants of *N* degree at (GLL) quadrature points, in a local element Ω^e. The Lagrangian interpolants satisfy the condition $h_i^N(\xi_j^N) = \delta_{ij}$ where, ξ_j^N is one of the *(N+1)* GLL quadrature points and δ_{ij} is the Kronecker delta.

The Gauss-Lobatto-Legendre integration scheme involves the integrated polynomials of the Galerkin projection. It is considered a very accurate integration scheme for smooth integrals, Karniadakis and Sherwin (2005). The form of the integral is:

$$\int_{-1}^{1} u(x)dx \tag{2.9}$$

The integrand represents a Lagrange polynomial of *Q* points x_i, specified as, e.g.:

$$u(x) = \sum_{i=0}^{Q-1} u(x_i) h_i(x) + e(u) \tag{2.10}$$

where $e(u)$ accounts for the integration error.

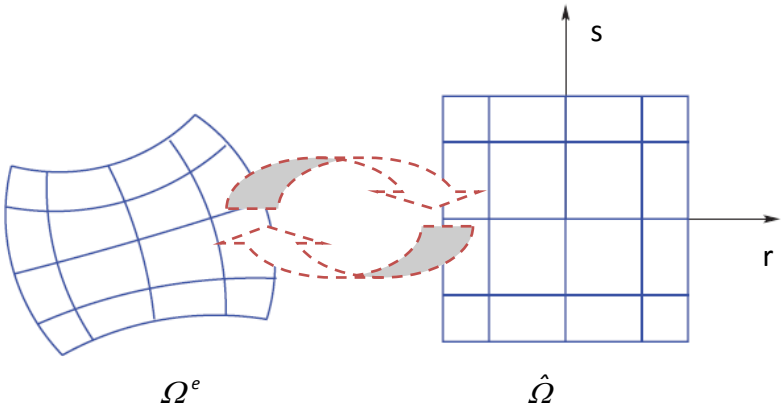

Figure 2-1: Sketch of transformation from physical domain Ω^e to a local spectral element (computational domain) $\hat{\Omega}$ and backwards, for a two-dimensional case. Deville et al. (2004)

Substituting this into Eq. (2.9) yields:

$$\int_{-1}^{1} u(x)dx = \sum_{i=0}^{Q-1} w_i u(x_i) + R(u) \tag{2.11}$$

where

$$w_i = \int_{-1}^{1} h_i(x)dx \quad \text{and} \quad R(u) = \int_{-1}^{1} e(u)dx \tag{2.12}$$

The integration of a polynomial *u(x)* of order *Q−1* or less is considered exact if *R(u)=0* for *u(x)* ∈ [−1, 1]. However, as introduced by Gauss a specific choice of integration points, results in an exact integration and can be accomplished even for polynomial order higher than *Q−1*. The Gauss-Lobatto-Legendre method differs from the other Gauss quadrature formulations in the selection of the end points.

Taking $x_{i,N}^{\alpha,\beta}$ as the *N* zeros of the N^{th}-order Jacobi polynomial such that:

$$P_N^{\alpha\beta}(x_{i,N}^{\alpha,\beta}) = 0, \qquad i = 0,1,\ldots,N-1 \tag{2.13}$$

where

$$x_{0,N}^{\alpha,\beta} < x_{1,N}^{\alpha,\beta} < \ldots < x_{N-1,N}^{\alpha,\beta} \tag{2.14}$$

For a Legendre polynomial of order *Q−1* the Gauss-Lobatto-Legendre quadrature can be defined as:

$$x_i = \begin{cases} -1, & i = 0 \\ x^{1,1}_{i-1,Q-2}, & i = 1,\ldots/Q-2 \\ 1, & i = Q-1 \end{cases}$$

$$w_i = \frac{2}{Q(Q-1)\left[L_{Q-1}(x_i)\right]^2}, \quad i = 0,\ldots,Q-1 \tag{2.15}$$

$$R(u) = 0, \qquad if \quad u(x) \in [-1,1]$$

where $L_{Q-1}(x_i)$ is the Legendre polynomial.

The last line in Eq. (2.15) denotes that the integration is exact for a polynomial order less than $2Q-1$. In other words, for a fixed order N, the integrand yields:

$$Q_{min} \geq \frac{N+1}{2} \tag{2.16}$$

Proceeding with the spectral element descretization we insert Eq. (2.8) into Eq. (2.4) and (2.5) and apply GLL quadrature for the integrals. Then, we write the semi-discretized equations in matrix notation:

$$B\frac{d\underline{\mathbf{u}}}{dt} = D^T \underline{p} - C(\underline{\mathbf{u}})\underline{\mathbf{u}} - \frac{1}{Re}K\underline{\mathbf{u}} \tag{2.17}$$

$$-D\underline{\mathbf{u}} = 0 \tag{2.18}$$

where B is the diagonal mass matrix, K is the stiffness matrix, $C(\underline{u})$ is the non-linear operator and D, D^T represent the discrete divergence operator and gradient operator, respectively.

2.5. Temporal discretization

The numerical treatment of the velocity and the pressure field in the Navier-Stokes equations involves methods for the correction of pressure as well as the correction of velocity. In pressure-correction methods first a Helmholtz equation is solved for an intermediate velocity field, and then a pressure-correction is calculated to satisfy incompressibility for the final velocity field, see Chorin (1968), Kim and Moin (1985), Israeli et al. (1986). In velocity-correction methods the non-linear terms are solved explicitly in an intermediate velocity field and then, the velocity is extended by treating the viscous term implicitly via a Helmholtz equation. Thus the exact incompressibility of velocity field at the end is lost. A new method of splitting schemes known as *consistent splitting* schemes was introduced by Guermond and Shen (2003). The method is based on a weak formulation of the pressure Poisson equation where the velocity is solved by a Helmholtz equation and the pressure by a Poisson equation.

The temporal descritization for the numerical solution of incompressible unsteady Navier-Stokes equations prescribes the form of the governing equations of pressure and velocity. In particular in our study the pressure governing equation is a Poisson equation taken from the momentum equation satisfying the constraint of incompressibility. It is known that in the equation of pressure the problem is to impose the correct boundary conditions. When Neumann boundary condition was implemented for pressure in the studies of Gresho and Sani (1987) and Orszag et al. (1986) a correct solution for pressure was reported.

2.5.1 Time splitting scheme

For the descritizaton of Eq. (2.1) and Eq. (2.2) we use the fractional-step scheme proposed by Karniadakis et al. (1991). The method treats the viscous term of the Navier Stokes equations implicitly using a backward difference scheme whereas it treats the convection terms explicitly. More details about the theoretical background of the method can be found in Yanenko (1971), Chorin (1968) as well as in Maday et al. (1990), where a general decomposition methodology is presented.

The time splitting scheme introduced by Karniadakis et al. (1991) is a stiffly stable scheme based on an operator splitting technique that decouples velocity and pressure into several substeps that can be solved separately with implicit and explicit techniques.

For a two-dimensional flow field the Navier Stokes equations can be written with the use of operator factors *L(u)* and *N(*u*)* as follows :

$$\nabla \cdot \mathbf{u} = 0$$

$$\frac{\partial \mathbf{u}}{\partial t} = -\nabla p + \frac{1}{Re} L(\mathbf{u}) + N(\mathbf{u}) \tag{2.19}$$

Where **u**, *p* are the normalized velocity and pressure, *Re* is the Reynolds number; *L(***u***)* is an operator for the linear diffusion term and *N(***u***)* for the non-linear convection term. Those operators are defined as:

$$\begin{aligned} L(\mathbf{u}) &= \nabla^2 \mathbf{u} \\ N(\mathbf{u}) &= -(\mathbf{u} \cdot \nabla)\mathbf{u} \end{aligned} \tag{2.20}$$

To estimate the time derivative of an equation $\frac{\partial u}{\partial t} = f$ in a multistep method we use:

$$\frac{1}{\Delta t}(\gamma_0 u^{n+1} - \sum_{i=0}^{J-1} a_i u^{n-i}) \tag{2.21}$$

where γ_0 is : $\gamma_0 = \sum_{i=0}^{J-1} a_i$ for consistency reasons.

Thus Eq. (2.21) can be written:

$$\frac{1}{\Delta t}\sum_{i=0}^{J-1} a_i (u^{n+1} - u^{n-i}) = \frac{1}{\Delta t}\sum_{i=0}^{J-1} a_i \int_{(n-1)\Delta t}^{(n+1)\Delta t} \frac{\partial u}{\partial t} dt = \frac{1}{\Delta t}\sum_{i=0}^{J-1} a_i \int_{(n-1)\Delta t}^{(n+1)\Delta t} f dt \tag{2.22}$$

The integrand on the right hand side of Eq. (2.22) can be split into several parts, and each part can be evaluated implicitly or explicitly. Thus the momentum equation in Eq. (2.19) can be written as:

$$\frac{\gamma_0 \mathbf{u}^{n+1} - \sum_{q=0}^{J_i-1} a_q (\mathbf{u}^{n-q})}{\Delta t} = -\nabla \overline{p}^{n+1} + \frac{1}{Re}\mathbf{L}(\mathbf{u}^{n+1}) + \sum_{q=0}^{J_e-1} \beta_q \mathbf{N}(\mathbf{u}^{n-q}) \tag{2.23}$$

The time integration of the Eq. (2.23) is done into three separate sub-steps. The first of the three sub-steps computes explicitly the non-linear term of the velocity field **u**, using a third order Adams-Bashforth technique as follows:

$$\frac{\hat{\mathbf{u}} - \sum_{q=0}^{J_i-1} a_q (\mathbf{u}^{n-q})}{\Delta t} = \sum_{q=0}^{J_e-1} \beta_q \mathbf{N}(\mathbf{u}^{n-q}) \tag{2.24}$$

Where $\hat{\mathbf{u}}$ is the intermediate velocity field, n refers to the level of time, $\mathbf{u}^{n+1}$ is an approximation from the previous iteration of velocity, a_q and β_q are the appropriate Adams-Bashforth coefficients for stiffly stable integration, and J_i, J_e are the order for the implicit and explicit solution, respectively. In **Table 2-1** the values of γ_0, a_q and β_q coefficients are presented for different values of scheme order. More details can be found in Karniadakis et al. (1991).

Table 2-1: Coefficients for up to third order stiffly stable schemes

Coefficient	*1st Order*	*2nd Order*	*3rd Order*
γ_0	1	3/2	11/6
α_0	1	2	3
α_1	0	-1/2	-3/2
α_2	0	0	1/3
β_0	1	2	3
β_1	0	-1	-3
β_2	0	0	1

The second sub-step is the pressure correction step which is written as:

$$\frac{\hat{\hat{\mathbf{u}}}-\hat{\mathbf{u}}}{\Delta t}=-\nabla \overline{p}^{n+1} \tag{2.25}$$

where $\hat{\hat{\mathbf{u}}}$ is the second intermediate value of the velocity field and $\overline{p}^{n+1}$ is the pressure field that ensures the incompressibility condition for the velocity at the end of *n+1* step:

$$\int_{t_n}^{t_{n+1}} \nabla p dt = \Delta t \nabla \overline{p}^{n+1} \tag{2.26}$$

The divergence of Eq. (2.25) leads to a Poisson equation for the pressure:

$$\nabla^2 \overline{p}^{n+1} = \nabla \cdot (\frac{\hat{\mathbf{u}}}{\Delta t}) \tag{2.27}$$

This requires the following Neumann pressure boundary condition to be implemented for this sub-step:

$$\frac{\partial \overline{p}^{n+1}}{\partial n} = \mathbf{n} \sum_{q=0}^{J_e-1} \beta_q \left[N(\mathbf{u}^{n-q}) - \frac{1}{Re} \nabla \times \nabla \times \mathbf{u}^{n-q} \right] \text{ on } \partial\Omega \tag{2.28}$$

where Ω is the boundary surface and **n** is the unit vector normal to the surface. This method, proposed by Karniadakis et al. (1991), sets a condition for the normal pressure gradient at the boundary using the solution from the previous steps. The accuracy of the time splitting scheme of Karniadakis et al. (1991) is found to be one order higher than the order used to extrapolate the pressure boundary conditions.

The third sub-step involves the viscous term, and consists in the solution of a Helmholtz equation:

$$\frac{\gamma \mathbf{u}^{n+1} - \hat{\hat{\mathbf{u}}}}{\Delta t} = \frac{1}{Re} L(\mathbf{u}^{n+1}) \tag{2.29}$$

The three sub-steps sequence is followed, with the updated fluid velocity u^{n+1} advancing the solution in time.

In this thesis we used a parallel code based on the SEM method discussed above to simulate the incompressible fluid flow past a cylinder. Details about the problem formulation and the boundary conditions can be found in section 4.3.2. Resolution tests, demonstrating the adequacy of the discretization utilized can be found in Appendix A.

Chapter 3

Parallel Processing

3.1 Background

The present study involves Direct Numerical Simulation (DNS) of two and three-dimensional flow past a circular cylinder, oscillating both transversely and in-line with respect to a uniform flow at Reynolds number *Re=400*. In this Reynolds number range, the flow is fully three-dimensional; thus three-dimensional simulations must be used to accurately predict the flow dynamics and forces.

We have used an MPI-based spectral element parallel code. The code has been tested in terms of parallel efficiency, both for three-dimensional and two-dimensional flow.

3.2 Code validation

We have validated the present code for: (a) the case of flow past a stationary cylinder against the computational two dimensional results of Henderson (1995) (b) the case of three-dimensional flow past a stationary cylinder against the experimental results of Wieselberger (1921) (c) the case of flow past a cylinder oscillating transversely to a free stream, against the computational results of Kaiktsis et al. (2007).

Here we have used a two-dimensional spatial discretization of 464 macro-elements, with *5×5* and *9×9* elemental resolution, for several values of Reynolds number from 10 to 400, in order to compare the results of the flow past a stationary cylinder with those of Henderson (1995). In **Figure 3-1** the computed values of the time-averaged drag coefficient, $<C_D>$ (see definition in section 4.2.1.2) are presented at different Reynolds numbers. We observe that our simulations match the numerical results of Henderson (1995). Further, in **Figure 3-1** results of three-dimensional simulations are presented, and compared against the experiment of Wieselberger (1921), indicating a very good agreement.

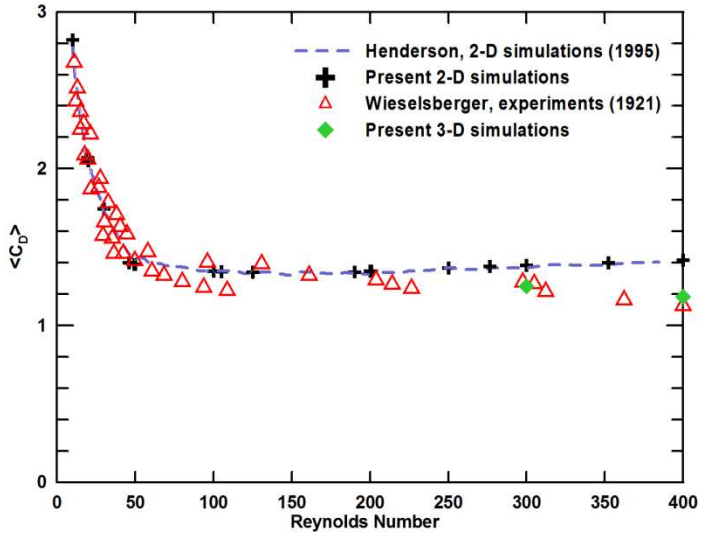

Figure 3-1: Time-averaged drag coefficient versus Reynolds number in flow past a stationary cylinder. Present two-dimensional and three-dimensional simulations and literature studies are presented.

We also compare the present results of two- and three-dimensional flow past a stationary cylinder with the numerical results in the review paper of Norberg (2003). In **Figure 3-2** the computed values of the RMS fluctuation of the lift coefficient, $C_{L,RMS}$ (see definition in section 4.2.1.1) are presented for different Reynolds numbers. A good agreement is demonstrated between the present simulations and the numerical results presented in Norberg (2003).

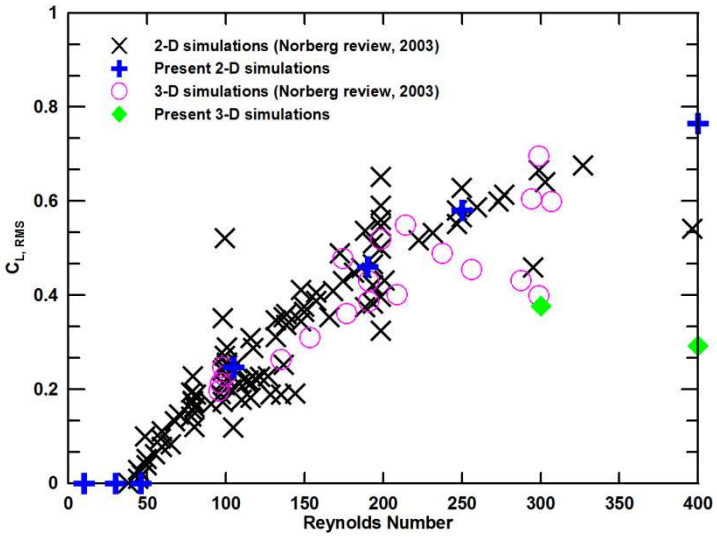

Figure 3-2: RMS fluctuation intensity of lift coefficient versus Reynolds number in flow past a stationary cylinder. Present two-dimensional and three-dimensional simulations and literature studies are presented.

To further validate the code, we performed two-dimensional simulations of the flow past a circular cylinder oscillating transversely to a uniform flow, at *Re=400.* The oscillation frequency ratio was $F=f_y/f_s=1.0$, where f_y is the excitation and f_s is the Strouhal frequency. The transverse oscillation amplitude was $A_y/D=0.10$. The computed values of force coefficients (see definitions in section 4.2.1) are presented in **Table 3-1**, illustrating a very good agreement with the results in Kaiktsis et al. (2007).

Table 3-1: Force coefficients of two-dimensional flow past a cylinder oscillating transversely with respect to a uniform stream, at Reynolds number 400. Here, the frequency ratio is $F=1.0$ and the transverse oscillation amplitude $A_y/D=0.10$.

	C_{Lv}	C_M	C_{La}	$C_{L,RMS}$	$<C_D>$	$C_{D,RMS}$
Kaiktsis et al. (2007)	0.952107	-1.955304	-0.587760	0.791597	1.523790	0.141632
Present work	0.949735	-1.967934	-0.591556	0.792110	1.522300	0.140870

3.3 Parallel performance

The simulations of the incompressible three-dimensional flow past an oscillating cylinder require fine resolution in all three flow directions. We have performed the present flow simulations with the spectral element parallel solver *Nek5000*. The solver is documented in detail by Fischer (1997), Fischer et al. (2000) and in the relevant webpage (*http://nek5000.mcs.anl.gov*).

The discretization consisted of spectral elements in the in line-vertical planes (x-y planes) as well as in the spanwise direction (z-direction). Within each element, the field unknowns are expressed in term of high-order interpolants, which are based on Legendre polynomials. The number of collocation points in one direction is equal to the polynomial degree plus one. Thus an elemental resolutions of e.g. $8\times8\times8$ corresponds to polynomials of seventh order. A third-order accurate semi-implicit splitting scheme was employed for time integration Karniadakis et al. (1991). Periodic boundary conditions are employed for the two end planes in the spanwise direction.

The present study evaluates the capability of the parallel algorithm to properly utilize an increasing number of processors (scalability). Parallel computing requires efficient communication between multiple processors. The scalability of an algorithm is characterized by the speed-up factor indicating the turnaround time gain, in comparison to execution on one single processor. Ideally, in the absence of communication latency, the speed-up factor should increase linearly with the number of processor cores. Here performance tests for the present problem and discretization parameters are reported.

The simulations have utilized a parallel cluster at ETH Zurich. Here, 12-core AMD CPUs were used, with 32 GB of RAM each. The cluster has a total of 17,000 cores with a peak performance of approximately 180 teraflops. The present tests consisted of simulations with a total of 100 time-steps. The computational grid consisted in total of 20560 elements.

Figure 3-3 presents the turnaround time per time-step for $6\times6\times6$ and $8\times8\times8$ elemental resolution. The computations illustrate a sharp decrease in CPU time for a number of processors up to 256, which is less pronounced at higher processor number. The results also indicate that the overhead at increased resolution decreases with the number of processors.

Speed-up factor: *The speed-up factor is expressed as the ratio of turnaround CPU time for a low number of processors to the corresponding time for a higher processor number*.

Here, the reference value is based on the CPU time for 64 processors. The results are presented in **Figure 3-4**. In accordance with the results of **Figure 3-3**, the speed-up increases almost linearly at relatively low number of processors. For a processor number higher of 512 ($N_{processors}$/64=8) the speed-up rate is lower than linear.

Similar tests of three-dimensional simulation were performed on a parallel cluster of CSLAB in the School of Electrical and Computer Engineering of NTUA; these tests also included two-dimensional simulations. In particular 8-core INTEL CPUs were used, with 2GB of RAM each.

The cluster has a total of 256 cores. Here a smaller number of processors were utilized ranging from 16 to 48 processors. The present tests consisted of simulations with a total of 100 time-steps. The computational grid of three-dimensional simulations consisted in total of 20560 elements with *7X7X7* elemental resolution whereas the grid of two-dimensional simulations consisted of 2056 elements with *9X9* elemental resolution. The corresponding plots of turnaround CPU time per time-step and speed-up factor are presented **Figure 3-5** and **Figure 3-6**, respectively. Noting the lower number of processors, the trends are those identified for the ETH Zurich cluster, at low processor number.

3.4 Conclusion

After a number of validation tests, scaling simulations were performed to measure the performance of the parallel code used in the DNS of flow past a cylinder. The results have demonstrated that the numerical algorithm is scaling well on different computing machines. The speed-up factor increases almost linearly with the number of processors, for a number of processors up to 256. For high number of processors the speed-up is not linear but remains satisfactory. In general, the speed-up increases with the problem size.

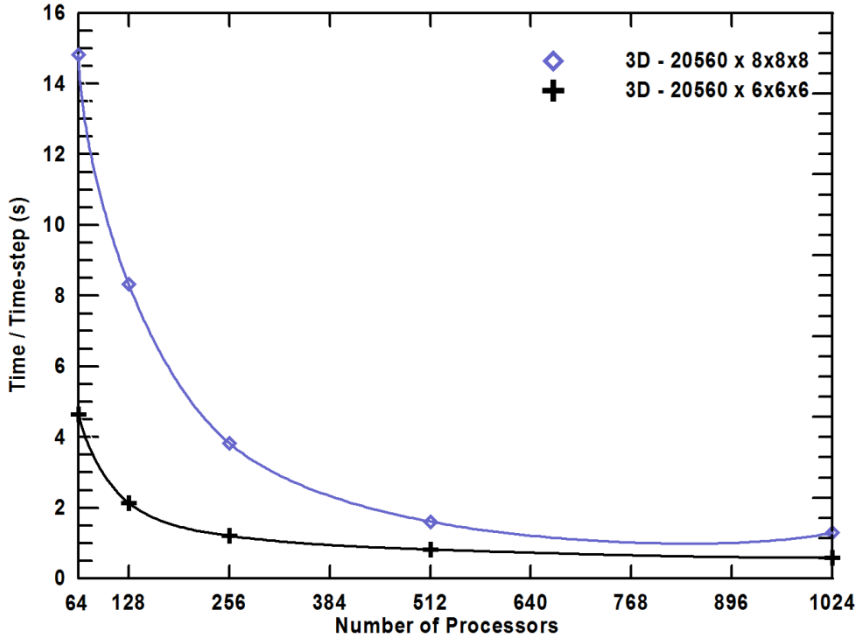

Figure 3-3: Turnaround time/time-step versus number of processors of three-dimensional simulations on a parallel AMD Opteron cluster.

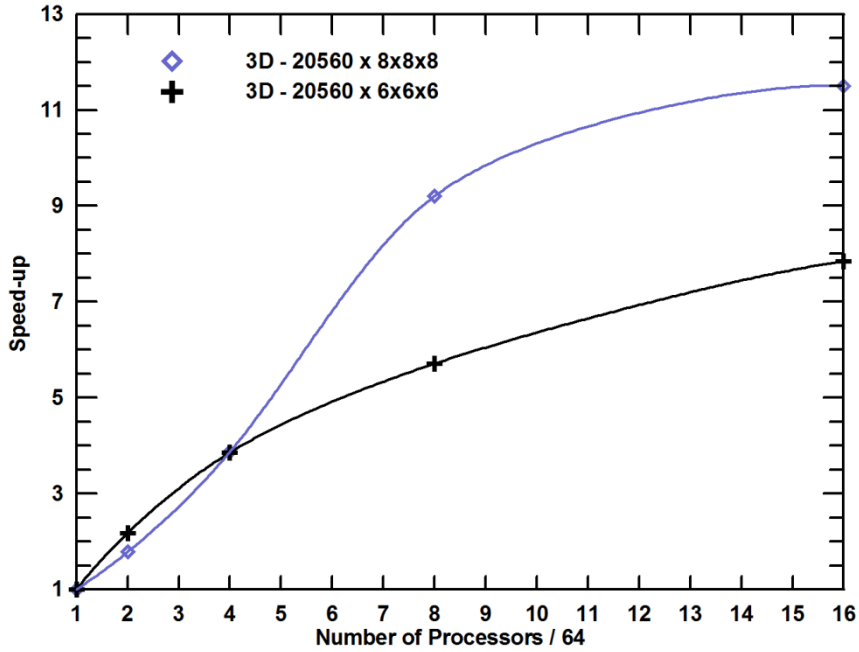

Figure 3-4: Speed-up factor versus normalized number of processors of three-dimensional simulations on a parallel AMD Opteron cluster. The reference simulation is performed on 64 processors.

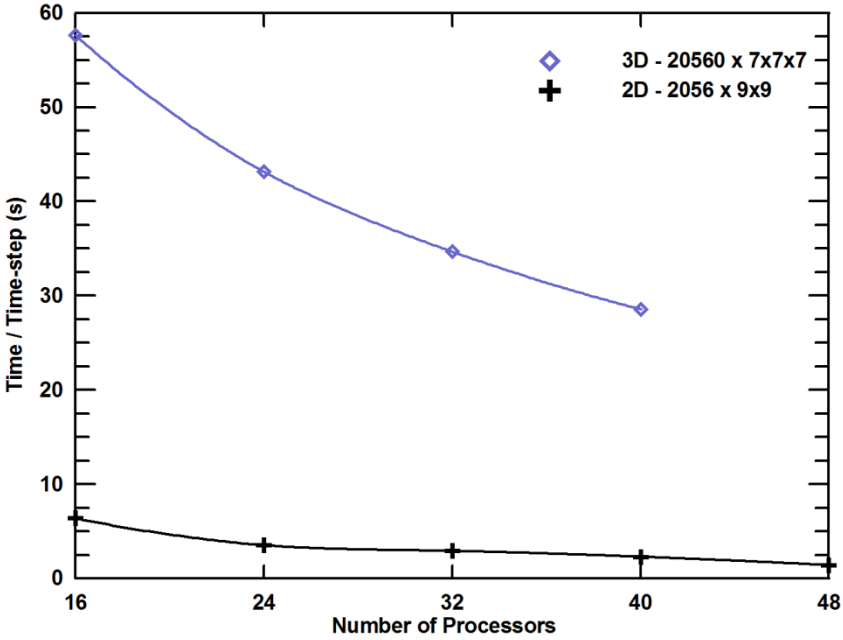

Figure 3-5: Turnaround time/time-step versus number of processors of two- and three-dimensional simulations on a parallel Intel Xeon cluster.

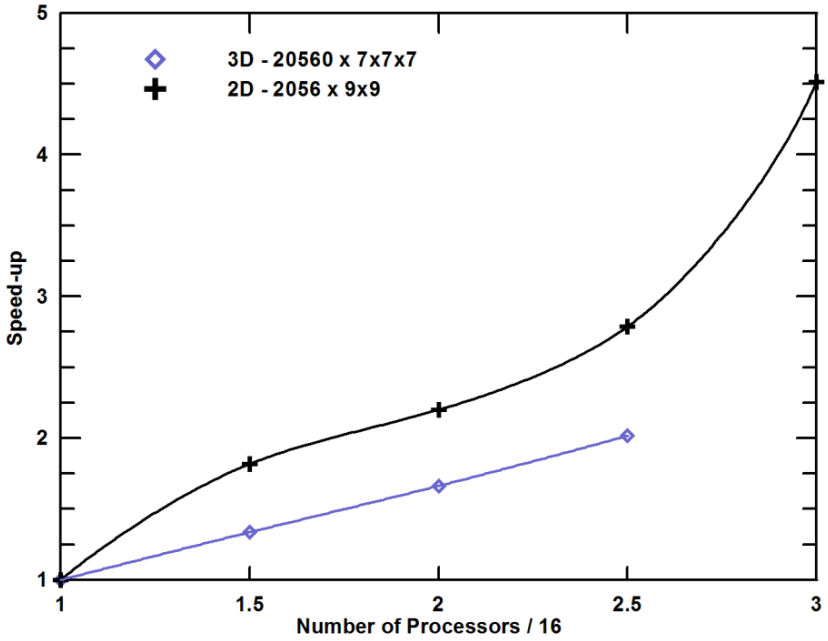

Figure 3-6: Speed-up factor versus normalized number of processors of two- and three-dimensional simulations on a parallel Intel Xeon cluster. The reference simulation is performed on 16 processors.

Chapter 4

Two-Dimensional Flow

4.1 Background

This chapter presents computational results of the two-dimensional flow past a cylinder oscillating transversely and in-line with respect to a uniform stream, at Reynolds number 400. The in-line oscillation frequency (f_x) is equal to twice the transverse frequency (f_y) thus, the cylinder follows a figure *eight* motion. Three values of the transverse oscillation frequency are considered, close to the natural frequency of the Kármán vortex street. The ratio of in-line to transverse oscillation amplitude, $\varepsilon = A_x / A_y$, is equal to 0.2 or 0.4, while the values of transverse amplitude over diameter ratio correspond to excitation, i.e. positive power transfer from the fluid to the cylinder.

For a flow stream from left to right, we distinguish between a counter-clockwise mode and a clockwise mode, if the upper part of the trajectory is traversed counter-clockwise or clockwise, respectively. We study the relation of force coefficients and power transfer to the direction of the cylinder trajectory (counter-clockwise or clockwise) and to the flow states. We use the time histories and power spectra to investigate the responses associating with vortex-induced vibrations. We correlate the wake structures to the calculated forces acting on the cylinder.

4.2 Problem definition

We consider a cylinder oscillating both transversely and in-line to a uniform stream, following a figure *eight* trajectory. The velocity of the fluid far upstream of the cylinder is U_∞, the density and kinematic viscosity of the fluid are ρ and ν respectively. The Reynolds number of the flow, defined in terms of the free stream velocity (U_∞) and the cylinder diameter *(D)*, is equal to *400*, the same value as in previous studies Kaiktsis et al. (2007). We use a Cartesian coordinate system formed by x-axis, parallel to the incoming flow, and y-axis, normal to the flow. The cylinder is oscillating around its mean position; the in-line oscillation frequency is twice the transverse frequency, $f_x=2f_y$. The instantaneous displacement of the cylinder in x- and y-direction is:

$$\eta_y = A_y \sin(2\pi f_y t) \tag{4.1}$$

$$\eta_x = \pm A_x \sin(2\pi f_x t) = \pm A_x \sin(4\pi f_y t) \tag{4.2}$$

For a flow stream from left to right, the plus (+) sign in Eq. (4.2) corresponds to a motion which is counter-clockwise in the upper x-y plane, and the minus (-) sign to a clockwise motion in the upper x-y plane.

4.2.1 Hydrodynamic forces and power transfer parameter

The fluid forces of the cylinder in the in-line and transverse direction are the drag and lift force acting on the cylinder. We calculate the lift and drag forces by integrating the pressure

and viscous stress terms around the cylinder. For a locked-in wake, the lift and drag forces per cylinder unit length, F_y, F_x are harmonic in time with frequency f_y and f_x respectively, and can be both decomposed into the excitation force and the inertia or added mass force, as follows:

$$F_y = F_v \cos(2\pi f_y t) + F_M \sin(2\pi f_y t) \tag{4.3}$$

$$F_x = F_{vx} \cos(2\pi f_x t) + F_{Mx} \sin(2\pi f_x t) \tag{4.4}$$

where F_v and F_{vx} are the amplitudes of the excitation forces, while F_M and F_{Mx} are the amplitudes of the added mass forces. The amplitudes of the harmonic forces can be readily calculated from the force signals:

$$F_v + iF_M = \frac{2}{T}\int_0^T F_y \exp(2\pi f_y t)dt \tag{4.5}$$

$$F_{vx} + iF_{Mx} = \frac{2}{T}\int_0^T F_x \exp(4\pi f_y t)dt \tag{4.6}$$

where $i = \sqrt{-1}$ και $T = 1/f_y$ is the period of the cylinder oscillation in the y-direction.

It is commonly assumed that the excitation forces are proportional to the dynamic pressure, and that the inertia forces are proportional to the cylinder acceleration. On this basis, non-dimensional excitation coefficients, C_{Lv}, C_{Dv} and inertia coefficients, C_M, C_{Mx} can be defined:

$$F_v = \frac{1}{2}\rho U_\infty^2 D C_{Lv} \tag{4.7}$$

$$F_{vx} = \frac{1}{2}\rho U_\infty^2 D C_{Dv} \tag{4.8}$$

$$F_M = \frac{\pi}{4}\rho D^2 A_y (2\pi f_y)^2 C_M \tag{4.9}$$

$$F_{Mx} = \frac{\pi}{4}\rho D^2 A_x (2\pi f_x)^2 C_{Mx} \tag{4.10}$$

As the excitation and inertia forces are components of the same force, we also consider scaling the inertia components with the dynamic pressure, thus introducing the inertia coefficients, C_{La}, C_{Da}:

$$F_M = \frac{1}{2}\rho U_\infty^2 D C_{La} \tag{4.11}$$

$$F_{Mx} = \frac{1}{2}\rho U_\infty^2 D C_{Da} \tag{4.12}$$

The relationship between the inertia coefficients can be readily obtained: $C_{La} = 2\pi^3 (A_y / D)(\frac{D/U_\infty}{T})^2 C_M$, $C_{Da} = 8\pi^3 (A_x / D)(\frac{D/U_\infty}{T})^2 C_{Mx}$ where T is the cylinder oscillation period in the y-direction.

From dimensional analysis it follows that all non-dimensional force coefficients are functions of: the Reynolds number, the reduced y-amplitude A_y / D, the relative x-amplitude $\varepsilon = A_x / A_y$ and the reduced oscillation frequency $F = f_y / f_s$, (where f_s is the natural frequency of the Kármán vortex street). Each of the two directions in which the figure *eight* trajectory is traversed defines a different physical problem, thus the dynamics also depends on the oscillation mode (counter-clockwise or clockwise).

4.2.1.1 Lift force

The total lift is scaled with the dynamic pressure, yielding the lift coefficient:

$$F_y = \frac{1}{2}\rho U_\infty^2 D C_L \tag{4.13}$$

The instantaneous lift coefficient, C_L can be decomposed into the time-averaged value, $< C_L >$ and an instantaneous fluctuation, C_L', i.e. $C_L = < C_L > + C_L'$ where $< C_L >= \frac{1}{T}\int_0^T C_L dt$.

We will denote the root mean square (R.M.S.) of C_L' by $C_{L,RMS}$. When the forces on the cylinder are harmonic in time, the value of $C_{L,RMS}$ is defined as:

$$C_{L,RMS} = \frac{1}{\sqrt{2}}\sqrt{C_{Lv}^2 + C_{La}^2} \tag{4.14}$$

In the present study, we use MATLAB to calculate mean and the RMS values of the hydrodynamic forces. The RMS value of a signal's fluctuations is defined as:

$$C_{L,RMS} = \sqrt{\overline{(C_L - < C_L >)^2}} \tag{4.15}$$

where the over-line signify mean value.

4.2.1.2 Drag force

The total drag force as showed above is also scaled with the dynamic pressure, yielding the drag coefficient, respectively:

$$F_x = \frac{1}{2}\rho U_\infty^2 D C_D \tag{4.16}$$

Correspondingly, the decomposition of the drag coefficient, C_D is: $C_D = < C_D > + C_D'$ where $< C_D >= \frac{1}{T}\int_0^T C_D dt$ and the root mean square (RMS) of C_D' by $C_{D,RMS}$ where:

$$C_{D,RMS} = \frac{1}{\sqrt{2}}\sqrt{C_{Dv}^2 + C_{Da}^2} \tag{4.17}$$

The RMS value of a signal's fluctuations is also defined as Eq. (4.15) : $C_{D,RMS} = \sqrt{\overline{(C_D - < C_D >)^2}}$

4.2.1.3 Power transfer parameter

In vortex-induced vibrations, the power transfer parameter is an important quantity, as positive values correspond to excitation, and negative values to damping. The power transfer parameter is defined as the integral in time over one cycle of motion of the total force times the velocity:

$$P(t) = F_{Hydro}(t) \cdot \frac{d\vec{\eta}}{dt} \tag{4.18}$$

where $\eta(t)$ is the instantaneous displacement of the cylinder from its mean position and $\frac{d\vec{\eta}}{dt}$ the instantaneous velocity of the cylinder.

For forced vibrations in two dimensions, the total power transfer parameter, *P*, consists of the sum of the corresponding contributions of energy in both the in-line and transverse directions:

$$P = P_x + P_y \tag{4.19}$$

where P_x and P_y denote the power transfer in the in-line and the transverse direction respectively. In general, these two components can be calculated by taking their time averaged values:

$$P = \lim_{T\to\infty} \frac{1}{T} \left\{ \int_t^{t+T} F_x(t) \frac{d\eta_x}{dt} dt + \int_t^{t+T} F_y(t) \frac{d\eta_y}{dt} dt \right\} \tag{4.20}$$

The time-averaged power transferred from the flow to the cylinder (per cylinder unit length) can be normalized by $\frac{1}{2}\rho U_\infty^3 D$ to yield the non-dimensional power transfer parameter:

$$P = \frac{2}{\rho U^3 D} \frac{1}{T} \left\{ \int_0^T F_x \frac{d\eta_x}{dt} dt + \int_o^T F_y \frac{d\eta_y}{dt} dt \right\} \tag{4.21}$$

4.2.1.4 Mean dissipation

The non-dimensional mean power dissipation $<P_d>$ is characteristic of the flow dynamics, with high values being representative of energetic flows. Considering that the energy of the flow-structure system is constant in mean, we apply the first law of thermodynamics to the system as $<P_d> + <P> = 0$ which is equivalent to $<P_d> = -(<P_x> + <P_y>)$ from Eq. (4.19).

Then the mean power dissipation is given by the following expression:

$$<P_d> = <F_x(U_\infty - \frac{d\eta_x}{dt})> - <F_y \frac{d\eta_y}{dt}> \tag{4.22}$$

where $\frac{d\eta_x}{dt}$ and $\frac{d\eta_y}{dt}$ are the in-line and vertical velocity components of the cylinder. Dividing by $\frac{1}{2}\rho U_\infty^3 D$ and using the definitions of coefficients $< C_D >$, C_{Dv} and C_{Lv} we obtain $< P_d >=< C_D > -2\pi C_{Dv}\frac{A_x}{D} f_y - \pi C_{Lv}\frac{A_y}{D} f_y$.

4.3 Flow field solution

4.3.1 Governing equations

The governing equations for the solution of our problem are the Navier–Stokes and incompressibility equations. For convenience, we non-dimensionalize all lengths with respect to *D*, all velocities with respect to the free stream velocity U_∞, time with respect to D/U_∞, and pressure with respect to ρU_∞^2. Then the incompressibility and Navier–Stokes read:

$$\nabla \cdot \vec{u} = 0 \tag{4.23}$$

$$\frac{\partial \vec{u}}{\partial t} + \vec{u} \cdot \nabla \vec{u} = -\nabla p + \frac{1}{Re}\nabla^2 \vec{u} \tag{4.24}$$

where $\vec{u}$ is the absolute velocity vector, and $Re = \frac{U_\infty D}{\nu}$ is the Reynolds number of the flow.

4.3.2 Problem formulation and boundary conditions

The boundary conditions to solve the equations (4.22) and (4.23) are as follows:

- On the cylinder surface, the instantaneous fluid velocity is equal to that of the cylinder:

$$\vec{u} = \vec{u}_x + \vec{u}_y = \frac{d\eta_x}{dt}\vec{i} + \frac{d\eta_y}{dt}\vec{j} \tag{4.25}$$

  where (η_x, η_y) is now the non-dimensional cylinder displacement, and $\vec{i}$, $\vec{j}$ are the unit vectors in the x and y directions.

- Far upstream and at the side boundaries we assume uniform flow with velocity equal to U_∞ :

$$\vec{u} = \vec{U}_\infty = 1\vec{i} \tag{4.26}$$

  where $\vec{i}$ is the unit vector in the x-direction.

- Far downstream we assume a Neumann-type boundary condition:

$$\frac{\partial \vec{u}}{\partial n} \approx 0 \tag{4.27}$$

To avoid the reconstruction of the computational grid at each time step, we use a frame of reference that is fixed on the cylinder. Taking that $\vec{u}$ represents the relative, with respect to the moving cylinder, velocity, the incompressibility equation remains the same, while the momentum equation changes to:

$$\frac{\partial \vec{u}}{\partial t} + \vec{u} \cdot \nabla \vec{u} = -\nabla p + \frac{1}{Re} \nabla^2 \vec{u} - \frac{d^2 \eta_x}{dt^2} \vec{i} - \frac{d^2 \eta_y}{dt^2} \vec{j} \tag{4.28}$$

i.e. at the right-hand side of Eq. (4.28) a d'Alambert acceleration is present. This means that, in order to find the actual force components acting on the cylinder, one has to subtract from the computed forces for lift and drag the "dynamic Archimedes" forces that are equal to $-(\frac{\pi}{4})\rho D^2 d^2 \eta_y / dt^2 \vec{j}$ and $-(\frac{\pi}{4})\rho D^2 d^2 \eta_x / dt^2 \vec{i}$ for the lift and drag force, respectively.

Moreover the flow boundary conditions are modified as follows:

- on the cylinder surface, the instantaneous fluid velocity is reduced to:

$$\vec{u} = 0 \tag{4.29}$$

- at the inflow and at the side boundaries :

$$\vec{u} = (\vec{U}_\infty - \frac{d\eta_x}{dt} \vec{i}) - (\frac{d\eta_y}{dt} \vec{j}) \tag{4.30}$$

- at the outflow the Neumann-type boundary condition is maintained, $\frac{\partial \vec{u}}{\partial n} \approx 0$.

4.4 Discretization

Equations (4.23), (4.28) subject to the above boundary conditions (4.27), (4.29) and (4.30) are solved using a spectral element method. The discretization in the x-y plane employs quadrilateral spectral elements, which are high-order finite elements with Legendre polynomials forming the expansion basis as tensor products in two dimensions. The size of the domain and discritization were selected according to previous numerical studies by Evangelinos and Karniadakis (1999), Blackburn and Henderson (1999), Delaunay and Kaiktsis (2001) and Kaiktsis et al. (2007) .

The inflow boundary is located at *x/D=-20*, the lateral boundaries at *y/D=±17*, and the outflow boundary at *x/D=60*. The spatial discretization consists of *464* macro-elements, with *9x9* elemental resolution. The time integration is based on a second-order accurate semi-implicit splitting scheme, Karniadakis et al. (1991). Typically, the values of the non-dimensional numerical time step were equal to *Δt=0.00075* to *0.0015*. The spectral element skeleton used is shown in **Figure 4-1**. Detailed spatial and temporal resolution tests have been performed, and are reported in Appendix A.1.

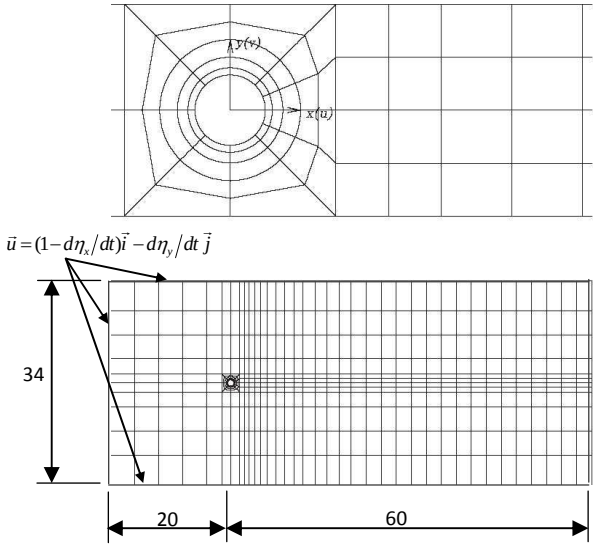

Figure 4-1: Spectral element skeleton for two-dimensional flow past a circular cylinder, including elements close to the cylinder, and the entire mesh. Velocity boundary conditions for a coordinate system fixed on the cylinder are also indicated.

4.5 Results

We have performed detailed numerical simulations of two-dimensional flow, for three values of frequency ratio *F* equal to *1.0*, *0.9* and *1.1*, corresponding to resonant, below-resonant and above resonant forcing. Two values of amplitude ratio $\varepsilon = A_x / A_y$ are considered, equal to *0.2* and *0.4*, for both the counter-clockwise and clockwise motion (see **Table 4-1**). The non-dimensional frequency of flow past a stationary cylinder is, f_s=0.22017 and the time-averaged drag coefficient is, $< C_D > = 1.4169$, values obtained from previous two-dimensional flow simulations (see Kaiktsis et al. (2007)) and verified by the present simulations.

Table 4-1: The parameter values of the present two-dimensional simulations

Parameter values	
Re	400
$F = f_y / f_s$	0.9, 1.0, 1.1
$\varepsilon = A_x / A_y$	0.2 , 0.4
A_y / D	0 – 0.80
motion	counter-clockwise & clockwise

The corresponding two-dimensional Navier-Stokes equations are integrated until a statistical "steady state" is reached, within which the flow mean quantities are time-independent. The reported flow statistics correspond to this state. In general, computations have been performed up to amplitudes for which negative values of the power transfer parameter are obtained.

4.5.1 Power transfer and hydrodynamic force coefficients

The total drag and lift signals of the statistical "steady state" are computed and analyzed as outlined in section 4.2.1, yielding the non-dimensional coefficients characterizing the flow. General statistics have been performed to the calculated forces over an integer number of periods when a "steady state" is reached. We present results for three different cases of cylinder oscillation frequency corresponding to oscillation at the natural frequency of vortex shedding (resonant forcing), oscillation at a frequency below the natural frequency and at a frequency above the natural frequency.

4.5.1.1 Resonant forcing

For *F*=1 (resonant forcing) the variation of power transfer parameter with respect to A_y / D is illustrated in **Figure 4-2**, for *ε=0.2* (counter-clockwise and clockwise modes), as well as for the case of transverse-only oscillation (*ε=0*). In counter-clockwise motion, the range of

A_y/D corresponding to positive *P* is larger, compared to either the clockwise mode or the case of transverse-only oscillation. The increase of the amplitude range of positive *P* is due primarily to the work of the fluctuating drag force which is in phase with the in-line velocity of the cylinder. (A small part of the increase is due to the work of the lift force, see **Figure 4-4**, A_y/D values greater than 0.50). We can conclude therefore that, for resonant forcing, the counter-clockwise mode is the worst case scenario for free vibrating cylinder, because it results to higher values of A_y/D.

Figure 4-3 illustrates the variation of the power transfer parameter versus A_y/D for *ε=0.4* (counter-clockwise and clockwise modes). In comparison to the *ε=0* case, the results shown in **Figure 4-3** illustrate a reduction in the y-amplitude range of positive power transfer, for both the oscillation modes. This reduction is larger for the clockwise motion.

Figure 4-4 - **Figure 4-11** illustrate the dependence of coefficients C_{Lv}, C_{Dv}, C_M, C_{La}, C_{Da}, $C_{L,RMS}$, $< C_D >$ and $C_{D,RMS}$ to the transverse oscillation amplitude, for *ε=0, 0.2* and *0.4*.

The variation of the coefficient C_{Lv} is shown in **Figure 4-4**. In all cases, there is correspondence with the *P* curves. For counter-clockwise mode, the C_{Lv} values are initially positive, drop at moderate oscillation amplitude, and eventually are becoming negative. For the clockwise mode, transition to negative values, corresponding to energy transfer from the cylinder to the flow, occurs at very low and at oscillation amplitudes higher than 0.30.

The variation of C_{Dv} is shown in **Figure 4-5**. For the counter-clockwise mode, the C_{Dv} values are in the majority of cases positive, i.e. the in-line cylinder motion transfers energy from the flow to the cylinder. The curves are characterized by a sudden drop at A_y/D values around *0.25*. In the case of clockwise motion, the C_{Dv} values remain negative, i.e. there is energy transfer from the cylinder to the flow.

Figure 4-6, presents the variations of the added mass coefficient C_M. For clockwise mode, as well as for *ε=0*, C_M tends to minus infinity for very low oscillations amplitudes, which suggests that there is a finite force in phase with the cylinder acceleration, see also Kaiktsis et al. (2007). Also in clockwise motion, C_M acquires very high positive values for oscillation amplitudes tending to zero, i.e., in this case, there is a finite force which is 180^o out of phase with the cylinder acceleration. This singular behaviour is eliminated by scaling the inertia force, F_M, with the dynamic pressure: the values of coefficient C_{La} shown in **Figure 4-7**, are bounded, and of the same sign as the values of the C_M coefficient.

The coefficient C_{Da} is illustrated in **Figure 4-8**. In counter-clockwise mode, the values are positive for small and moderate oscillation amplitudes, i.e. the inertia force F_{Mx} is 180^o out of phase with the cylinder acceleration in the in-line direction. The C_{Da} values are negative

for the clockwise mode, with the exception of a region of moderate oscillation amplitudes for *ε=0.2*.

The magnitude of non-dimensional lift forces versus the transverse oscillation amplitude, expressed in terms of the coefficient $C_{L,RMS}$ is illustrated in **Figure 4-9**. It is shown that, in clockwise motion, the lift fluctuations increase substantially with oscillation amplitude, while, in counter-clockwise motion, there is a milder dependence on A_y/D.

Figure 4-10 shows the variation of mean drag coefficient with respect to A_y/D. It is illustrated that the in-line oscillation in most cases increases the value of the mean drag coefficient. Exception to this is observed for a narrow range of high A_y/D values, for which counter-clockwise mode is associated with lower mean drag coefficient. The drag coefficient fluctuations, expressed by $C_{D,RMS}$ (**Figure 4-11**), follow qualitatively the same dependence on oscillation amplitude as the mean drag coefficient.

The mean power dissipation parameter values, shown in **Figure 4-12**, are increasing functions of oscillation amplitude, i.e. correspond to more energetic flows, and characterized by higher levels in the case of clockwise cylinder motion and *ε=0.4*.

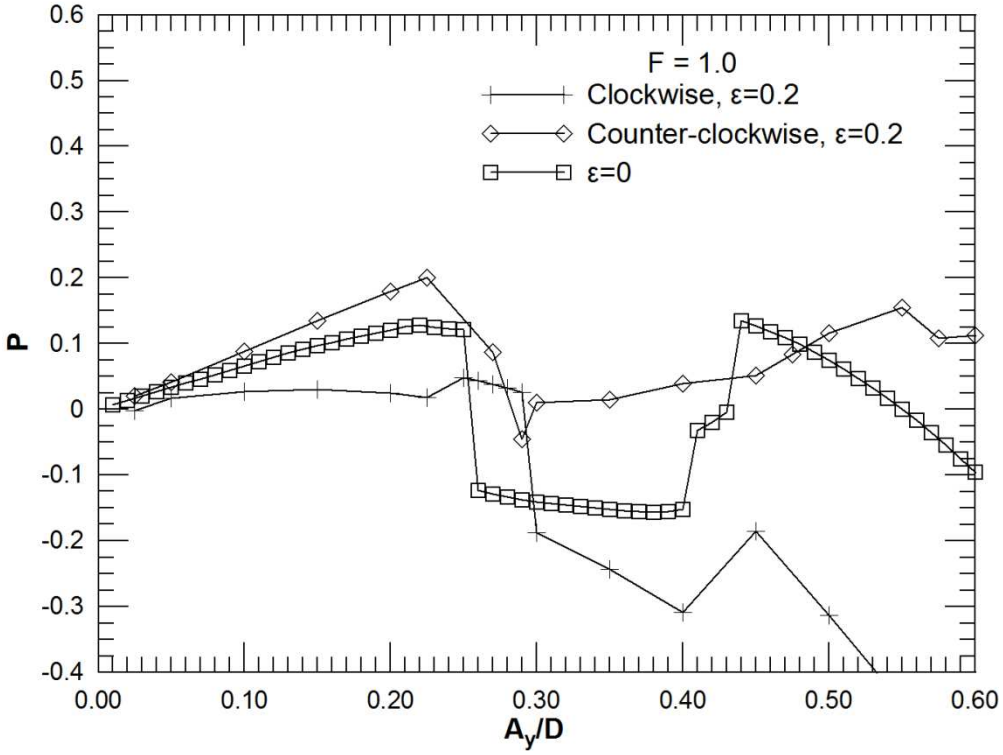

Figure 4-2: Non-dimensional total power transfer, *P*, versus the reduced y-amplitude, for frequency ratio $F = f_y/f_s = 1.0$; here, the cases $\varepsilon = 0$ (transverse-only oscillation), and $\varepsilon = 0.2$ (counter-clockwise and clockwise modes) are shown.

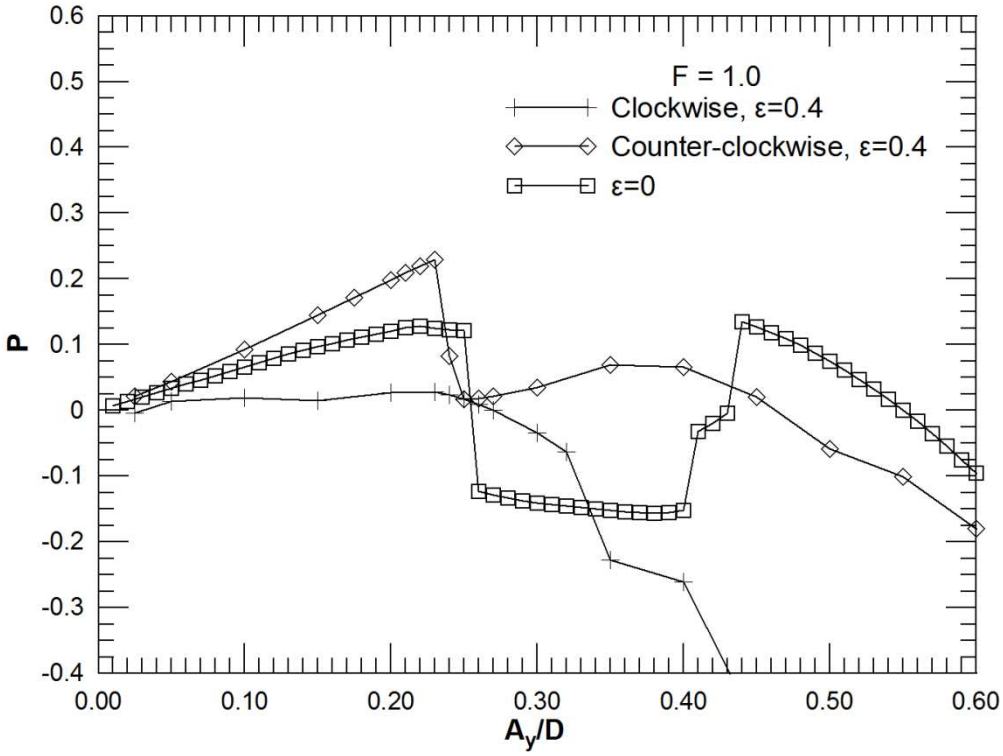

Figure 4-3: Non-dimensional total power transfer, *P*, versus the reduced y-amplitude, for frequency ratio $F = f_y/f_s = 1.0$; here, the cases $\varepsilon = 0$ (transverse-only oscillation), and $\varepsilon = 0.4$ (counter-clockwise and clockwise modes) are shown.

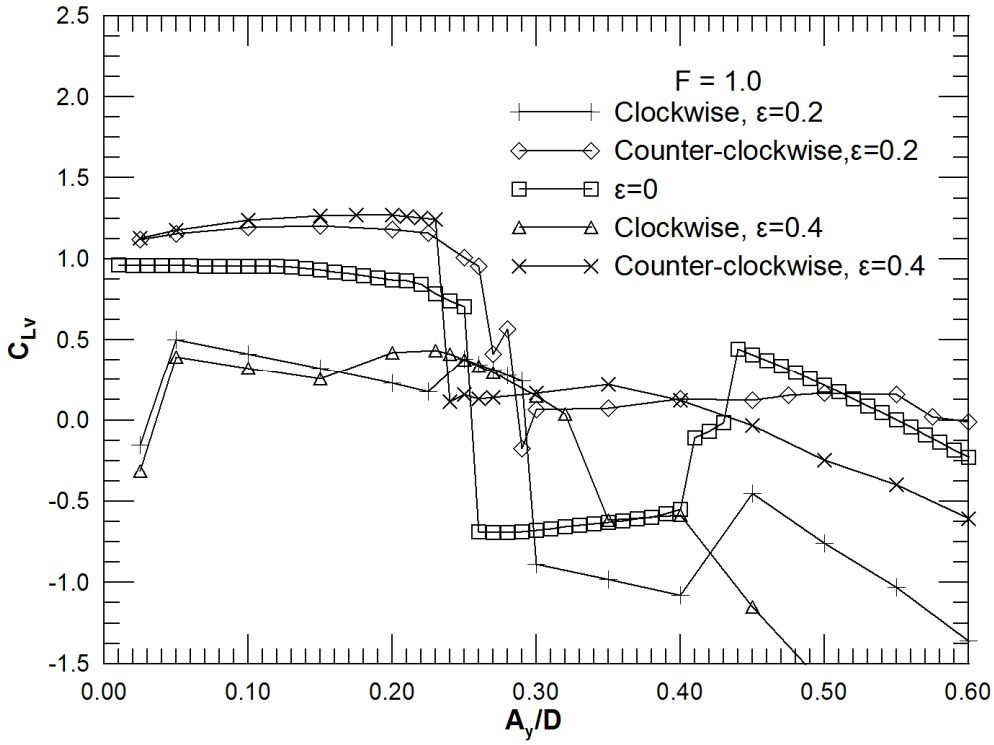

Figure 4-4: Excitation force coefficient, C_{Lv}, versus the reduced y-amplitude, for frequency ratio $F = f_y/f_s = 1.0$; here, the cases $\varepsilon = 0$ (transverse-only oscillation), $\varepsilon = 0.2$ and $\varepsilon = 0.4$ (counter-clockwise and clockwise modes) and shown.

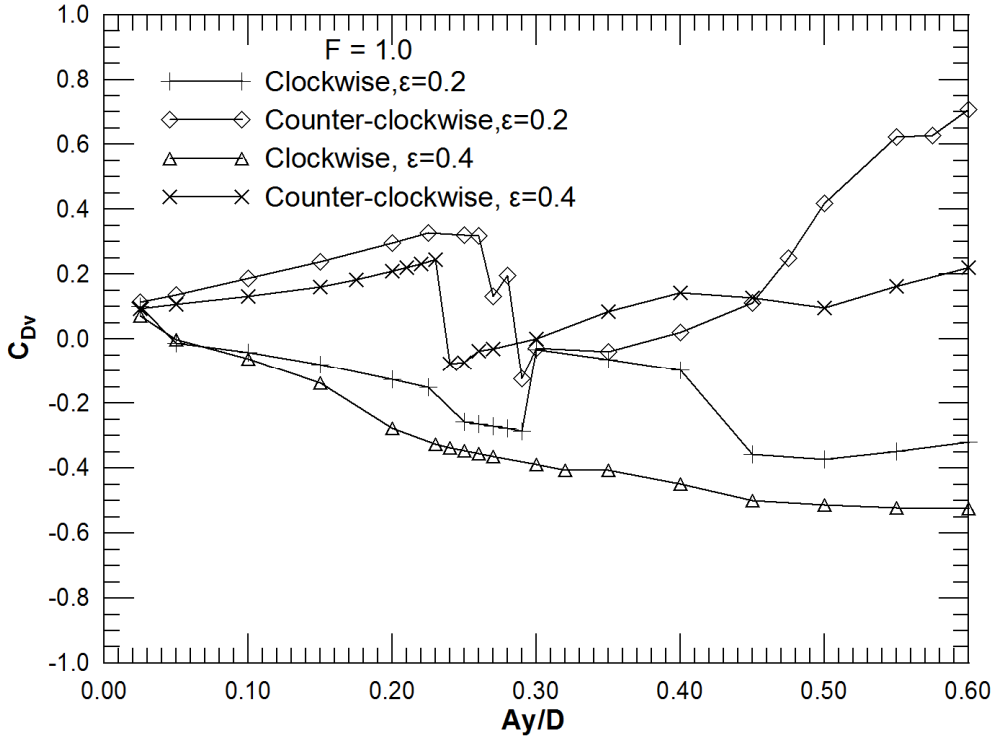

Figure 4-5: Excitation force coefficient, C_{Dv}, versus the reduced y-amplitude, for frequency ratio $F = f_y/f_s = 1.0$; here, the cases $\varepsilon = 0$ (transverse-only oscillation), $\varepsilon = 0.2$ and $\varepsilon = 0.4$ (counter-clockwise and clockwise modes) are shown.

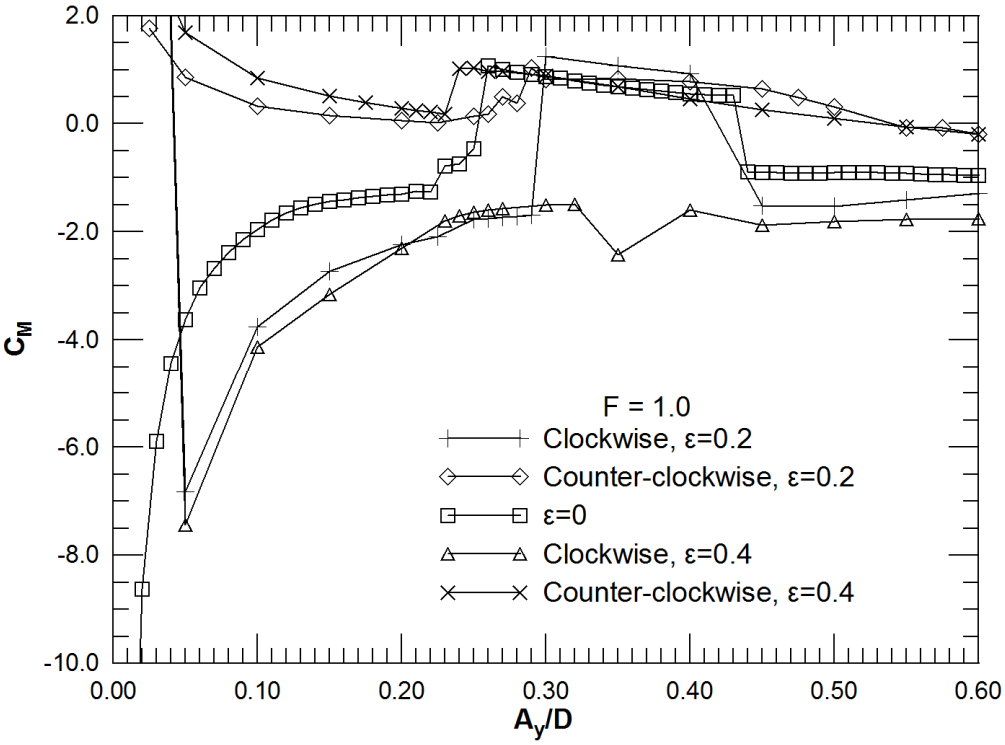

Figure 4-6: Inertia force coefficient, C_M, versus the reduced y-amplitude, for frequency ratio $F = f_y/f_s = 1.0$; here, the cases $\varepsilon = 0$ (transverse-only oscillation), $\varepsilon = 0.2$ and $\varepsilon = 0.4$ (counter-clockwise and clockwise modes) are shown.

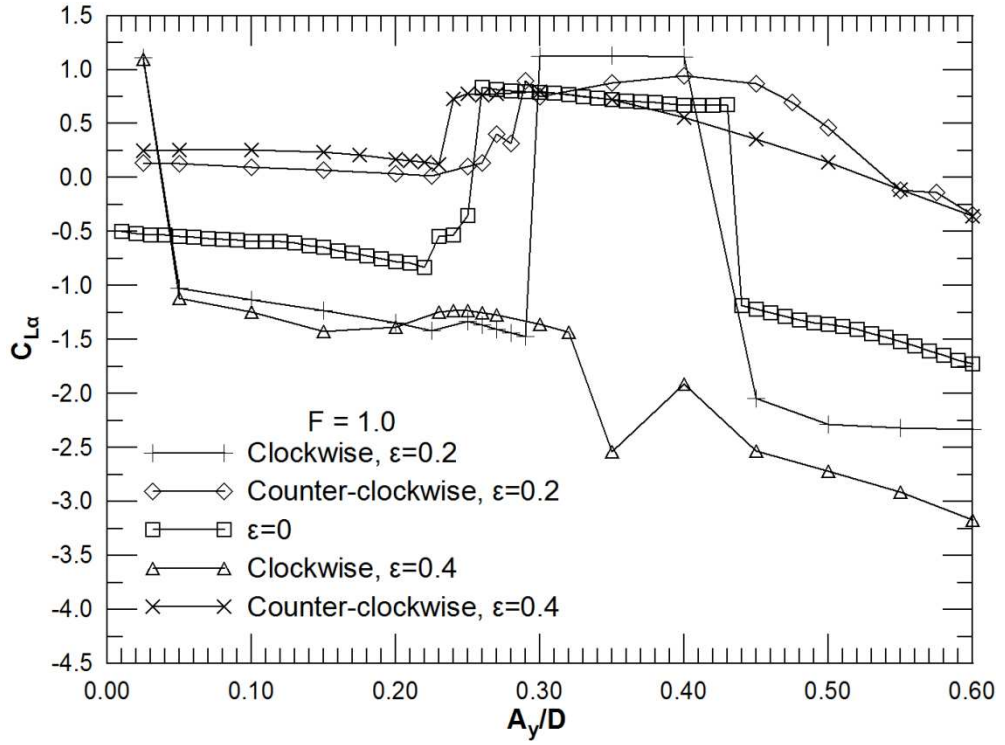

Figure 4-7: Inertia force coefficient, C_{La}, versus the reduced y-amplitude, for frequency ratio $F = f_y/f_s = 1.0$; here, the cases $\varepsilon = 0$ (transverse-only oscillation), $\varepsilon = 0.2$ and $\varepsilon = 0.4$ (counter-clockwise and clockwise modes) are shown.

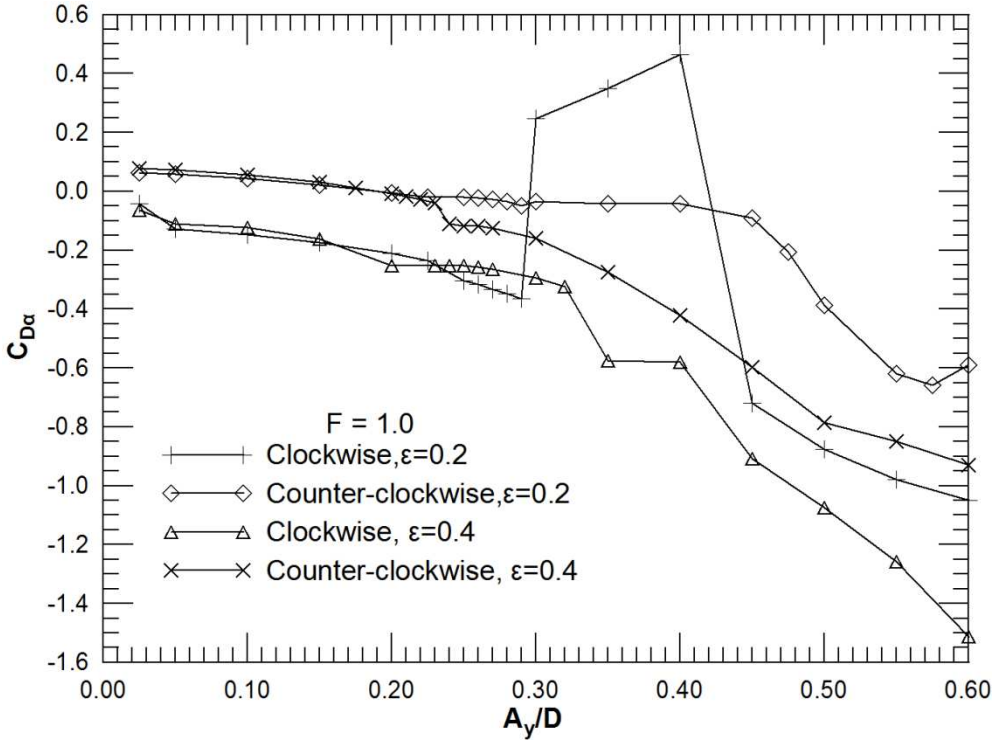

Figure 4-8: Inertia force coefficient, $C_{D\alpha}$, versus the reduced y-amplitude, for frequency ratio $F = f_y/f_s = 1.0$; here, the cases $\varepsilon = 0$ (transverse-only oscillation), $\varepsilon = 0.2$ and $\varepsilon = 0.4$ (counter-clockwise and clockwise modes) are shown.

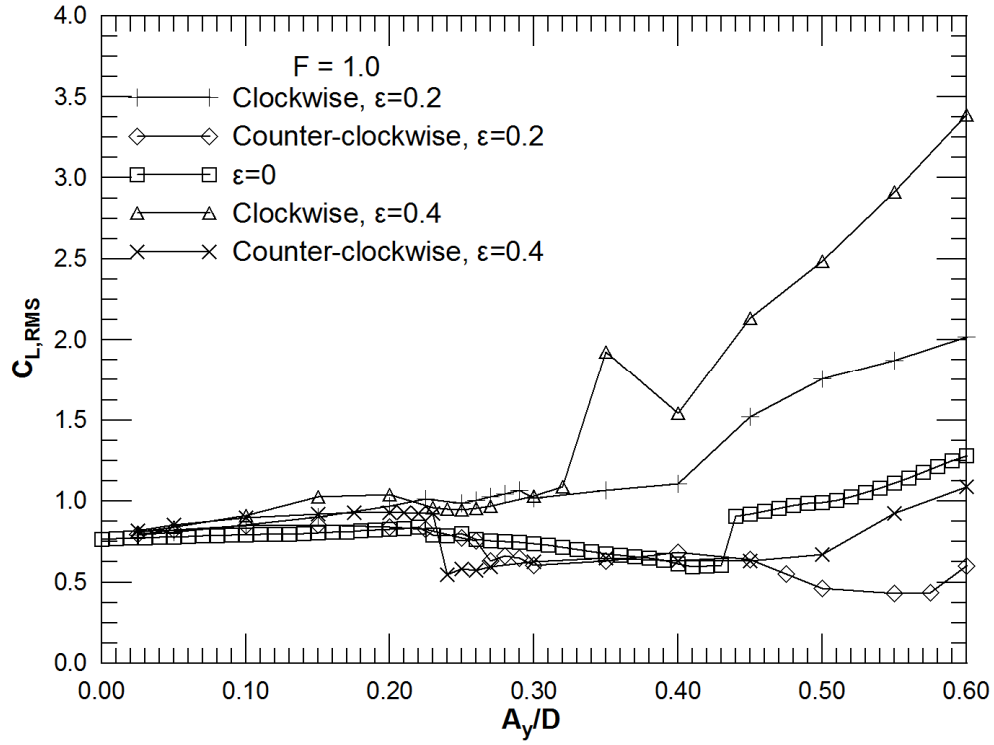

Figure 4-9: RMS fluctuation intensity of lift coefficient versus the reduced y-amplitude, for frequency ratio $F = f_y/f_s = 1.0$; here, the cases $\varepsilon = 0$ (transverse-only oscillation), $\varepsilon = 0.2$ and $\varepsilon = 0.4$ (counter-clockwise and clockwise modes) are shown.

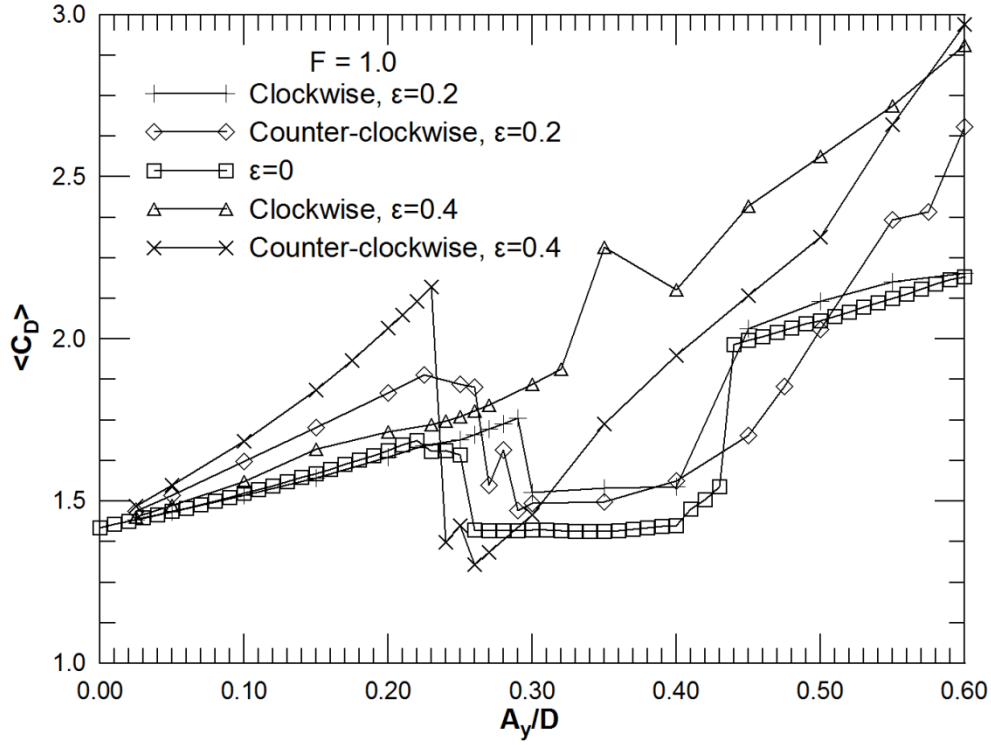

Figure 4-10: Time-averaged drag coefficient versus the reduced y-amplitude, for frequency ratio $F = f_y/f_s = 1.0$; here, the cases $\varepsilon = 0$ (transverse-only oscillation), $\varepsilon = 0.2$ and $\varepsilon = 0.4$ (counter-clockwise and clockwise modes) are shown.

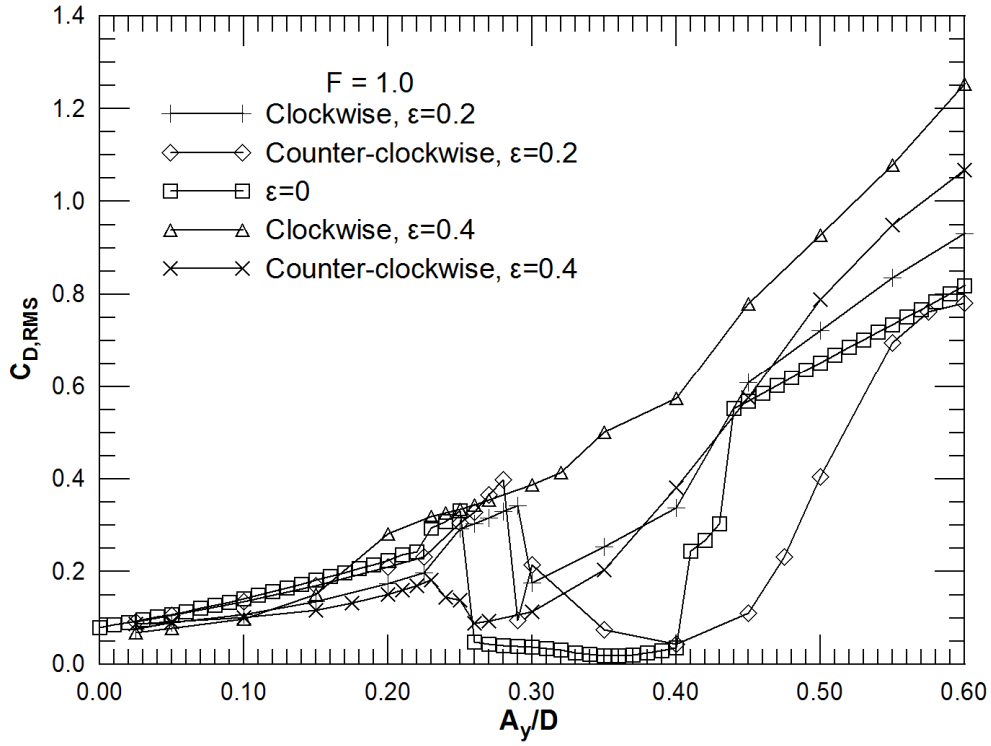

Figure 4-11: RMS fluctuation intensity of drag coefficient versus the reduced y-amplitude, for frequency ratio $F = f_y/f_s = 1.0$; here, the cases $\varepsilon = 0$ (transverse-only oscillation), $\varepsilon = 0.2$ and $\varepsilon = 0.4$ (counter-clockwise and clockwise modes) are shown.

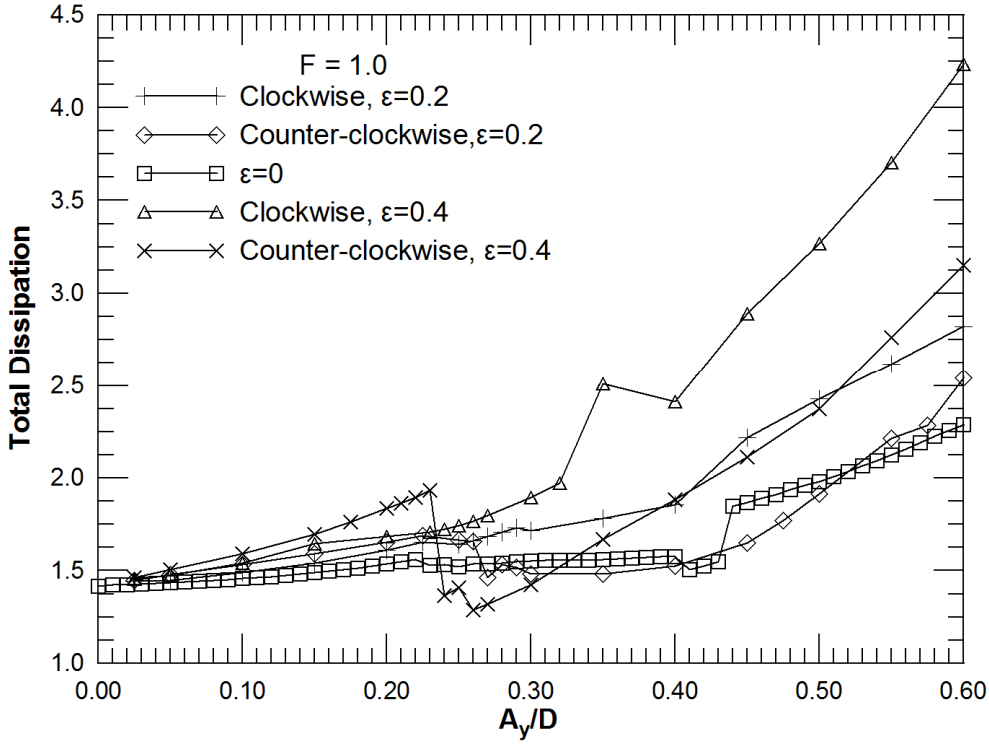

Figure 4-12: Time-averaged non-dimensional power dissipation versus the reduced y-amplitude, for frequency ratio $F = f_y/f_s = 1.0$; here, the cases $\varepsilon = 0$ (transverse-only oscillation), $\varepsilon = 0.2$ and $\varepsilon = 0.4$ (counter-clockwise and clockwise modes) are shown.

4.5.1.2 Forcing below the natural frequency

We consider the case where the cylinder oscillates at a frequency below the natural frequency, *F=0.9*. The variation of the power transfer parameter corresponding to the total value *P* is shown in **Figure 4-13** and **Figure 4-14**, for *ε=0.2* and *ε=0.4*, respectively, for the counter-clockwise and clockwise modes; the case corresponding to *ε=0* is also included. **Figure 4-13** and **Figure 4-14** demonstrate that for *ε=0.2* and *ε=0.4*, counter-clockwise motion is associated with an increased amplitude range of positive *P* values, in comparison to the other two oscillation cases (transverse-only oscillating cylinder and clockwise motion). We conclude that, for oscillation frequency below the natural frequency, counter-clockwise motion is the worst case scenario for a free vibrating cylinder, in accordance with the case of oscillation at resonant forcing.

The variations of coefficients C_{Lv}, C_{Dv}, C_M, C_{La}, C_{Da}, $C_{L,RMS}$, $<C_D>$, and $C_{D,RMS}$ are shown in **Figure 4-15** to **Figure 4-22**. The values that correspond to transverse-only oscillation (*ε=0*) are also illustrated. The variation of the coefficient C_{Lv} is shown in **Figure 4-15**. In all cases, the variation follows qualitatively the corresponding behaviour of the *P* curves. For counter-clockwise mode, the C_{Lv} values are initially negative, then positive and increasing, reach a plateau, and acquire negative values at oscillation amplitudes higher than half a diameter. In clockwise mode, the form of the two curves is qualitatively similar, but the values remain positive only for low oscillation amplitudes.

The variation of C_{Dv} is shown in **Figure 4-16**. It is illustrated that, for counter-clockwise mode, the in-line cylinder motion transfers energy from the flow to the cylinder, as demonstrated from the positive values of the C_{Dv} coefficient; the effect is stronger for the *ε=0.2* case. The in-line cylinder motion has the opposite effect (i.e. is associated with negative power transfer) for clockwise motion.

The curve of added mass coefficient C_M illustrated in **Figure 4-17** remains negative for all combinations of modes, ε and A_y/D (i.e. is in phase with the cylinder acceleration in the transverse direction) except a range of A_y/D in counter-clockwise mode and *ε=0.4*. The variation of the coefficient C_{La} shown in **Figure 4-18** follows qualitatively the corresponding variation of C_M. The curve of coefficient C_{Da}, illustrated in **Figure 4-19**, remains negative, except for a small range of low amplitudes for clockwise motion.

The magnitude of non-dimensional forces for lift and drag is illustrated in **Figure 4-20, Figure 4-21** and **Figure 4-22** (variation of $C_{L,RMS}$, $< C_D >$, and $C_{D,RMS}$). When forcing below the natural frequency, the lift fluctuations increase with oscillation amplitude for clockwise motion, and remain flat for counter-clockwise motion. The time-averaged and fluctuating drag values are increasing functions of oscillation amplitude, with higher levels corresponding to higher relative x-amplitude (case *ε=0.4)*.

The variations of mean power dissipation parameter are shown in **Figure 4-23** demonstrating more energetic flow as they are increasing functions of oscillation amplitude. The case of clockwise cylinder motion and *ε=0.4* is characterized by higher levels of mean power dissipation parameter.

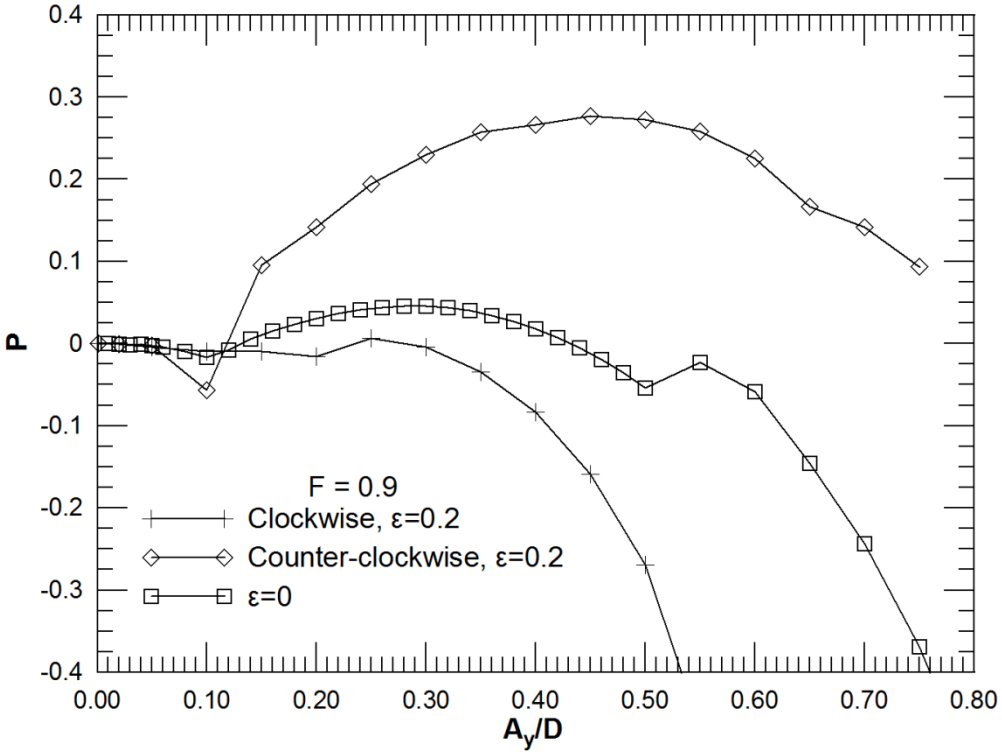

Figure 4-13: Non-dimensional total power transfer, *P*, versus the reduced y-amplitude, for frequency ratio $F = f_y/f_s = 0.9$; here, the cases $\varepsilon = 0$ (transverse-only oscillation), and $\varepsilon = 0.2$ (counter-clockwise and clockwise modes) are shown.

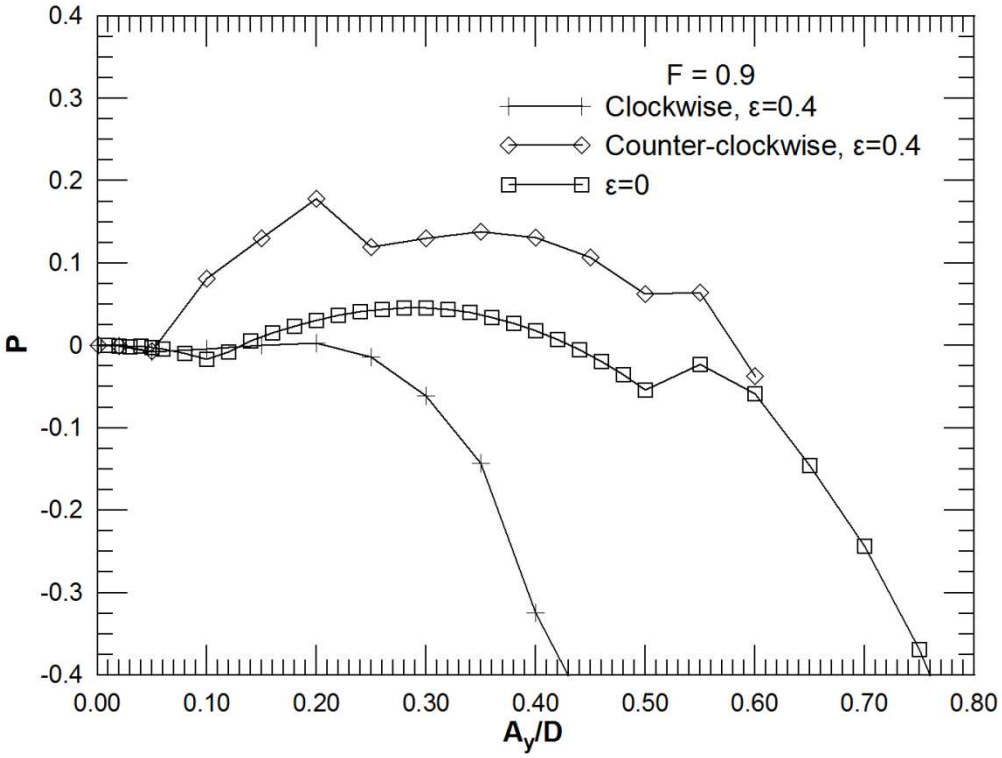

Figure 4-14: Non-dimensional total power transfer, *P*, versus the reduced y-amplitude, for frequency ratio $F = f_y/f_s = 0.9$; here, the cases $\varepsilon = 0$ (transverse-only oscillation), and $\varepsilon = 0.4$ (counter-clockwise and clockwise modes) are shown.

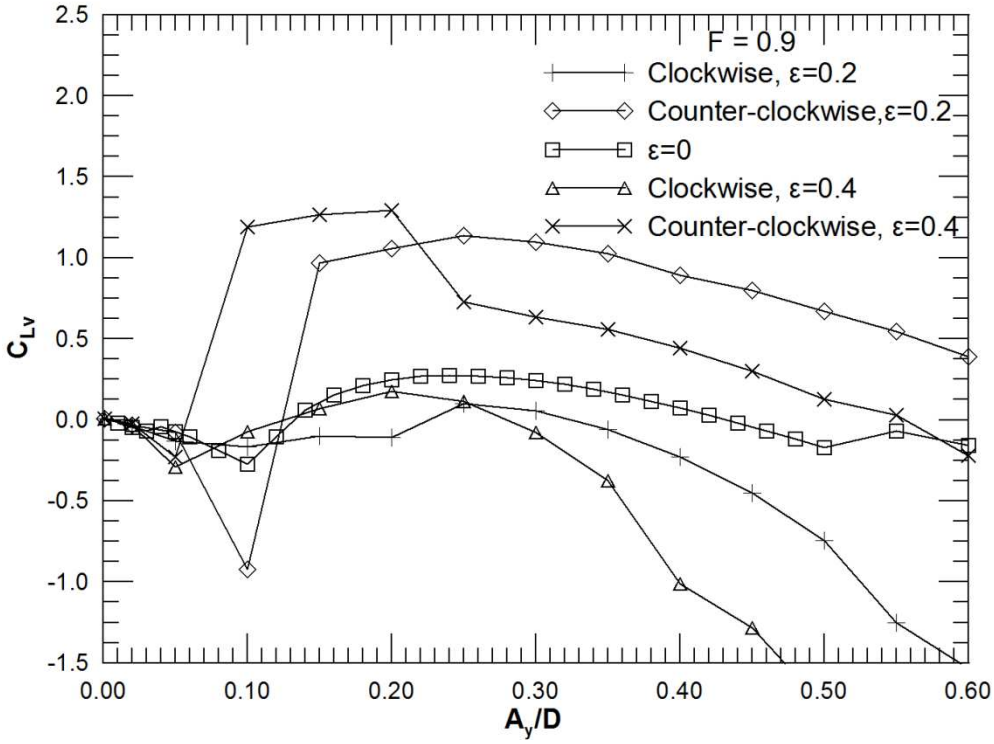

Figure 4-15: Excitation force coefficient, C_{Lv}, versus the reduced y-amplitude, for frequency ratio $F = f_y/f_s = 0.9$; here, the cases $\varepsilon = 0$ (transverse-only oscillation), $\varepsilon = 0.2$ and $\varepsilon = 0.4$ (counter-clockwise and clockwise modes) are shown.

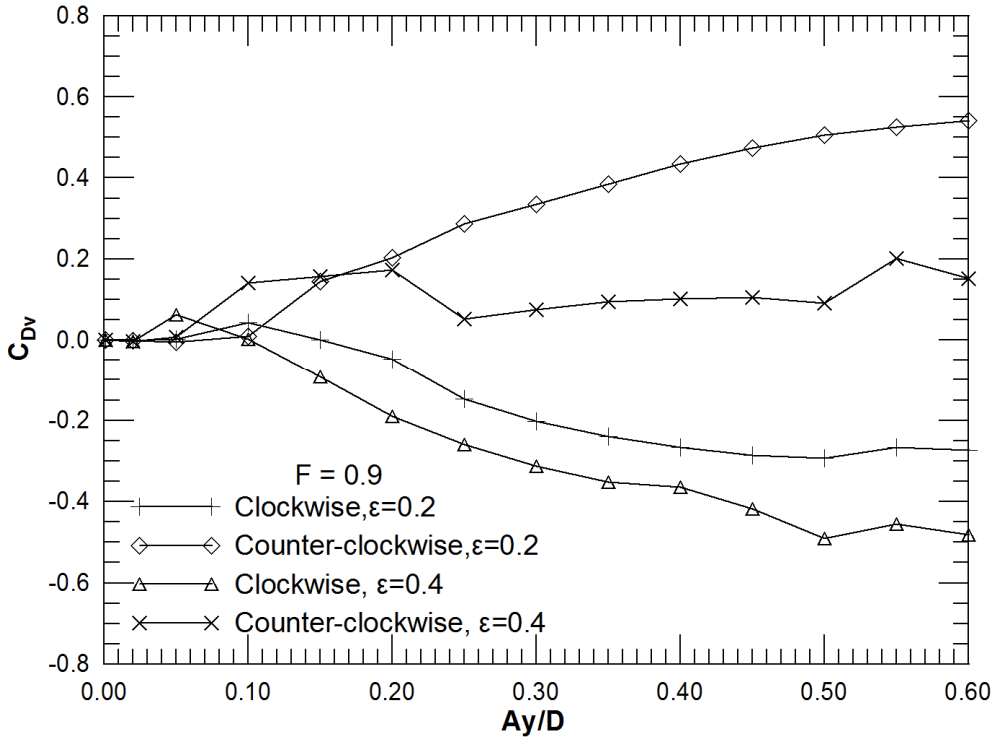

Figure 4-16: Excitation force coefficient, C_{Dv}, versus the reduced y-amplitude, for frequency ratio $F = f_y/f_s = 0.9$; here, the cases $\varepsilon = 0.2$ and $\varepsilon = 0.4$ (counter-clockwise and clockwise modes) are shown.

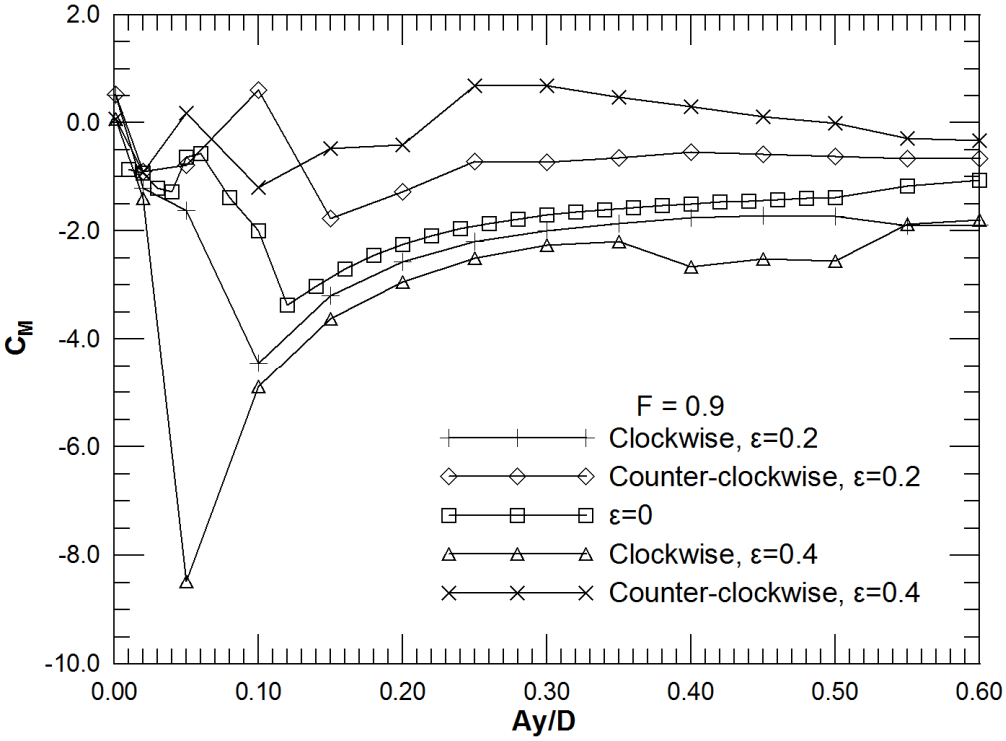

Figure 4-17: Inertia force coefficient, C_M, versus the reduced y-amplitude, for frequency ratio $F = f_y/f_s = 0.9$; here, the cases $\varepsilon = 0$ (transverse-only oscillation), $\varepsilon = 0.2$ and $\varepsilon = 0.4$ (counter-clockwise and clockwise modes) are shown.

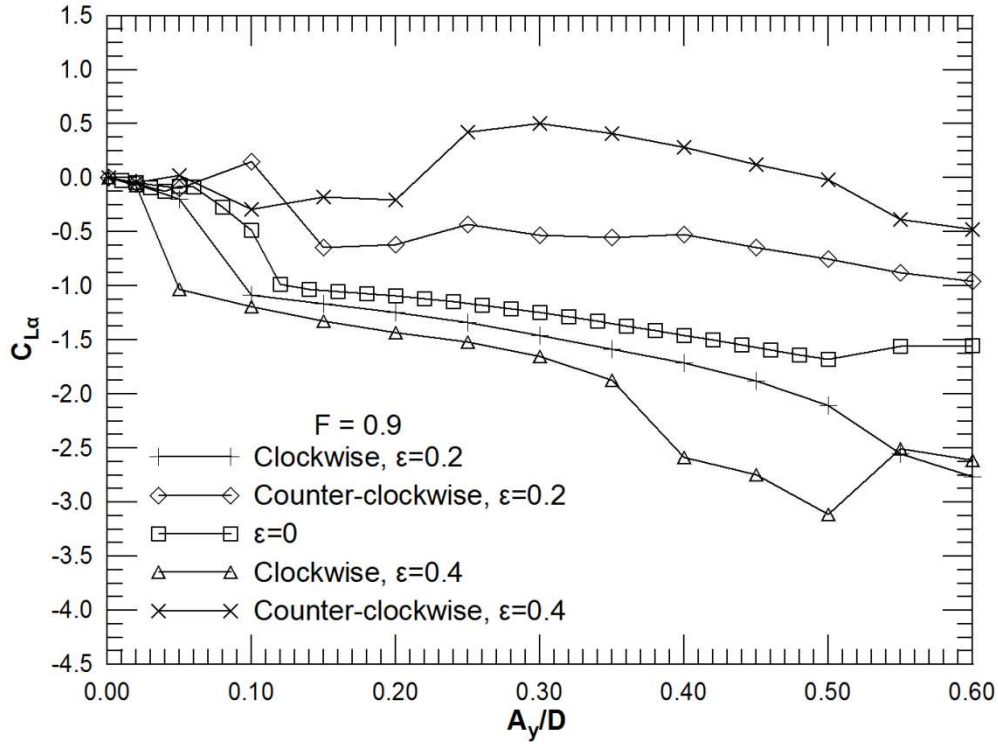

Figure 4-18: Inertia force coefficient, $C_{L\alpha}$, versus the reduced y-amplitude, for frequency ratio $F = f_y/f_s = 0.9$; here, the cases $\varepsilon = 0$ (transverse-only oscillation), $\varepsilon = 0.2$ and $\varepsilon = 0.4$ (counter-clockwise and clockwise modes) are shown.

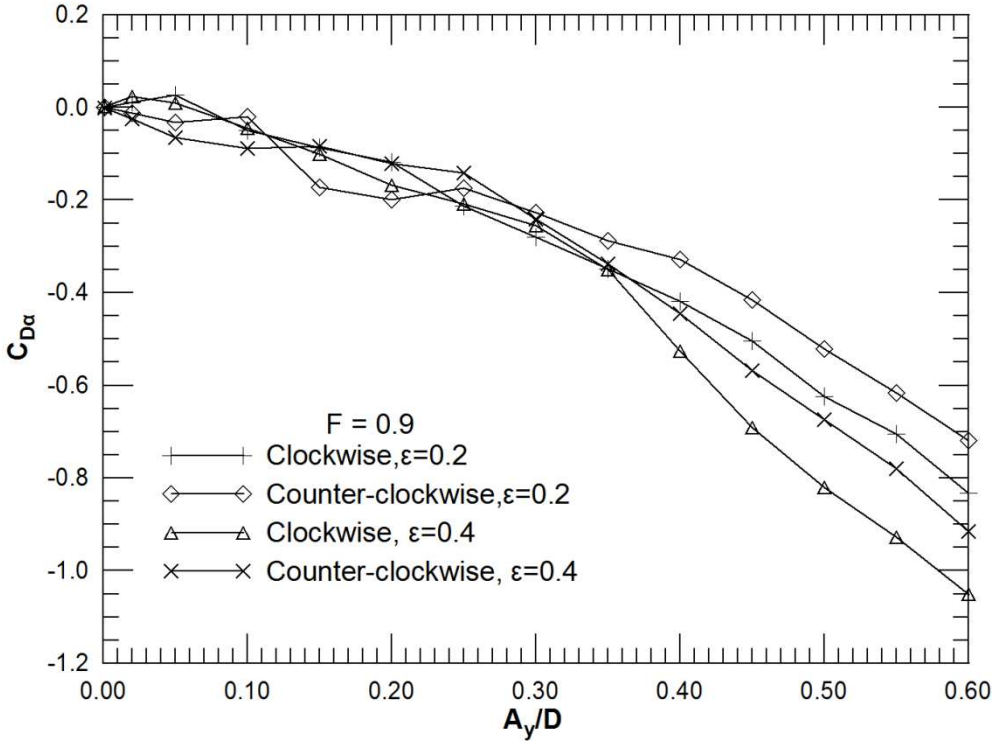

Figure 4-19: Inertia force coefficient, C_{Da}, versus the reduced y-amplitude, for frequency ratio $F = f_y/f_s = 0.9$; here, the cases $\varepsilon = 0.2$ and $\varepsilon = 0.4$ (counter-clockwise and clockwise modes) are shown.

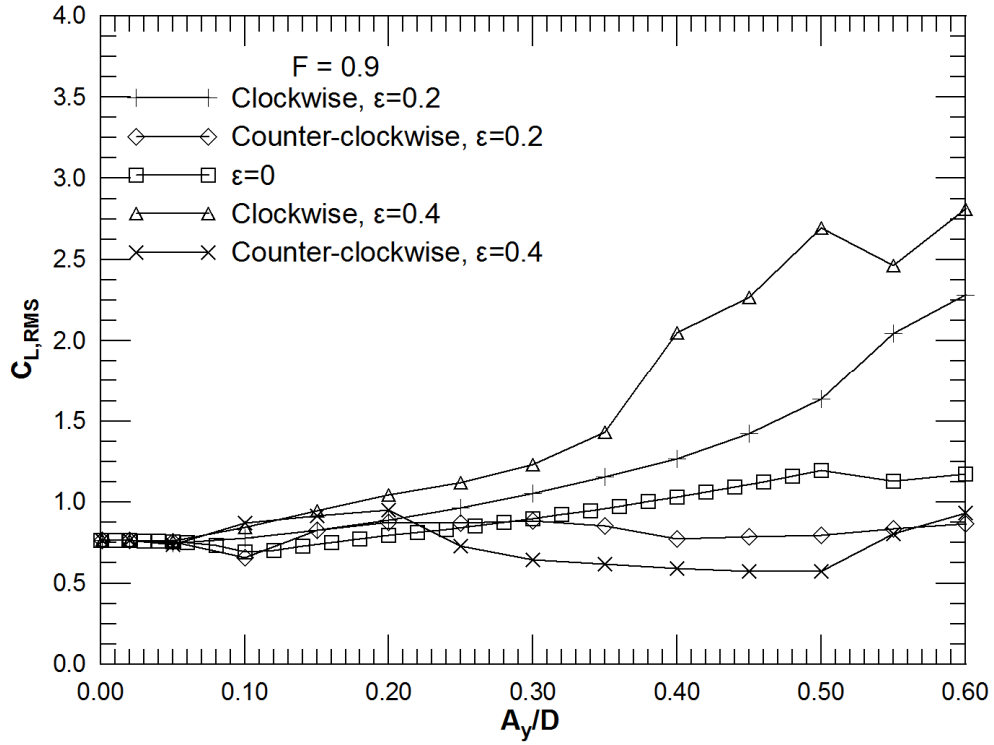

Figure 4-20: RMS fluctuation intensity of lift coefficient versus the reduced y-amplitude, for frequency ratio $F = f_y/f_s = 0.9$; here, the cases $\varepsilon = 0$ (transverse-only oscillation), $\varepsilon = 0.2$ and $\varepsilon = 0.4$ (counter-clockwise and clockwise modes) are shown.

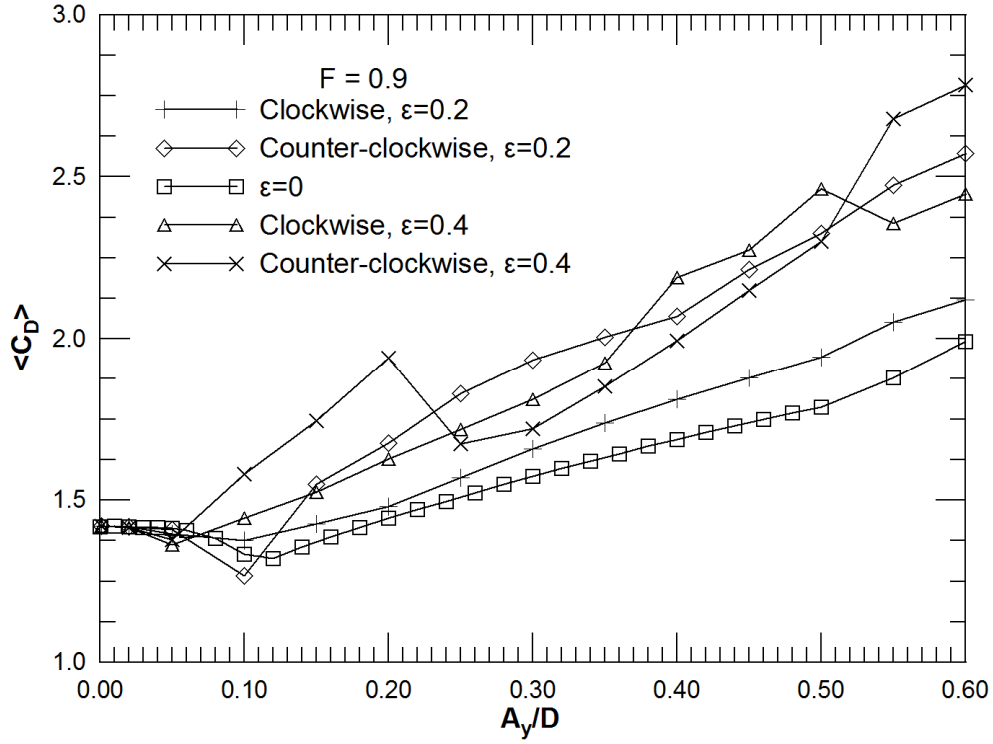

Figure 4-21: Time-averaged drag coefficient versus the reduced y-amplitude, for frequency ratio $F = f_y/f_s = 0.9$; here, the cases $\varepsilon = 0$ (transverse-only oscillation), $\varepsilon = 0.2$ and $\varepsilon = 0.4$ (counter-clockwise and clockwise modes) are shown.

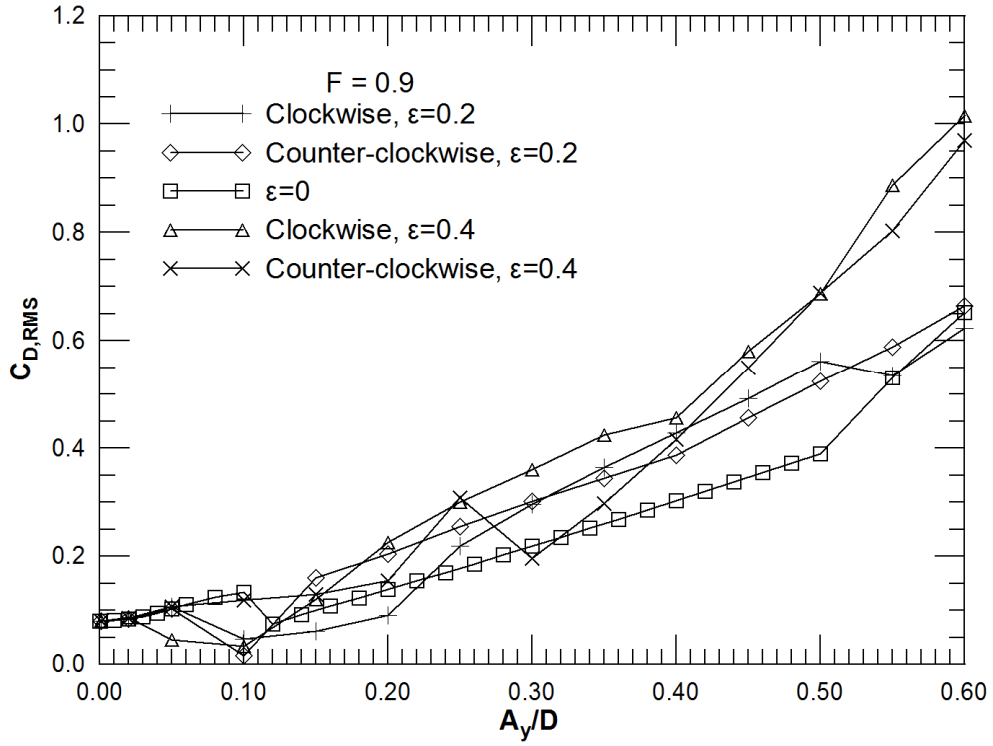

Figure 4-22: RMS fluctuation intensity of drag versus the reduced y-amplitude, for frequency ratio $F = f_y/f_s = 0.9$; here, the cases $\varepsilon = 0$ (transverse-only oscillation), $\varepsilon = 0.2$ and $\varepsilon = 0.4$ (counter-clockwise and clockwise modes) are shown.

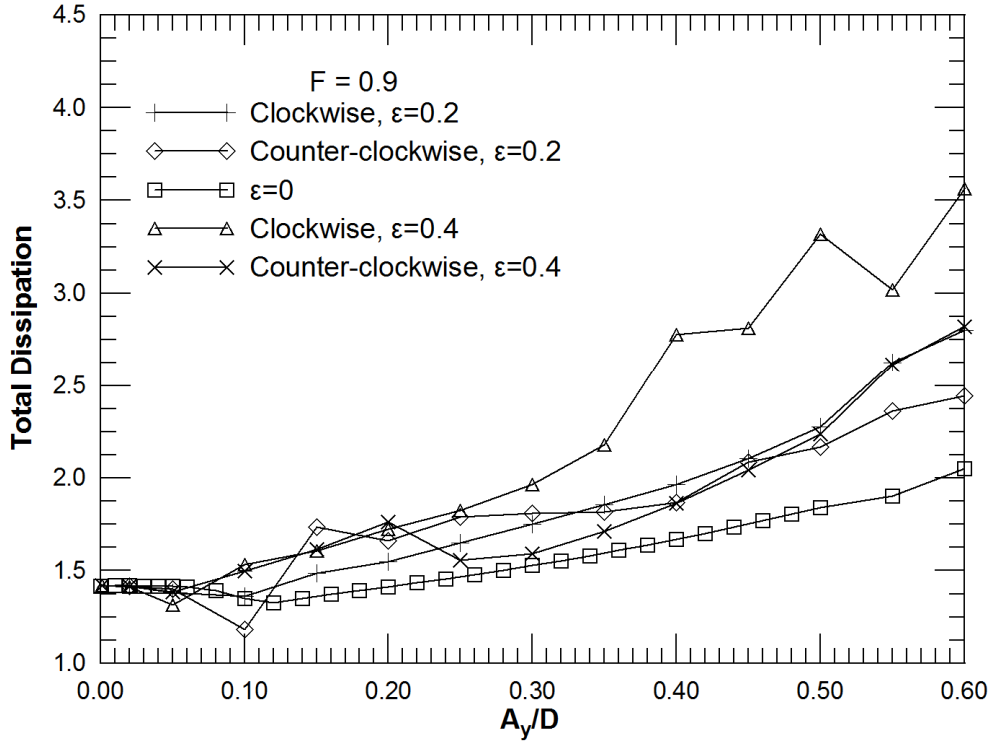

Figure 4-23: Time-averaged non-dimensional power dissipation versus the reduced y-amplitude, for frequency ratio $F = f_y/f_s = 0.9$; here, the cases $\varepsilon = 0$ (transverse-only oscillation), $\varepsilon = 0.2$ and $\varepsilon = 0.4$ (counter-clockwise and clockwise modes) are shown.

4.5.1.3 Forcing above the natural frequency

Finally, we consider forcing above the natural frequency, with the frequency of oscillation in the y-direction equal to 1.1 times the natural frequency of vortex shedding (*F=1.1*). The variation of the power transfer parameters is shown in **Figure 4-24** and **Figure 4-25**, for *ε=0.2* and *ε=0.4*, respectively, for counter-clockwise and clockwise modes, along with the *ε=0* case. It is demonstrated that the variation of *P* can be characterized by alterations between positive and negative values, with the positive values of *P* being higher for counter-clockwise motion in comparison to either the transverse-only oscillation or clockwise motion. Thus, it is demonstrated that counter-clockwise mode remains the most hazardous one when forcing above the natural frequency for low oscillation amplitudes.

The variations of coefficients C_{Lv}, C_{Dv}, C_M, C_{La}, C_{Da}, $C_{L,RMS}$, $< C_D >$, and $C_{D,RMS}$ are illustrated in **Figure 4-26** - **Figure 4-33;** the values corresponding to transverse-only oscillation (*ε=0*) are also included.

The variation of the coefficient C_{Lv} shown in **Figure 4-26** follows the corresponding behaviour of the *P* curves, shown in **Figure 4-24** and **Figure 4-25**.

The variation of C_{Dv} is illustrated in **Figure 4-27**. In counter-clockwise motion, the C_{Dv} values are positive, while they are negative for clockwise motion, e.g. the in-line motion transfers energy from the flow to the cylinder when oscillating counter-clockwise.

The variation of the added mass coefficient C_M is presented in **Figure 4-28**; the values are positive for counter-clockwise motion, whereas they vary from positive to negative values for clockwise motion. The variation of C_{La} illustrated in **Figure 4-29** exhibit the same qualitative behaviour with the C_M. The values of the coefficient C_{Da} shown in **Figure 4-30** illustrate that, for counter-clockwise mode, C_{Da} remains positive until a certain value of oscillation amplitude, while it varies between positive and negative values for clockwise mode.

The non-dimensional forces for lift and drag are shown in **Figure 4-31**, **Figure 4-32** and **Figure 4-33**, in terms of $C_{L,RMS}$, $< C_D >$ and $C_{D,RMS}$ values. **Figure 4-31** demonstrates that, for clockwise oscillation, lift fluctuations acquire high values at high oscillation amplitude, and remain rather flat for counter-clockwise mode. **Figure 4-32** and **Figure 4-33** illustrate that the values of time-averaged and fluctuation intensities of drag are increasing functions of oscillation amplitude for high oscillation amplitude while sharp transitions occur in a region of oscillation amplitudes around 0.25-0.30.

The values of mean power dissipation parameter illustrated in **Figure 4-34** vary smoothly up to A_y / D values of order 0.30, and increase subsequently.

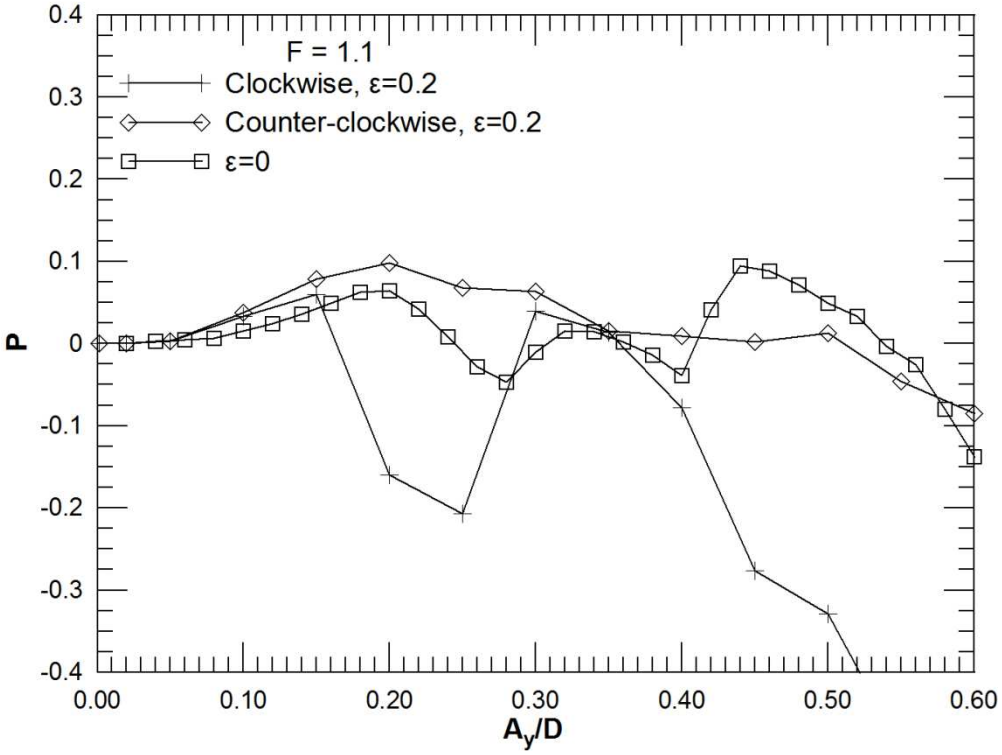

Figure 4-24: Non-dimensional total power transfer, *P*, versus the reduced y-amplitude, for frequency ratio $F = f_y/f_s = 1.1$; here, the cases $\varepsilon = 0$ (transverse-only oscillation), and $\varepsilon = 0.2$ (counter-clockwise and clockwise modes) are shown.

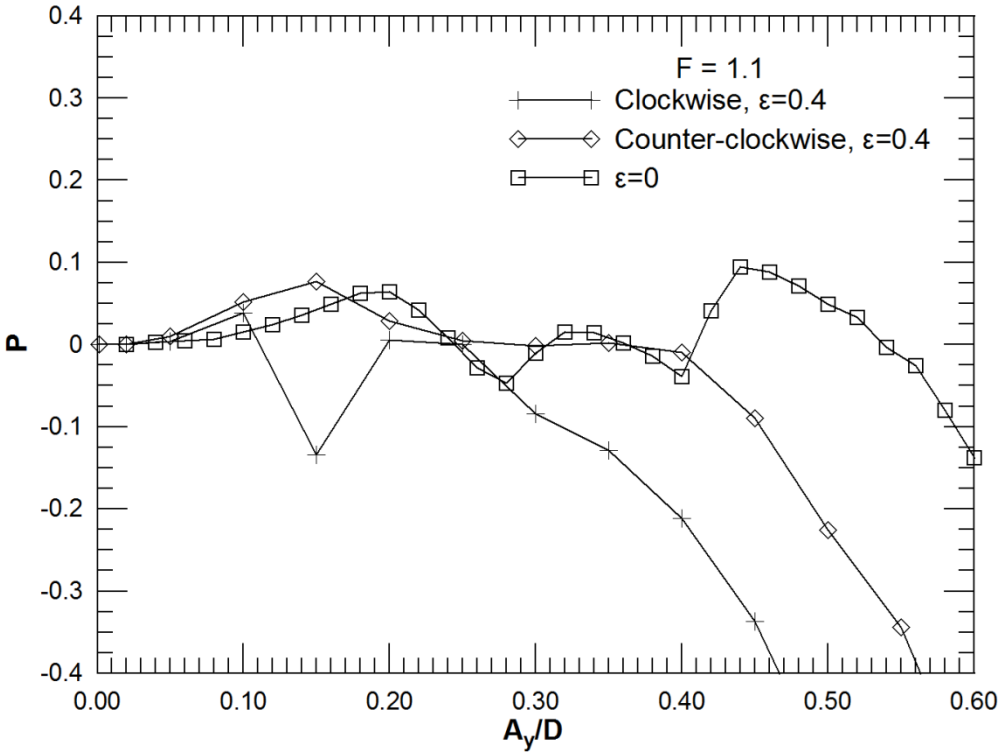

Figure 4-25: Non-dimensional total power transfer, *P*, versus the reduced y-amplitude, for frequency ratio $F = f_y/f_s = 1.1$; here, the cases $\varepsilon = 0$ (transverse-only oscillation), and $\varepsilon = 0.4$ (counter-clockwise and clockwise modes) are shown.

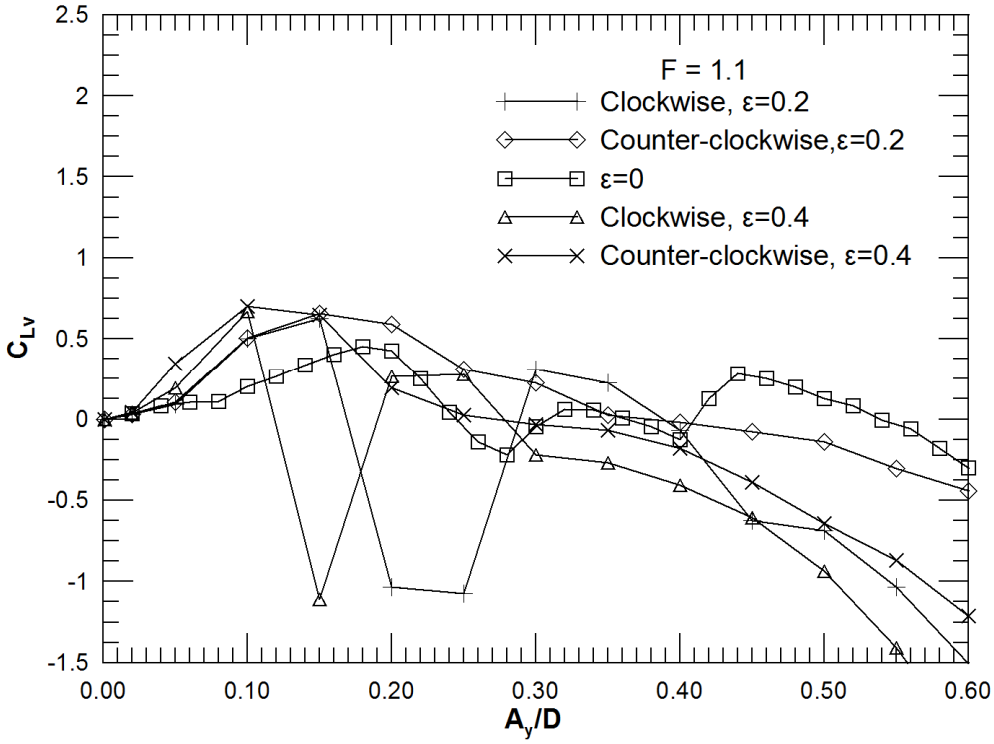

Figure 4-26: Excitation force coefficient, C_{Lv}, versus the reduced y-amplitude, for frequency ratio $F = f_y/f_s = 1.1$; here, the cases $\varepsilon = 0$ (transverse-only oscillation), $\varepsilon = 0.2$ and $\varepsilon = 0.4$ (counter-clockwise and clockwise modes) are shown.

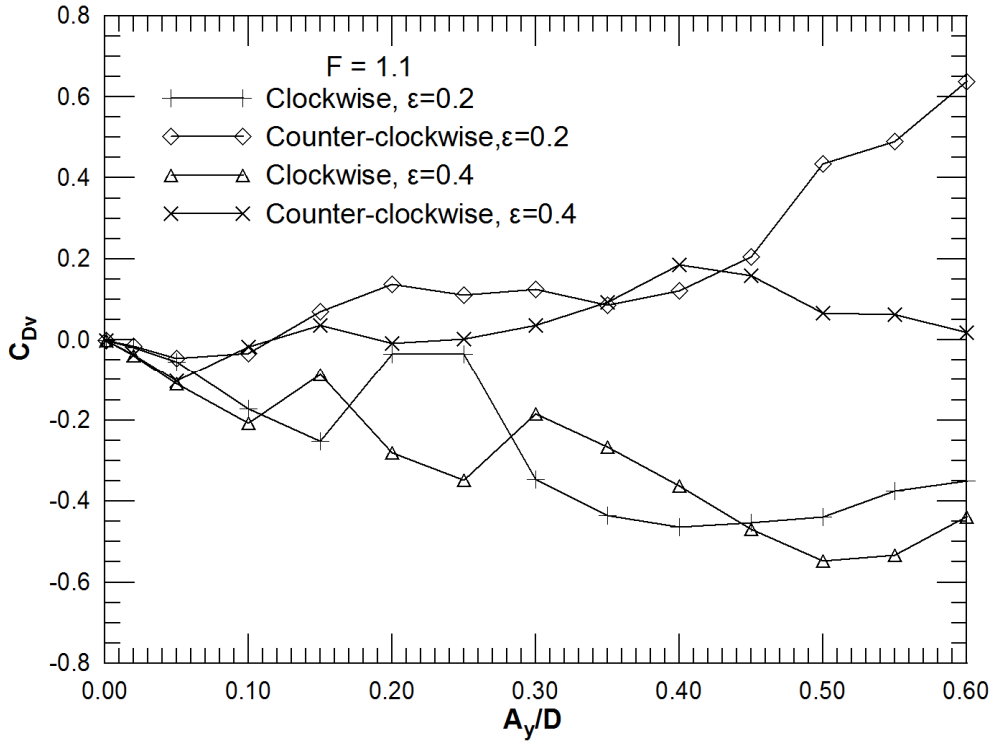

Figure 4-27: Excitation force coefficient, C_{Dv}, versus the reduced y-amplitude, for frequency ratio $F = f_y/f_s = 1.1$; here, the cases $\varepsilon = 0.2$ and $\varepsilon = 0.4$ (counter-clockwise and clockwise modes) are shown.

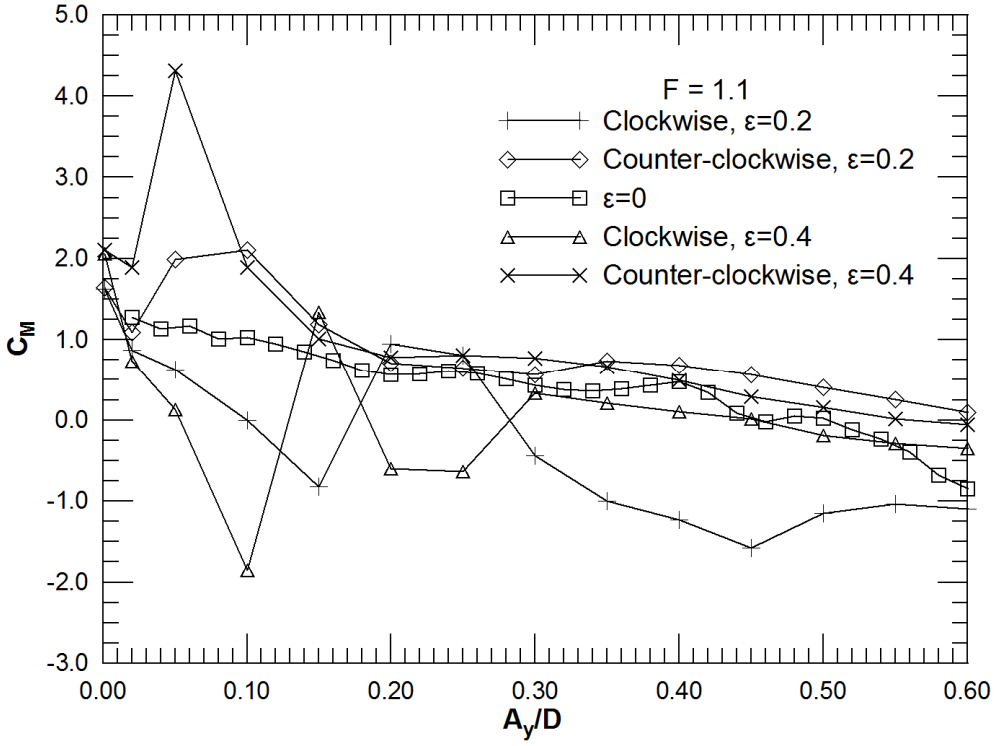

Figure 4-28: Inertia force coefficient, C_M, versus the reduced y-amplitude, for frequency ratio $F = f_y/f_s = 1.1$; here, the cases $\varepsilon = 0$ (transverse-only oscillation), $\varepsilon = 0.2$ and $\varepsilon = 0.4$ (counter-clockwise and clockwise modes) are shown.

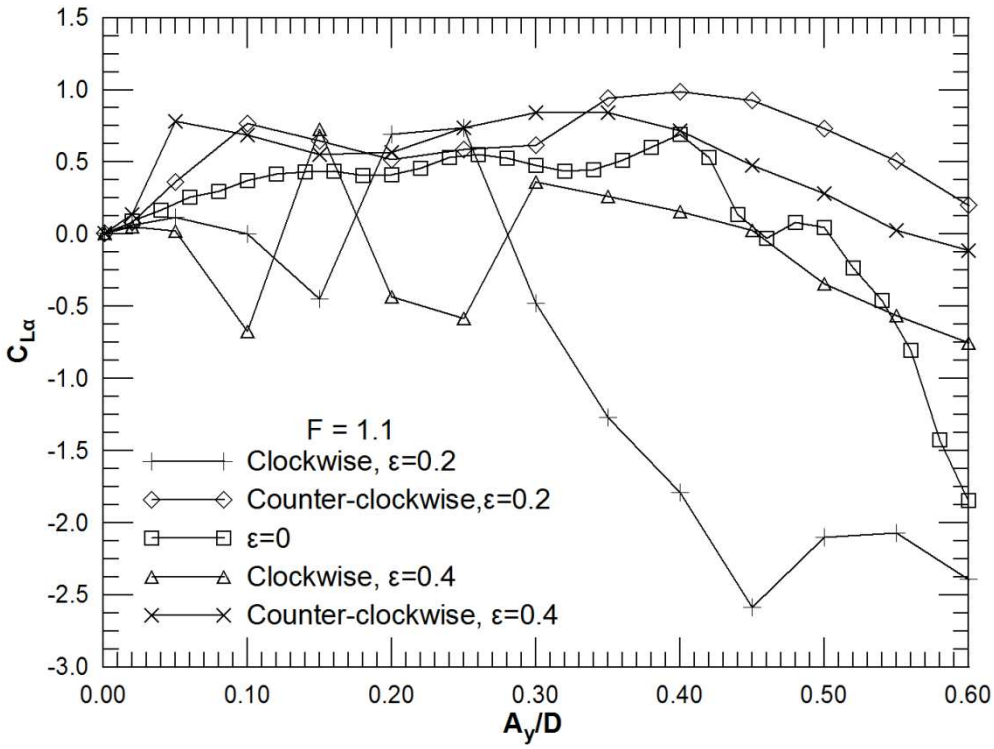

Figure 4-29: Inertia force coefficient, $C_{L\alpha}$, versus the reduced y-amplitude, for frequency ratio $F = f_y/f_s = 1.1$; here, the cases $\varepsilon = 0$ (transverse-only oscillation), $\varepsilon = 0.2$ and $\varepsilon = 0.4$ (counter-clockwise and clockwise modes) are shown.

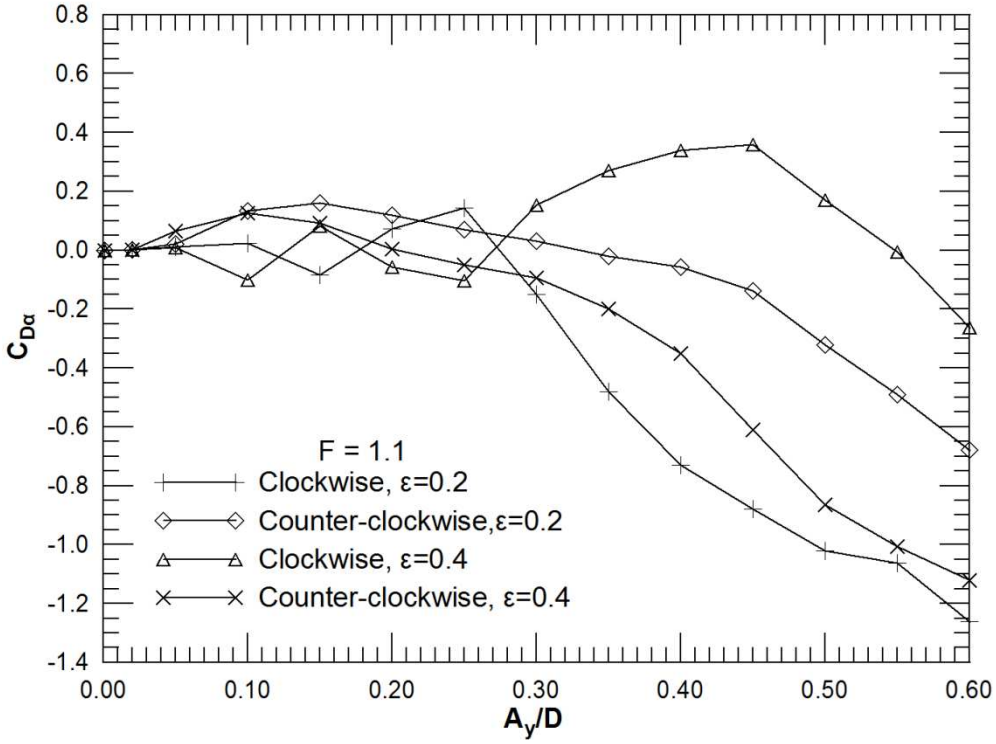

Figure 4-30: Inertia force coefficient, C_{Da}, versus the reduced y-amplitude, for frequency ratio $F = f_y/f_s = 1.1$; here, the cases $\varepsilon = 0.2$ and $\varepsilon = 0.4$ (counter-clockwise and clockwise modes) are shown.

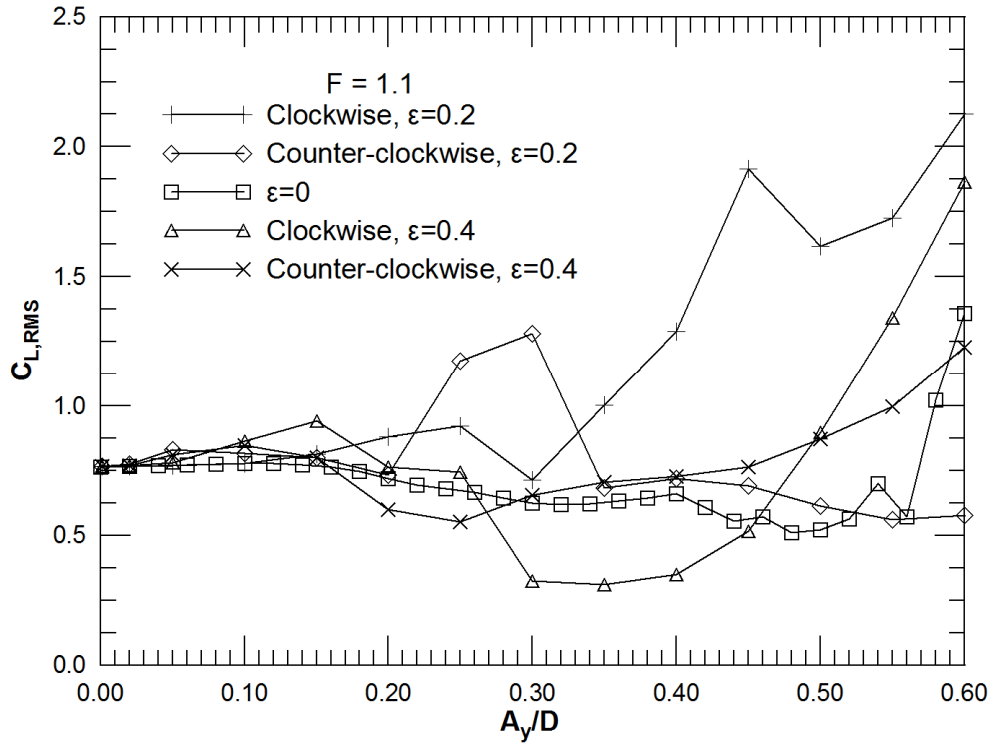

Figure 4-31: RMS fluctuation intensity of lift coefficient versus versus the reduced y-amplitude, for frequency ratio $F = f_y/f_s = 1.1$; here, the cases $\varepsilon = 0$ (transverse-only oscillation), $\varepsilon = 0.2$ and $\varepsilon = 0.4$ (counter-clockwise and clockwise modes) are shown.

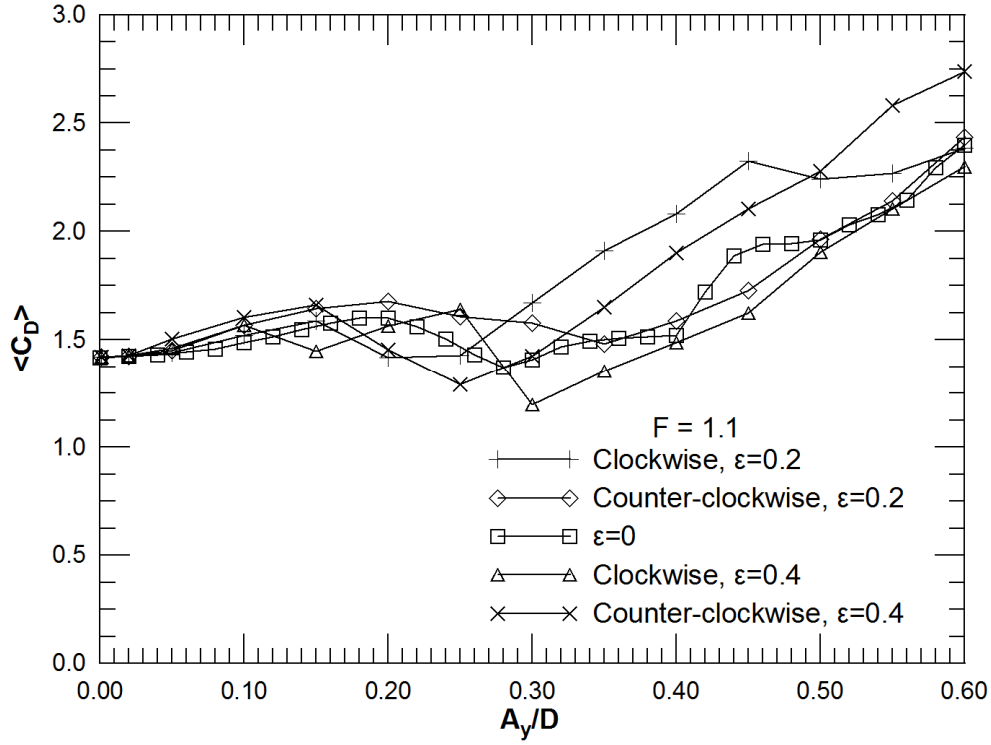

Figure 4-32: Time-averaged drag coefficient versus the reduced y-amplitude, for frequency ratio $F = f_y/f_s = 1.1$; here, the cases $\varepsilon = 0$ (transverse-only oscillation), $\varepsilon = 0.2$ and $\varepsilon = 0.4$ (counter-clockwise and clockwise modes) are shown.

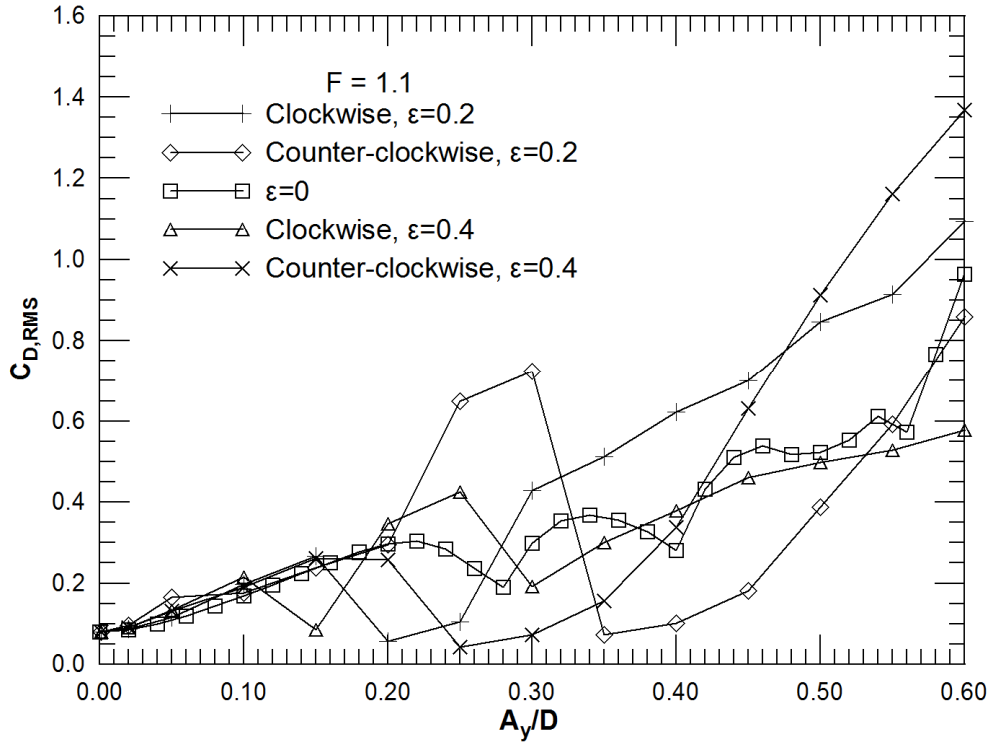

Figure 4-33: RMS fluctuation intensity of drag coefficient versus versus the reduced y-amplitude, for frequency ratio $F = f_y/f_s = 1.1$; here, the cases $\varepsilon = 0$ (transverse-only oscillation), $\varepsilon = 0.2$ and $\varepsilon = 0.4$ (counter-clockwise and clockwise modes) are shown.

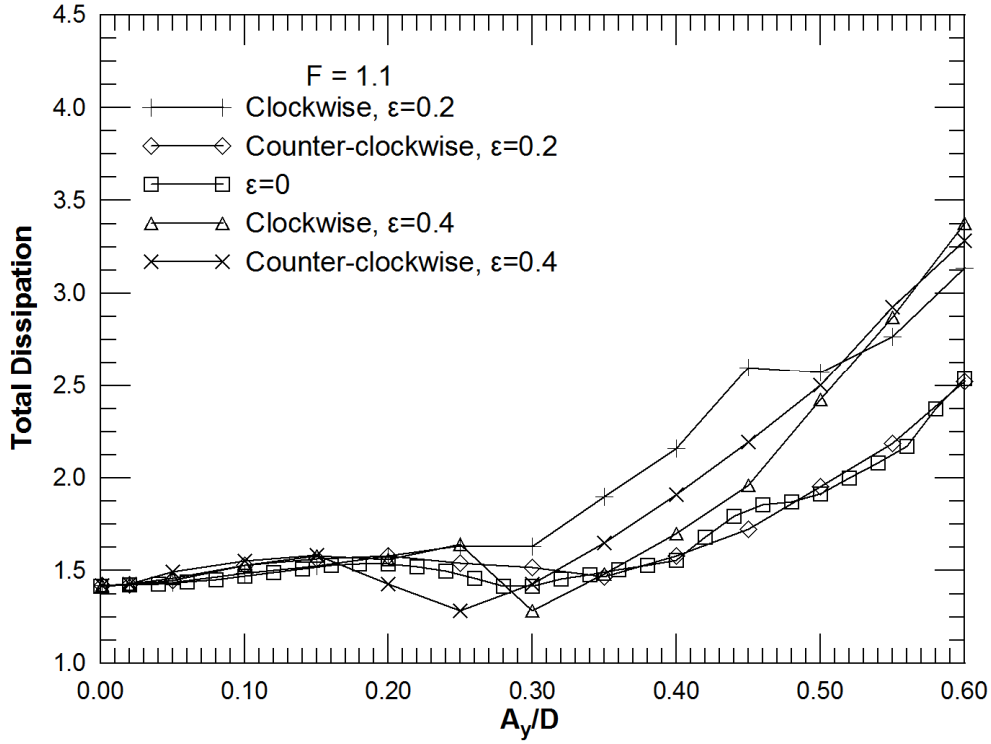

Figure 4-34: Time-averaged non-dimensional power dissipation versus the reduced y-amplitude, for frequency ratio $F = f_y/f_s = 1.1$; here, the cases $\varepsilon = 0$ (transverse-only oscillation), $\varepsilon = 0.2$ and $\varepsilon = 0.4$ (counter-clockwise and clockwise modes) are shown.

4.5.2 Wake modes

In this section we characterize the wake modes of two-dimensional flow past an oscillating cylinder. We use the time histories and power spectra of the lift force to characterize the behavior of the response and relate the trends to the flow dynamics. Visualization of the flow in terms of vorticity isocontours is used to illustrate the vortex shedding and identify the wake structures.

4.5.2.1 Time-histories of lift forces

We use the time histories of the computed lift coefficient to characterize the flow dynamics in the wake of the cylinder. In **Figure 4-35** to **Figure 4-40** we illustrate the time histories of C_L for three cases of frequency ratios ($F=f_y/f_s$) equal to 1.0, 0.9 and 1.1, corresponding to resonant forcing, forcing at below and at above the natural frequency. A value of amplitude ratio $\varepsilon = A_x / A_y$ is considered, equal to 0.2, for counter-clockwise and clockwise modes and representative values of amplitude ratios A_y/D.

Figure 4-35 and **Figure 4-36** illustrate the cases with frequency ratio, *F=1.0*, counter-clockwise and clockwise cylinder motion, and transverse oscillation amplitude: (a) $A_y/D = 0.10$, (b) $A_y/D = 0.30$ and (c) $A_y/D = 0.60$ respectively. In **Figure 4-35** (a), (b) the time history of C_L fluctuates periodically with a uniform dominant frequency. At oscillation amplitudes higher than $A_y/D = 0.30$ the C_L time series show a modulation with different oscillation frequencies in each cycle, see **Figure 4-35** (c). On the other hand, for clockwise cylinder motion, the time history of C_L illustrated in **Figure 4-36** (a) and (b) is regular (harmonic) and has a dominant frequency, which is the excitation frequency (f_y). In **Figure 4-36**(c) the C_L is nearly harmonic with indications of superharmonic frequencies.

In **Figure 4-37** the time series of C_L are illustrated for frequency ratio *F=0.9*, counter-clockwise cylinder motion and transverse oscillation amplitude: (a) $A_y/D = 0.10$, (b) $A_y/D = 0.40$ and (c) $A_y/D = 0.60$. The time series of C_L shown in **Figure 4-37** (a) are regular and have a dominant frequency, which is the excitation frequency, f_y. In **Figure 4-37 (**b), C_L is nearly harmonic but with indication of superharmonics. At higher amplitudes as presented in **Figure 4-37** (c) C_L has a modulation within each cycle. For clockwise motion the time history of C_L illustrated in **Figure 4-38**(a) is periodic with a dominant frequency, the excitation frequency (f_y). In **Figure 4-38** (b) and (c) C_L is nearly harmonic but with indications of superharmonics. For frequency ratio *F=1.1*, counter-clockwise and clockwise cylinder motion, the time series of C_L are shown in **Figure 4-39** and **Figure 4-40.** They are also characterized by periodic signals in low oscillation amplitudes and indication of modulation and superharmonic frequencies at higher amplitudes.

In **Figure 4-41** to **Figure 4-45** phase portraits of C_L-C_D for some of the cases are shown.

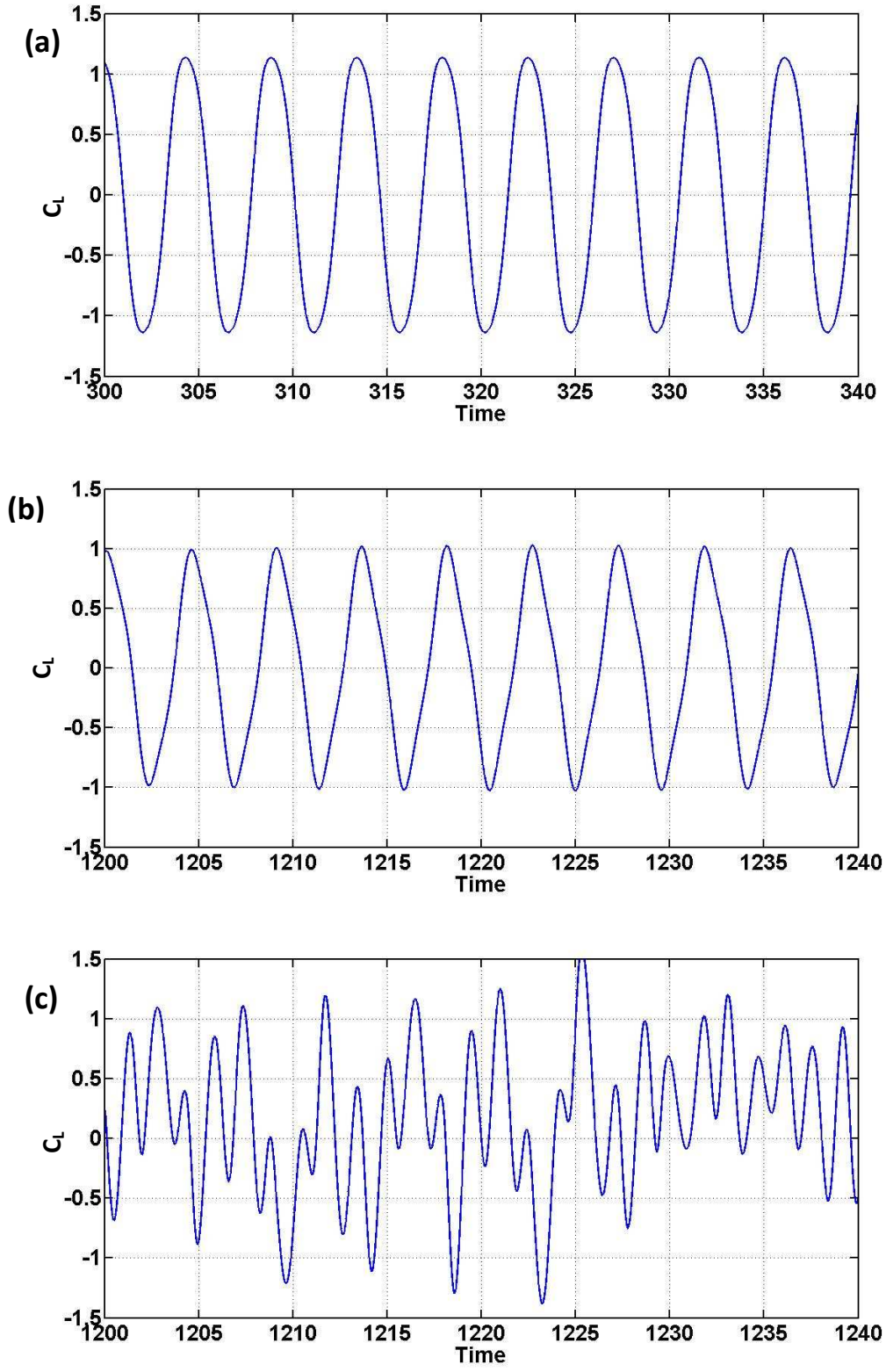

Figure 4-35: Time histories of C_L for the cases with frequency ratio $F=f_y/f_s=1.0$, counter-clockwise cylinder motion, $\varepsilon=0.2$, and transverse oscillation amplitude: (a) $A_y/D=0.10$, (b) $A_y/D=0.30$ and (c) $A_y/D=0.60$.

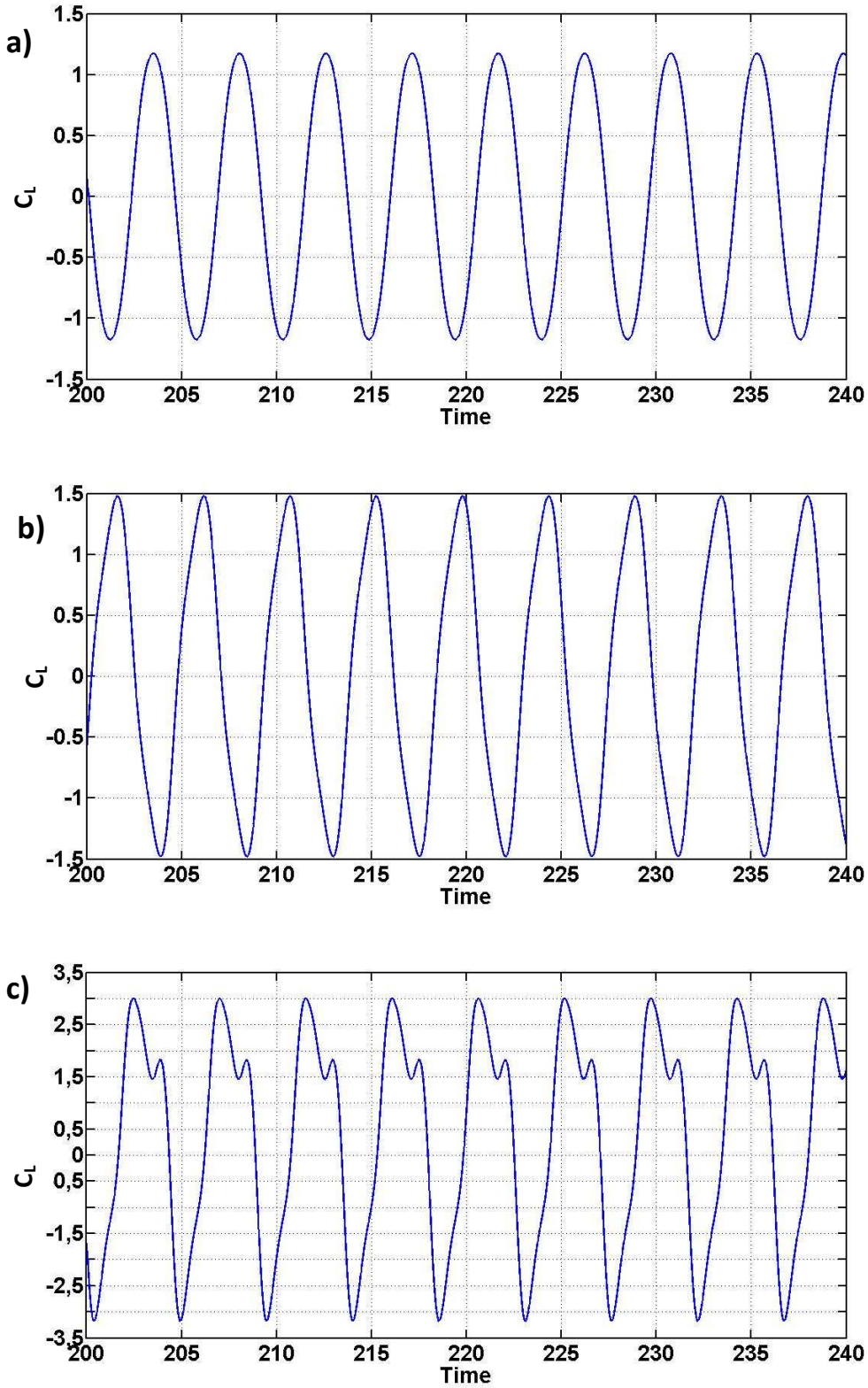

Figure 4-36: Time histories of C_L for the cases with frequency ratio $F=f_y/f_s=1.0$, clockwise cylinder motion, $\varepsilon=0.2$, and transverse oscillation amplitude: (a) $A_y/D=0.10$, (b) $A_y/D=0.30$ and (c) $A_y/D=0.60$.

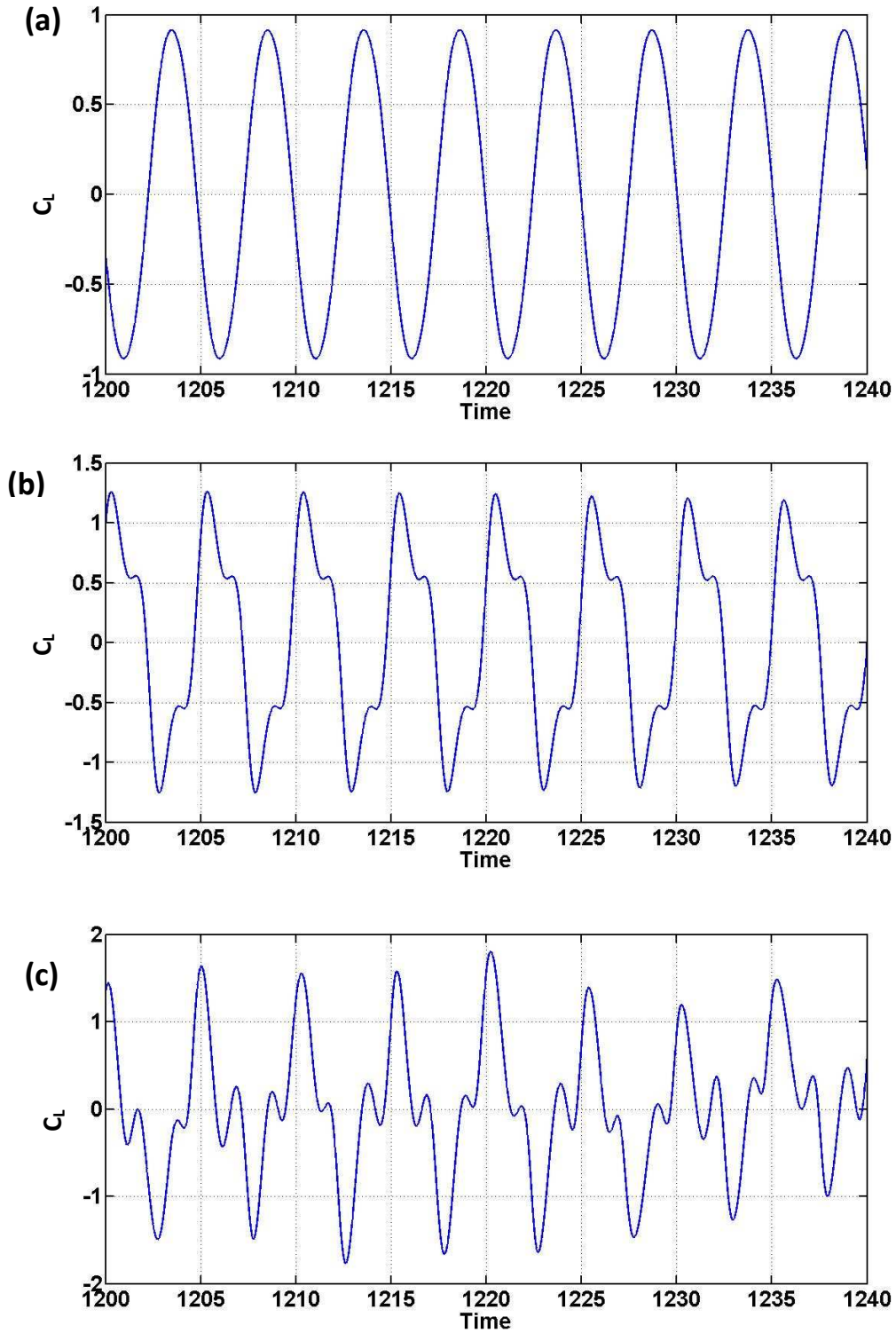

Figure 4-37: Time histories of C_L for the cases with frequency ratio $F=f_y/f_s=0.9$, counter-clockwise cylinder motion, $\varepsilon=0.2$, and transverse oscillation amplitude: (a) $A_y/D=0.10$, (b) $A_y/D=0.40$ and (c) $A_y/D=0.60$.

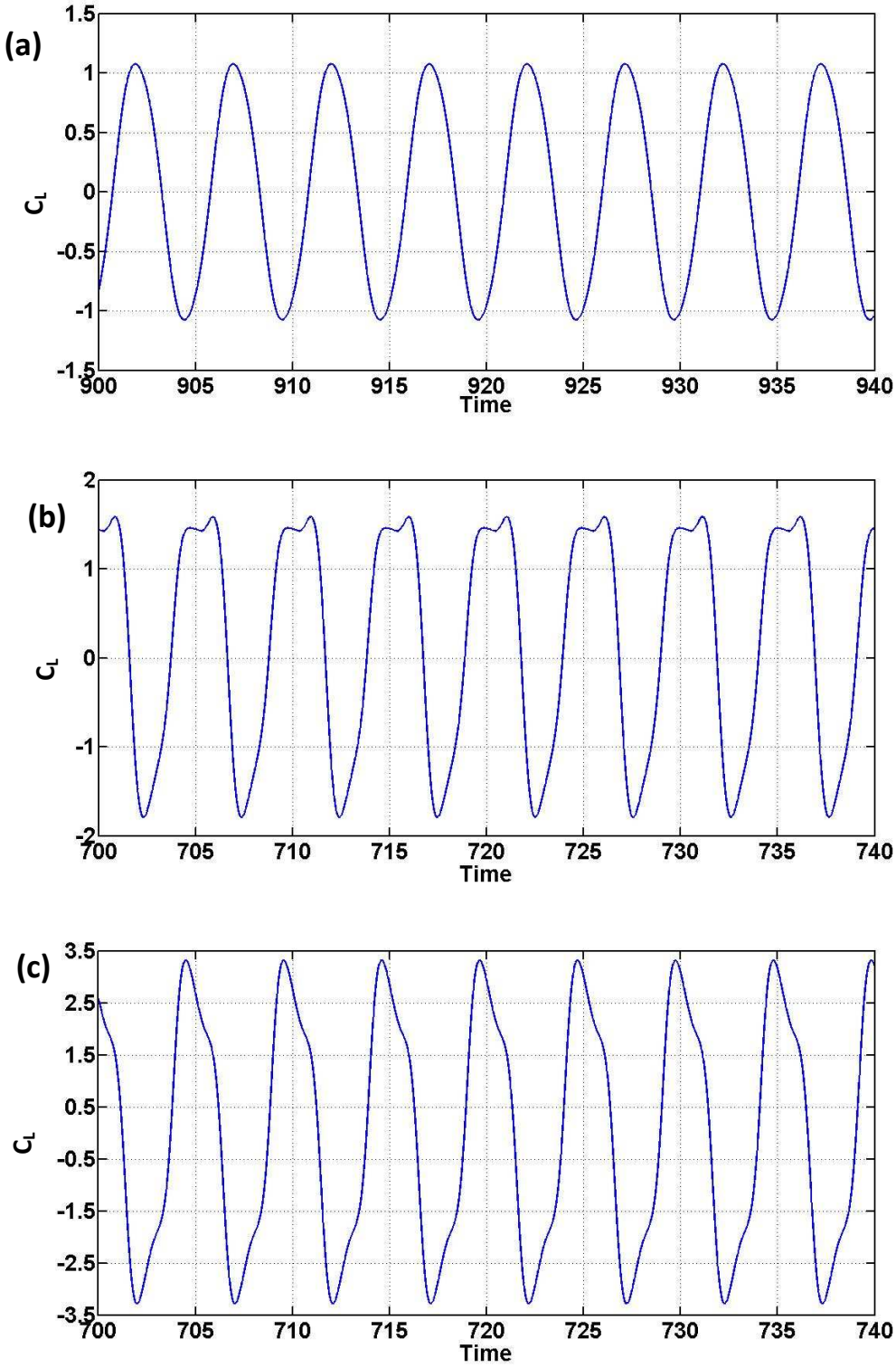

Figure 4-38: Time histories of C_L for the cases with frequency ratio $F=f_y/f_s=0.9$, clockwise cylinder motion, $\varepsilon=0.2$, and transverse oscillation amplitude: (a) $A_y/D=0.10$, (b) $A_y/D=0.40$ and (c) $A_y/D=0.60$.

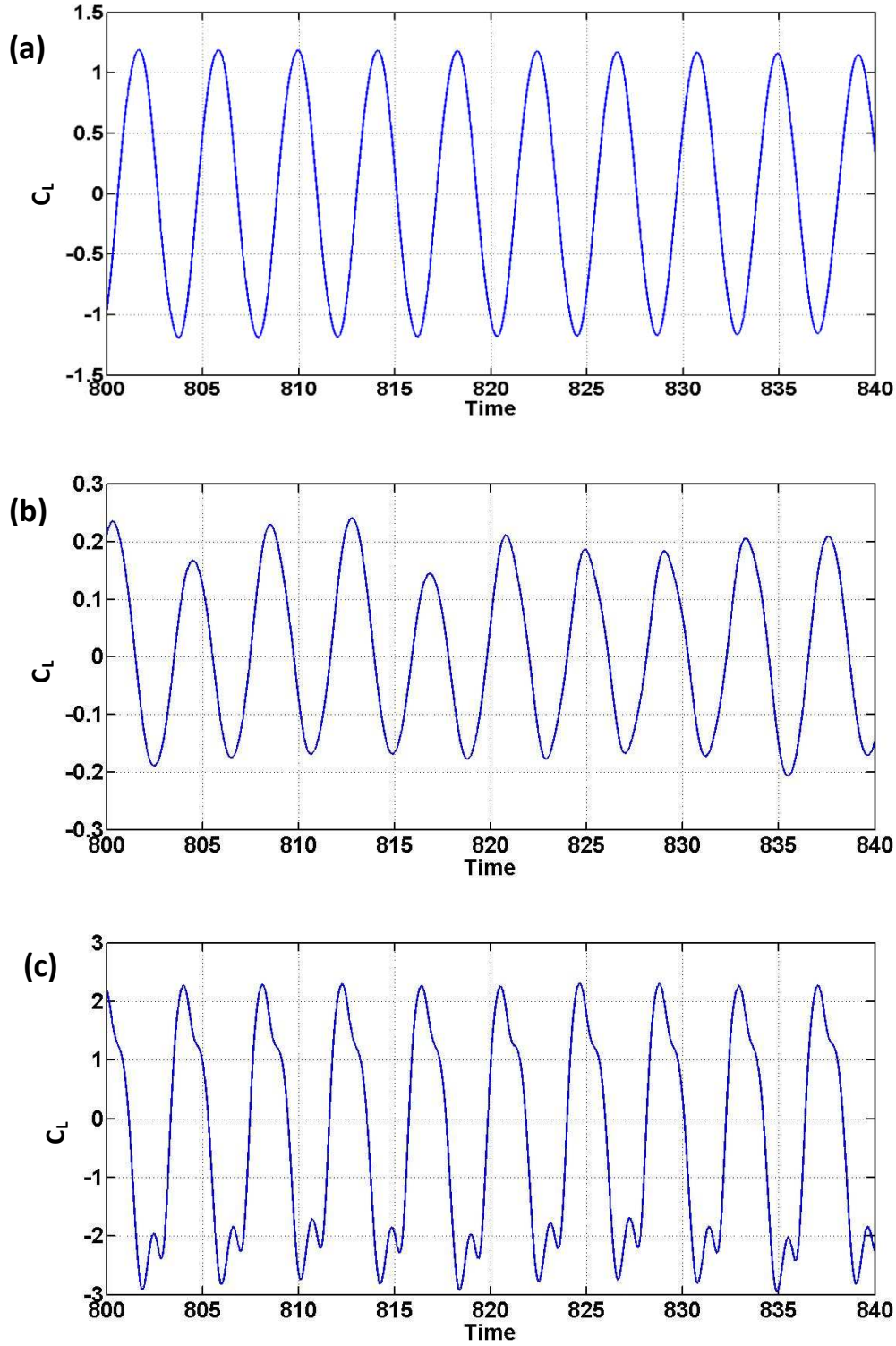

Figure 4-39: Time histories of C_L for the cases with frequency ratio $F=f_y/f_s=1.1$, counter-clockwise cylinder motion, $\varepsilon=0.2$, and transverse oscillation amplitude: (a) $A_y/D=0.10$, (b) $A_y/D=0.30$ and (c) $A_y/D=0.60$.

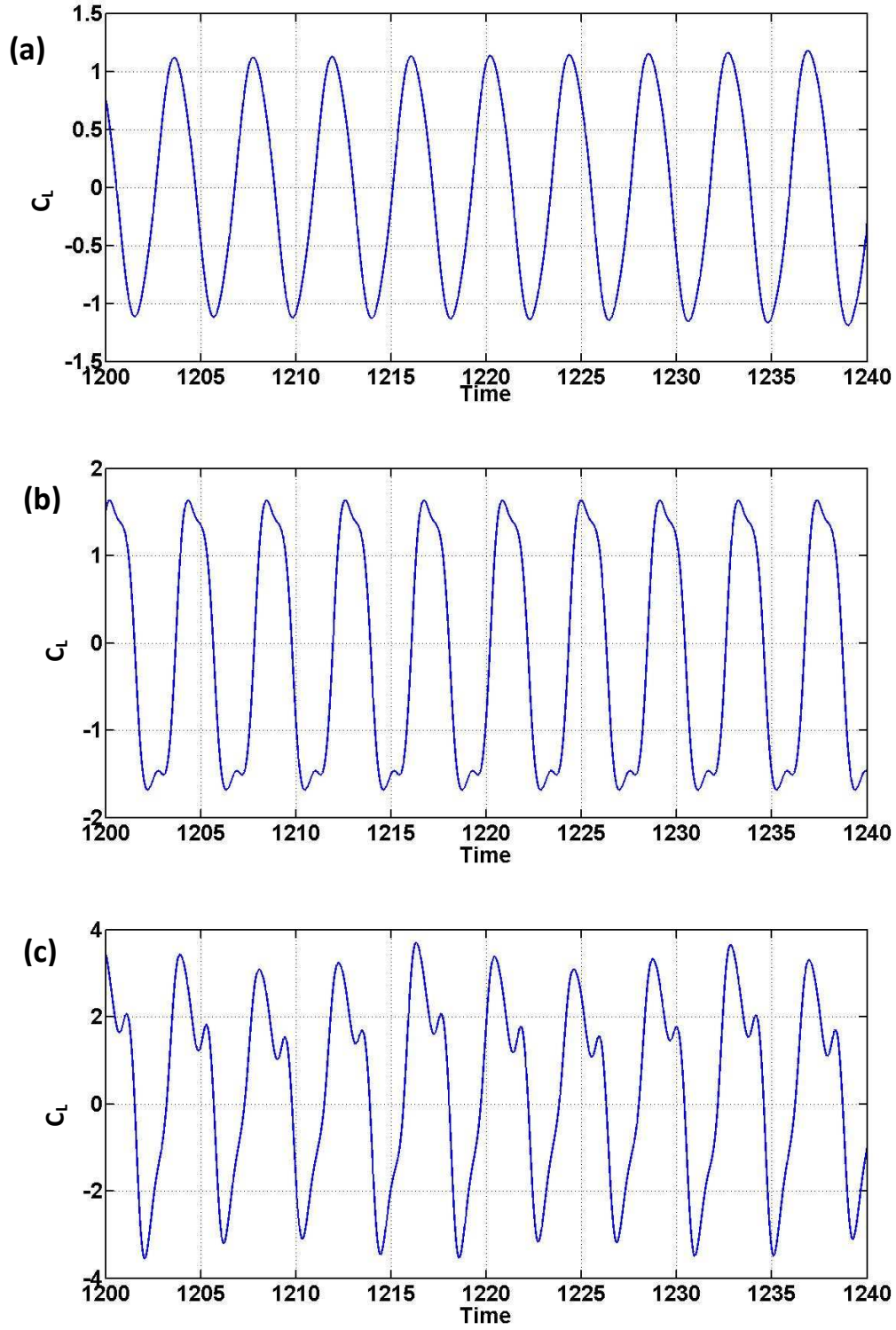

Figure 4-40: Time histories of C_L for the cases with frequency ratio $F=f_y/f_s=1.1$, clockwise cylinder motion, $\varepsilon=0.2$, and transverse oscillation amplitude: (a) $A_y/D=0.10$, (b) $A_y/D=0.40$ and (c) $A_y/D=0.60$.

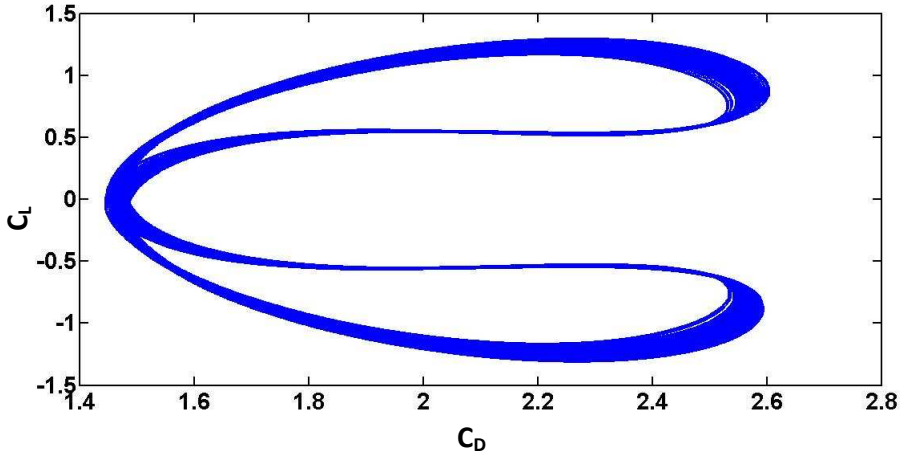

Figure 4-41: Orbits in the C_L – C_D plane for a case with frequency ratio $F=f_y/f_s=0.9$, counter-clockwise cylinder motion, $\varepsilon=0.2$, and transverse oscillation amplitude $A_y/D=0.40$.

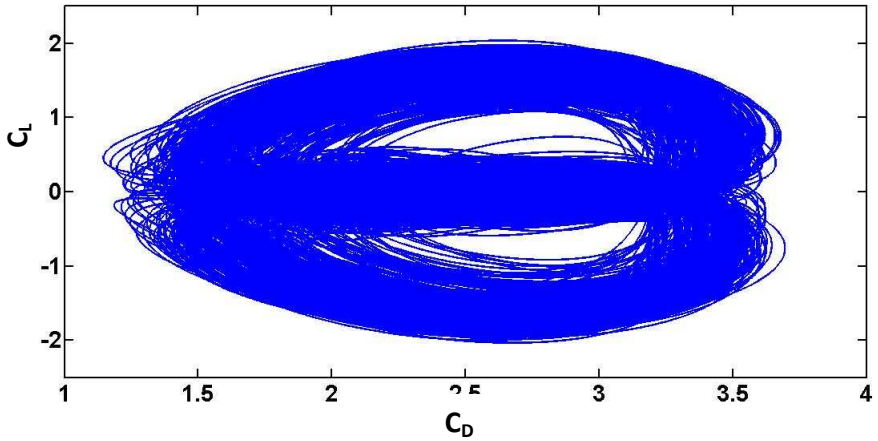

Figure 4-42: Orbits in the C_L – C_D plane for a case with frequency ratio $F=f_y/f_s=0.9$, counter-clockwise cylinder motion, $\varepsilon=0.2$, and transverse oscillation amplitude $A_y/D=0.60$.

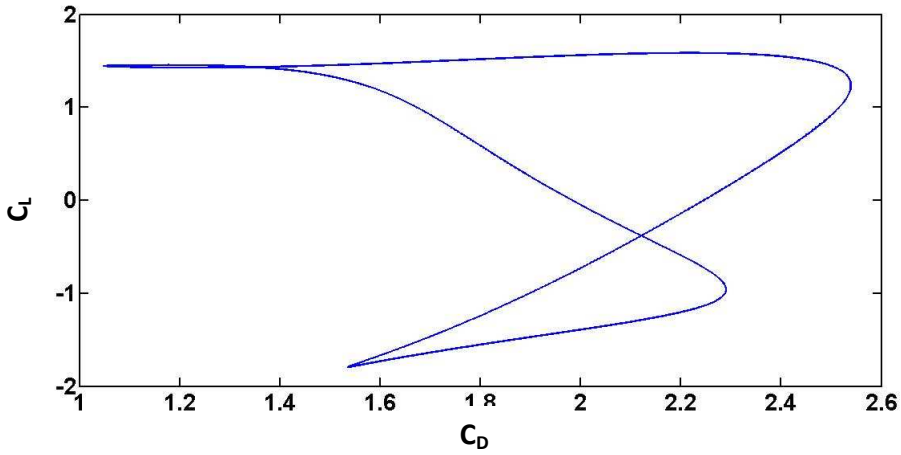

Figure 4-43: Orbits in the C_L – C_D plane for a case with frequency ratio $F=f_y/f_s=0.9$, clockwise cylinder motion, $\varepsilon=0.2$, and transverse oscillation amplitude $A_y/D=0.40$.

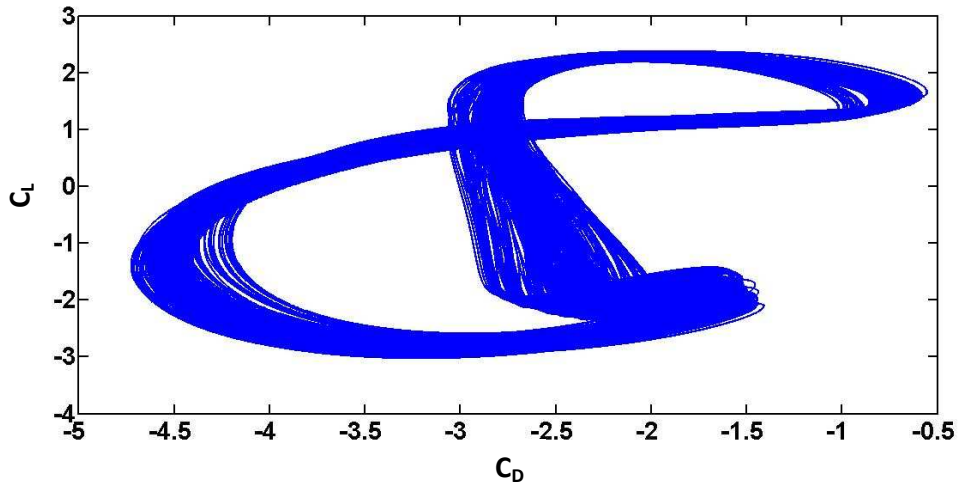

Figure 4-44: Orbits in the C_L – C_D plane for a case with frequency ratio $F=f_y/f_s=1.1$, counter-clockwise cylinder motion, $\varepsilon=0.2$, and transverse oscillation amplitude $A_y/D=0.60$.

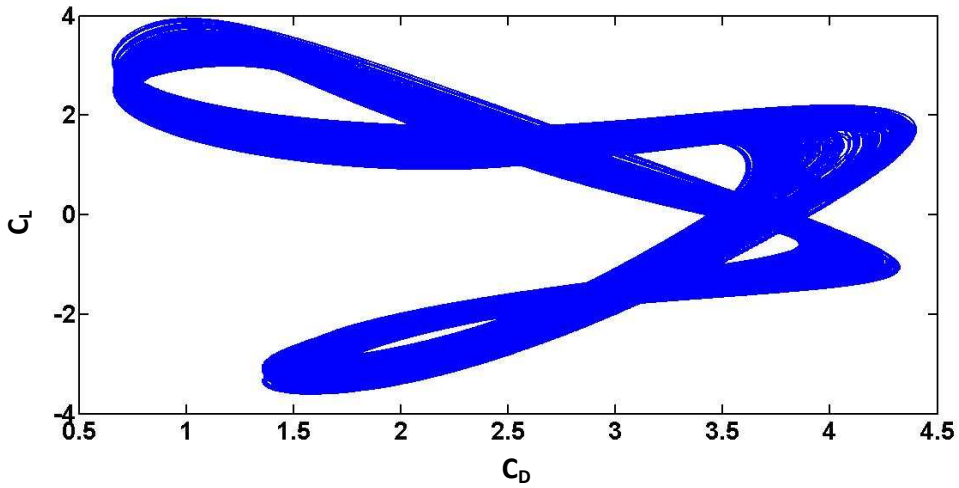

Figure 4-45: Orbits in the C_L – C_D plane for a case with frequency ratio $F=f_y/f_s=1.1$, clockwise cylinder motion, $\varepsilon=0.2$, and transverse oscillation amplitude $A_y/D=0.60$.

4.5.2.2 Spectral analysis

Spectral analysis is used to post process the results of the simulation. More specifically we use Fast Fourier Transform to process the time series obtained from the simulation. The time series include the calculated forces and are sampled every ΔT interval, whereas the time interval is integer multiple of the Δt used for the calculations of the solver.

The required length of simulation is long enough to achieve the required accuracy on the calculation of the dominant frequency. Thus simulation is carried on until a "steady state" is reached. We use MATLAB's graphical interface to create Power Spectral Density diagrams and to identify the dominant frequencies.

In **Figure 4-46** - **Figure 4-51** are illustrated the results of the lift spectra for three values of frequency ratio ($F=f_y/f_s$) equal to 1.0, 0.9 and 1.1, corresponding to resonant forcing, forcing below and above the natural frequency. A value of amplitude ratio $\varepsilon=A_x/A_y$ is considered, equal to 0.2, for both the counter-clockwise and clockwise modes. The non-dimensional frequency of flow past a stationary cylinder is f_s=0.22017.

For counter-clockwise motion when forcing at *F=1.0* and *F=0.9*, lock-in of the lift is observed at relatively low values of the transverse oscillation amplitude (in the order of 0.1 cylinder diameters), whereas there is a strong peak at the third harmonic of f_y in the lift spectra, see **Figure 4-46**(a) and **Figure 4-48**(a). At higher oscillation amplitudes the lift spectra is characterized by very rich frequency content, but still contains two strong peaks, at the excitation frequency and its third harmonic, see in **Figure 4-46**(c), **Figure 4-48**(b) and **Figure 4-48**(c). For resonant forcing (*F=1.0*), multiple harmonics are present at even lower oscillation amplitudes (0.3 cylinder diameters), see **Figure 4-46**(b). A similar picture is obtained in the case of forcing at above the natural frequency (*F=1.1*), see **Figure 4-50**. In all cases, the third harmonic of the excitation frequency has a strong presence in the lift spectra.

On the other hand, for clockwise cylinder motion at *F=1.0* and *F=0.9*, odd harmonics are present in the spectra at low amplitude, and both odd and even harmonics at high amplitude (**Figure 4-47** and **Figure 4-49**). The presence of the third harmonic remains pronounced at both oscillation frequencies, while complex spectra have only been obtained for forcing above the natural frequency (*F=1.1*), see **Figure 4-51**.

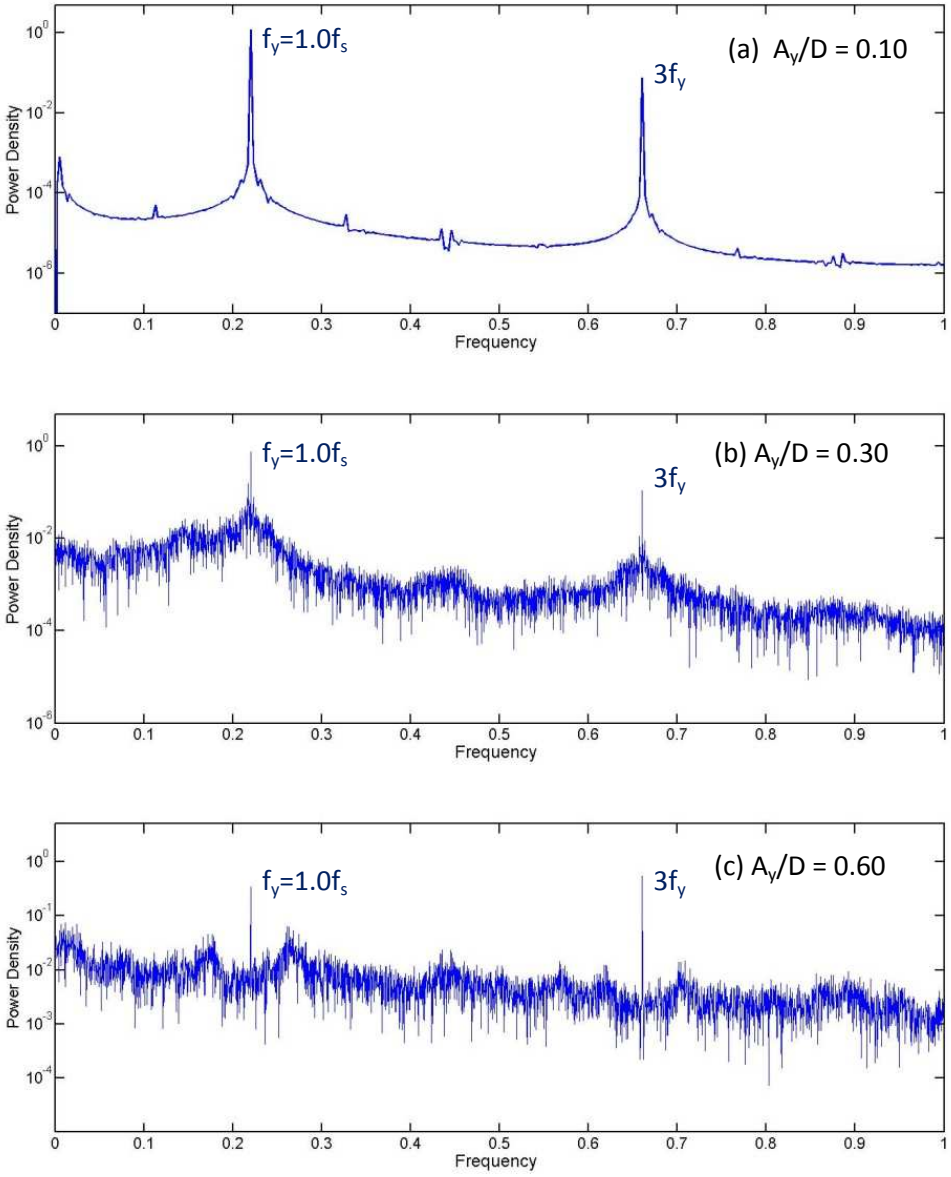

Figure 4-46: Lift coefficient spectra for a case with frequency ratio $F=f_y/f_s=1.0$, counter-clockwise cylinder motion, $\varepsilon=0.2$ and transverse oscillation amplitudes: (a) $A_y/D=0.10$, (b) $A_y/D=0.30$ and (c) $A_y/D=0.60$.

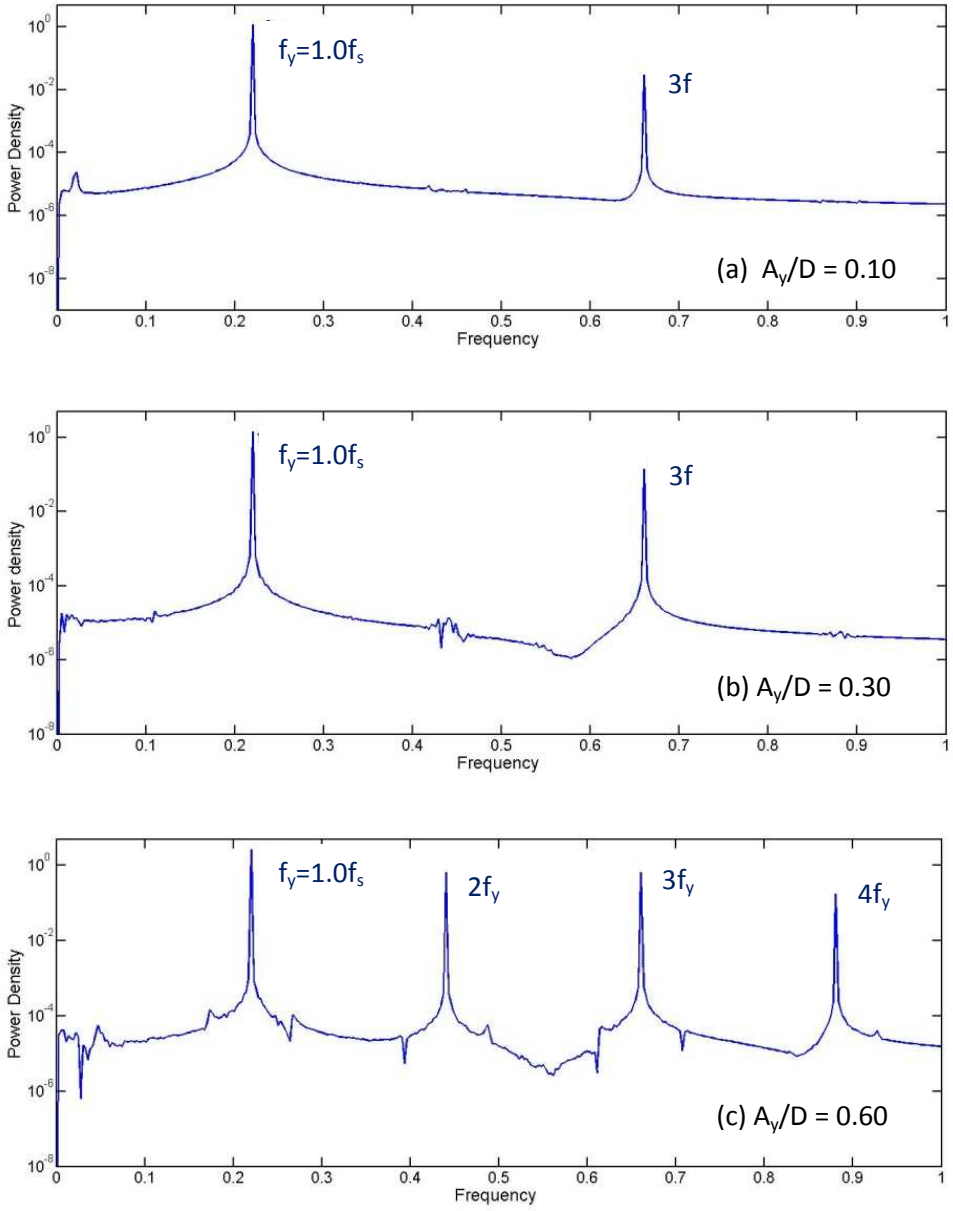

Figure 4-47: Lift coefficient spectra for a case with frequency ratio $F=f_y/f_s=1.0$, clockwise cylinder motion, $\varepsilon=0.2$ and transverse oscillation amplitudes: (a) $A_y/D=0.10$, (b) $A_y/D=0.30$ and (c) $A_y/D=0.60$.

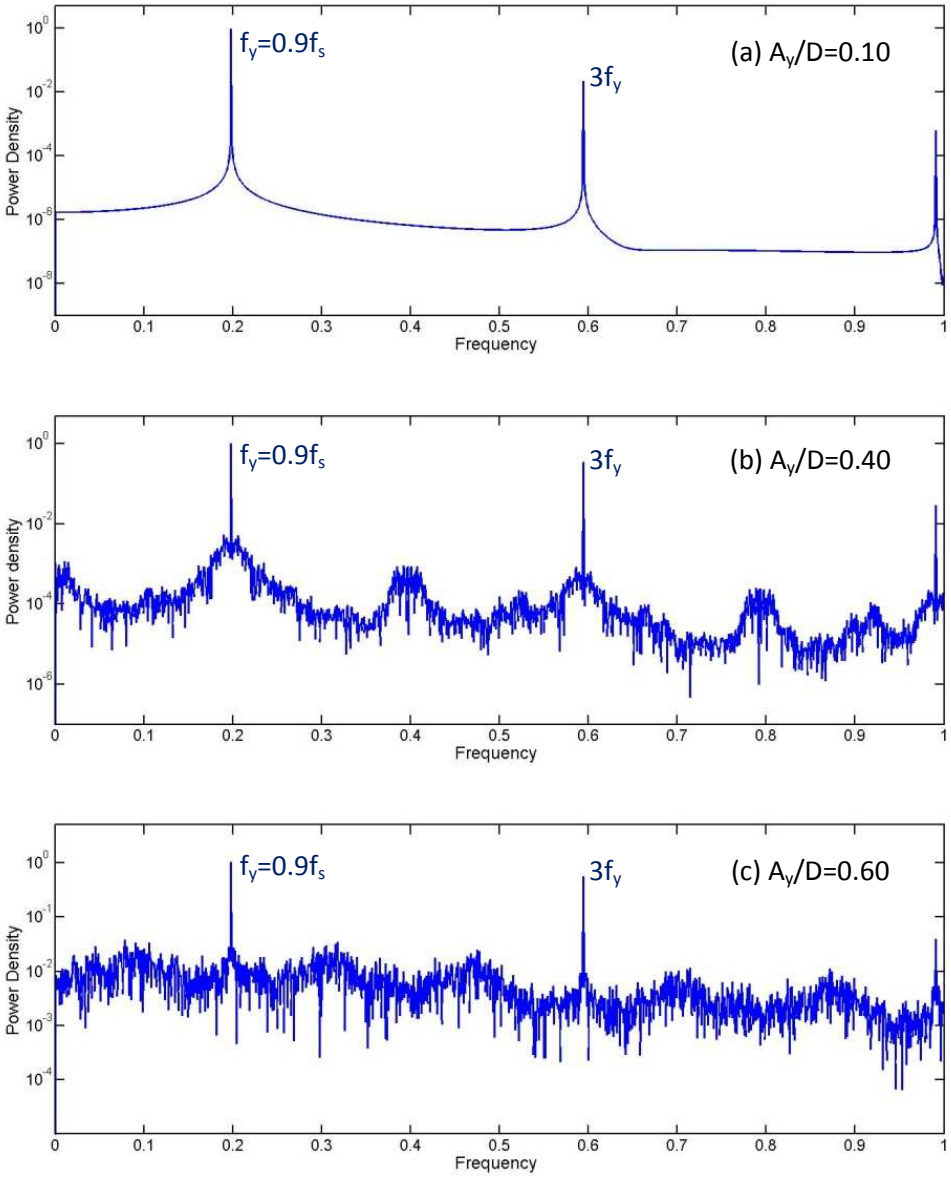

Figure 4-48: Lift coefficient spectra for a case with frequency ratio $F=f_y/f_s=0.9$, counter-clockwise cylinder motion, $\varepsilon=0.2$ and transverse oscillation amplitudes: (a) $A_y/D=0.10$, (b) $A_y/D=0.40$ and (c) $A_y/D=0.60$.

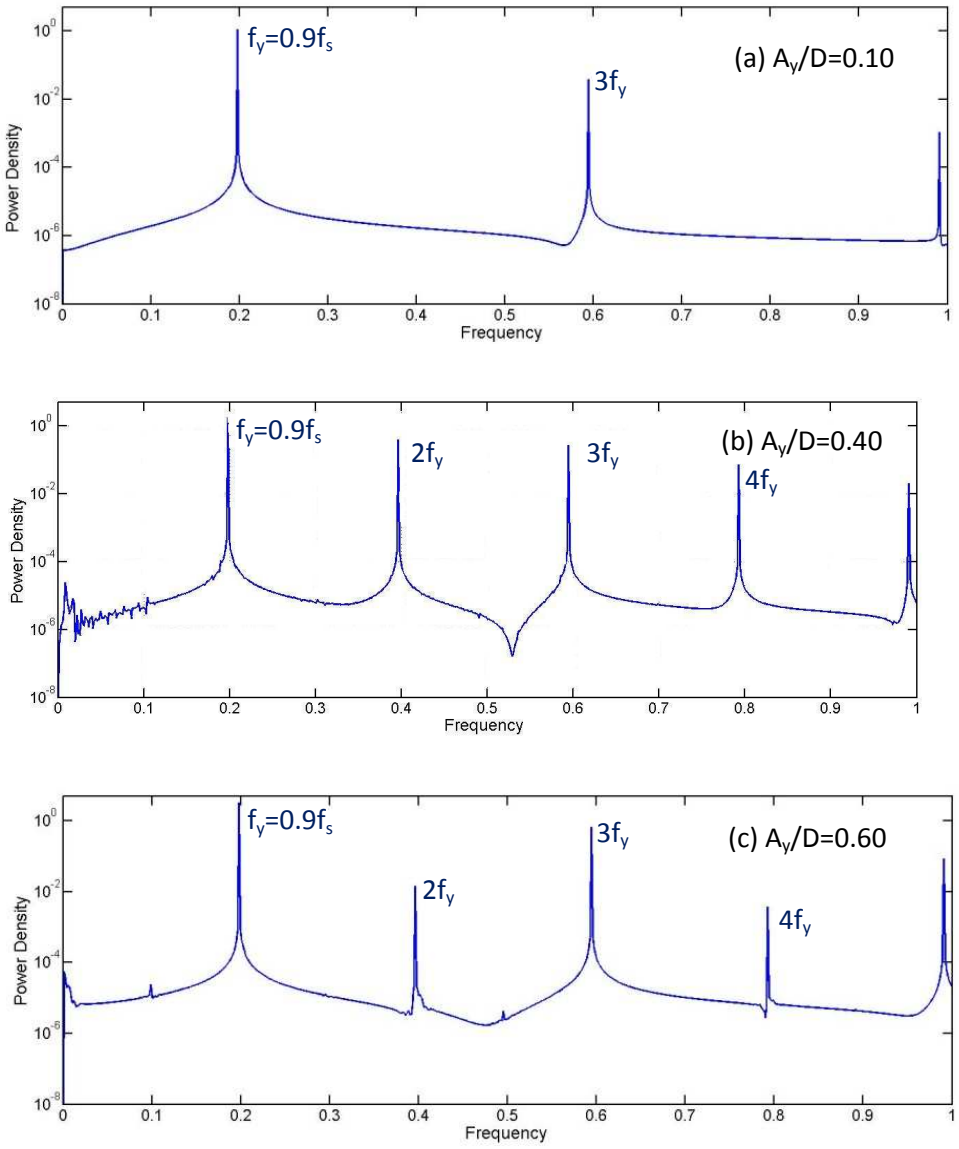

Figure 4-49: Lift coefficient spectra for a case with frequency ratio $F=f_y/f_s=0.9$, clockwise cylinder motion, $\varepsilon=0.2$ and transverse oscillation amplitudes: (a) $A_y/D=0.10$, (b) $A_y/D=0.40$ and (c) $A_y/D=0.60$.

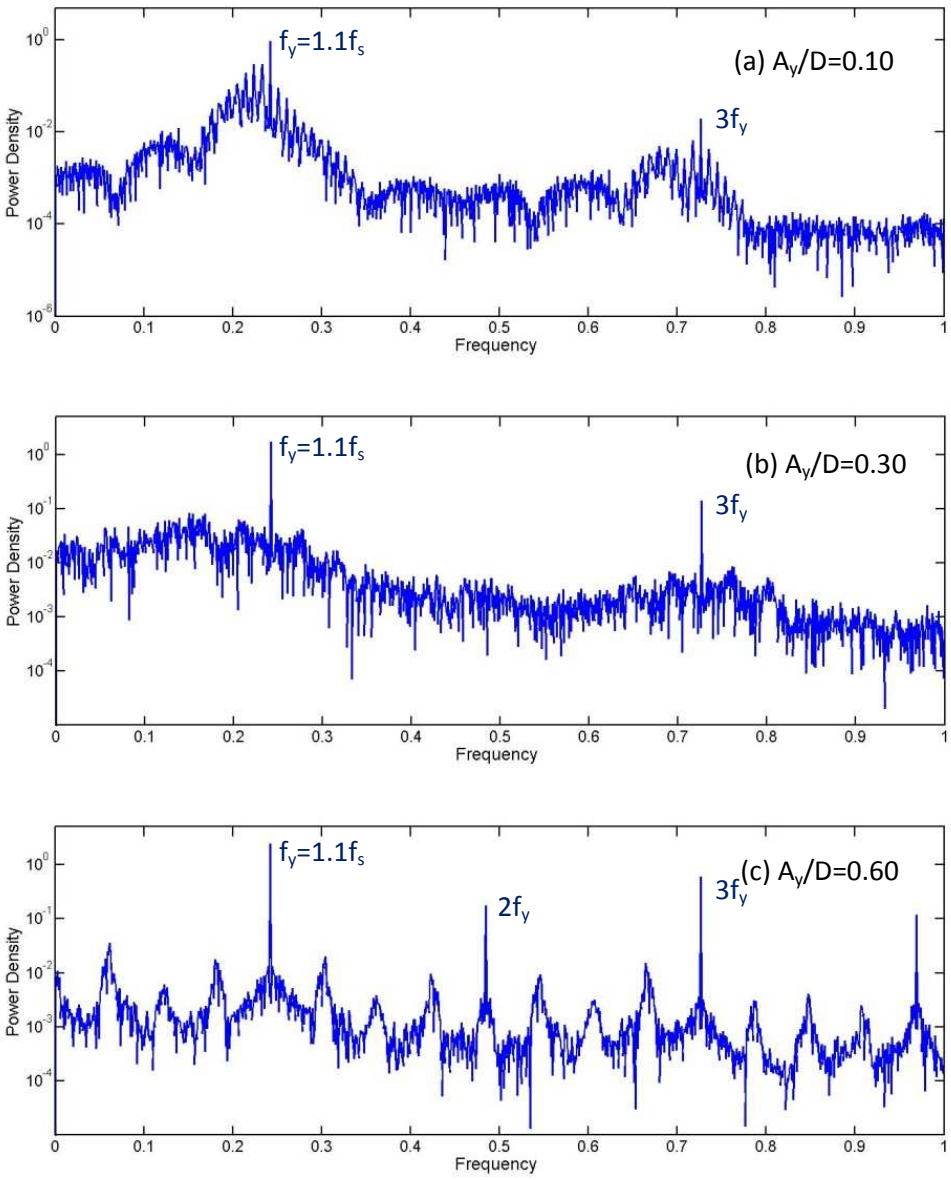

Figure 4-50: Lift coefficient spectra for a case with frequency ratio $F=f_y/f_s=1.1$, counter-clockwise cylinder motion, $\varepsilon=0.2$ and transverse oscillation amplitudes: (a) $A_y/D=0.10$, (b) $A_y/D=0.30$ and (c) $A_y/D=0.60$.

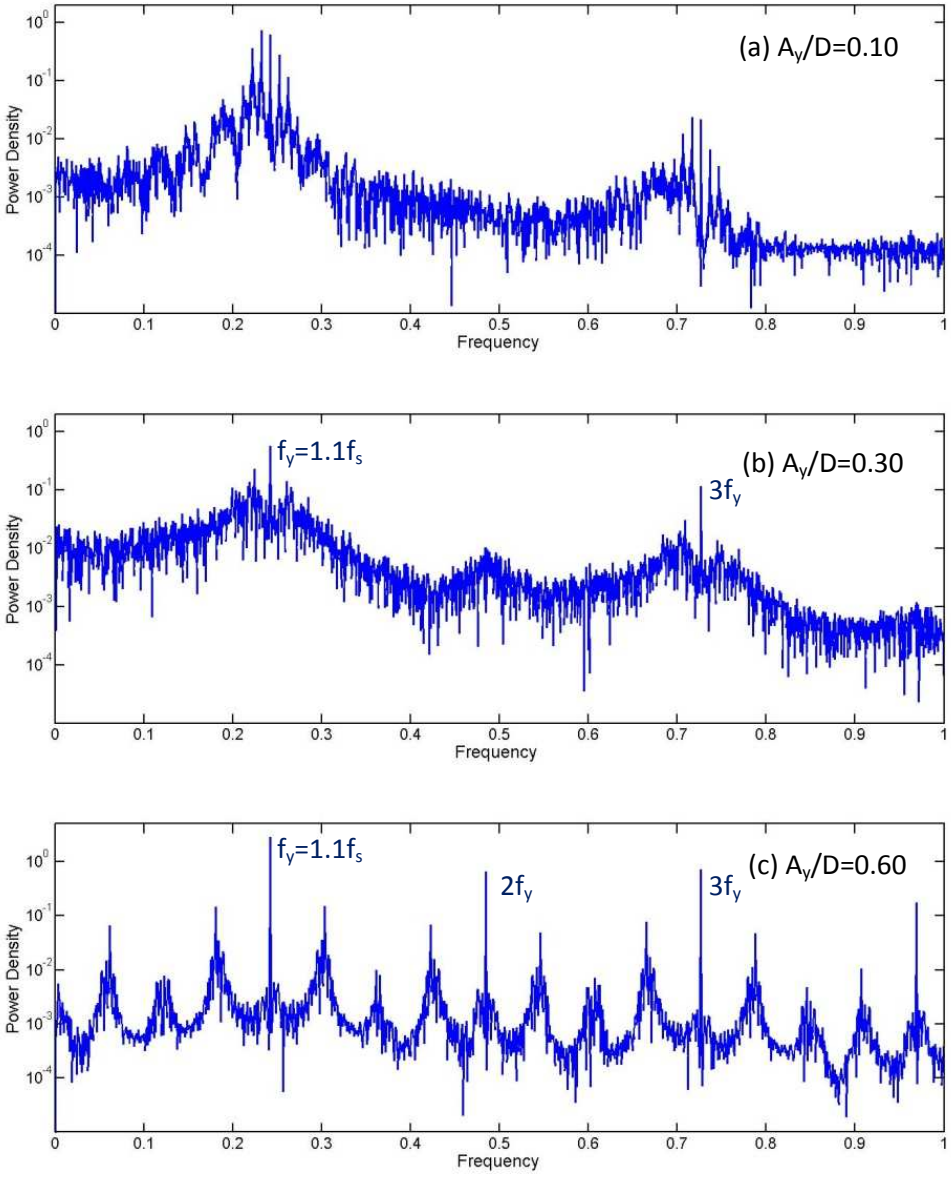

Figure 4-51: Lift coefficient spectra for a case with frequency ratio $F=f_y/f_s=1.1$, clockwise cylinder motion, $\varepsilon=0.2$ and transverse oscillation amplitudes: (a) $A_y/D=0.10$, (b) $A_y/D=0.30$ and (c) $A_y/D=0.60$.

4.5.2.3 Visualization of the flow in the wake

In this section we present visualizations of the wake in terms of vorticity isocontours for different values of A_y/D in order to study the wake of the cylinder for all the cases. We will make a comparison between our observations and the three basic patterns observed experimentally by Williamson and Roshko (1988), which we summarize here for easy reference: (a) a 2S type of vortex street, in which single vortices are formed on both sides of the cylinder, (b) an S+P type of vortex street, in which a single vortex is formed on one side of the cylinder, and a pair of vortices of opposite sign on the other side, and (c) a 2P type of vortex street, in which pairs of vortices of opposite sign are formed on both sides of the cylinder. Also we should refer to another type of vortex pattern observed in the previous studies by Kaiktsis et al. (2007), the "partial S+P" mode. This mode originates as a regular 2S mode, and is modified through vortex splitting; thus, in an instantaneous field, vortex pairs appear on the one side, and single vortices on the other.

Representative flow visualizations for the three oscillation frequencies of the present study are shown in **Figure 4-52** - **Figure 4-63** for the two studied motions (counter-clockwise and clockwise) and two representative ratios of the in-line vibration amplitude to the transverse amplitude, equal to 0.2 and 0.4. Several values of A_y/D from 0.05 to 0.60 are considered. The visualizations correspond to the moment that the cylinder occupies its mean position ($\eta_y/D = \eta_x/D = 0$).

In **Figure 4-52** - **Figure 4-55** different flow visualizations are illustrated for the case of resonant forcing, *F=1.0.* Most of the *ε=0.2* cases are representative of a 2S mode, i.e. single vortices are present on each side of the wake. High A_y/D values correspond to a type of wake characterized as a "partial S+P" mode, Kaiktsis et al. (2007) as well as complex vortex patterns in the wake, dominated by triplets or other combinations of vortices. This is in accordance with the variation of hydrodynamic forces acting on the cylinder. The dependence of flow structure on transverse oscillation amplitude remains the same for the *ε=0.4* cases.

Figure 4-56 - **Figure 4-59** show the vortex streets at forcing below the natural frequency, *F=0.9*. For *ε=0.2,* counter-clockwise motion the wake resembles a 2S type whereas it becomes disordered at increasing A_y/D values. Qualitatively, the same structures are present in the case of counter-clockwise motion and *ε=0.4*. For clockwise motion and *ε=0.2*, 2S wakes are present at low oscillation amplitudes, asymmetric wakes for A_y/D values of 0.25 and higher, while structures resembling a 2P type of mode are present for A_y/D values of order 0.6. For clockwise motion and *ε=0.4*, the patterns are qualitatively the same, with the "partial S+P" mode already present at $A_y/D = 0.20$, whereas complex asymmetric wakes are present at high oscillation amplitudes. These complex structures can be related to non-zero time-averaged lift forces, together with a significant increase of drag force.

Figure 4-60 to **Figure 4-63** show representative flow visualizations for *F=1.1*. For *ε=0.2,* when the cylinder is moving counter-clockwise, 2S structures are present, becoming more complicated downstream at high amplitudes. The visualization for *ε=0.4* shows that counter-clockwise motion is characterized by 2S structures at low oscillation amplitudes, and "partial S+P" wakes for A_y/D values of 0.45 and higher. For clockwise mode and *ε=0.2*, 2S structures are present for A_y/D up to 0.25. An alteration between "partial S+P" and 2S mode occurs at higher amplitudes, with the "partial S+P" mode dominating at A_y/D values of 0.50 and higher. Visualizations for ε=0.4 and clockwise motion show a qualitatively similar behavior, with "partial S+P" mode already present at A_y/D values of order 0.20, followed by a transition to 2S wakes at slightly higher oscillation amplitudes, and a return to the "partial S+P" mode at A_y/D values of order 0.50. At higher amplitudes, the vortex patterns in the wake remain complex, dominated by triplets or other combinations of vortices. This is in accordance with the variation of hydrodynamic forces acting on the cylinder.

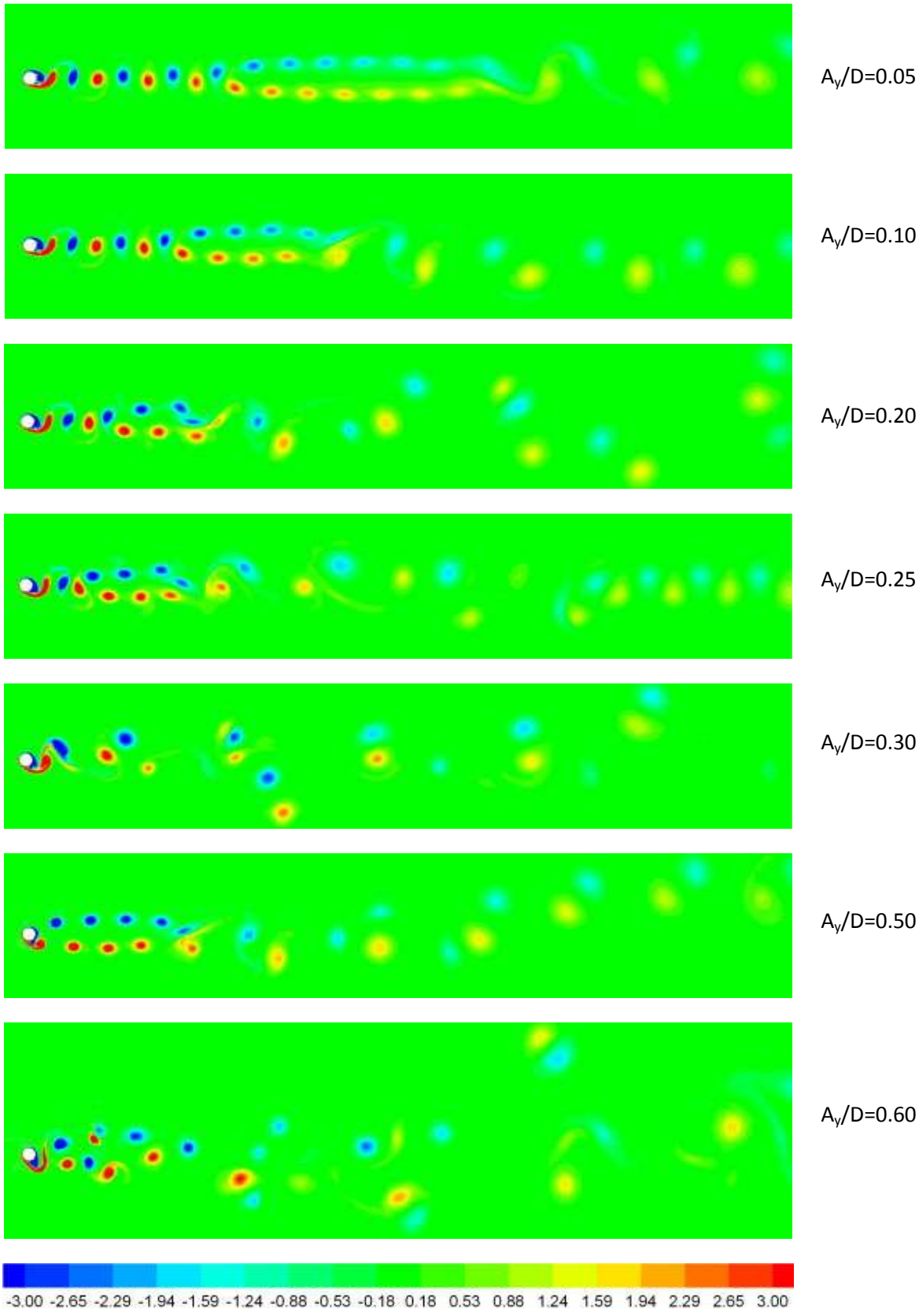

Figure 4-52: Instantaneous vorticity isocontours for various A_y/D, for *F=1.0, ε=0.2*, counter-clockwise mode.

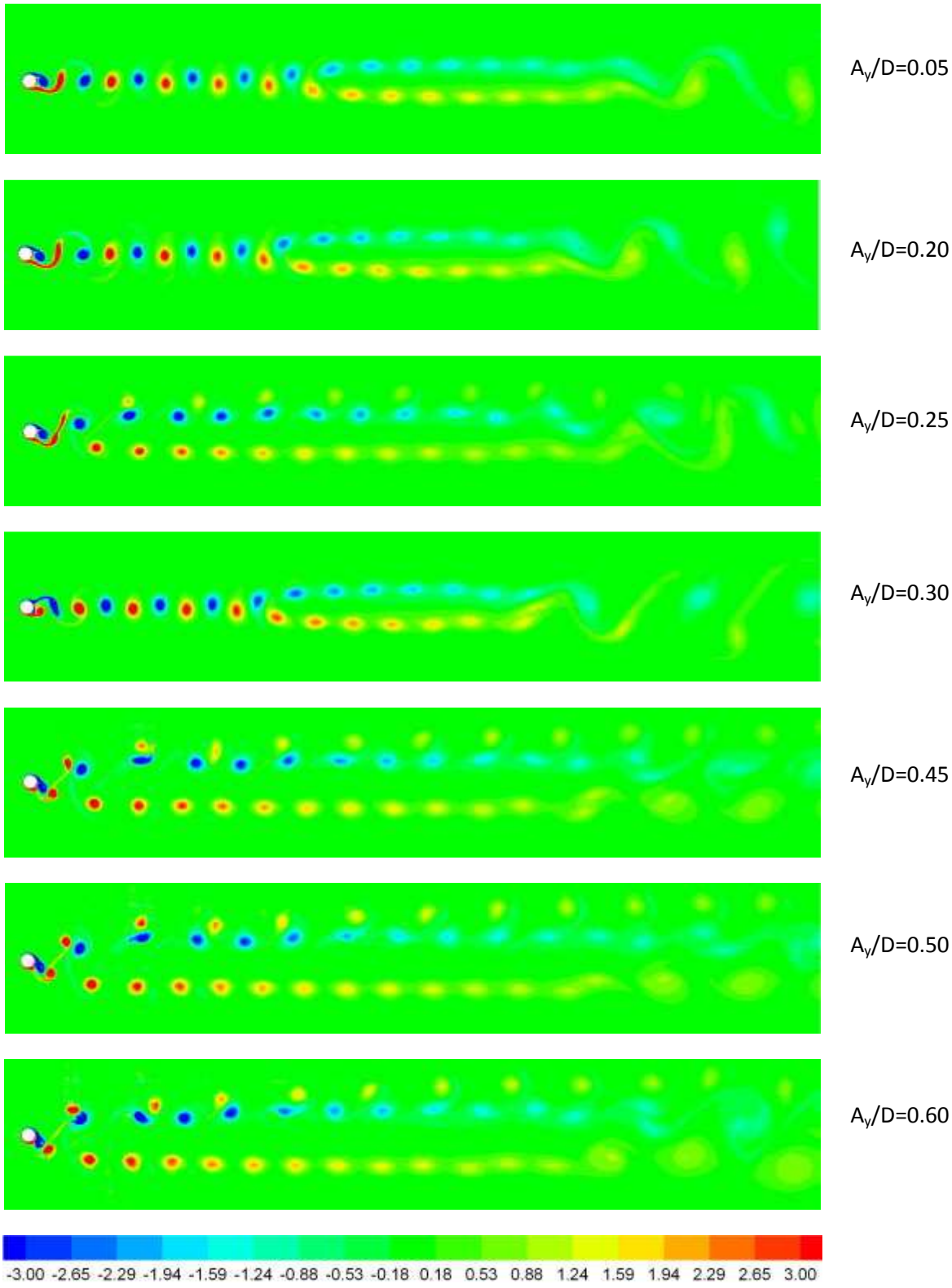

Figure 4-53: Instantaneous vorticity isocontours for various A_y/D, for *F=1.0, ε=0.2*, clockwise mode.

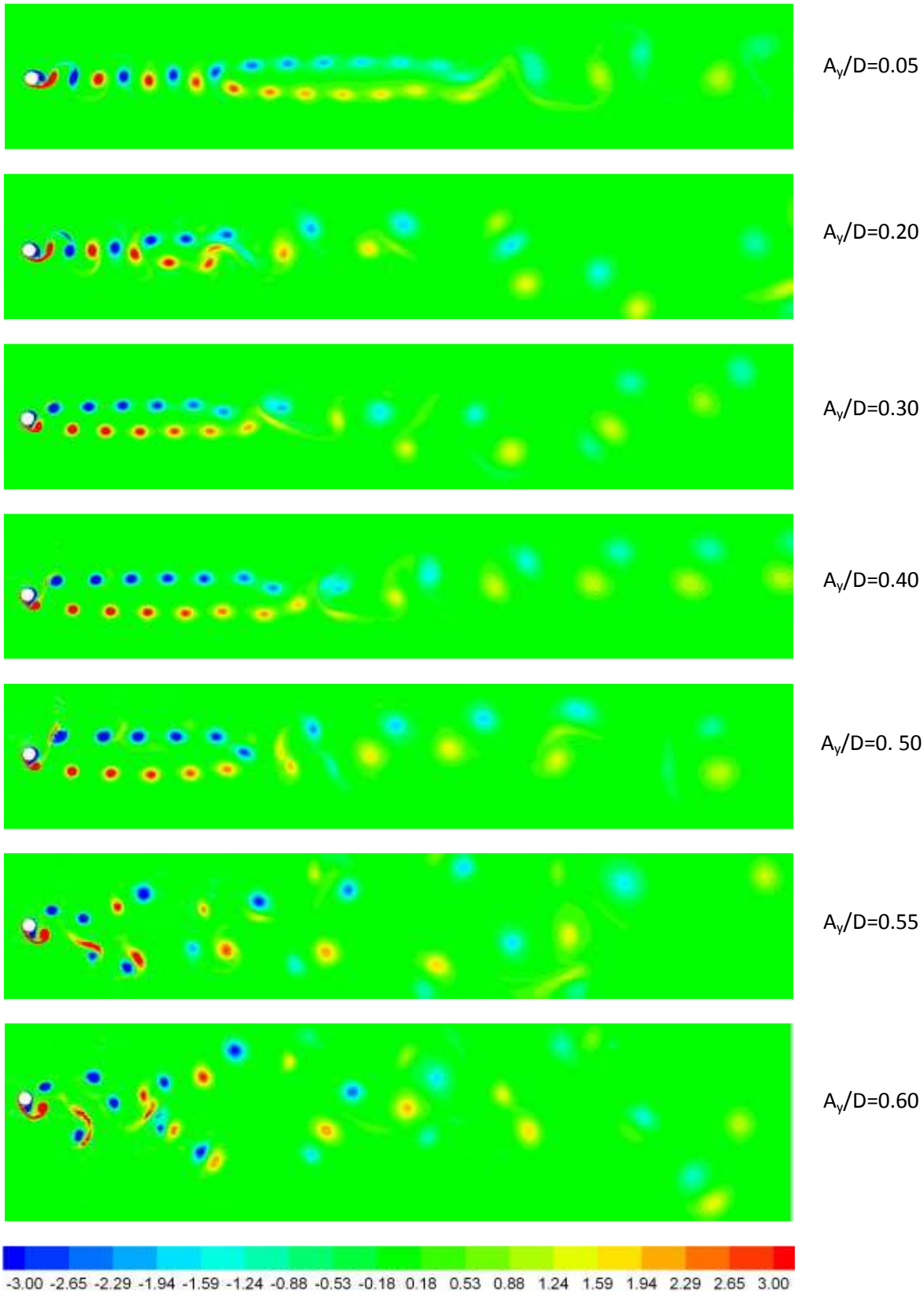

Figure 4-54: Instantaneous vorticity isocontours for various A_y/D, for *F=1.0, ε=0.4*, counter-clockwise mode.

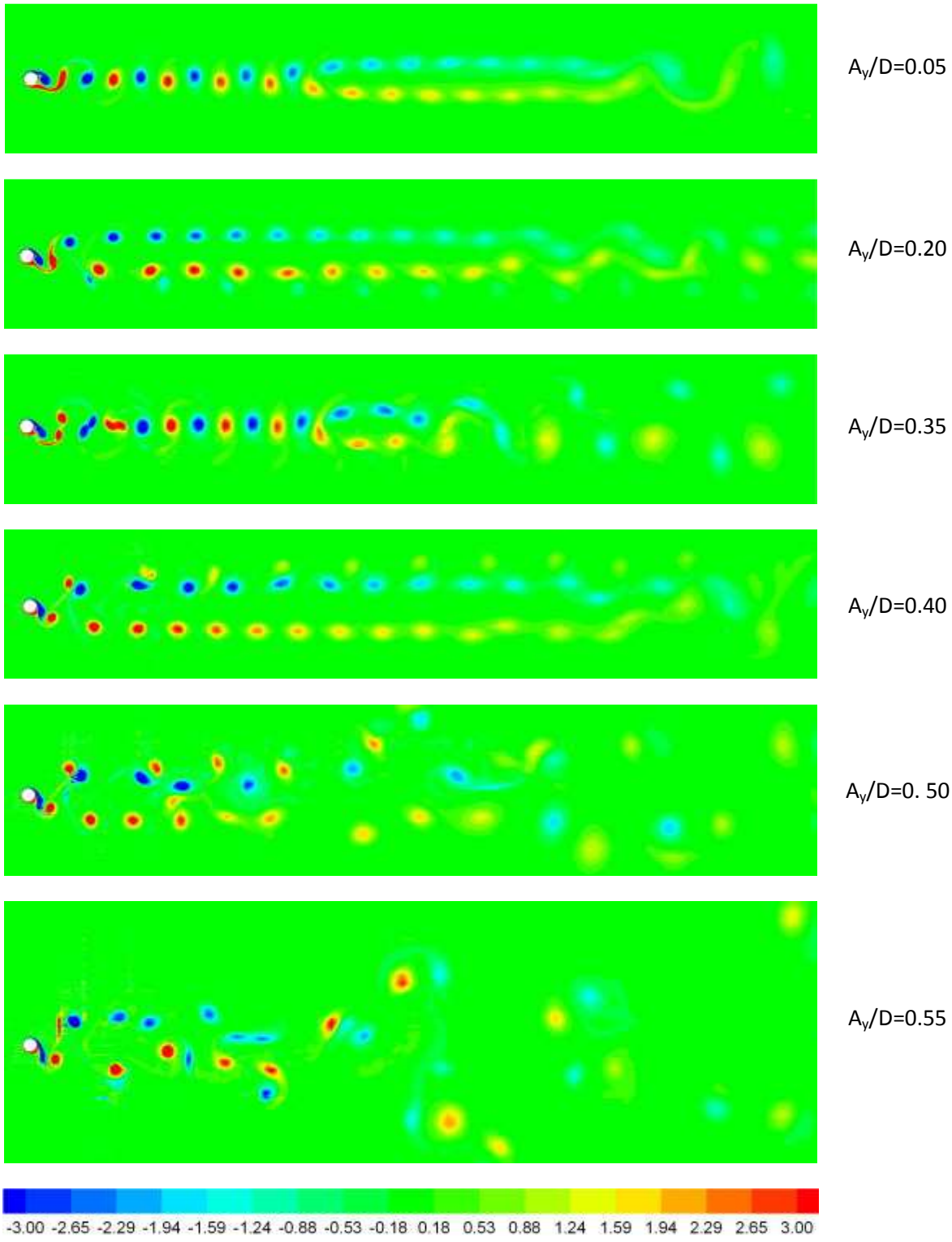

Figure 4-55: Instantaneous vorticity isocontours for various A_y/D, for *F=1.0, ε=0.4*, clockwise mode.

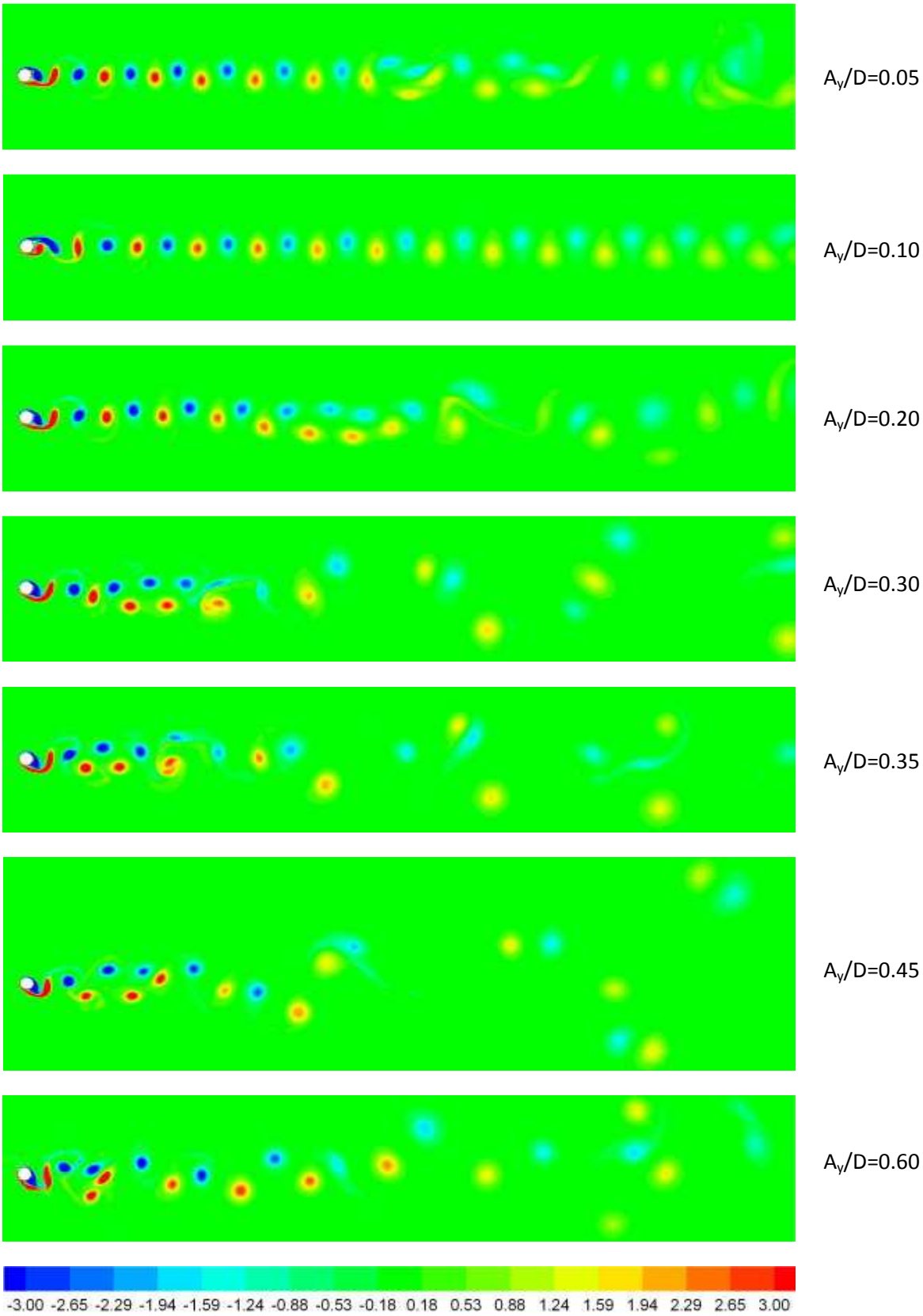

Figure 4-56: Instantaneous vorticity isocontours for various A_y/D, for *F=0.9, ε=0.2*, counter-clockwise mode.

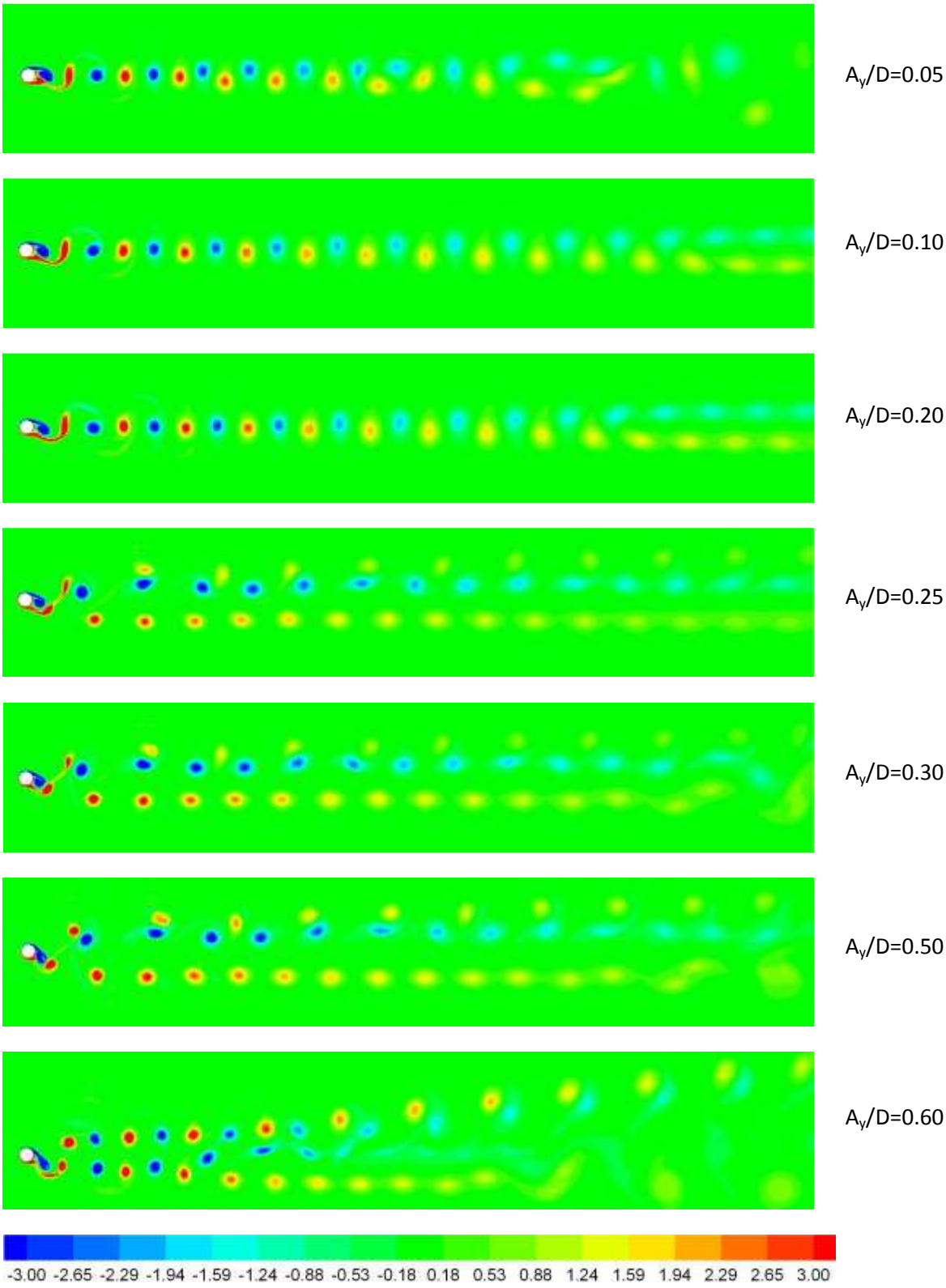

Figure 4-57: Instantaneous vorticity isocontours for various A_y/D, for *F=0.9, ε=0.2*, clockwise mode.

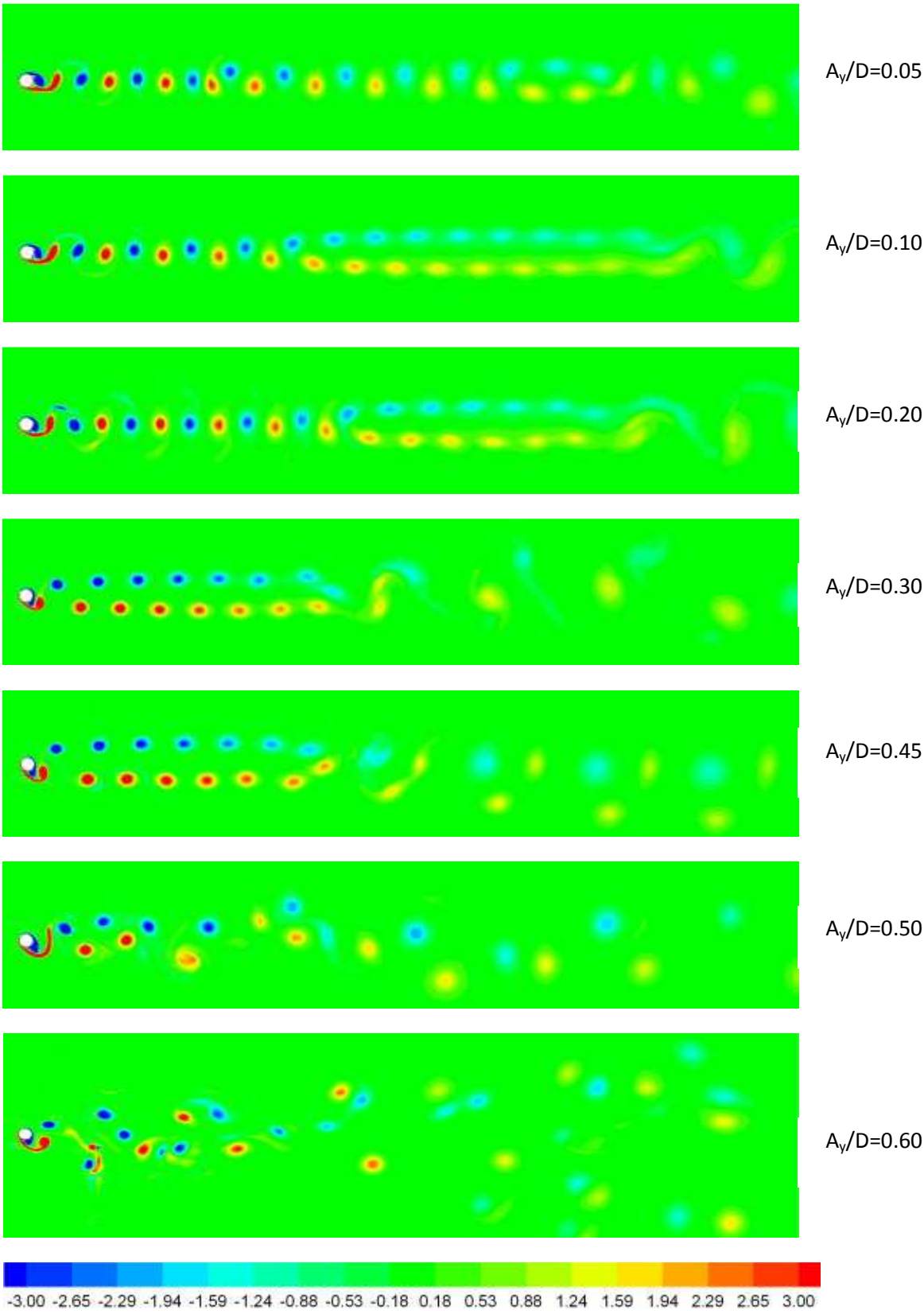

Figure 4-58: Instantaneous vorticity isocontours for various A_y/D, for *F=0.9, ε=0.4*, counter-clockwise mode.

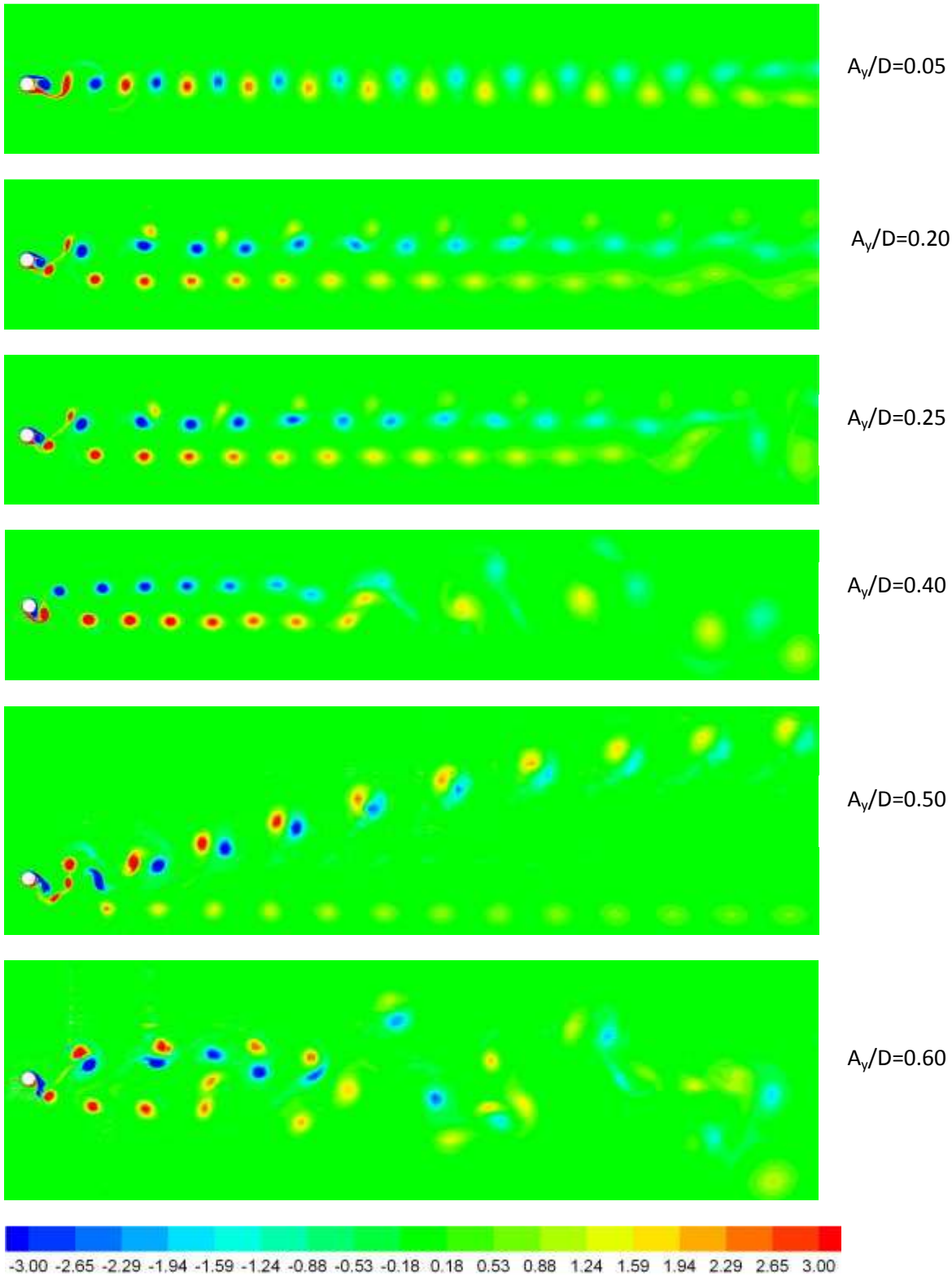

Figure 4-59: Instantaneous vorticity isocontours for various A_y/D, for *F=0.9, ε=0.4*, clockwise mode.

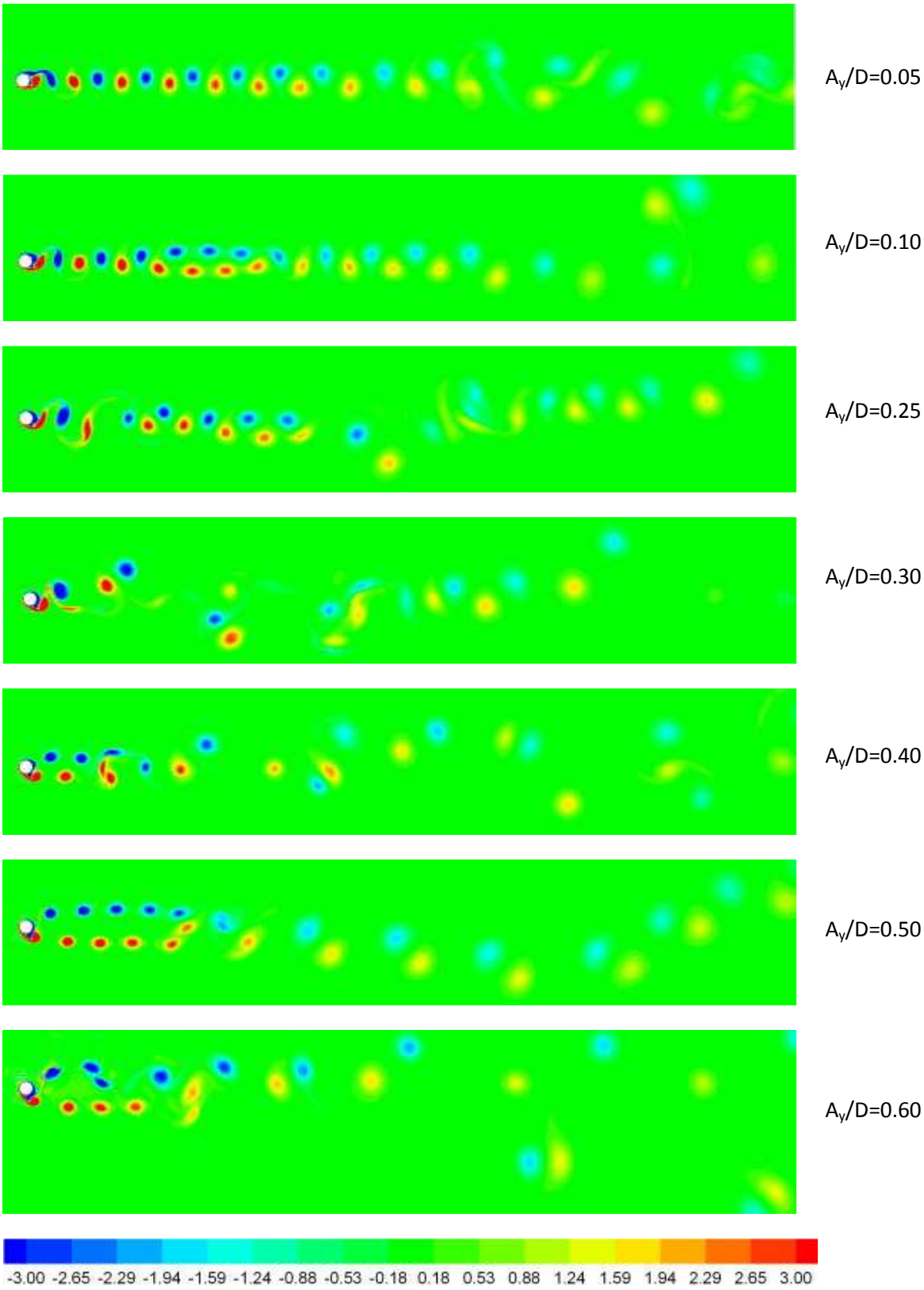

Figure 4-60: Instantaneous vorticity isocontours for various A_y/D, for *F=1.1, ε=0.2*, counter-clockwise mode.

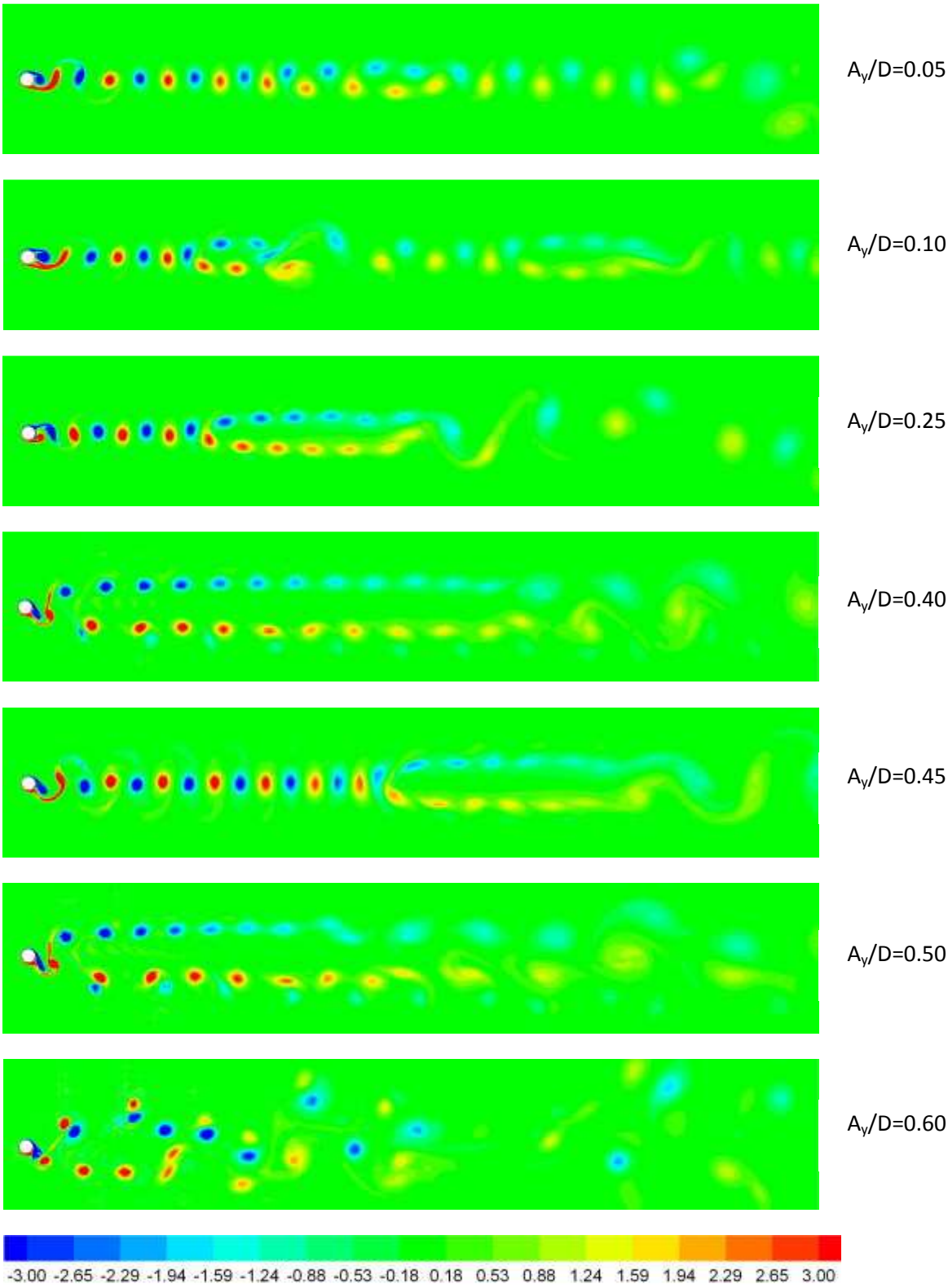

Figure 4-61: Instantaneous vorticity isocontours for various A_y/D, for *F=1.1, ε=0.2*, clockwise mode.

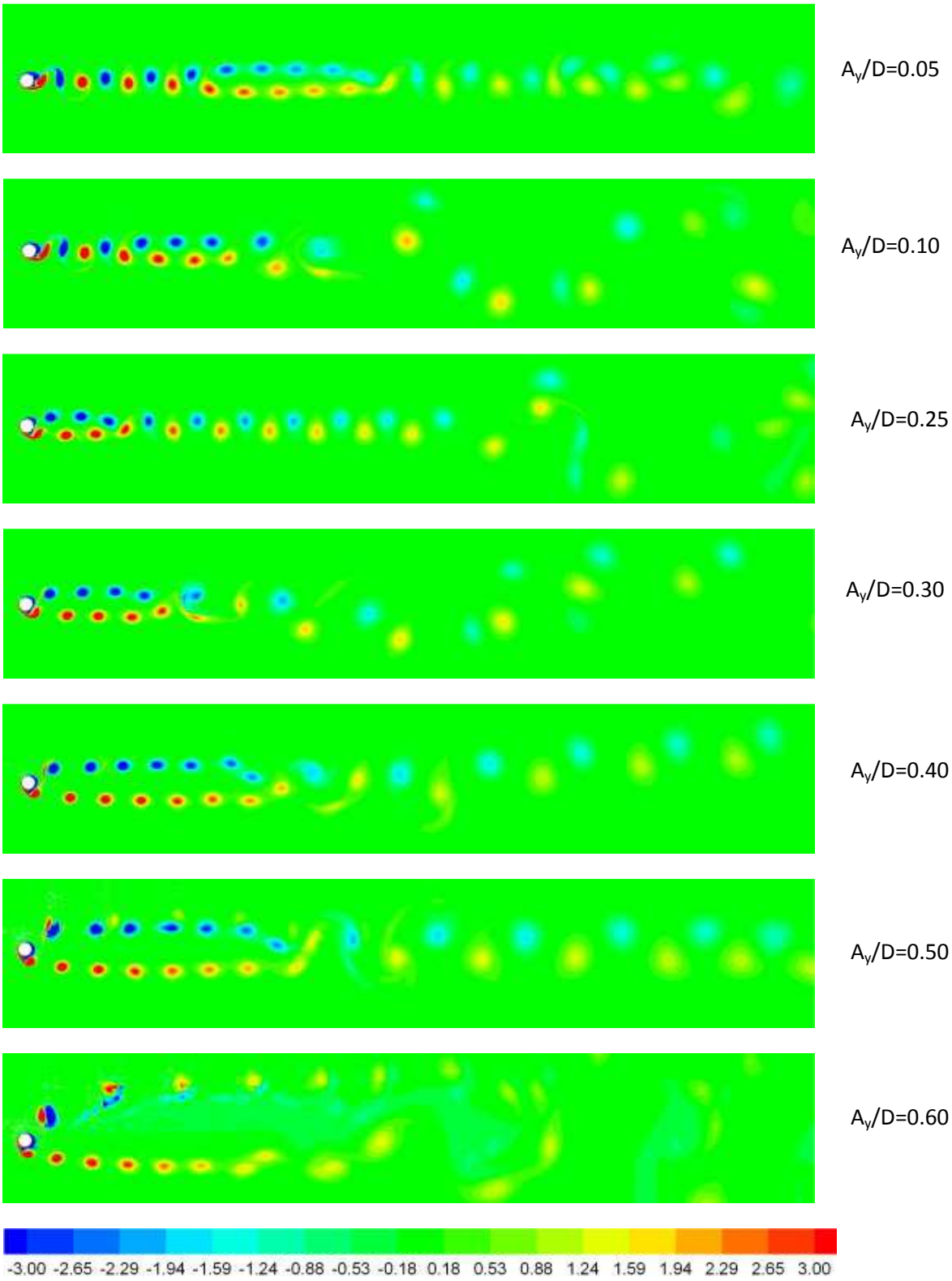

Figure 4-62: Instantaneous vorticity isocontours for various A_y/D, for *F=1.1, ε=0.4*, counter-clockwise mode.

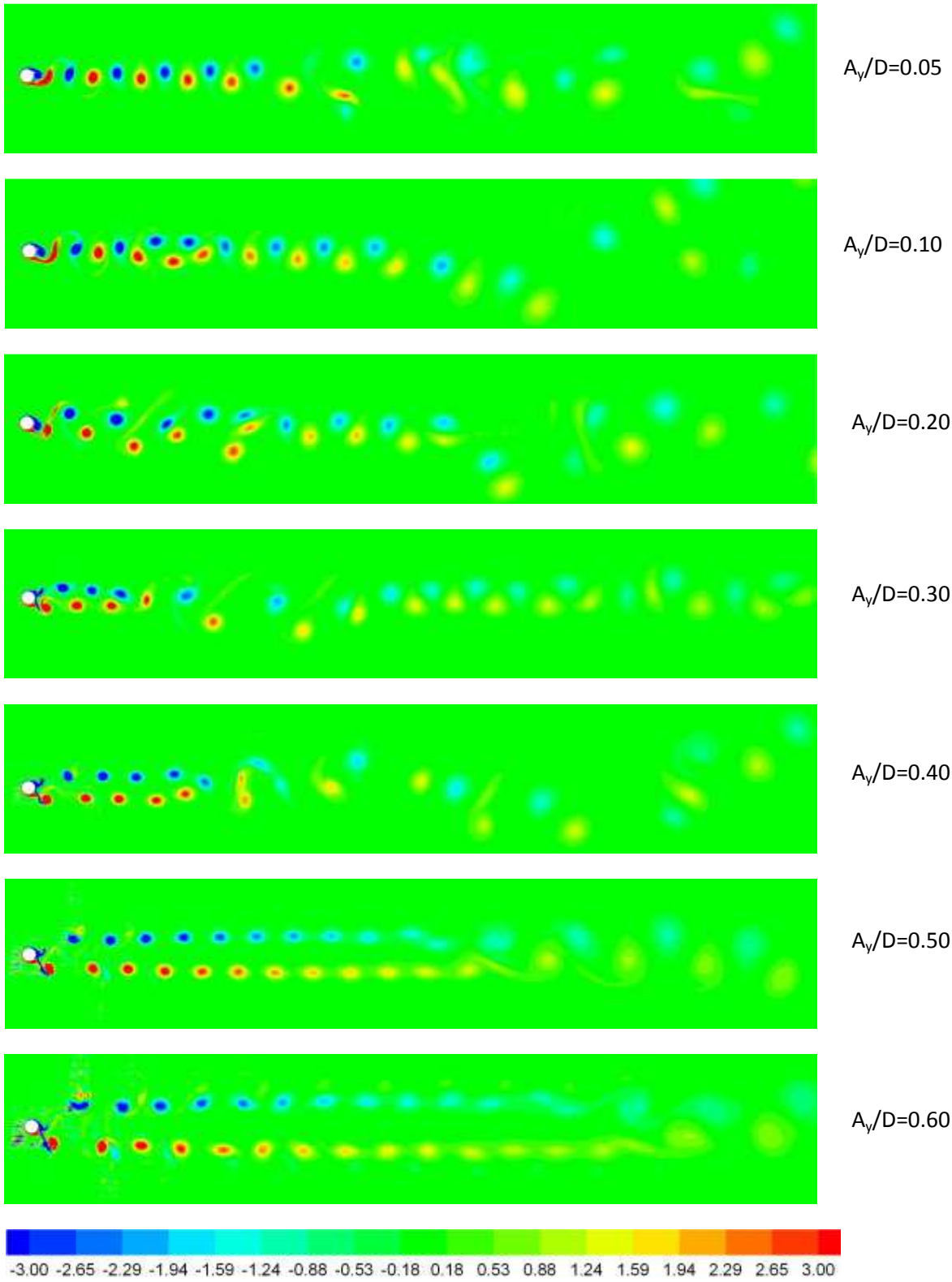

Figure 4-63: Instantaneous vorticity isocontours for various A_y/D, for *F=1.1, ε=0.4*, clockwise mode.

4.6 Discussion

In this chapter, we have presented computational results of the forces acting on a cylinder oscillating both transversely and in-line with respect to a free stream, following a figure *eight* trajectory, as in free vortex-induced vibration. Reynolds number is equal to 400. For a flow stream from left to right, we have studied both the counter-clockwise and clockwise oscillation modes (corresponding to a counter-clockwise or clockwise cylinder motion in the upper part of the trajectory, respectively). Two values of the in-line to the transverse oscillation amplitude were considered, *ε=0.2* and *ε=0.4*, and the results were compared against the *ε=0* case (transverse-only oscillation). The oscillation amplitude was varied from zero to values corresponding to negative power transfer from the flow to the cylinder. Three values of transverse oscillation frequency were considered, corresponding to *F= 1.0, 0.9* and *1.1*.

For *F=1.0*, counter-clockwise motion, the range of A_y/D corresponding to positive *P* is larger, in comparison to the other two oscillation modes. In addition, the presence of in-line motion increases, in most cases, the drag forces exerted on the cylinder, compared to transverse-only oscillation.

For *F*=0.9 (*ε=0.2* and *0.4*), counter-clockwise motion is associated with an increased amplitude range of positive *P* values, in comparison to the other two oscillation modes (transverse-only oscillation and clockwise motion). The corresponding variation of the drag force for *ε=0.2* is an increasing function of oscillation amplitude, with higher levels corresponding to counter-clockwise oscillation mode.

Finally, for *F=1.1* the variation of *P* is characterized by alterations between positive and negative values, with the maximum values of positive *P* being lower in comparison to the cases of resonant and below-resonant forcing. With respect to the drag force, the variations are also non-monotonic and quite complex.

The computed flow states depend strongly on the direction in which the cylinder trajectory is traversed. The present study has demonstrated that the counter-clockwise motion of the cylinder is, in most cases, associated with higher non-dimensional forces than the clockwise motion. For counter-clockwise motion, the power transfer to the cylinder remains, in most cases, positive for higher oscillation amplitudes, in comparison to the clockwise motion; for ε=0.2, these oscillation amplitude values are also higher in comparison to those of the case of transverse only oscillation. Also for the majority of oscillation amplitudes the C_{Dv} coefficient is positive for counter-clockwise motion indicating that in-line motion transfers energy from the flow to the cylinder. Thus, the counter-clockwise motion appears to be the most hazardous one for applications of vortex-induced vibrations.

The flow dynamics can be characterized by considering the spectra of the computed lift coefficient signals. For cases illustrated at *F=0.9* the flow is locked-in to the excitation frequency, even at the low amplitude. For counter-clockwise mode, the frequency content becomes rich at high amplitude, while a strong peak at the third harmonic is present. For

clockwise mode, odd harmonics are present in the spectra at low amplitude, and both odd and even harmonics at high amplitude. The presence of the third harmonic remains pronounced at *F=1.0*, while the spectra are characterized by very rich frequency content for *F=1.1*. The presence of significant third harmonic component in lift force at high oscillation amplitudes can lead to higher fatigue stresses on marine structures.

Flow visualizations demonstrate that for frequency ratios less than or equal to *1.0,* the observed wakes are characterized by a 2S type mode at low to medium amplitudes, and "partial S+P" modes at higher amplitudes. As the amplitude increases, the state of the wake becomes disordered, with complex vortex patterns. For higher frequency ratio (*F=1.1*), 2S structures are present in the near wake at low oscillation amplitude, becoming more complicated downstream. At higher amplitudes, the vortex patterns in the wake remain complex, dominated by triplets or other combinations of vortices. The present results are in accordance with the experiments of Ongoren and Rockwell (1988) and Williamson and Roshko (1988); the latter are at almost the same Reynolds number with the present study. Further the formation of the asymmetric "partial S+P" mode, which was found in the computational study by Kaiktsis et al. (2007), is also observed in our computations at higher amplitudes. The presence of the third harmonic component in lift force being more pronounced in higher amplitude can be attributed to these complex wake structures.

In general, the observed wakes are characterized by 2S structure at low amplitudes, and more complicated wake structure at high amplitudes, especially at higher values of amplitude ratio, ε i.e. at higher in-line oscillation amplitudes. This tendency towards complex and chaotic flow states at increasing in-line oscillation amplitude should be interpreted on the basis of the pattern competition between two modes, a symmetric flow mode due to the in-line oscillation and the asymmetric mode of the Kármán street, with entirely different spatial structures, see Ciliberto and Gollub (1984) and Perdikaris et al. (2009).

Chapter 5

Three-Dimensional Flow

5.1 Background

In this chapter we present computational results of the three-dimensional flow past a cylinder oscillating transversely and in-line with respect to a uniform stream. The in-line oscillation has a frequency equal to twice that of the transverse frequency, thus the cylinder follows a figure *eight* trajectory. We investigate the wake structure and hydrodynamic forces at the lock in, i.e. the transverse oscillation frequency is equal to the vortex shedding frequency. The corresponding oscillation amplitude is varied from 0.10 to 0.60 of the cylinder diameter and we assume that flow is past an infinitely long circular cylinder. This problem is approximated here with a finite domain length in the spanwise direction with periodic boundary conditions for the end planes.

The Reynolds number is equal to 400, i.e. a regime where the flow is fully three-dimensional, characterized by three-dimensionality of the vortex street, see **Figure 5-1**. In this regime, most experiments (Williamson (1988; 1992; 1996; 1996a), Wu et al. (1994)) and numerical simulations (Karniadakis and Triantafyllou (1992), Zhang et al. (1995), Barkley and Henderson (1996), Thompson et al. (1996), Braza et al. (2001)) introduce the definition of two modes, Mode A and Mode B, in the wake transition. These two modes of vortex shedding have been identified as the dominant features of three-dimensionality in the wake and are characterized by the formation of primary spanwise vortex rolls and streamwise vortex pairs. In Mode A, which is introduced at low Reynolds number (around *Re=190*) the primary vortex rolls become distorted by the streamwise vortex pairs with a spanwise wavelength around 3 and 4 diameters. At higher Reynolds number (approximately *Re=250*) the Mode B wake structure is dominated by primary vortex rolls which are more uniform in the spanwise direction and streamwise vortex pairs with spanwise wavelength of around one diameter.

We present the results of our three-dimensional simulations and highlight the differences with two-dimensional simulations. For transverse cylinder oscillation, it was reported by Tutar and Holdo (2000) that the results of three-dimensional simulations provide better agreement with experimental data. Although several studies, using different numerical tools, have reported comparability between two-dimensional and three-dimensional simulations of flow past a stationary cylinder, however, corresponding comparisons for an oscillating cylinder are limited. It is well known that two-dimensional simulations generally over-predict force coefficients; nonetheless they provide a reasonably accurate estimation. Two-dimensional simulations are conceived to provide more realistic estimates for oscillating cylinders, as oscillation reduces the three-dimensionality of vortex shedding, thereby increasing the correlation length of the vortices in the wake, Al-Jamal and Dalton (2004).

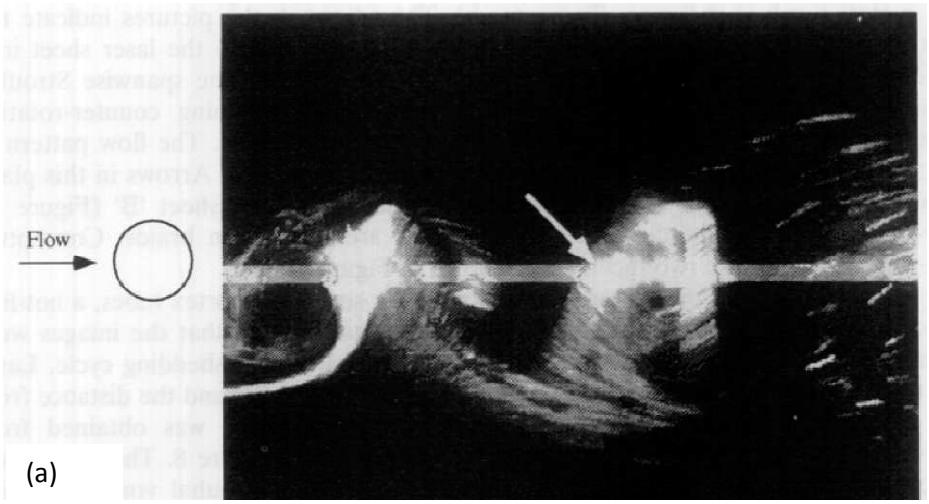

(a)

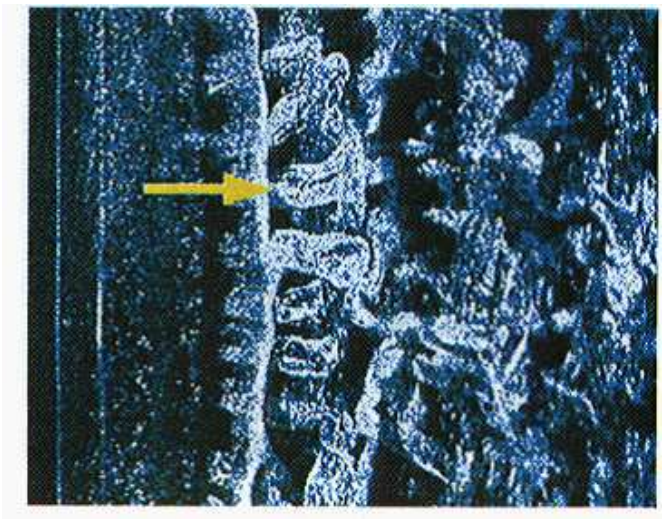

(b)

Figure 5-1: Experimental visualization of the flow past a stationary cylinder at Re=440 by Wu et al. (1994): (a) spanwise Strouhal vortices (counter-rotating streamwise vortices are also indicated by white arrow) (b) snapshot of instantaneous vortex structure isosurfaces (rib structure is indicated by yellow arrow).

5.2 Discretization

A fully three-dimensional discretization is employed. The computational domain extends from 20 diameters upstream from the center of the cylinder to 60 diameters downstream from the center of the cylinder. In the vertical direction the domain is symmetrical, extending up to 17 diameters from the cylinder center. The domain length in the spanwise dimension (z direction) is chosen to be $L_z = z/D = 2\pi$ which is deemed sufficient based on the previous literature studies summarized subsequently.

For a Reynolds number equal to 400 the flow is characterized by three-dimensionality of the vortex street, while the wake structure corresponds to the B-mode. In the present work, the selection of spanwise periodicity length of the flow domain has been based on experimental observations regarding the spanwise wavelength of B-mode, as well as on published three-dimenional computational studies of flow past a cylinder. In general, the spanwise length should be equal to several spanwise wavelengths.

Kim and Kim (2010) studied numerically the characteristics of three-dimensional flow past a circular cylinder at Reynolds number ranging between 300 and 1000, characterized by the presence of Mode B. For a Reynolds number characterized by the presence of Mode B, a proper spanwise length was assessed. The streamwise vortices interacted with the Karman vortices and significantly affected the behavior of the vortex street. An outcome of the study by Kim & Kim (2010) is that a minimum spanwise length of approximately πD is necessary to preserve the dynamics of three-dimensional flow in the presence of Mode B. This study follows previous experimental and numerical results, summarized in Williamson (1996), suggesting that the B mode is characterized by a spanwise wavelength of approximately one cylinder diameter (see **Figure 5-2**). Based on the above, in the present study at *Re=400* a spanwise periodicity length of $2\pi D$ has been selected.

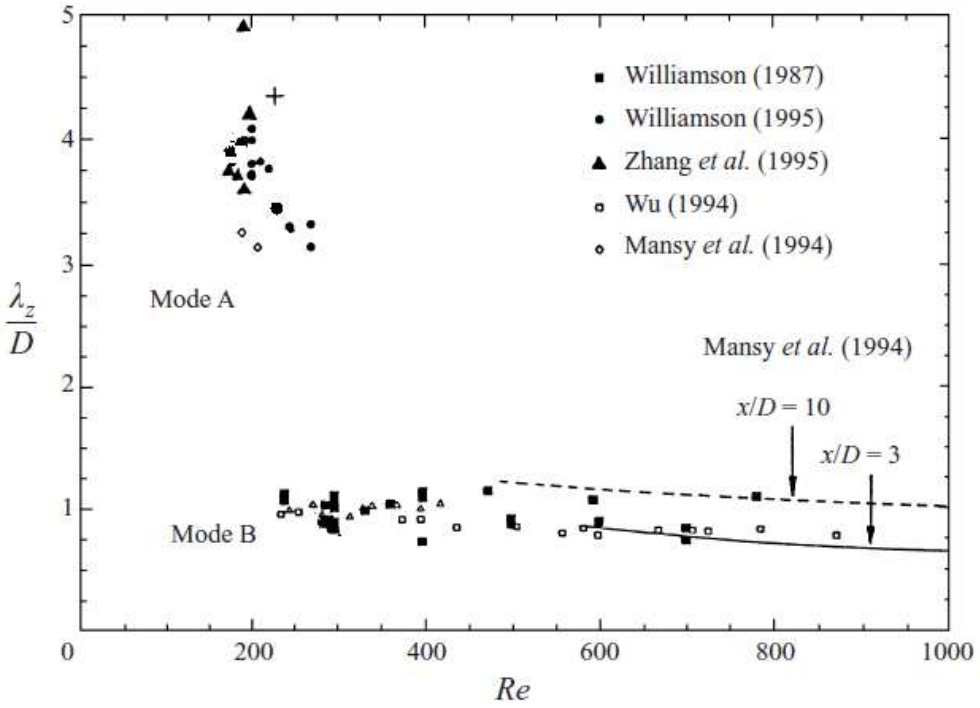

Figure 5-2: Normallized spanwise wavelength of Mode A and Mode B versus Reynolds number from experimental and computational literature studies, Williamson (1996).

In x-y planes the discretization consists of 2056 elements. In the z-direction, a total of 10 element layers are used. In total 20560 three-dimensional spectral elements are utilized, each with *8×8×8* elemental resolution. The spectral element grid is illustrated in **Figure 5-3**. Detailed spatial resolution tests have been performed, and are reported in Appendix A.2.

The boundary conditions corresponding to x-y cross sections are identical to those utilized in two-dimensional simulations, see section 4.3.2. As previously indicated, periodic boundary conditions are prescribed for the end planes in the spanwise direction.

A third order semi-implicit temporal scheme is employed for time discretization, Karniadakis et al. (1991). The time step was $\Delta t = 0.0010$. The present three-dimensional simulations at $Re=400$ show that the non-dimensional shedding frequency (Strouhal number) is $f_s=0.204$. Thus, the shedding period is $T = 1/f_s = 4.902$, and the value of $\Delta t = 0.0010$ corresponds to approximately 4900 time-steps per shedding period.

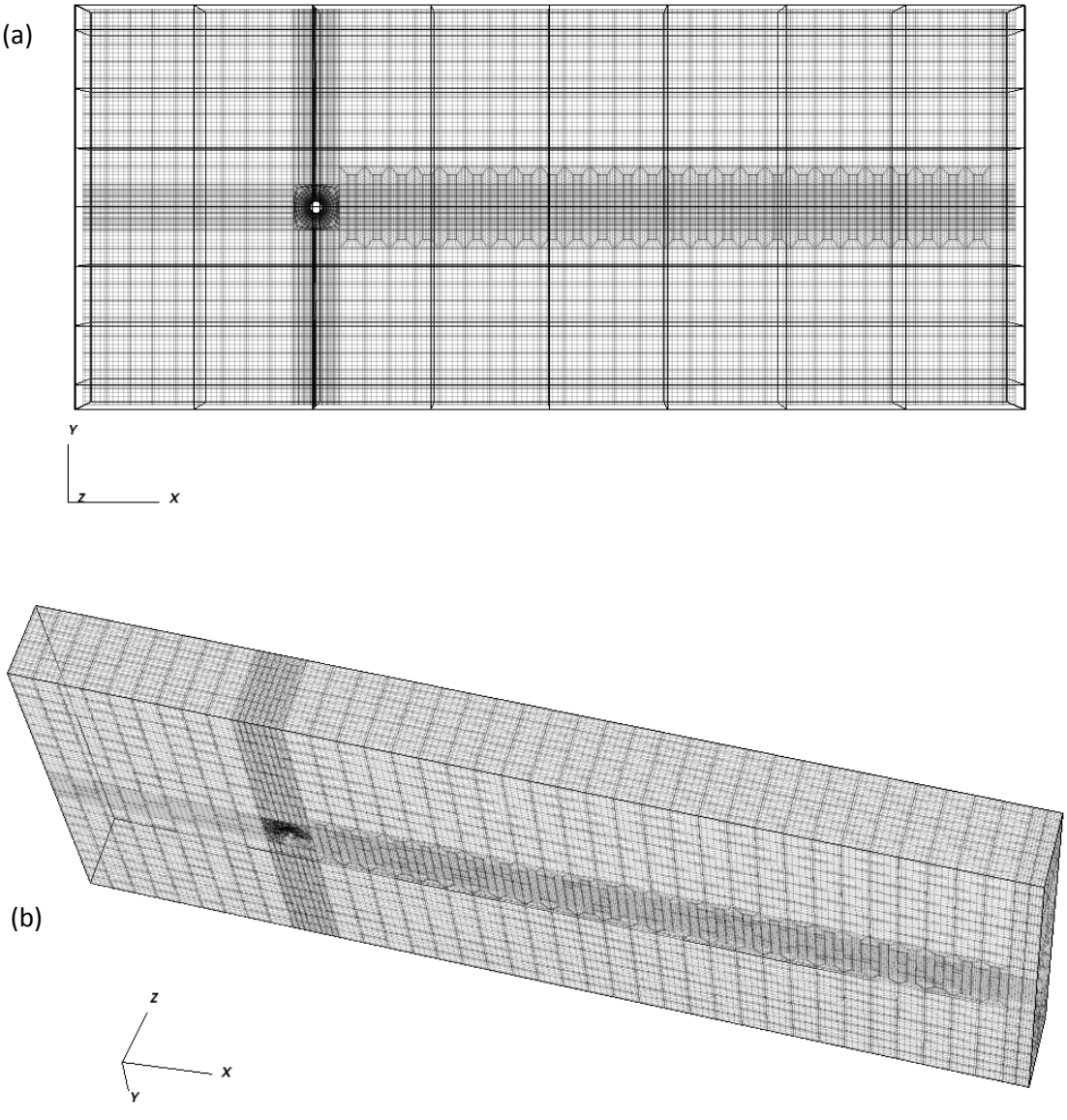

Figure 5-3: Illustration of spectral element grid for three-dimensional flow past a circular cylinder, including: (a) a x-y plane and (b) a three-dimensional perspective view.

5.3 Results

We conducted detailed Direct Numerical Simulation (DNS) studies of three-dimensional flow, for a frequency ratio, $F = f_y / f_s$ equal to 1.0 corresponding to resonant forcing. We considered a value of amplitude ratio $\varepsilon = A_x / A_y$ equal to 0.2 and counter-clockwise cylinder motion (see **Table 5-1**); as indicated in Chapter 4, counterclockwise motion is characterized by higher levels of the power transfer parameter and its presence is more probable in VIV applications. Accordingly, the choice of *ε=0.2* is based on experimental observations, Vandiver (1983).

Table 5-1: The parameter values of the present three-dimensional simulations

Parameter values	
Re	400
$F = f_y / f_s$	1.0
$\varepsilon = A_x / A_y$	0.2
A_y / D	0 – 0.60
motion	counter-clockwise

Simulations were initialized from flow fields corresponding to lower oscillation amplitudes with a smooth increase in amplitude. In this constant amplitude regime, the governing equations were further integrated in time until a statistical *"steady state"* was reached, within which the flow mean quantities are time-independent. For the case of flow past a stationary cylinder, computed statistical flow quantities for *Re=300, 400* are presented in **Table 5-2** and **Table 5-3** respectively; a very good agreement with literature data, also included, is found.

Table 5-2: Comparison of present three-dimensional simulations results with experimental values for stationary cylinder at *Re=300*.

	$< C_D >$	$C_{D,RMS}$	$C_{L,RMS}$	Strouhal Freq. (f_s)
Present 3D simulations	1.251	0.037	0.376	0.196
Wieselberger (1921)	1.22			
Norberg (2003)				0.203

Table 5-3: Comparison of present two-dimensional simulations results with present three-dimensional ones and experimental values for stationary cylinder at *Re=400*.

	$< C_D >$	$C_{D,RMS}$	$C_{L,RMS}$	Strouhal Freq. (f_s)
Present 2D simulations	1.417	0.056	0.735	0.220
Present 3D simulations	1.183	0.044	0.292	0.204
Wieselberger (1921)	1.13			
Norberg (1994)				0.20

5.3.1 Power transfer and hydrodynamic force coefficients

In **Figure 5-4** to **Figure 5-12** we present the non-dimensional flow coefficients, see definitions in section 4.3.1. The simulation results are processed for an integer number of periods, corresponding to the *"steady state"*. Here the power transfer parameter and the force coefficients defined in section 4.3.1 are calculated for three-dimensional flow. **Figure 5-4** to **Figure 5-12** also include two-dimensional results for direct comparisons.

The variation of the total power transfer parameter, *P* with respect to A_y/D is presented in **Figure 5-4**, for three-dimensional and two-dimensional flow. *P* values corresponding to three-dimensional flow are higher than those of two-dimensional flow for oscillation amplitudes higher than approximately 0.23. *P* remains positive for the entire range of oscillation amplitudes i.e. they correspond to excitation considered here.

The variation of the C_{Lv} with respect to A_y/D coefficient is shown in **Figure 5-5**. In all cases, there is correspondence with the *P* curves. The variation of C_{Dv} with respect to A_y/D is shown in **Figure 5-6**. Both for the three-dimensional and two-dimensional flow, the values remain, in general, positive i.e. the inline motion contributes to excitation.

Figure 5-7, presents the variation of the added mass coefficient C_M with respect to A_y/D. The results of two-dimensional simulation are characterized by positive values, whereas the three-dimensional simulation by negative values. The values of coefficient C_{La} shown in **Figure 5-8**, are of the same sign as the values of the C_M coefficient.

The variation of coefficient C_{Da} with A_y/D is presented in **Figure 5-9**. The C_{Da} values are negative for two-dimensional and three-dimensional simulation, with the three-dimensional ones to exhibit lower negative values. The form of both curves suggests that the variation of drag force is generally in phase with the acceleration in the in-line direction.

The magnitude of non-dimensional lift forces, expressed in terms of the coefficient $C_{L,RMS}$ versus the transverse oscillation amplitude is presented in **Figure 5-10**. The results demonstrate that, in two-dimensional flow there is a decrease in the overall $C_{L,RMS}$ levels for oscillation amplitudes higher than approximately *0.23,* followed by comparatively higher levels for the three-dimensional flow. The decrease in the force level of two-dimensional flow at A_y/D levels of order 0.25 is also observed for the time averaged and RMS drag force (**Figure 5-11** and **Figure 5-12** respectively). In three-dimensional flow, a monotonic increase is observed for the averaged and RMS drag force indicating a wide wake (**Figure 5-11** and **Figure 5-12**).

In summary, in three-dimensional simulations forces are lower than in two-dimensional simulations at relatively low oscillation amplitudes (up to 0.20-0.25). At higher amplitudes, a decrease in forces corresponding to two-dimensional flow is observed, which results in relatively higher levels of the three-dimensional flow forces. It is noted that, in the case of *ε=0* (transverse-oscillation only), two-dimensional simulations for *Re=400* predict two abrupt transitions at A_y/D levels near 0.25 and 0.40, Kaiktsis et al. (2007). These transitions are accompanied by a phase shift in timing of vortex shedding, as well as corresponding drastic changes in the force levels, see **Figure 5-13** and **Figure 5-14**. Regarding flow past a cylinder oscillating both in transverse and in-line directions, our results show that, in two-dimensional flow, there is a *"memory"* of the first transition at $A_y/D \approx 0.25$ which is not accompanied by a corresponding *"memory"* of the second transition. In three-dimensional flow, there is no "*memory"* of such transitions suggesting that, in all likelihood, they are not present in the case of three-dimensional flow past a cylinder exhibiting only transverse oscillation. Thus, at high oscillation amplitudes, there is substantial deviation between the results of two- and three-dimensional flow e.g. see **Figure 5-13** and **Figure 5-14** for results in the limit of $A_y/D = 0$ (stationary cylinder).

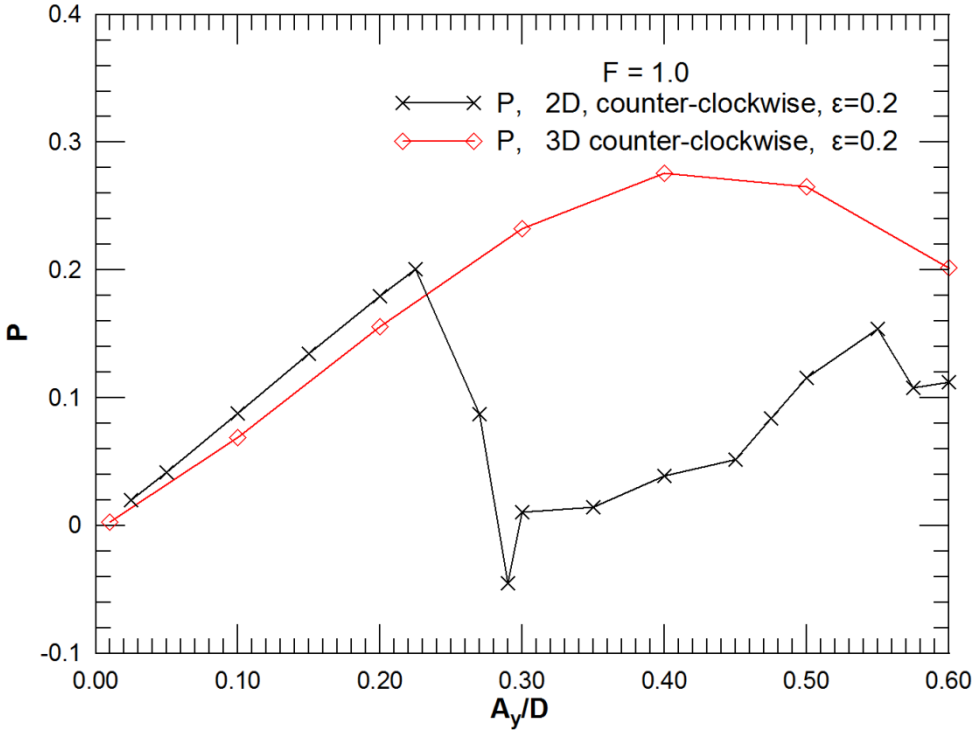

Figure 5-4: Non-dimensional total power transfer, *P*, versus the reduced y-amplitude, for frequency ratio $F = f_y / f_s = 1.0$; here the case *ε=0.2* (counter-clockwise mode) for two- and three-dimensional flow is shown.

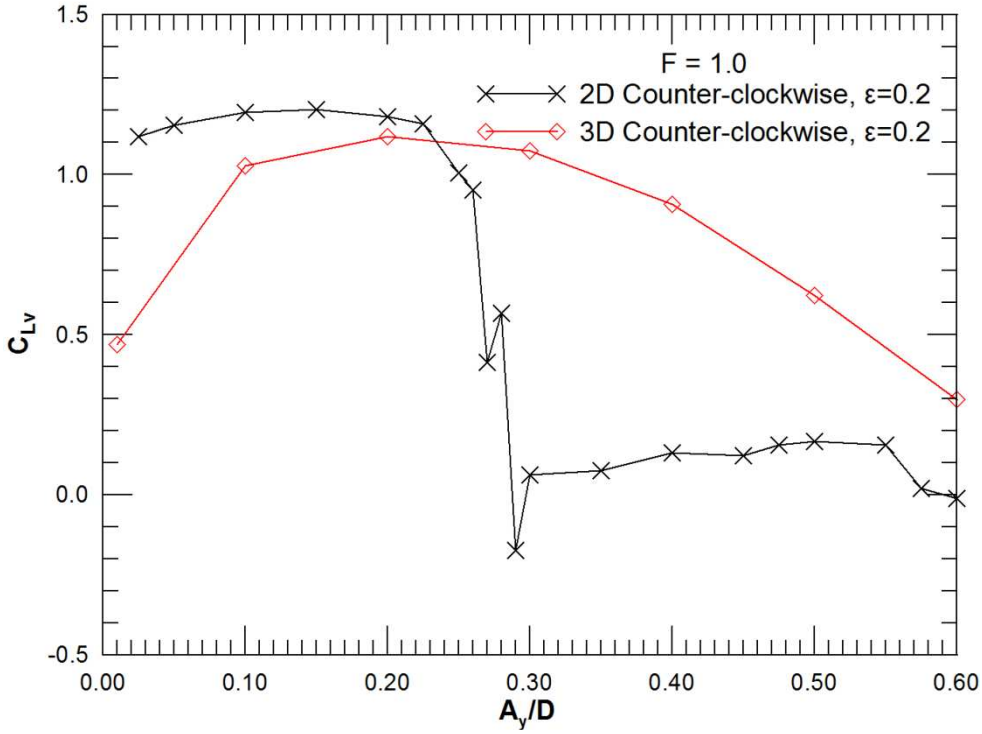

Figure 5-5: Excitation force coefficient, C_{Lv}, versus the reduced y-amplitude, for frequency ratio $F = f_y / f_s = 1.0$; here the case *ε=0.2* (counter-clockwise mode) for two- and three-dimensional flow is shown.

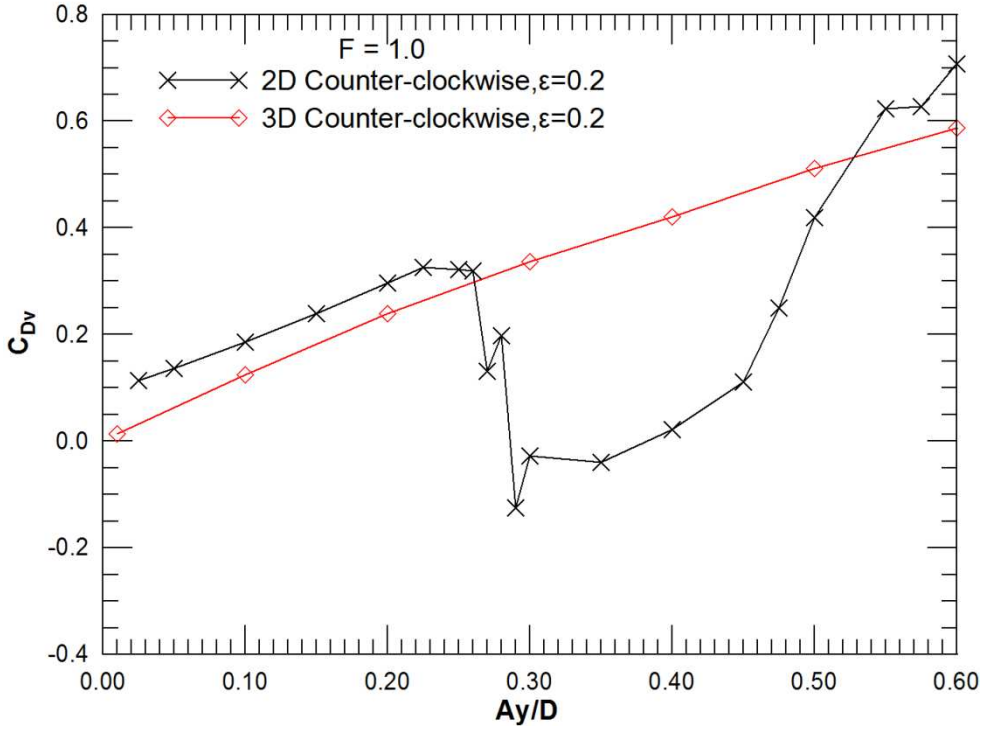

Figure 5-6: Excitation force coefficient, C_{Dv}, versus the reduced y-amplitude, for frequency ratio $F = f_y / f_s = 1.0$; here the case $\varepsilon = 0.2$ (counter-clockwise mode); two- and three-dimensional flow is shown.

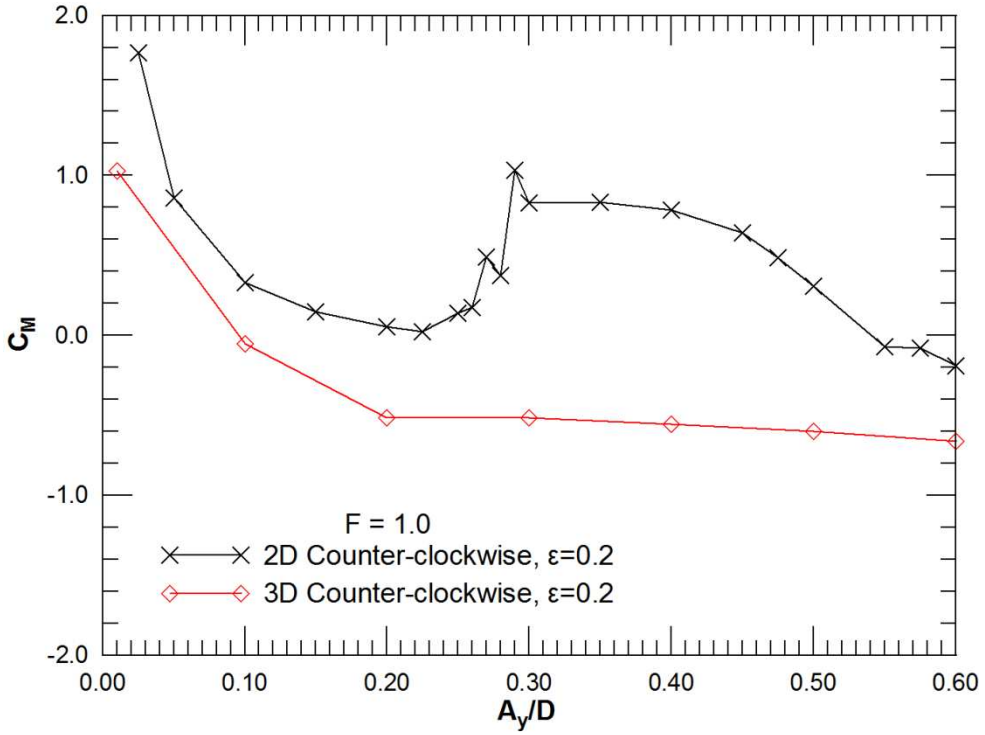

Figure 5-7: Inertia force coefficient, C_M, versus the reduced y-amplitude, for frequency ratio $F = f_y / f_s = 1.0$; here the case $\varepsilon = 0.2$ (counter-clockwise mode) for two- and three-dimensional flow is shown.

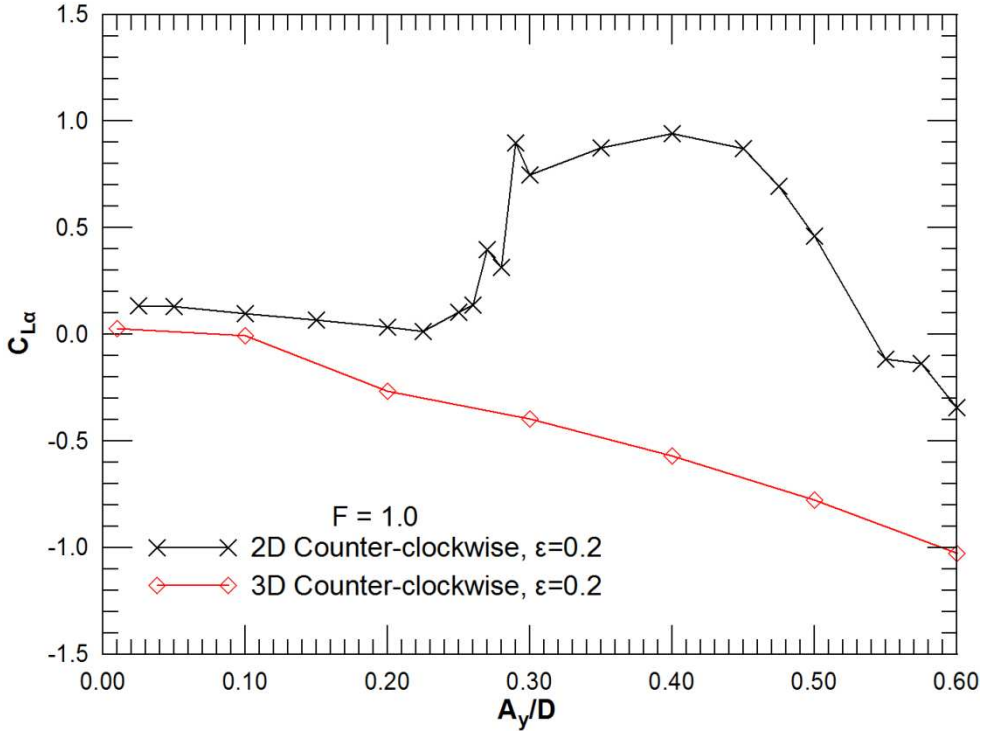

Figure 5-8: Inertia force coefficient, C_{La}, versus the reduced y-amplitude, for frequency ratio $F = f_y / f_s = 1.0$; here the case $\varepsilon = 0.2$ (counter-clockwise mode) for two- and three-dimensional flow is shown.

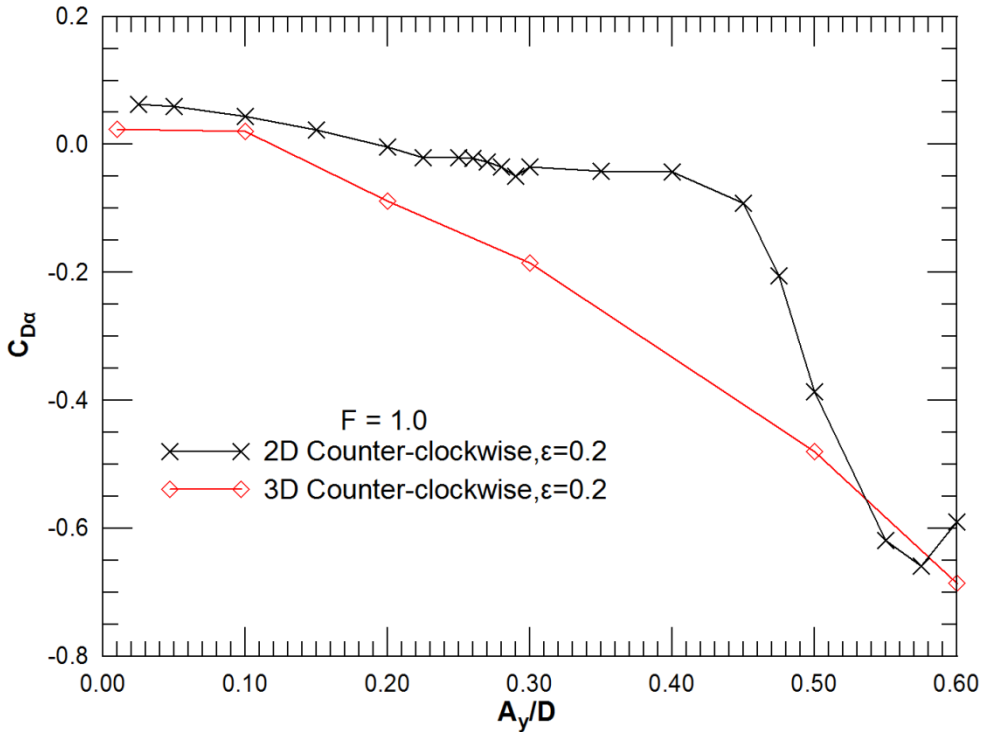

Figure 5-9: Inertia force coefficient, C_{Da}, versus the reduced y-amplitude, for frequency ratio $F = f_y / f_s = 1.0$; here the case $\varepsilon = 0.2$ (counter-clockwise mode) for two- and three-dimensional flow is shown.

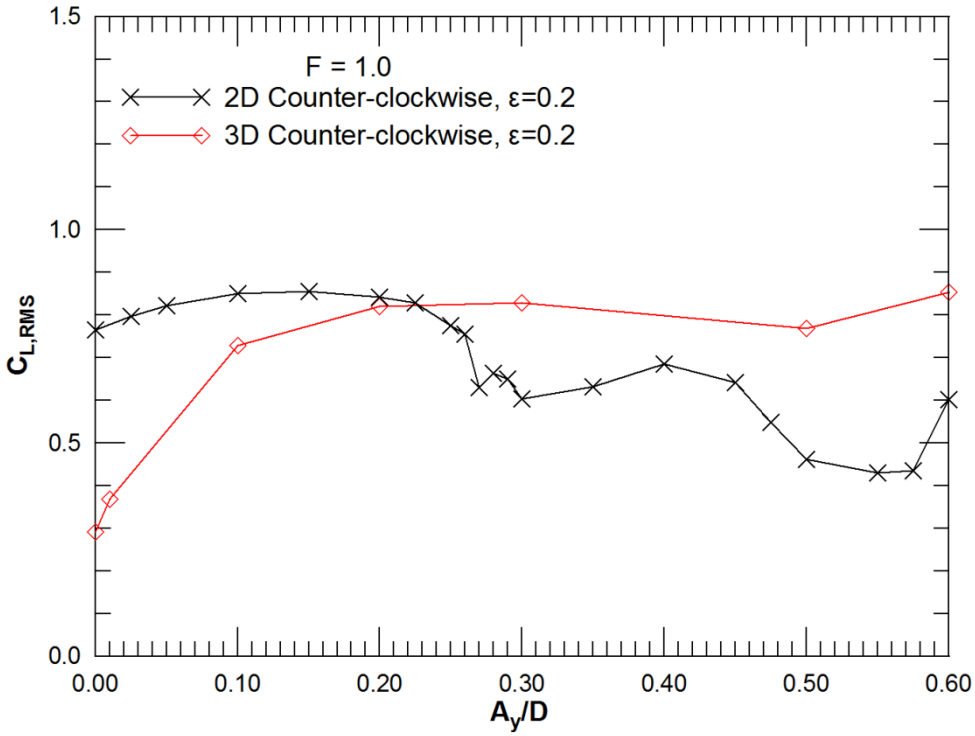

Figure 5-10: R.m.s. fluctuation intensity of lift coefficient versus the reduced y-amplitude, for frequency ratio $F = f_y / f_s = 1.0$; here the case *ε=0.2* (counter-clockwise mode) for two- and three-dimensional flow is shown.

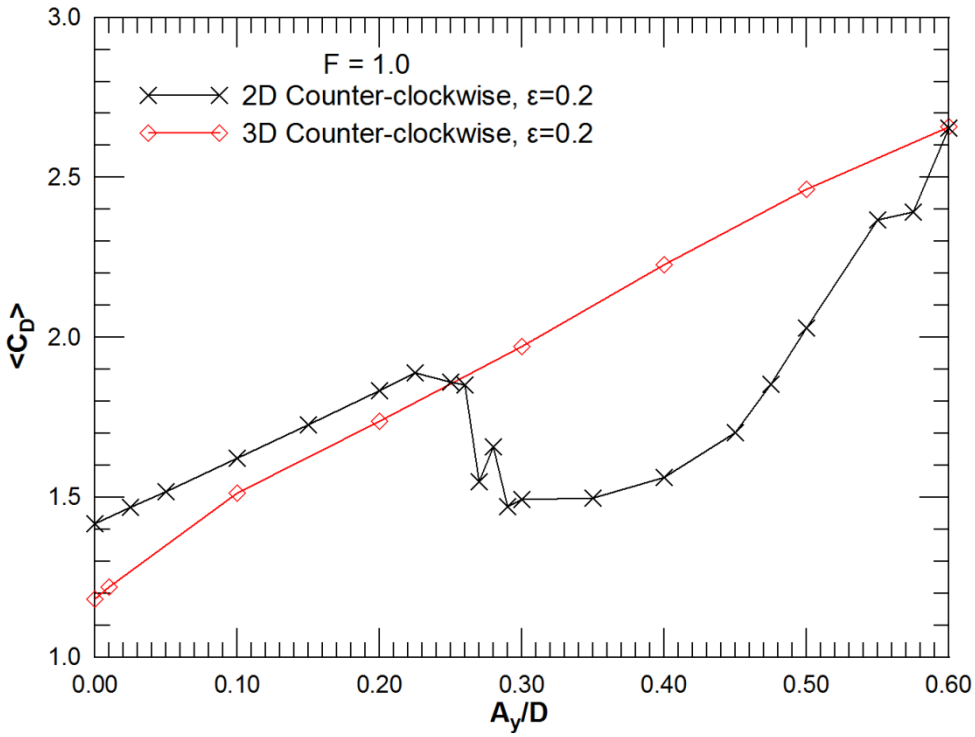

Figure 5-11: Time-averaged drag coefficient versus the reduced y-amplitude, for frequency ratio $F = f_y / f_s = 1.0$; here the case *ε=0.2* (counter-clockwise mode) for two- and three-dimensional flow is shown.

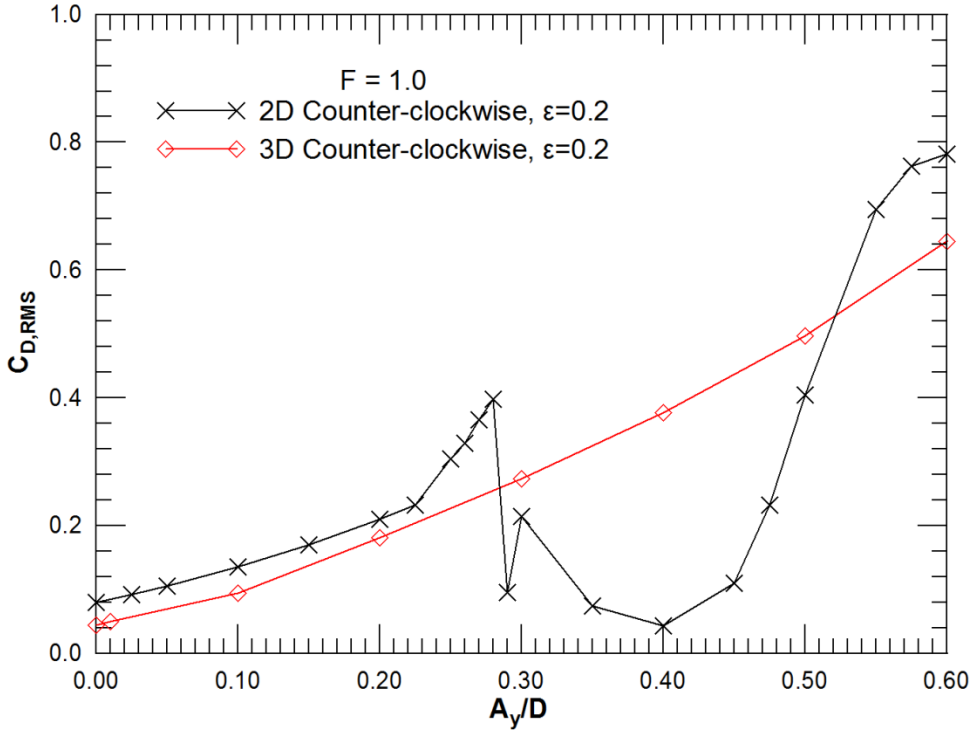

Figure 5-12: RMS fluctuation intensity of drag coefficient versus the reduced y-amplitude, for frequency ratio $F = f_y / f_s = 1.0$; here the case *ε=0.2* (counter-clockwise mode) two- and three-dimensional flow is shown.

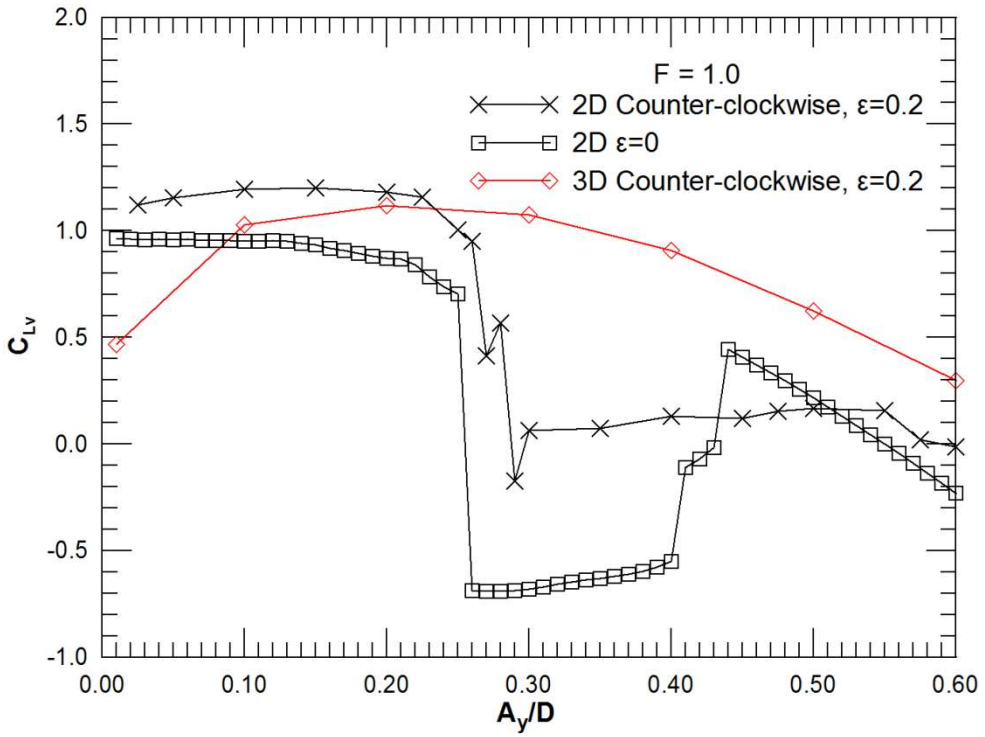

Figure 5-13: Excitation force coefficient, C_{Lv}, versus the reduced y-amplitude, for frequency ratio $F = f_y / f_s = 1.0$; here, the cases: $\varepsilon = 0$ (transverse-oscillation only) for two-dimensional flow and *ε=0.2* (counter-clockwise mode) for two- and three-dimensional flow, are shown.

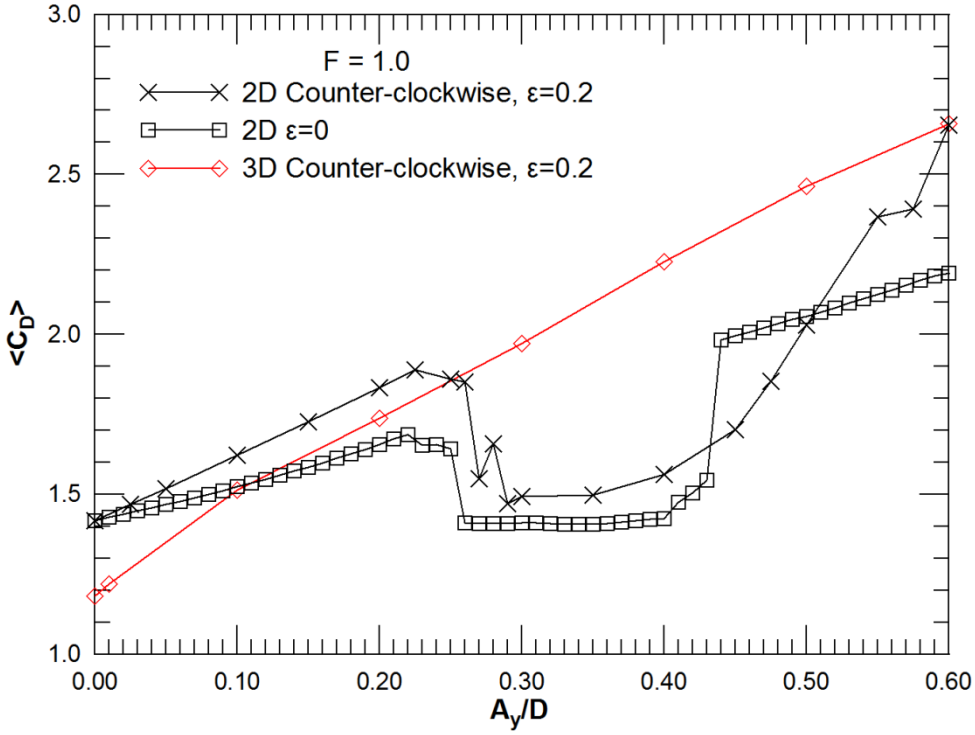

Figure 5-14: Time-averaged drag coefficient versus the reduced y-amplitude, for frequency ratio $F = f_y / f_s = 1.0$; here, the cases: *ε=0* (transverse-oscillation only) for two-dimensional flow and *ε=0.2* (counter-clockwise mode) for two- and three-dimensional flow, are shown.

5.3.2 Force time histories and spectra

In this section we present force coefficients, signals and corresponding spectra. We study the temporal behavior of force coefficients, in order to characterize the effect of cylinder oscillation on forces. Sufficiently long signals are analyzed by means of MATLAB routines.

The drag and lift coefficient signals and the spectra of the lift coefficient are shown in **Figure 5-15** and **Figure 5-16** for flow past a stationary cylinder at *Re=300* and *400*, respectively; the dominant frequency is f_s*=0.196* at *Re=300*, while f_s*=0.204* for *Re=400* as illustrated in **Figure 5-15**(b) and **Figure 5-16**(b)).

The time histories of the drag coefficient are shown in **Figure 5-17**, for three representative values of oscillation amplitude, both for three-dimensional and two-dimensional flow. In general the drag signals of three-dimensional flow are more ordered than their two-dimensional counterparts. At $A_y / D = 0.40$, the two-dimensional flow drag oscillation is minimal.

Lift coefficients signals are presented in **Figure 5-18**. For low oscillation amplitudes ($A_y / D = 0.20$) both two-dimensional and three-dimensional signals are nearly periodic. At higher amplitudes, there is increasing evidence of higher harmonics. **Figure 5-18**

demonstrates that the motion has the same effect on the lift force in two- and three-dimensions.

Lift coefficient spectra based on the three-dimensional flow signals, are presented in **Figure 5-19**. The spectra demonstrate the strong presence of the Strouhal frequency, as well as the existence of the third superharmonic. The latter is more pronounced at high oscillation amplitudes.

Finally, phase portraits of C_L-C_D are presented in **Figure 5-20** suggesting the existence of ordered three-dimensional flows.

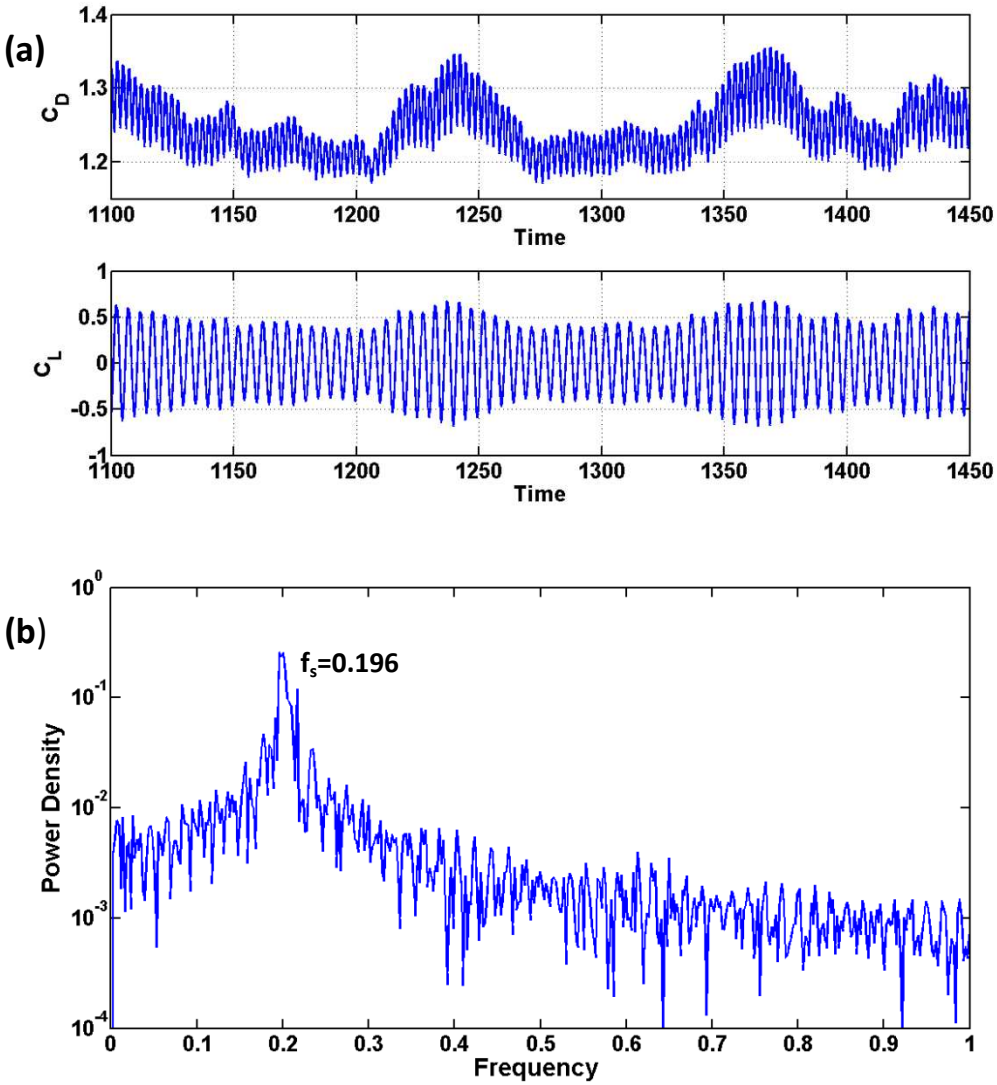

Figure 5-15: Three-dimensional simulations of flow past a stationary cylinder at *Re=300*: (a) Time histories of C_D and C_L and (b) Lift coefficient spectra.

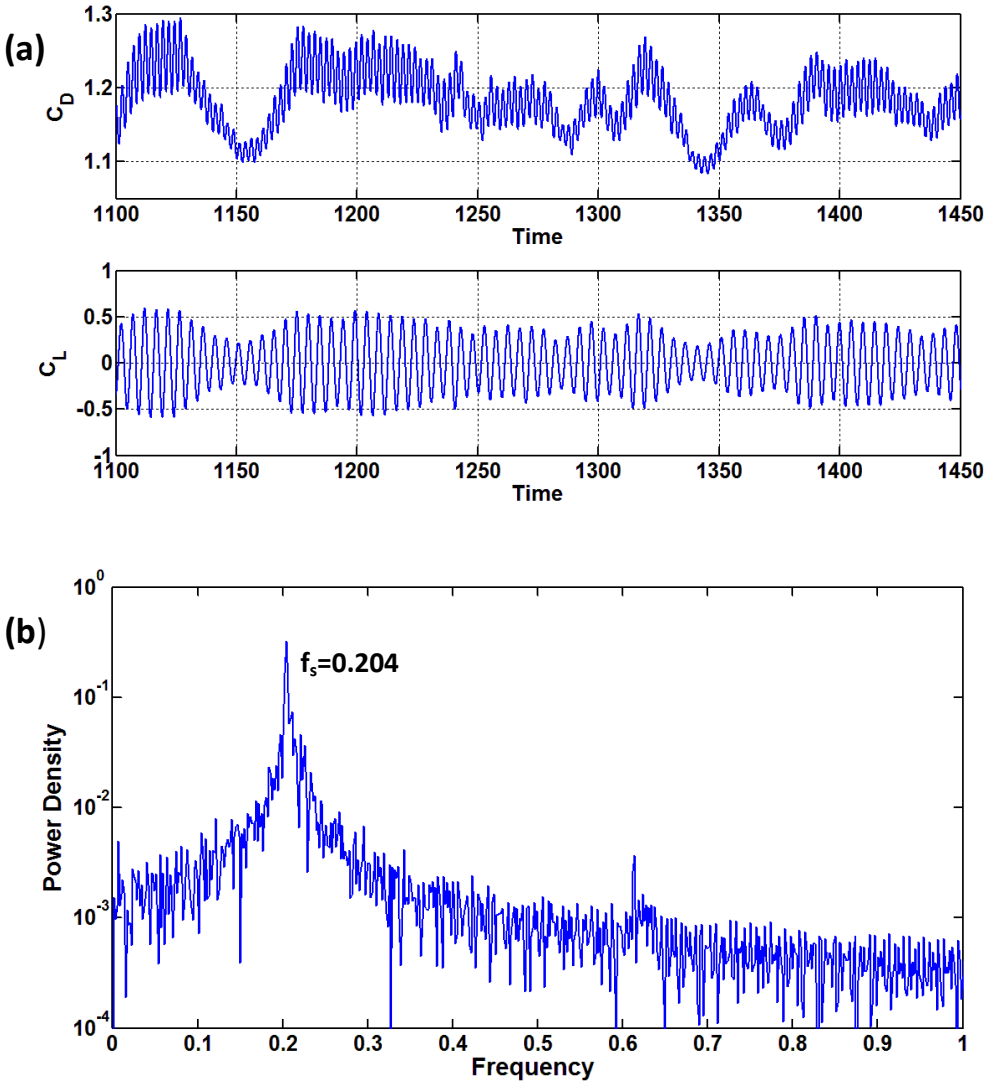

Figure 5-16: Three-dimensional simulations of flow past a stationary cylinder at *Re=400*: (a) Time histories of C_D and C_L and (b) Lift coefficient spectra.

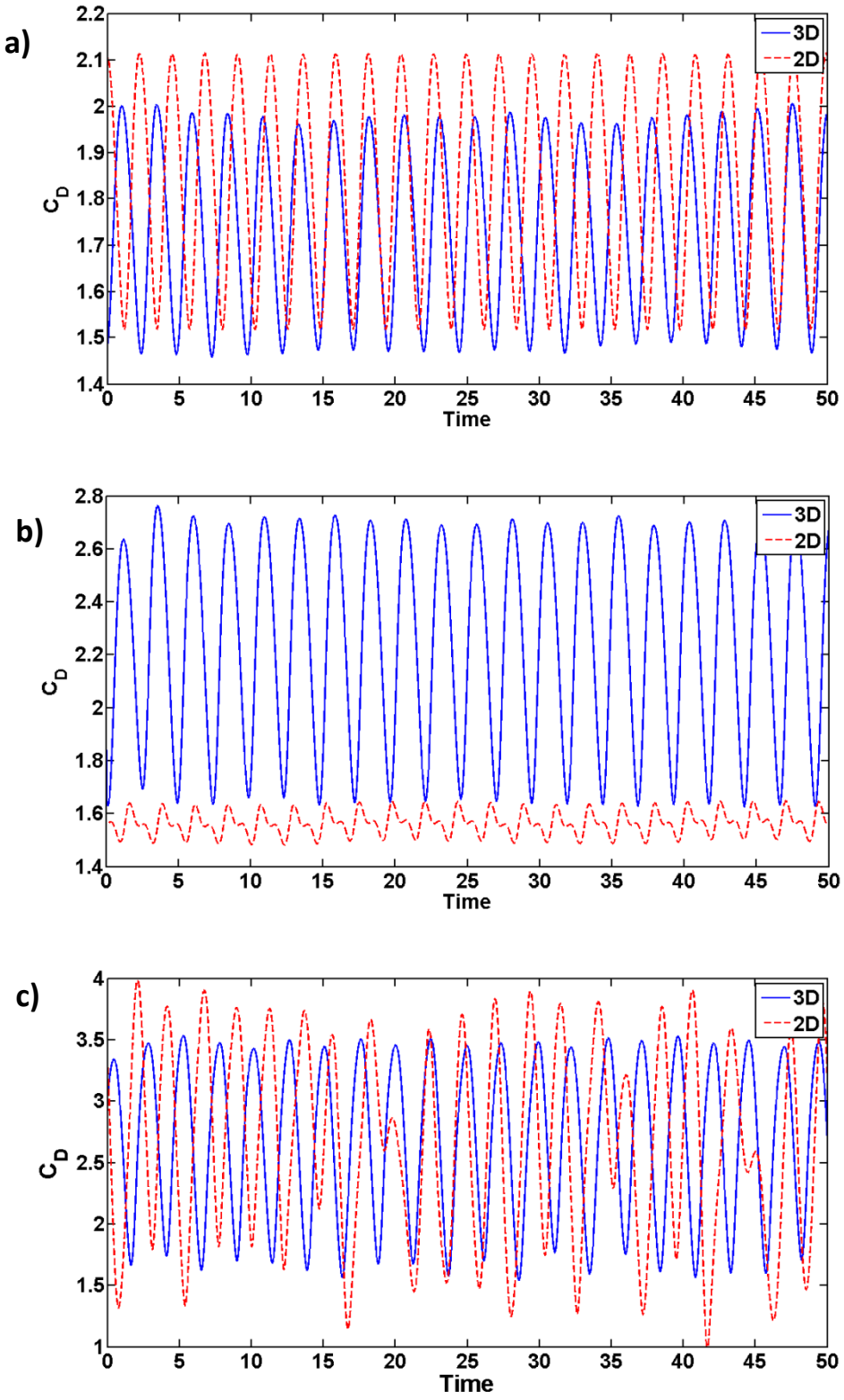

Figure 5-17: Time histories of C_D for the two and three-dimensional simulations with frequency ratio $F = f_y / f_s = 1.0$, counter-clockwise cylinder motion, $\varepsilon=0.2$ and transverse oscillation amplitudes: (a) $A_y/D=0.20$, (b) $A_y/D=0.40$ and (c) $A_y/D=0.60$.

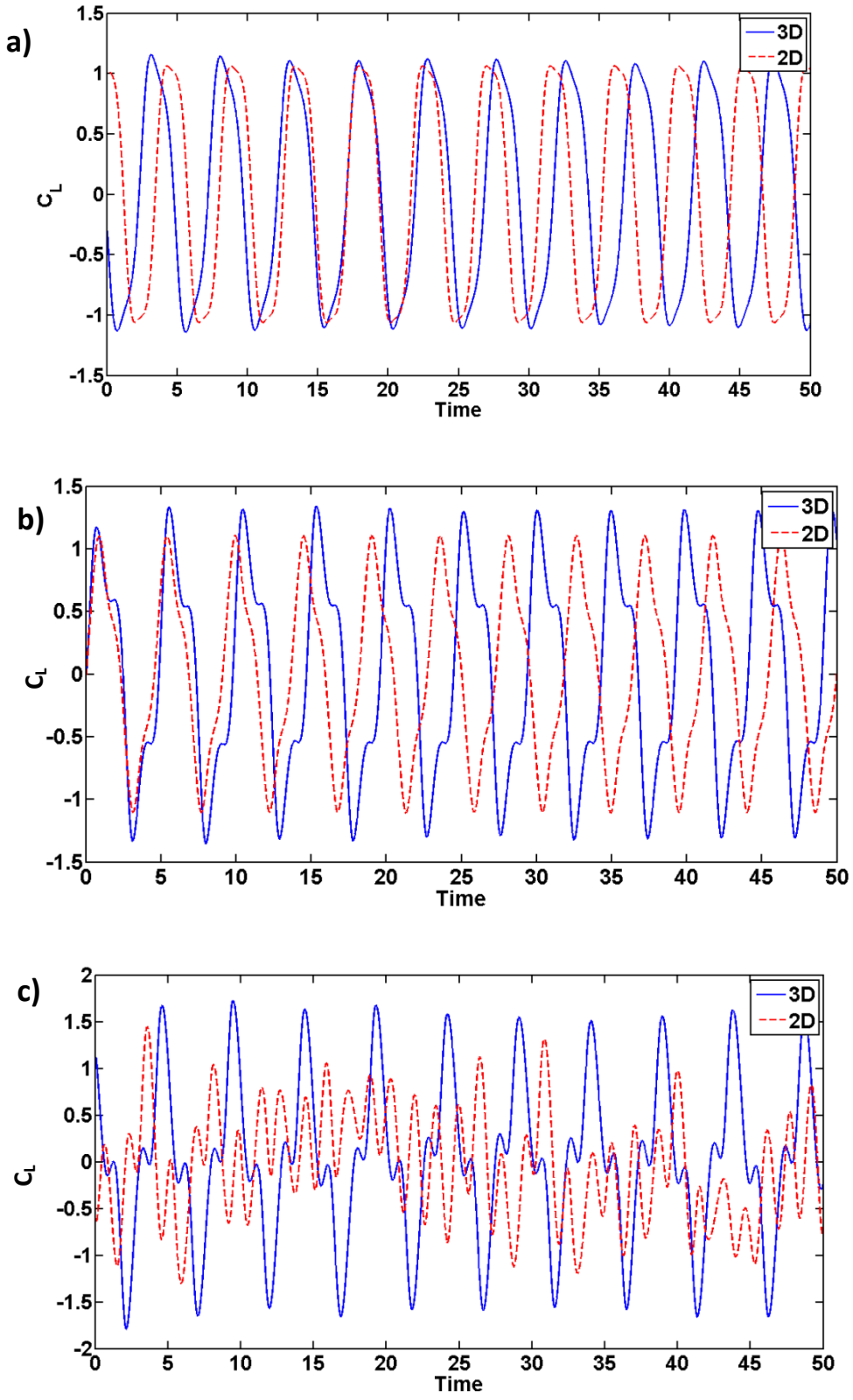

Figure 5-18: Time histories of C_L for the two and three-dimensional simulations with frequency ratio $F = f_y / f_s = 1.0$, counter-clockwise cylinder motion, $\varepsilon=0.2$ and transverse oscillation amplitudes: (a) $A_y/D=0.20$, (b) $A_y/D=0.40$ and (c) $A_y/D=0.60$.

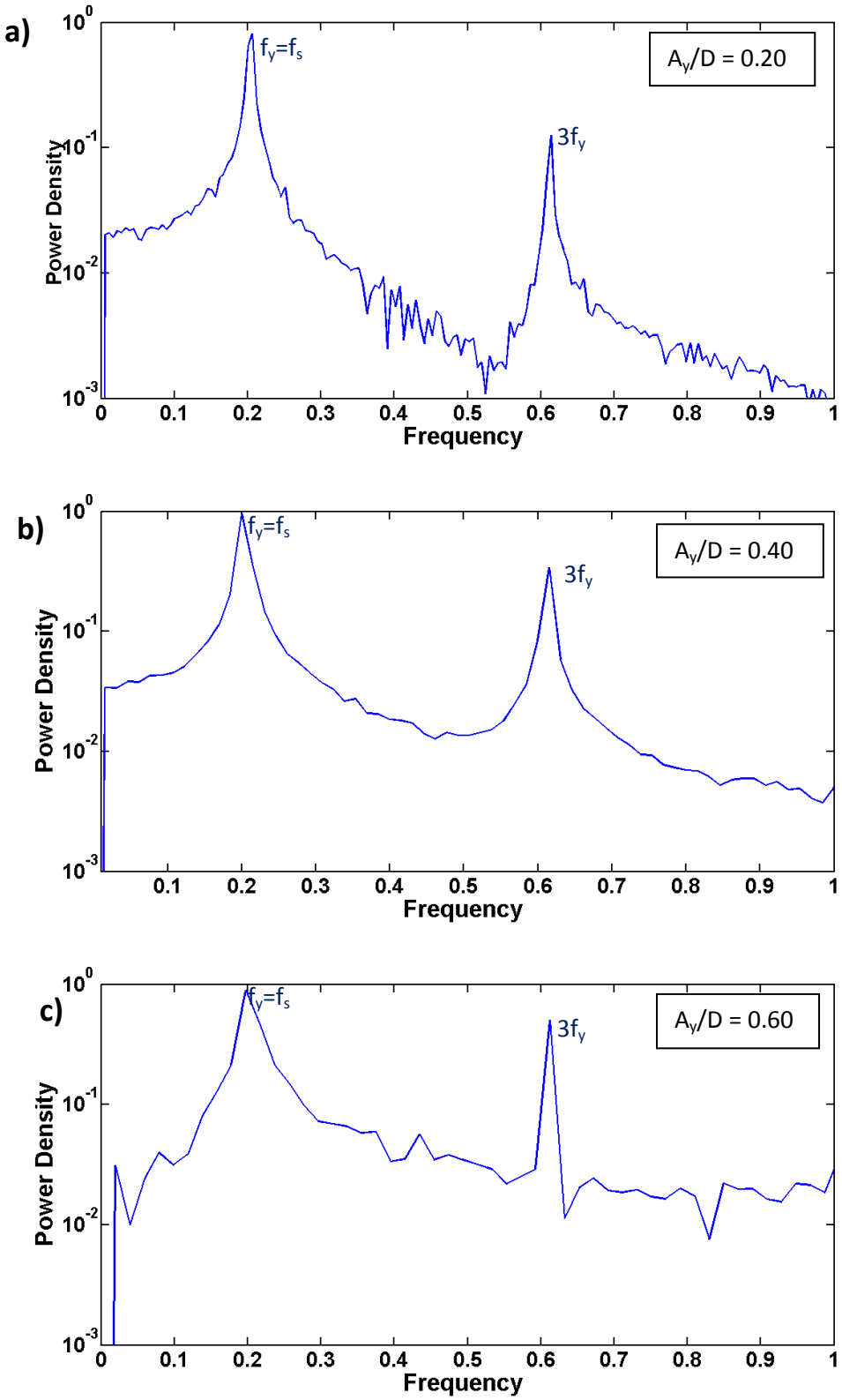

Figure 5-19: Lift coefficient spectra for the three-dimensional simulations with frequency ratio $F = f_y/f_s = 1.0$, counter-clockwise cylinder motion, $\varepsilon = 0.2$ and transverse oscillation amplitudes: (a) $A_y/D = 0.20$, (b) $A_y/D = 0.40$ and (c) $A_y/D = 0.60$.

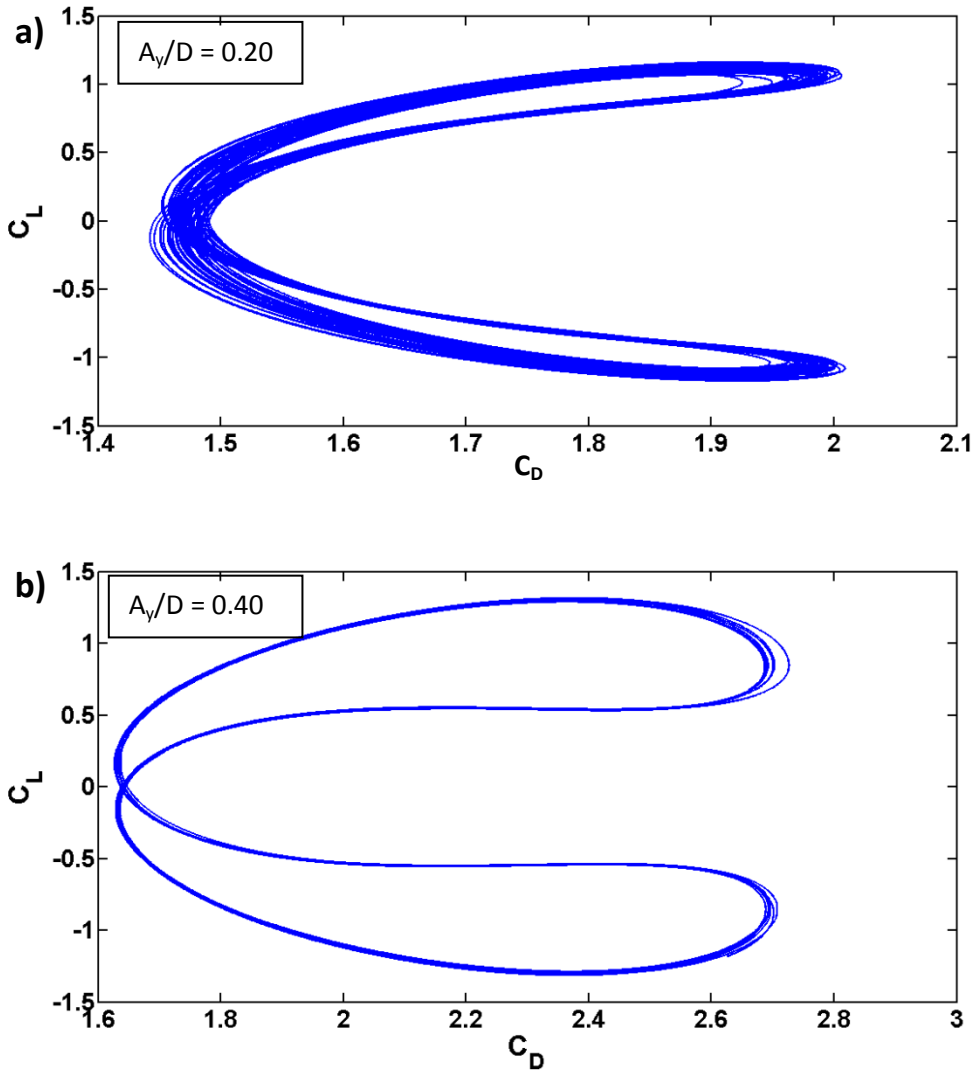

Figure 5-20: Orbits in the C_L – C_D plane for the three-dimensional simulations with frequency ratio $F = f_y / f_s = 1.0$, counter-clockwise cylinder motion, $\varepsilon=0.2$ and transverse oscillation amplitudes: (a) $A_y/D=0.20$, (b) $A_y/D=0.40$

5.3.3 Visualization of the flow in the wake

In this section we study the vortex structures in the three-dimensional wake of an oscillating cylinder following a figure *eight* trajectory, with counter-clockwise direction in the upper x-y plane at *Re=400*. The vortex structures consist of spanwise rolls and streamwise vortices (ribs). The generation of streamwise ribs induces a three-dimensional flow behind the cylinder. The flow three-dimensionality is expected to affect the hydrodynamic forces.

In **Figure 5-21** to **Figure 5-24** snapshots of the three-dimensional flow past a stationary cylinder are presented, for different time instants, at *Re=300* and *Re=400*. More specifically, for *Re=300* instantaneous isosurfaces of spanwise (ω_z), vertical (ω_y) and streamwise (ω_x) vorticity components are shown in **Figure 5-21** and **Figure 5-23** (top view), illustrating the presence of streamwise vortices forming rib-like structures in the braid region, in-between the spanwise (Karman) vortices. The spacing of the streamwise vortices in the spanwise directon is suggestive of Mode B vortex shedding. The results show that by increasing the Reynolds number from 300 to 400 the vortex structures are more persistant, while the complexity of the wake is increased. Isocontours of ω_z for the plane *z=3* are shown in **Figure 5-22** and **Figure 5-24**, illustrating the 2S vortex mode in the wake. These visualizations are in accordance with the experimental visualizations by Williamson (1996) and those of Wu et al. (1994) at *Re=400* as illustrated in **Figure 5-1**.

Figure 5-25 and **Figure 5-26** show isosurfaces $\omega=\pm 2$ for all three vorticity components (ω_x, ω_y, ω_z) for oscillating cylinder. The visualizations correspond to the cylinder mean position, i.e. $\eta_y/D = \eta_x/D = 0$. At *Re=400* the wake is characterized by the formation of three-dimensional vortex structures. First, the visualizations indicate the presence of Karman vortices, which are modulated in the spanwise direction. The visualizations also indicate the presence of counter-rotating streamwise vortices, in agreement with previous experimental studies (Williamson (1996)) and numerical simulations (Thompson et al. (1996)). The spanwise separation of streamwise vortices is suggestive of Mode B structure, Williamson (1996). While the primary rolls deform significantly as they roll up due to the generation of streamwise vorticity, the counter-rotating vortex pairs are stretched by the primary rolls. The vortex structures are quite coherent at $A_y/D = 0.30$, while the wake becomes more complex at higher oscillation amplitudes.

In **Figure 5-27** four subsequent snapshots of the instantaneous vorticity are plotted for oscillation amplitudes equal to 0.30 illustrating the formation and development of wake structures. Comparing them with the vortex structures in the wake of a stationary cylinder illustrated in **Figure 5-21**, it is realized that at $A_y/D = 0.30$ the wake is characterized by reduced levels of vortex tube deformation in the near wake. This demonstrates that, for relatively low amplitudes, forcing has a stabilizing effect, resulting in a more coherent wake structure. **Figure 5-28** presents a surface of constant pressure, *p=-0.25*, over a range of A_y/D, demonstrating the spanwise vortex structures and their increasing complexity for oscillation values higher than $A_y/D = 0.40$.

Figure 5-29 shows isocontours of spanwise vorticity, in planes of z=constant, demonstrating that the flow is not uniform along the cylinder's span. This suggests that the phase of primary vortex shedding varies with the spanwise direction.

In **Figure 5-30, Figure 5-31** and **Figure 5-32** we present contour plots of the vorticity components for the plane *z=3* when the cylinder occupies its mean position. In particular **Figure 5-30** presents the contours of spanwise vorticity and shows substantial discrepancies in comparison to two-dimensional flow (see Chapter 4, **Figure 4-52**). The vorticity plots depict a clear 2S vortex mode in the wake at low oscillation amplitudes, which becomes increasingly distorted at high oscillation amplitudes. In **Figure 5-31** the streamwise vorticity component is plotted, showing the evolving streamwise structures (ribs). The vertical component of the vorticity is also plotted in **Figure 5-32**. The streamwise and vertical vorticity components illustrate strong vortex pairs in regions between the spanwise rolls. Finally in **Figure 5-33** isocontours of total vorticity magnitude are presented for the plane *z=3* when the cylinder occupies its mean position showing good qualitative agreement with experimental visualizations.

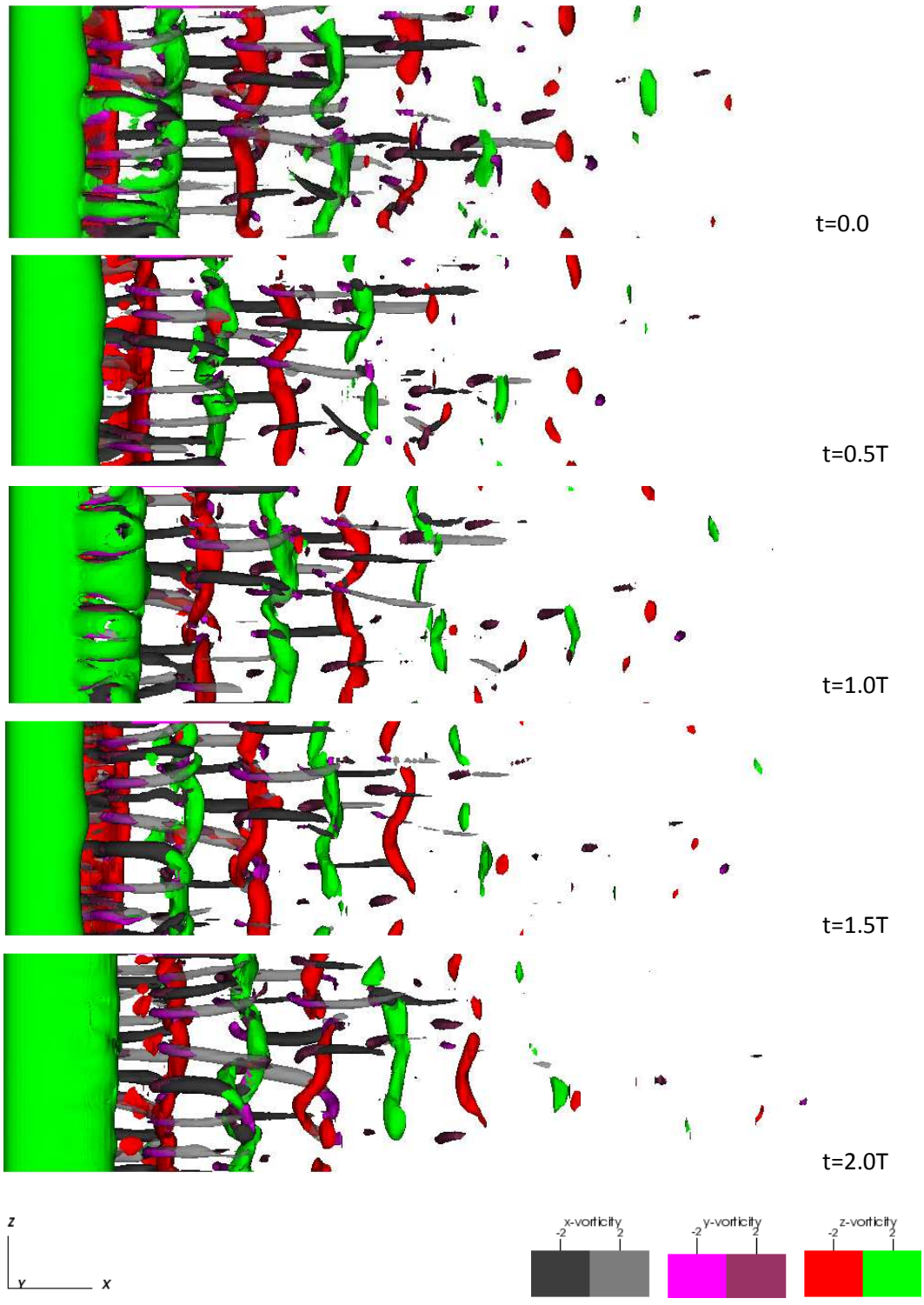

Figure 5-21: Flow past a stationary cylinder at *Re=300*: Snapshots of instantaneous isosurfaces of spanwise (ω_z), vertical (ω_y) and streamwise (ω_x) vorticity components (top view). The snapshots are separated by half of a Strouhal period, T. Here, two levels of vorticity field are identified: *ω=-2.0* and *ω=+2.0*.

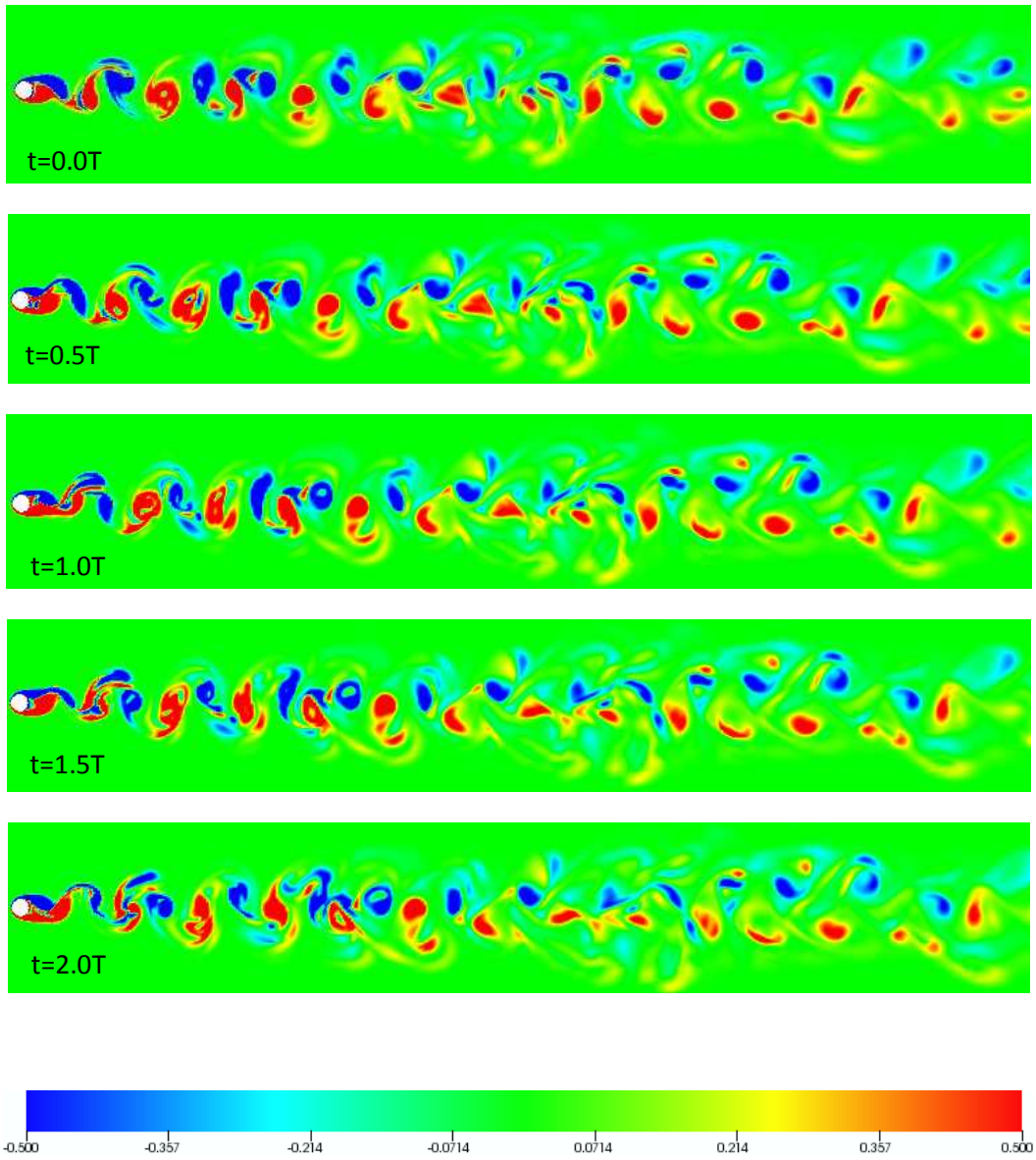

Figure 5-22: Flow past a stationary cylinder at *Re=300*: Snapshots of instantaneous isocontours of spanwise vorticity (ω_z) for the plane *z=3.* The snapshots are separated by half of a Strouhal period, T.

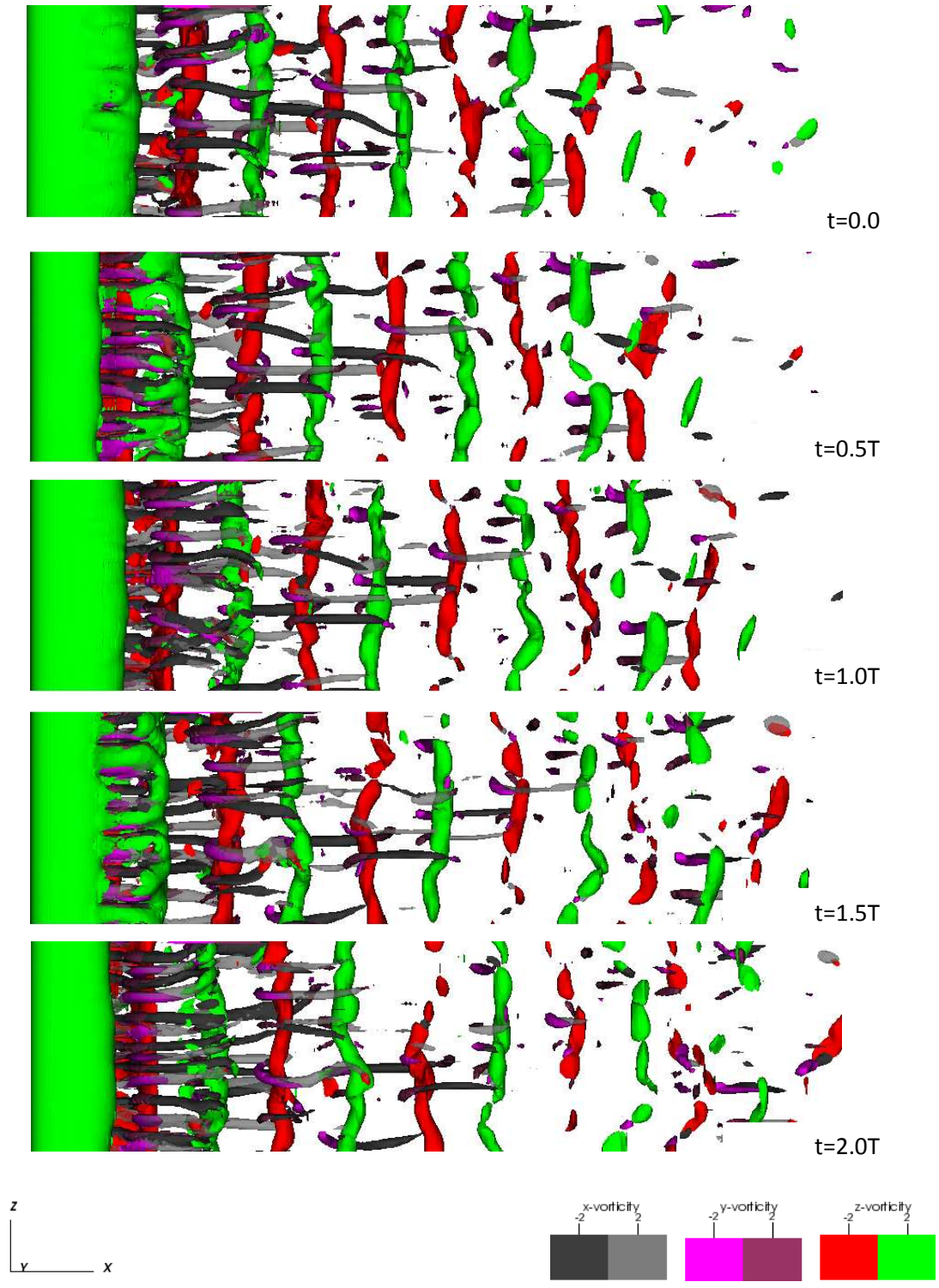

Figure 5-23: Flow past a stationary cylinder at *Re=400*: Snapshots of instantaneous isosurfaces of spanwise (ω_z), vertical (ω_y) and streamwise (ω_x) vorticity components (top view). The snapshots are separated by half of a Strouhal period, T. Here, two levels of vorticity field are identified: *ω=-2.0* and *ω=+2.0*.

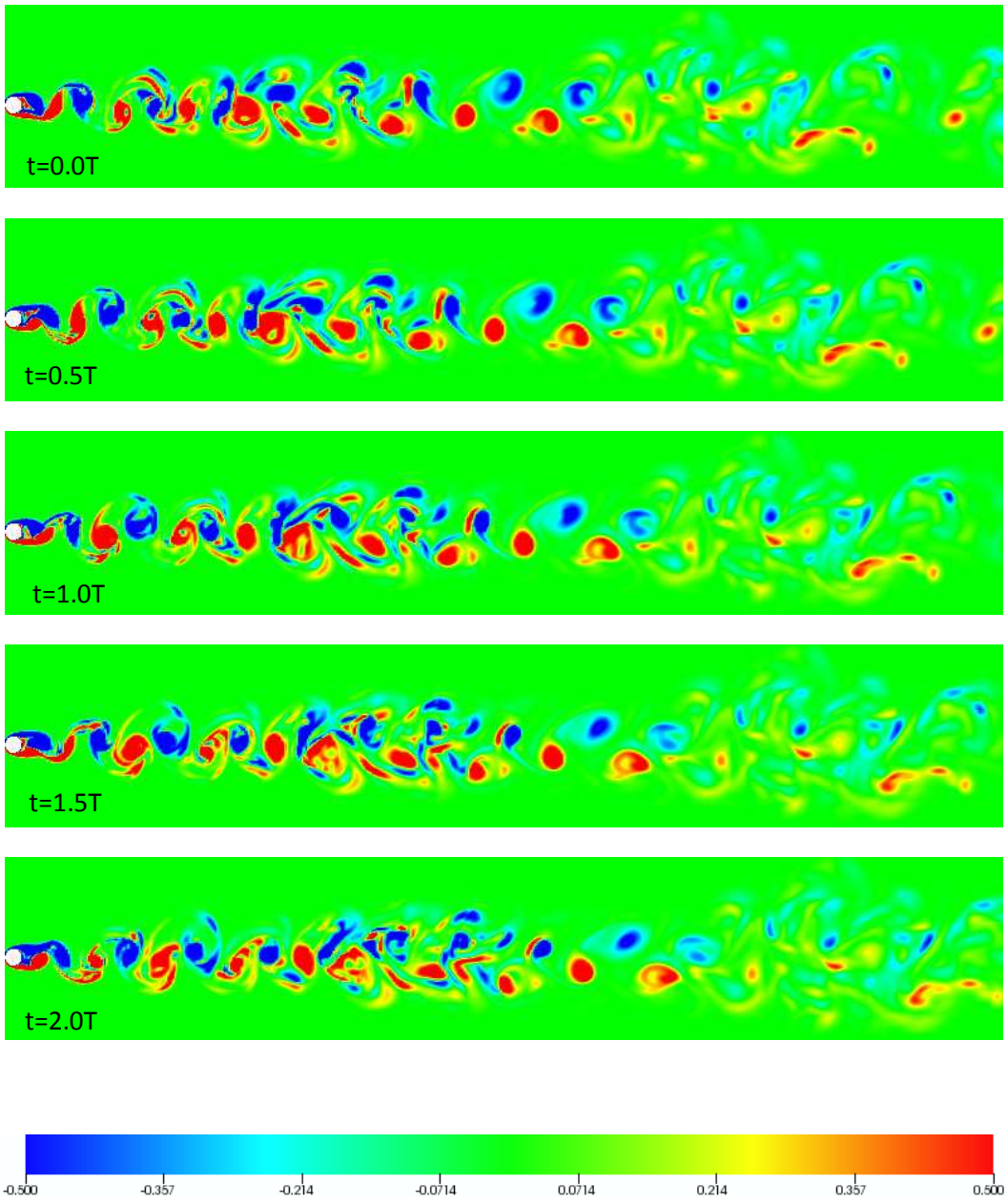

Figure 5-24: Flow past a stationary cylinder at *Re=400*: Snapshots of instantaneous isocontours of spanwise vorticity (ω_z) for the plane *z=3.* The snapshots are separated by half of a Strouhal period, T.

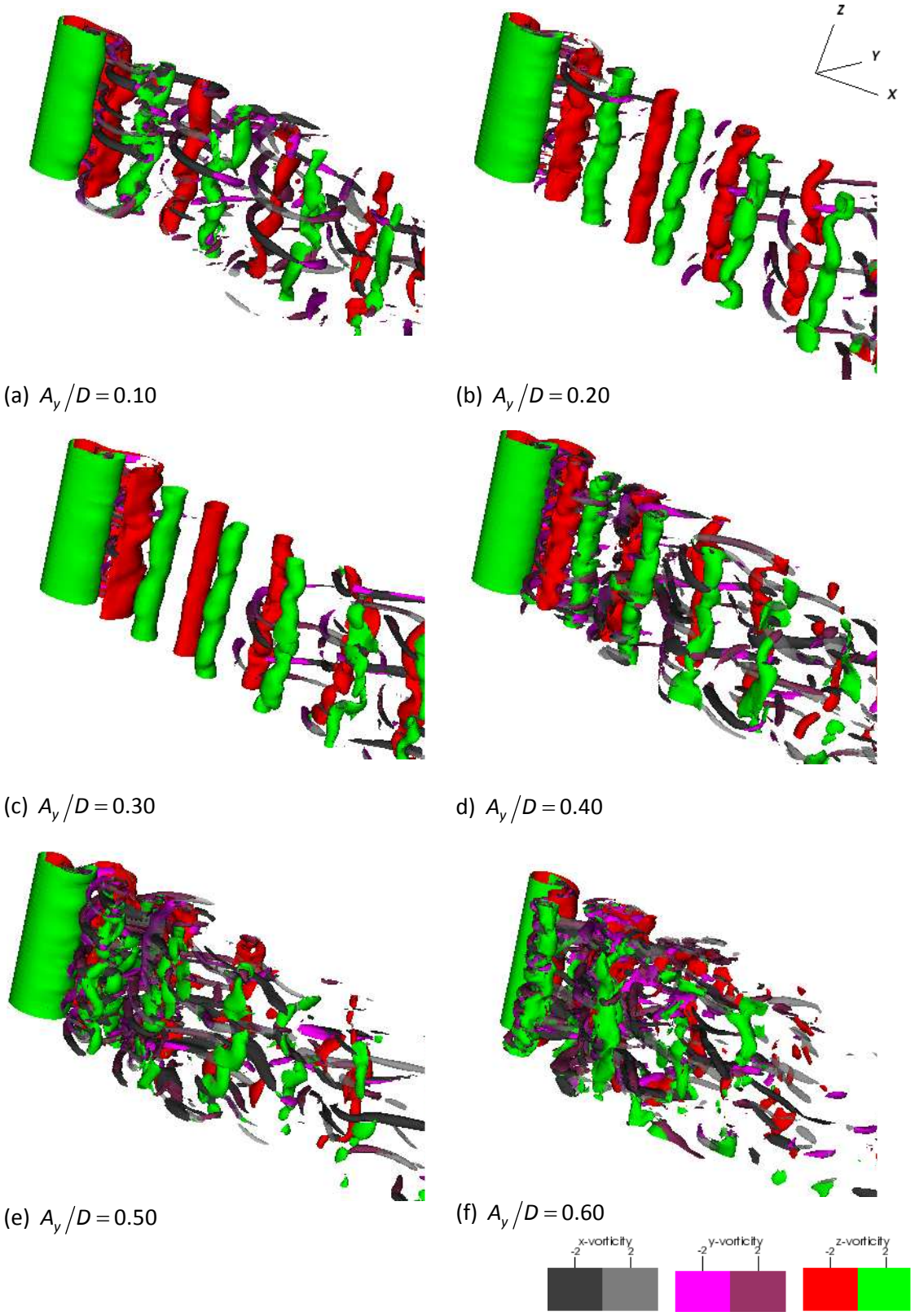

(a) $A_y/D = 0.10$

(b) $A_y/D = 0.20$

(c) $A_y/D = 0.30$

d) $A_y/D = 0.40$

(e) $A_y/D = 0.50$

(f) $A_y/D = 0.60$

Figure 5-25: Instantaneous isosurfaces of spanwise (ω_z), vertical (ω_y) and streamwise (ω_x) vorticity components (side view) for *F=1.0, ε=0.2*, counter-clockwise motion. The cylinder occupies its mean position. Here, two levels of vorticity field are identified: *ω=-2.0* and *ω=+2.0*.

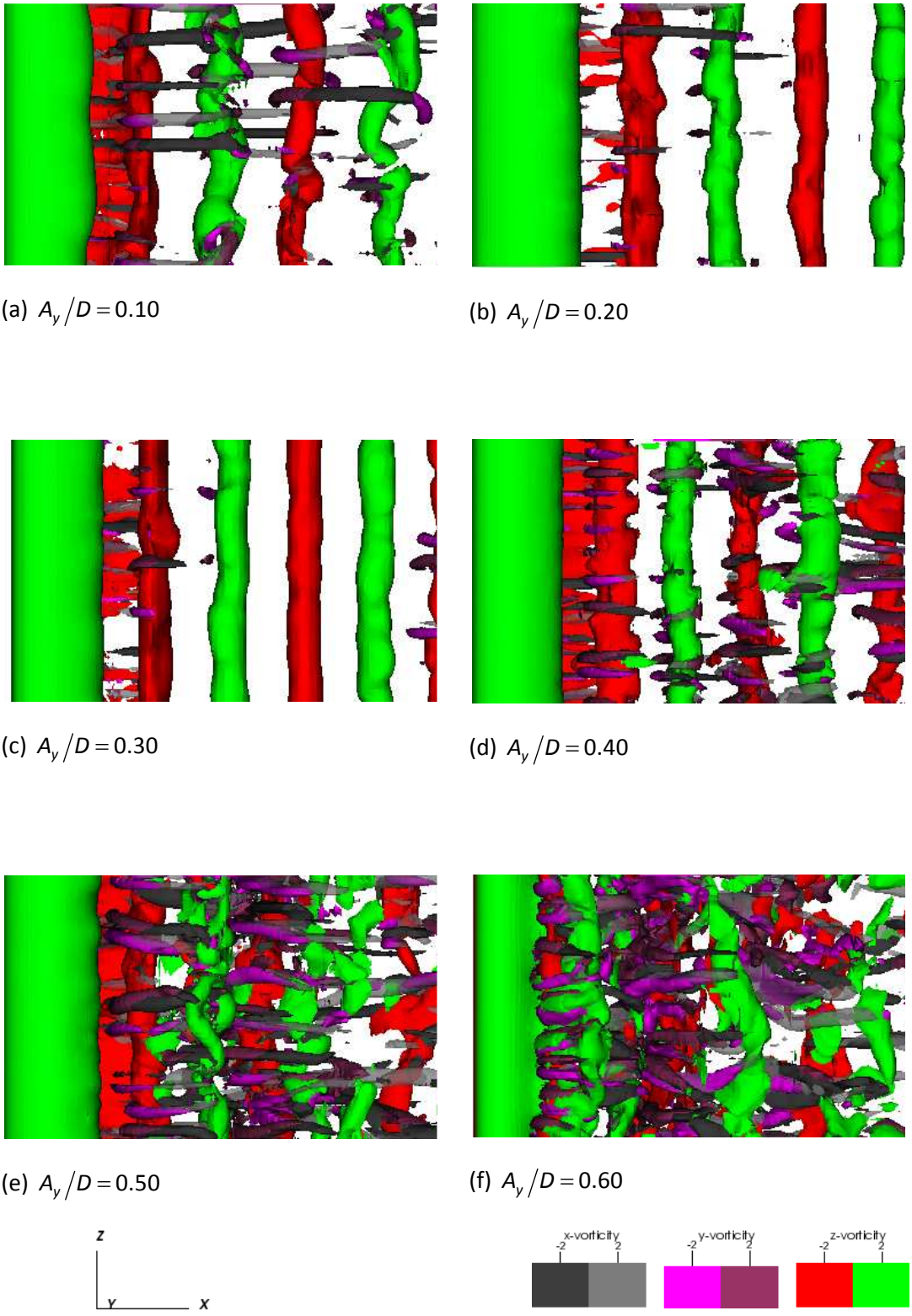

Figure 5-26: Instantaneous isosurfaces of spanwise (ω_z), vertical (ω_y) and streamwise (ω_x) vorticity components (top view) for *F=1.0*, *ε=0.2*, counter-clockwise motion. The cylinder occupies its mean position. Here, two levels of vorticity field are identified: *ω=-2.0* and *ω=+2.0*.

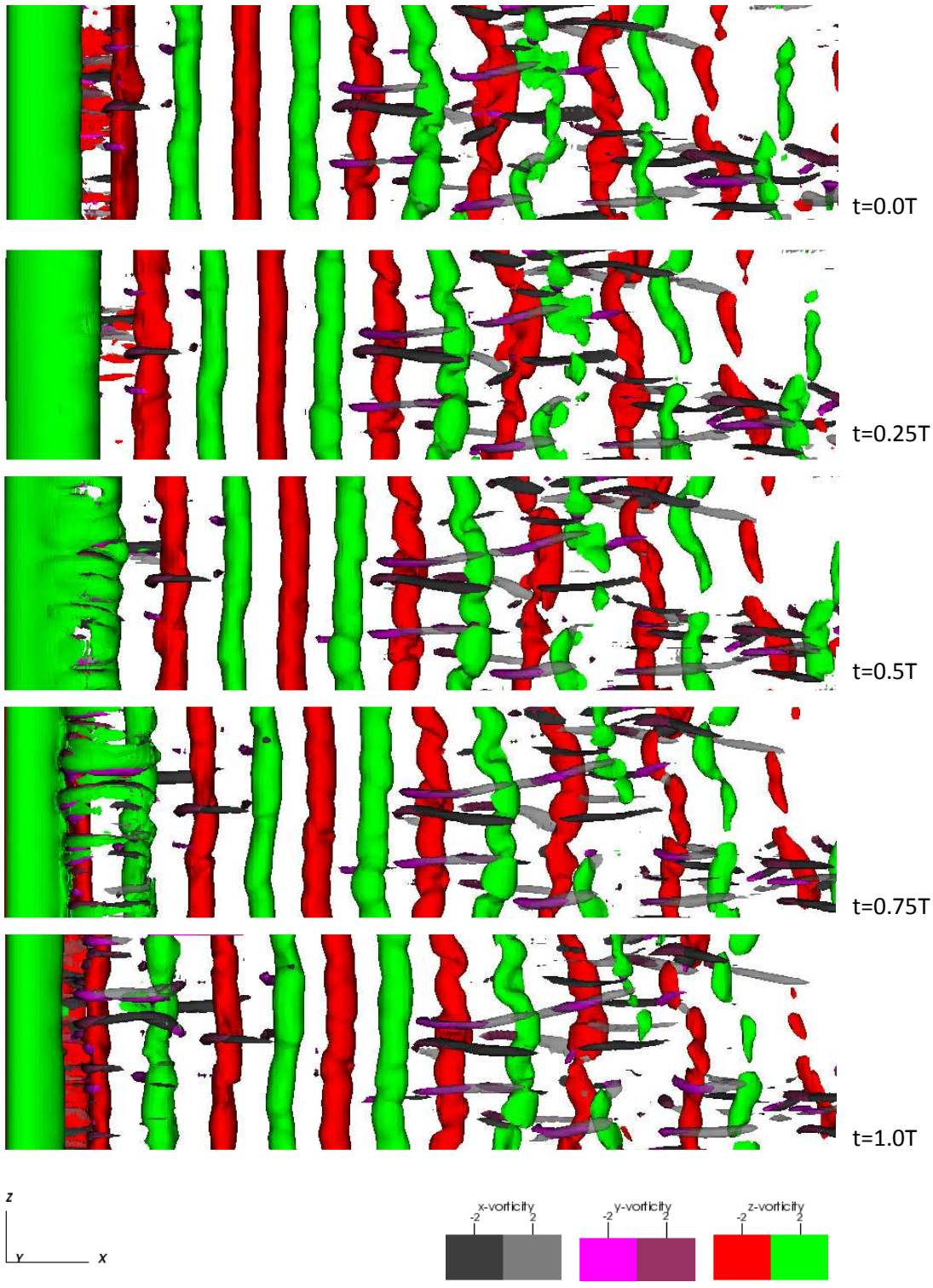

Figure 5-27: Snapshots of instantaneous isosurfaces of spanwise (ω_z), vertical (ω_y) and streamwise (ω_x) vorticity components (top view) for *F=1.0*, *ε=0.2*, counter-clockwise motion and transverse oscillation amplitude A_y/D *=0.30*. The snapshots are separated by a quarter of an oscillating period, T. Here, two levels of vorticity field are identified: *ω=-2.0* and *ω=+2.0*.

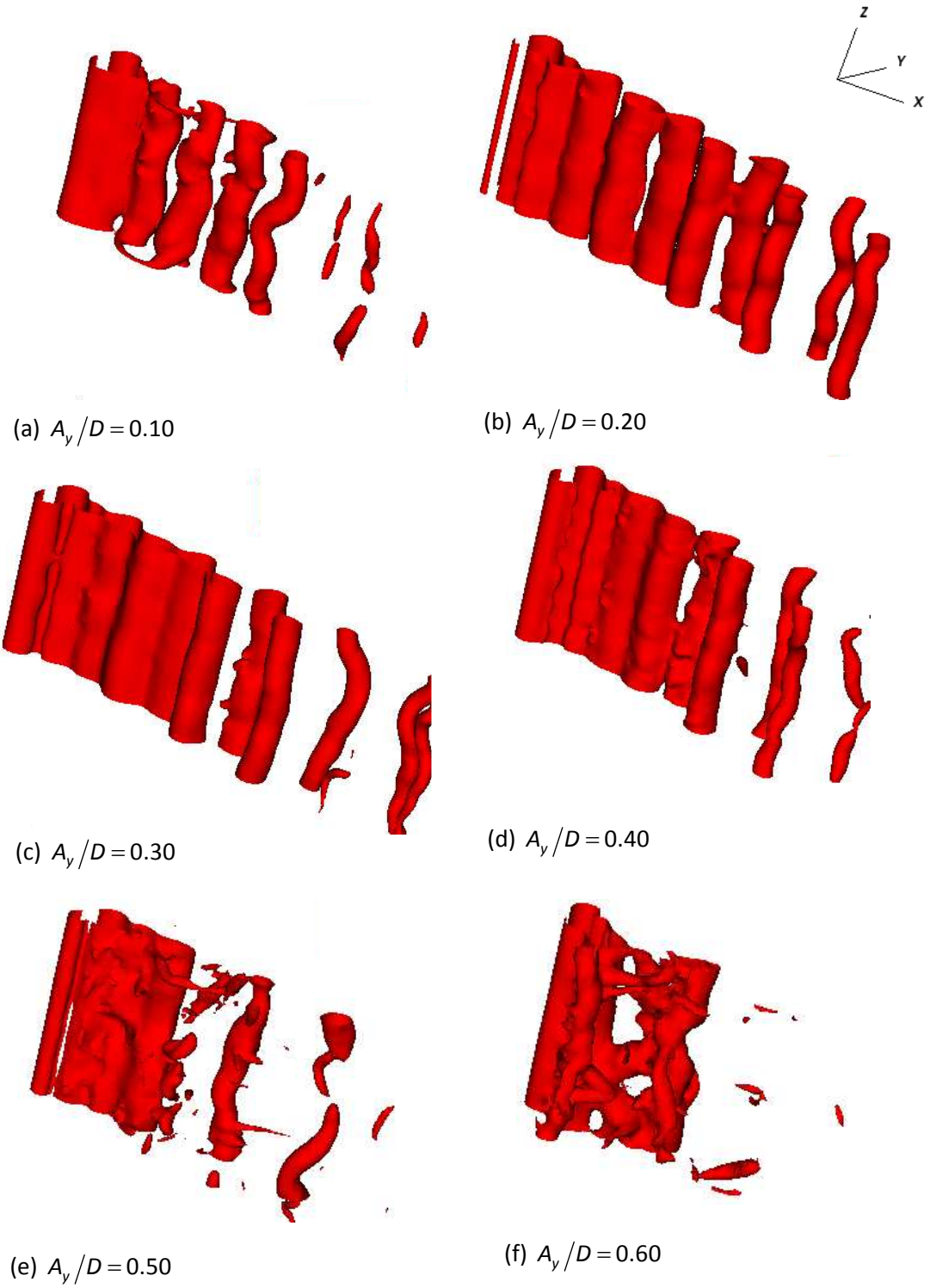

Figure 5-28: Instantaneous isosurfaces of pressure, *p=-0.25* for *F=1.0*, *ε=0.2*, counter-clockwise motion. The cylinder occupies its mean position.

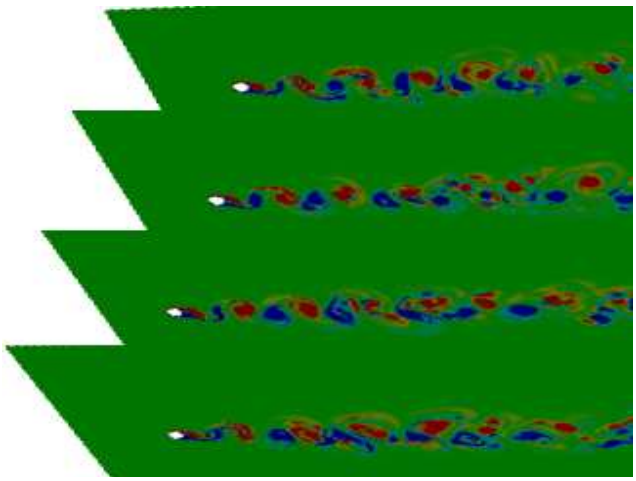

(a) $A_y/D = 0.10$

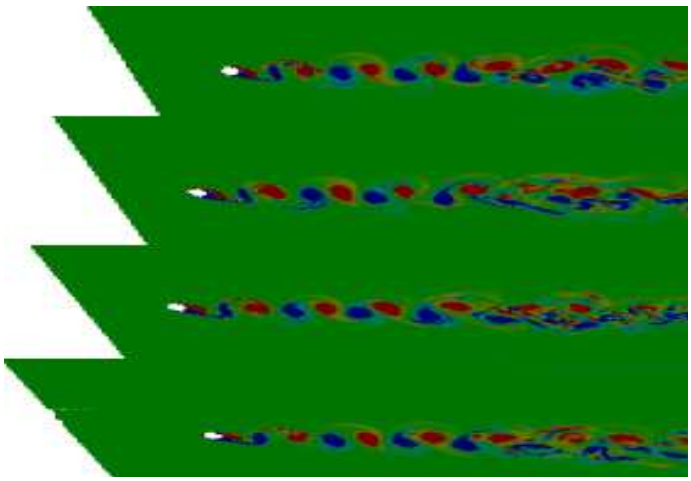

(b) $A_y/D = 0.20$

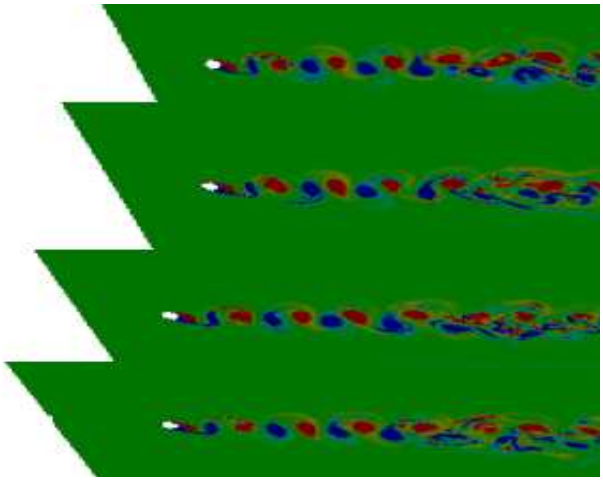

(c) $A_y/D = 0.30$

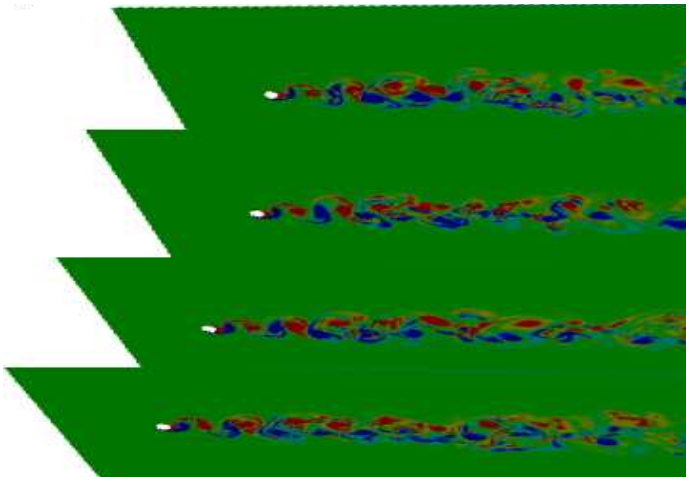

(d) $A_y/D = 0.40$

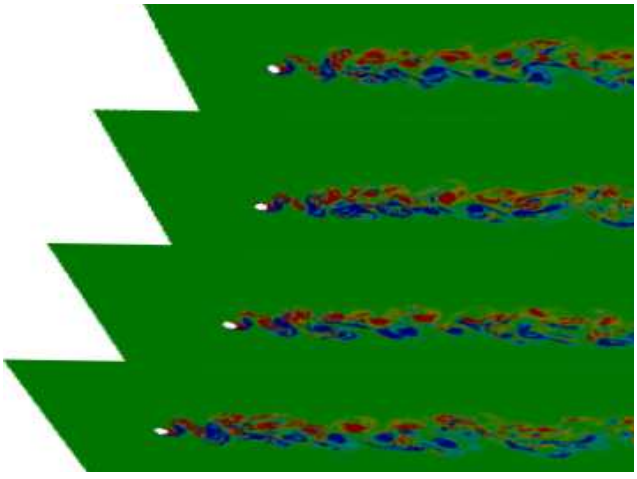

(e) $A_y/D = 0.50$

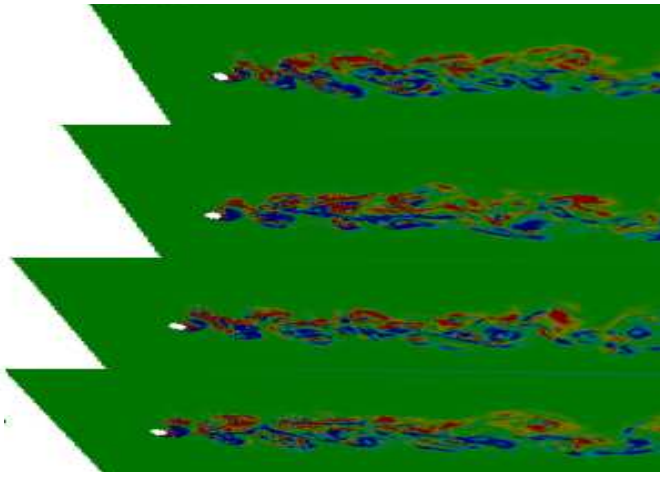

(f) $A_y/D = 0.60$

Figure 5-29: Instantaneous isocontours of spanwise vorticity, in planes of z=constant, for *F=1.0*, *ε=0.2*, counter-clockwise motion.

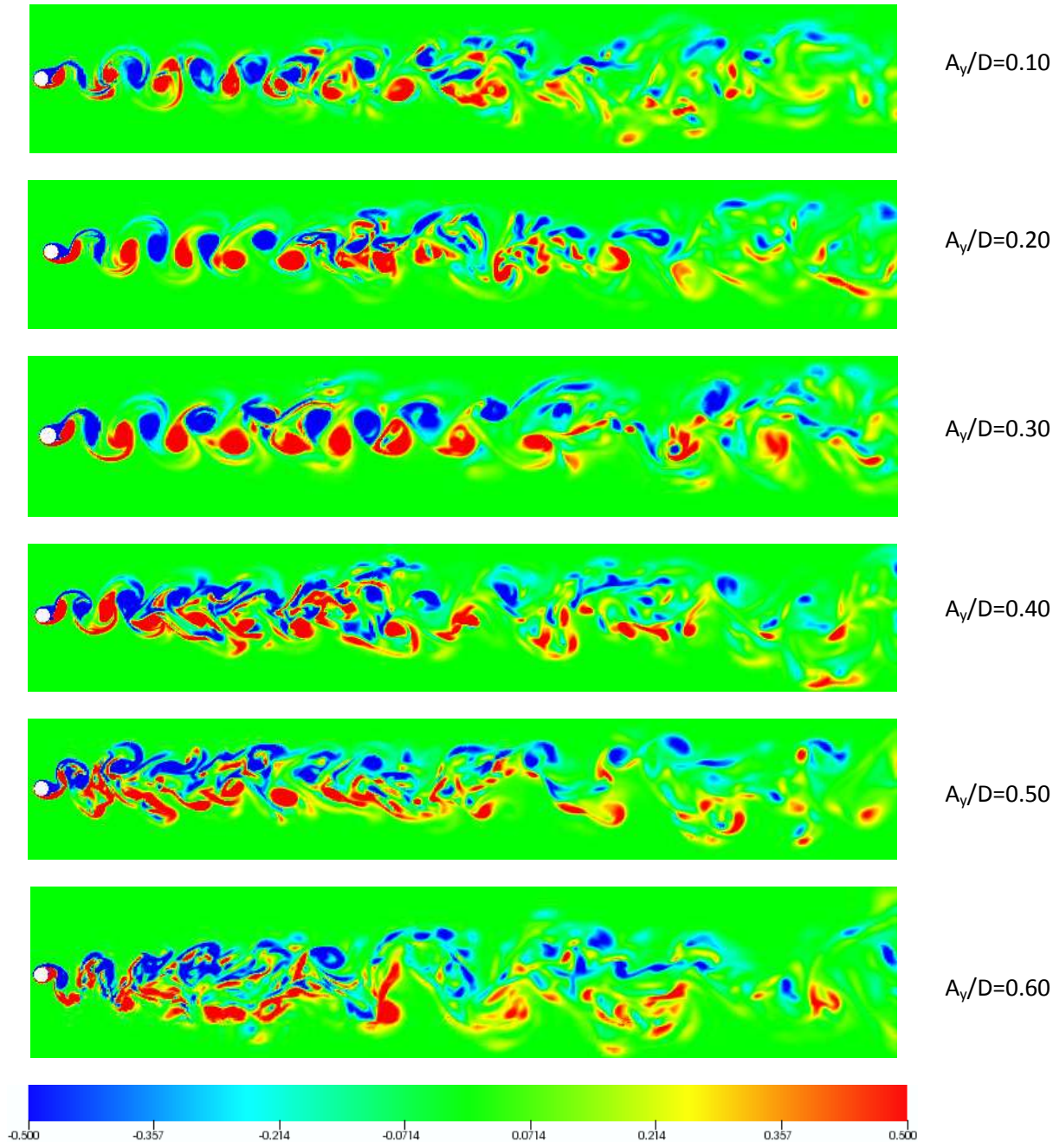

Figure 5-30: Isocontours of spanwise vorticity (ω_z) for the plane *z=3*, *F=1.0, ε=0.2*, counter-clockwise motion and different oscillation amplitudes. The cylinder occupies its mean position.

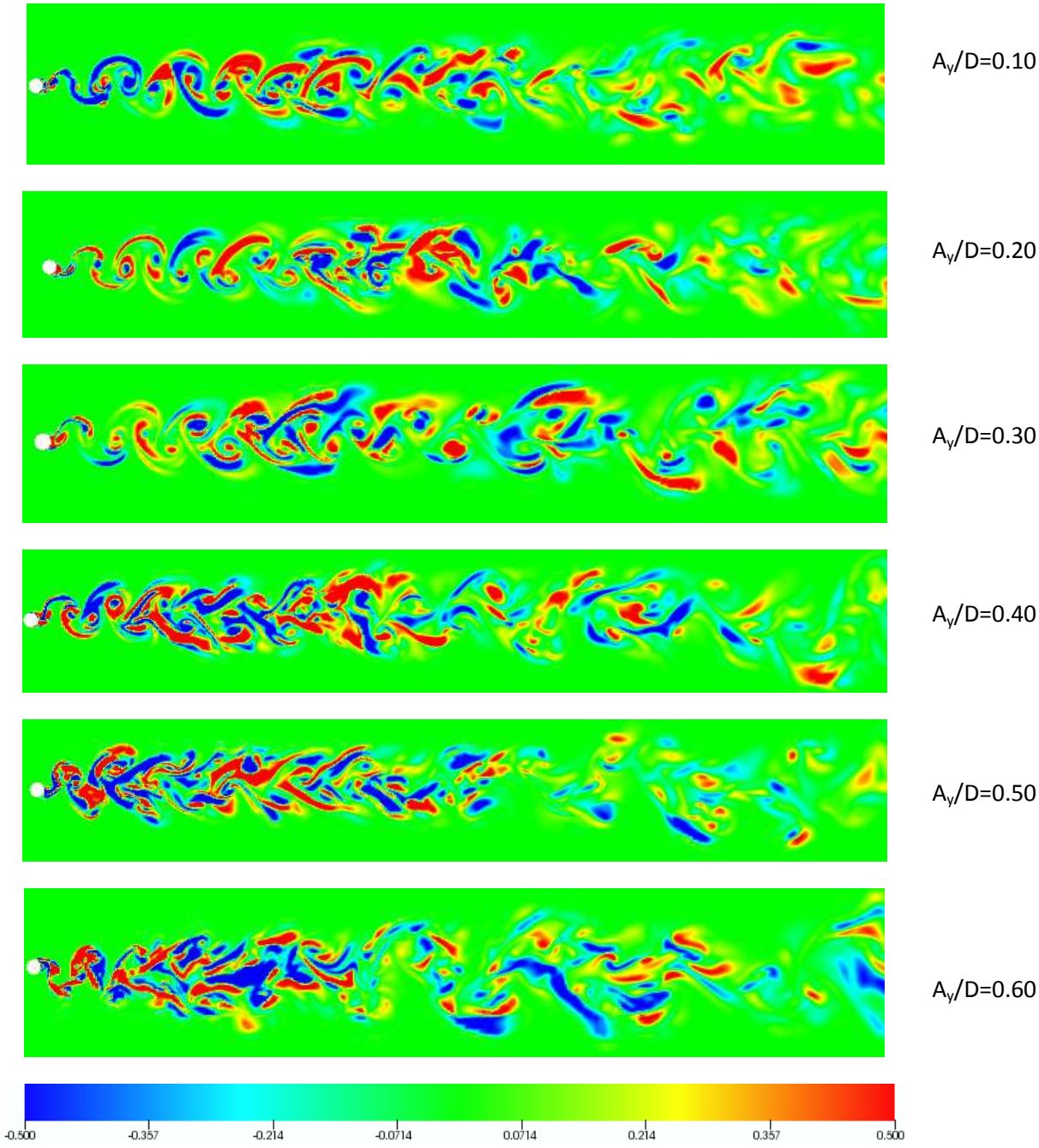

Figure 5-31: Isocontours of streamwise vorticity (ω_x) for the plane *z=3*, *F=1.0, ε=0.2*, counter-clockwise motion and different oscillation amplitudes. The cylinder occupies its mean position.

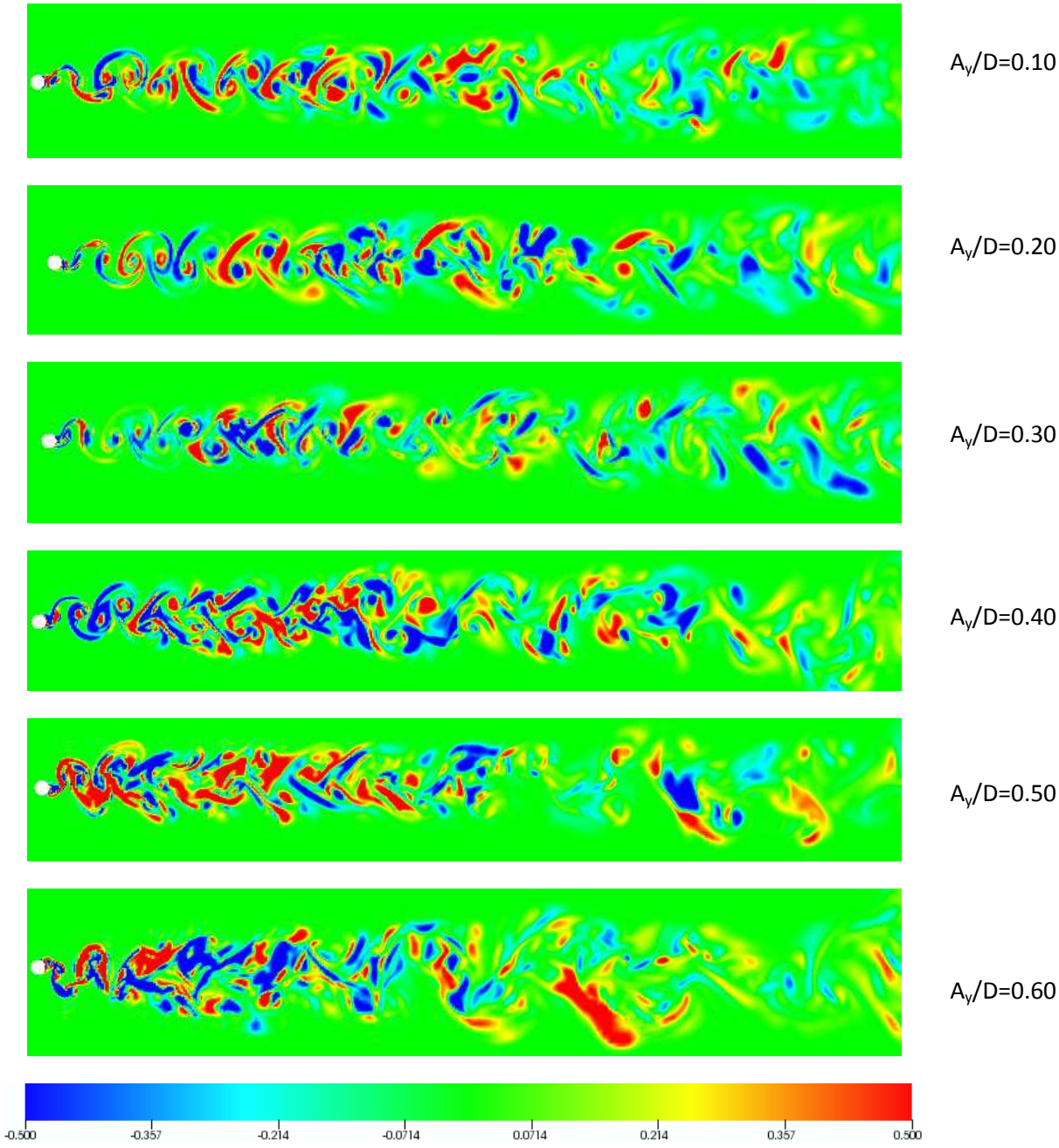

Figure 5-32: Isocontours of vertical vorticity (ω_y) for the plane *z=3*, *F=1.0, ε 0.2*, counter-clockwise motion and different oscillation amplitudes. The cylinder occupies its mean position.

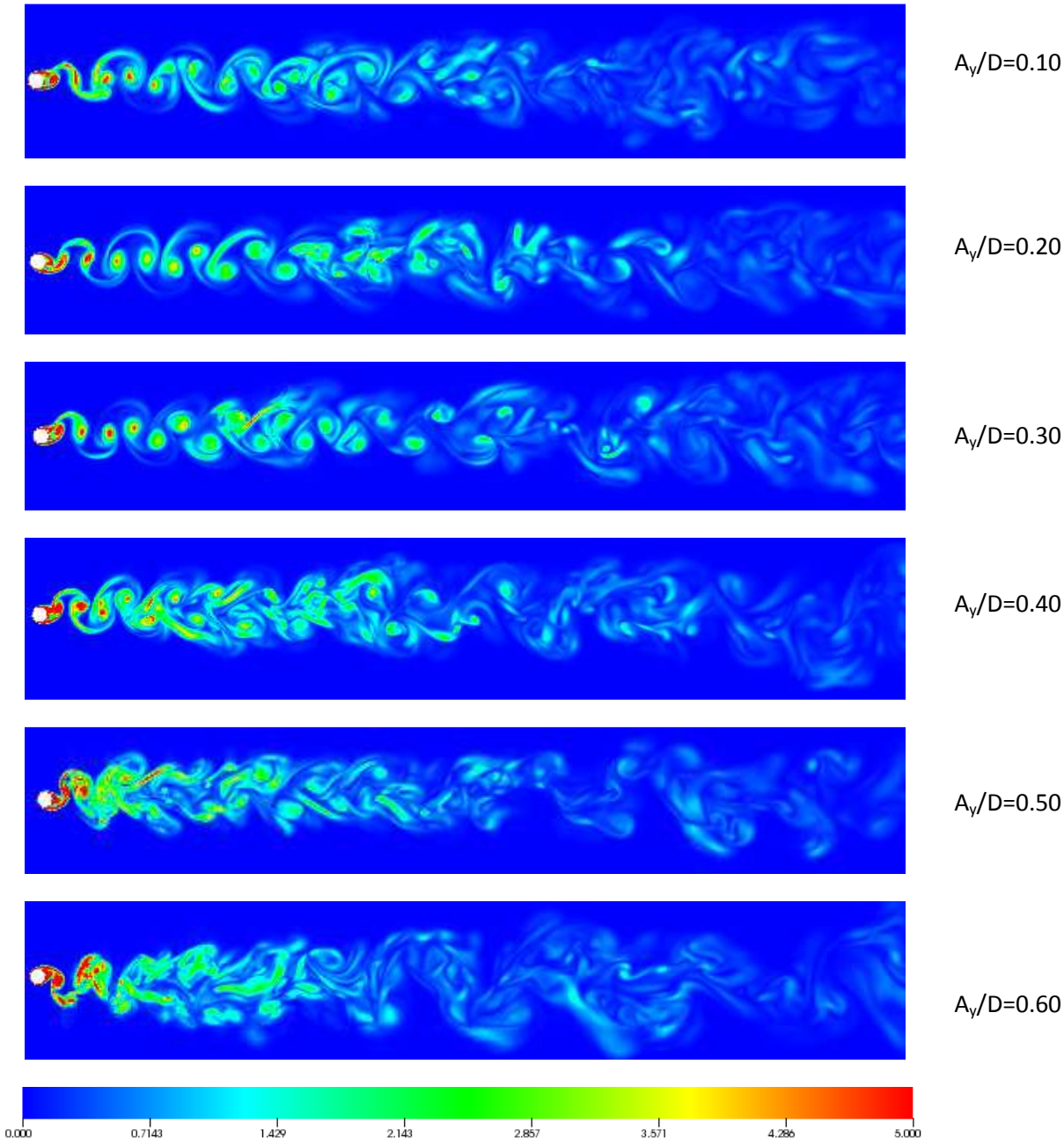

Figure 5-33: Isocontours of total vorticity magnitude for the plane *z=3*, *F=1.0, ε=0.2*, counter-clockwise motion and different oscillation amplitudes. The cylinder occupies its mean position.

5.4 Discussion

In this chapter, we have presented computational results of three-dimensional flow past a circular cylinder oscillating both transversely and in-line to a steady stream, following a figure *eight* trajectory, for a Reynolds number, *Re=400*. For a flow stream from left to right, we have studied the cylinder motion in a counter-clockwise direction. The transverse oscillation frequency is equal to the vortex shedding frequency, thus *F=1.0*, and the ratio of in-line to transverse oscillation amplitude is equal to *ε=0.2*.

We investigated the three-dimensionality of the vorticity field and its effect on the force components. We compared the results of three-dimensional simulations with those of the two-dimensional simulations (Chapter 4). Although the results, in general, follow the same trends, there is no *"memory*" of the transition observed in two-dimensional simulations at oscillation amplitudes $A_y/D \approx 0.25$. Since the transition is also present in two-dimensional flow past a cylinder exhibiting transversely only oscillation, we postulated that, the transition will not be present in such a case of three-dimensional flow.

The spectra of the computed lift coefficient characterize the flow dynamics in the wake. In the present case of resonant forcing, the flow is locked-in to the excitation frequency at all amplitudes, in both two- and three-dimensional simulations. Also, the power spectra indicate multiple frequency peaks, while a strong third harmonic component is present.

In three-dimensional simulations, flow visualization demonstrates the formation of 2S vortices, with streamwise vortex pairs in the regions in-between. These results are in accordance with experimental visualizations, Wu et al. (1994) and Williamson (1996). The present computational results show that, in comparison to the structure of flow past a stationary cylinder, the wake is characterized by reduced levels of vortex tube deformation in the near wake, at relatively low oscillation amplitudes, i.e. forcing has a stabilizing effect, making the wake more coherent. The wake structure is very complex for values of oscillation amplitude A_y/D higher than approximately 0.50.

Chapter 6

Conclusions

6.1. Summary

In this thesis we have studied numerically the flow past a forced oscillating cylinder. Both two- and three-dimensional simulations have been performed over a wide range of amplitudes for different cases of cylinder oscillation, at a constant Reynolds number equal to 400.
The main conclusions of our study, are summarized as follows:

6.1.1 Two-dimensional flow

Simulations of two-dimensional flow have been performed for different cases, characterized by the type of cylinder motion (counter-clockwise or clockwise), the ratio of the in-line to the transverse oscillation amplitude (*ε=0.2* and *ε=0.4)* and the ratio of transverse oscillation frequency to the natural frequency of vortex shedding (*F= 1.0, 0.9* and *1.1*). Here, the oscillation amplitude (A_y/D) varies from zero to approximately half the cylinder diameter. The results are compared against the case of transverse-only oscillation (*ε=0*).

6.1.1.1 Resonant forcing (F=1.0)

- Counter-clockwise motion maintains positive power transfer at higher values of A_y/D, in comparison to clockwise or to transverse-only cylinder oscillation (*ε=0*).
- The presence of in-line motion in most cases increases, the drag forces exerted on the cylinder in comparison to transverse-only oscillation (*ε=0*).

6.1.1.2 Forcing below the natural frequency (F=0.9)

- Counter-clockwise motion is associated with an increased amplitude range of positive *P* values in comparison to the other two oscillation modes (transverse-only oscillation and clockwise motion).
- The variation of the drag force for *ε=0.2* is an increasing function of oscillation amplitude, with higher levels corresponding to the counter-clockwise oscillation mode.

6.1.1.3 Forcing above the natural frequency (F=1.1)

- The power transfer parameter *(P)* varies between positive and negative values, with the maximum values of positive power transfer being lower compared to the cases of resonant and below resonant forcing.
- Clockwise oscillation is characterized by high values of lift force at high oscillation amplitudes.
- The curve of drag force is also non-monotonic and complex.

6.1.1.4 Effect of in-line oscillation

The presence of an in-line oscillation component has the following significant effects on the hydrodynamic forces acting on the cylinder:

- a strong third harmonic component of the lift force, for transverse oscillation frequencies less than or equal to the Strouhal frequency. This can cause higher fatigue stresses on vibrating structures.

- aperiodic lift forces for counter-clockwise motion, for transverse oscillation frequencies less than or equal to the Strouhal frequency, and for transverse oscillation amplitudes equal to at least one third of the cylinder diameter. The complexity in the force signals characterizes both the counter-clockwise and the clockwise mode, at higher frequency ratios.

- complex force signals for both the counter-clockwise and the clockwise mode and for transverse oscillation frequencies higher than the Strouhal frequency.

In summary, the computational results of two-dimensional flow for force coefficients and power transfer parameter demonstrate a strong interrelation between the flow states and the direction in which the cylinder trajectory is traversed. Counter-clockwise cylinder motion is, in most cases associated with higher non-dimensional forces; also the power transfer to the cylinder remains positive for high oscillation amplitudes, in comparison to the clockwise motion and the transverse-only oscillation, especially at resonant forcing. Thus, the counter-clockwise cylinder motion appears to be the most hazardous one for engineering applications exhibiting vortex-induced vibrations.

6.1.1.5 Flow visualization

- The visualization of the flow demonstrates 2S structures in the wake at low amplitudes, whereas more complicated wake structures are observed at increasing oscillation amplitudes, dominated by vortex splitting and combinations of vortices. The present results are in close agreement with the experiments of Ongoren and Rockwell (1988) and Williamson and Roshko (1988) and the computational study by Kaiktsis et al. (2007).

- Rich wake dynamics and asymmetric flow are identified, becoming more pronounced at increasing in-line oscillation amplitude. This should be interpreted on the basis of the pattern competition between a symmetric flow mode (induced by in-line oscillation) and the asymmetric Kármán street mode, which exhibit entirely different spatial structures, see Ciliberto and Gollub (1984) and Perdikaris et al. (2009).

6.1.2 Three-dimensional flow

Simulations of three-dimensional flow have been performed for the counter-clockwise oscillation mode, in particular for transverse oscillation frequency equal to the natural shedding frequency (*F=1.0*) and ratio of in-line to transverse oscillation amplitude equal to ε=0.2.

The following conclusions can be drawn:

- The three-dimensional flow is characterized by a smooth variation of force components with oscillation amplitude. This contradicts the sharper variation in two-dimensional flow, especially at transverse amplitudes around $A_y/D = 0.25$. Since a sharp transition is present in two-dimensional flow past a cylinder exhibiting transverse-only oscillation ($\varepsilon=0$), we expect that the transition will not be present in three-dimensional flow past a transverse-only oscillating cylinder. Nonetheless, in the absence of transitions, flow statistical parameters as force coefficients are surprisingly close to those of two-dimensional simulations.
- The flow is locked-in to the excitation frequency at all amplitudes.
- The power spectra of the lift force indicate multiple frequency peaks while a strong third harmonic component is present.
- Flow visualizations illustrate the three-dimensional character of the wake, involving the formation of Karman vortices modulated in the spanwise direction and the presence of counter-rotating streamwise vortices. The spanwise separation of streamwise vortices is suggestive of the Mode B structure Williamson (1996). As the oscillation amplitude increases, and up to $A_y/D = 0.30$, the wake structure becomes more coherent, in comparison to that of a stationary cylinder; the wake becomes increasingly more complex at higher oscillation amplitudes.
- The vortex shedding is characterized by a 2S type mode, with complex wake structures at high oscillation amplitudes.

6.1.3 Parallel processing

The MPI parallel code provides a basis for the efficient computation of two- and three-dimensional flow. The code has been validated against numerical and experimental literature data for flow past a stationary cylinder. Benchmarking simulations with grid points up to 10^7 demonstrate that the code scales well on different computer hardware. The parallel speed-up increases almost linearly with up to 256 processors. For a number of processors equal to 256, a total 20560 elements correspond to 80 elements per processor. It is expected that for a higher number of processors the local work per processor will decrease resulting in an increased speed-up, possibly linear. However, this has not been the case for a number of 512 and 1024 processors; we attribute the deviation from a linear speed-up to the increase in communication cost.

6.2. Future directions

This thesis has aimed at contributing to the understanding of vortex-induced vibrations in flow past a cylinder. To this end, the flow past an oscillating cylinder following a figure *eight* trajectory has been studied. Summarizing the conclusions of the present chapter, the following avenues for future research are suggested:

Study of the three-dimensional flow, for both the counter-clockwise and clockwise cylinder mode, in a wider range of oscillation frequency, around F=1. In addition to two-dimensional simulations already presented in the thesis, the performance of three-dimensional simulations over a range of oscillating frequencies and amplitudes for the two oscillation modes will enable a deeper understanding of the relation between the flow states and the direction in which the cylinder trajectory is traversed. An interesting question thereby is the dependence of important integral parameters as power transfer and lift/drag force amplitude on the direction in which the figure *eight* is traversed.

Numerical studies at higher Reynolds number, being more representative of VIV applications. DNS of three-dimensional flow with the use of spectral methods in a parallel code allows a sensible reduction of the CPU time, and is considered to be the most accurate numerical method in VIV predictions ITTC (2008). Unfortunately DNS is restricted to low Reynolds numbers, due to the associated high computational cost. Considering Kolmogorov's law, the number of grid points that are required for a reasonably accurate simulation in three dimensions is proportional to the Reynolds number raised to the 9/4 power ($Re^{9/4}$) Rogallo and Moin (1984). Thus, a twofold increase in the Reynolds number results in about a fivefold increase in the number of grid points required for simulations. In flow past an oscillating cylinder, considering a Reynolds number of practical interest, say *Re=10000*, an increase in resolution requirements by three orders of magnitude is estimated, in comparison to that of the present study for *Re=400*. For the present resolution of approximately 10 million grid points, a total of about 3 days has been required to integrate for a total of 60 oscillation periods on 512 cores; this is considered close to the upper limit of the computational resources available to us. Evidently, to simulate high Reynolds number flows, the DNS approach is still not applicable. Thus, the approach of Large Eddy Simulations (LES) should be considered in future studies.

Computational study of three-dimensional flow past a cylinder undergoing free oscillation. The present study has demonstrated the capability of the numerical approach to accurately simulate the flow past an oscillating cylinder. Following the present work, simulations of flow past a freely oscillating cylinder, both at low and high Reynolds numbers (with DNS and LES, respectively) can provide deeper understanding of VIV phenomena.

Numerical study of a circular cylinder forced to oscillate at a yaw angle to incoming flow. Most of ocean structures as marine risers (pipes) are lied in different ocean current conditions where the flow angle of attack and direction may vary along their length. The study of the flow past a cylinder oscillating at an angle to the free stream will reveal the wake response and the variation of forces and may predict hazardous implications in the flow-structure system being of great engineering interest in the structural design process.

Appendix A

Resolution Tests

A.1. Two-dimensional simulations: Resolution tests

To further validate the accuracy of the present results, we performed resolution tests for two-dimensional flow: a) spatial resolution tests for stationary cylinder and b) temporal and spatial resolution tests for a high-amplitude forcing case at below resonant frequency, in particular for counter-clockwise cylinder motion with $F=0.9$, $\varepsilon=0.20$ and $A_y/D=0.50$ at $Re=400$. The oscillation amplitude $A_y/D=0.50$ is appropriate for the validation tests, as high amplitude is associated with sharper flow field gradients.

Stationary cylinder

In **Table A.1-1**, the computed force coefficient values obtained from spatial resolution tests are presented; here statistics are obtained for a time of 1092 non-dimensional units, corresponding to 240 shedding cycles. Here, we have used the standard spatial discretization, consisting of 464 macro-elements. The numerical time-step was equal to $\Delta t=0.0030$. In almost all cases, the deviations of the computed values are in the third decimal point, demonstrating that the results are converged, i.e. that the spatial resolution utilized is adequate.

Table A.1-1: Spatial resolution tests for two-dimensional flow past a stationary cylinder at $Re=400$.

Resolution	$C_{L,RMS}$	$< C_D >$	$C_{D,RMS}$
7×7	0.765810	1.420500	0.080061
9×9	0.765600	1.419400	0.079949
11×11	0.764890	1.418000	0.079853

Counter-clockwise cylinder motion at F= 0.9, ε=0.20 and $A_y/D=0.50$

In **Table A.1-2,** the computed force coefficient values obtained from spatial resolution tests, corresponding to different elemental resolutions, are presented. Here, $\Delta t = 0.0015$. We have maintained the standard spectral element skeleton (464 macro-elements), and used different polynomial degrees, corresponding to *7x7*, *9x9*, and *11x11* elemental resolution. The values presented correspond to averaging over 1009 time units, i.e. 200 forcing cycles. The differences of the calculated forces between the elemental resolutions *7x7* and *9x9* to *11x11* varied from 0.07% to a maximum of 2.6% whereas comparing the results of *9x9* to *11x11* smaller differences were found ranging from 0.05% to 0.94%. Given the small differences between the *9x9* and the *11x11* resolution, grid with *9x9* elemental resolution was utilized.

Resolution Tests

Next, we performed temporal resolution tests using the standard spatial discretization of 464 macro-elements with *9×9* elemental resolution. The numerical time-step used for the temporal resolutions tests was equal to equal to *Δt=0.00075*, *0.0015*, and *0.00225*. The computed values of force coefficients are presented in **Table A.1-3**. The variation between the computed values ranged from 0.01% to 0.50%. Thus, the numerical time-steps of *Δt=0.00075* and *Δt=0.0015* are considered adequate for temporal discretization and were used in the present two-dimensional simulations.

Table A.1-2: Spatial resolution tests for counter-clockwise cylinder motion at *F=0.9*, *ε=0.20* and $A_y/D=0.50$. Here, *Δt=0.0015*.

Resolution	C_{Lv}	C_M	C_{La}	C_{Dv}	C_{mx}	C_{Da}	$C_{L,RMS}$	$<C_D>$	$C_{D,RMS}$
7×7	0.705106	-0.635578	-0.773765	0.512740	-0.528355	-0.514584	0.818390	2.339900	0.523330
9×9	0.708771	-0.642409	-0.782081	0.519883	-0.536438	-0.522456	0.831400	2.345620	0.532860
11×11	0.705586	-0.636408	-0.774776	0.522078	-0.539033	-0.524983	0.829080	2.346800	0.537580

Table A.1-3: Temporal resolution tests for counter-clockwise cylinder motion at *F=0.9*, *ε=0.20* and $A_y/D=0.50$. Here, a grid of 464 macro-elements with *9x9* elemental resolution was used.

Δt	C_{Lv}	C_M	C_{La}	C_{Dv}	C_{mx}	C_{Da}	$C_{L,RMS}$	$<C_D>$	$C_{D,RMS}$
0.00075	0.708392	-0.641990	-0.781571	0.519953	-0.536330	-0.522351	0.830460	2.344200	0.532740
0.00150	0.708771	-0.642409	-0.782081	0.519883	-0.536438	-0.522456	0.831400	2.345620	0.532860
0.00225	0.711653	-0.644383	-0.784484	0.518892	-0.537278	-0.523274	0.834640	2.349400	0.533450

A.2. Three-dimensional simulations: Resolution tests

Spatial resolution tests for three-dimensional flow past an oscillating cylinder were performed, at *Re=400*. A low oscillation amplitude equal to $A_y/D=0.20$ was taken for counter-clockwise cylinder motion at $F=1.0$, $\varepsilon=0.20$. The oscillation amplitude $A_y/D=0.20$ is considered appropriate for the validation tests since the flow field gradients are characterized by smooth variation.

In **Table A.2-1,** the computed force coefficient values obtained from spatial resolution tests, corresponding to *7x7x7* and *8x8x8* elemental resolution, are presented. We have utilized the spectral element skeleton of 20560 macro-elements and a time step of $\Delta t = 0.0010$. The values obtained correspond to averaging over 294 time units, i.e. 60 forcing cycles. The differences of the calculated forces between the elemental resolutions *7x7x7* and *8x8x8* varied from 0.02% to a maximum of 2.8%. Thus the spatial *8x8x8* resolution used in the present three-dimensional simulations is considered adequate.

Table A.2-1: Spatial resolution tests for counter-clockwise cylinder motion at $F=1.0$, $\varepsilon=0.20$ and $A_y/D=0.20$. Here, $\Delta t=0.0010$.

Resolution	C_{Lv}	C_M	C_{La}	C_{Dv}	C_{mx}	C_{Da}	$C_{L,RMS}$	$<C_D>$	$C_{D,RMS}$
7×7×7	1.118021	-0.514612	-0.265609	0.238706	-0.214515	-0.088575	0.820140	1.737300	0.181740
8×8×8	1.117695	-0.526488	-0.271739	0.237013	-0.220518	-0.091054	0.821150	1.737000	0.181100

References

Al-Jamal, H. and C. Dalton (2004). "Vortex-induced vibrations using large eddy simulation at a moderate Reynolds number." Journal of Fluid and Structures, **19**: 73–92.

Anagnostopoulos, P. (2000). "Numerical study of the flow past a cylinder excited transversely to the incident stream. Part 1: Lock-in zone, hydrodynamic forces and wake geometry." Journal of Fluids and Structures, **14**(6): 819-851.

Atluri, S., V. K. Rao and C. and Dalton (2009). "A numerical investigation of the near-wake structure in the variable frequency forced oscillation of a circular cylinder " Journal of Fluids and Structures, **25**: 229-244.

Barkley, D. and R. D. Henderson (1996). "Three-dimensional Floquet stability analysis of the wake of a circular cylinder." Journal of Fluid Mechanics, **322**: 215-241.

Bearman, P. W. (1984). "Vortex shedding from oscillating bluff bodies." Annual Review of Fluid Mechanics, **16**: 195–222.

Bearman, P. W. (2009). "Understanding and predicting vortex-induced vibrations." Journal of Fluid Mechanics, **634**: 1-4.

Bearman, P. W. (2011). "Circular cylinder wakes and vortex-induced vibrations." Journal of Fluids and Structures, **27**: 648–658.

Bishop, R. E. D. and A. Y. Hassan (1964). "The lift and drag forces on a circular cylinder in a flowing fluid." Proceedings of Royal Society of London (Series A 277): 32–50, 51–75.

Blackburn, H. M. and R. D. Henderson (1999). "A study of two-dimensional flow past an oscillating cylinder." Journal of Fluid Mechanics, **385**: 255-286.

Blevins, R. D. (1990). Flow-induced vibration. Van Nostrand Reinhold.

Bloor, M. S. (1964). "The Transition to Turbulence in the Wake of a Circular Cylinder " Journal of Fluid Mechanics, **19**: 290-304.

Braza, M., P. Chassaing and H. Ha Minh (1986). "Numerical study and physical analysis of the pressure and velocity fields in the near wake of a circular cylinder." Journal of Fluid Mechanics, **165**: 79-130.

Braza, M., D. Faghani and H. Persillon (2001). "Successive stages and the role of natural vortex dislocations in three-dimensional wake transition." Journal of Fluid Mechanics, **439**: 1-41.

Brede, M., H. Eckelmann and D. Rockwell (1996). "On secondary vortices in the cylinder wake." Physics of Fluids, **8**: 2117-2124.

Brika, D. and A. Laneville (1993). "Vortex-induced vibrations of a long flexible circular cylinder." Journal of Fluid Mechanics, **250**: 481–508.

Canuto, C., M. Y. Hussaini, A. Quarteroni and T. A. Zang (1988). Spectral Methods in Fluid Dynamics. Springer Series in Computational Physics. Springer, Berlin.

Carberry, J., J. Sheridan and D. Rockwell (2001). "Forces and wake modes of an oscillating cylinder." Journal of Fluids and Structures, **15**(3-4): 523-532.

Carberry, J., J. Sheridan and D. Rockwell (2005). "Controlled oscillations of a cylinder: Forces and wake modes." Journal of Fluid Mechanics, **538**: 31-69.

Chorin, A. J. (1968). "Numerical solution of the Navier-Stokes equations." Mathematics of Computation, **22**(104): 745–762

Ciliberto, S. and J. P. Gollub (1984). "Pattern competition leads to chaos." Physical Review Letters, **52**(11): 922-925.

Dahl, J. M., F. S. Hover, M. S. Triantafyllou, S. Dong and G. E. Karniadakis (2007). "Resonant vibrations of bluff bodies cause multivortex shedding and high frequency forces." Physical Review Letters, **99**(14).

Dahl, J. M., F. S. Hover, M. S. Triantafyllou and O. H. Oakley (2010). "Dual resonance in vortex-induced vibrations at subcritical and supercritical Reynolds numbers." Journal of Fluid Mechanics, **643**: 395-424.

Delaunay, Y. and L. Kaiktsis (2001). "Control of circular cylinder wakes using base mass transpiration." Physics of Fluids, **13**(11): 3285-3302.

Deville, M., P. F. Fischer and E. Mund (2004). High-Order Methods for Incompressible Fluid Flow. Cambridge University Press.

Didier, E. and A. R. J. Borges (2007). "Numerical predictions of low Reynolds number flow over an oscillating circular cylinder." Journal of Computational and Applied Mechanics, **8**(1): 39-55.

Dong, S. and G. E. Karniadakis (2005). "DNS of flow past a stationary and oscillating cylinder at Re = 10000." Journal of Fluids and Structures, **20**(4 SPEC. ISS.): 519-531.

Evangelinos, C. and G. E. Karniadakis (1999). "Dynamics and flow structures in the turbulent wake of rigid and flexible cylinders subject to vortex-induced vibrations." Journal of Fluid Mechanics, **400**: 91-124.

Feng, C. C. (1968). "The measurement of vortex induced effects in flow past stationary and oscillating circular and d-section cylinders." Master's Thesis, Department of Mechanical Engineering, The University of British Columbia, Canada.

Fischer, P. F. (1994). "Parallel domain decomposition for incompressible fluid dynamics." Contemp. Math., **157:** 313–322.

Fischer, P. F. and A. T. Patera (1991). "Parallel spectral element solution of the Stokes problem." Journal of Computational Physics, **92**: 380-421.

Fischer, P. F. and E. M. Rønquist (1994). "Spectral element methods for large scale parallel Navier Stokes calculations." Comput. Methods Appl. Mech. Engr., **116**: 414-443.

Fischer, P.F. (1997). "An overlapping schwarz method for spectral element solution of the incompressible Navier-Stokes equations." Journal of Computational Physics, **133**: 84–101.

Fischer, P.F., N. I. Miller, and H. M. Tufo (2000). "An overlapping schwarz method for spectral element simulation of three-dimensional incompressible flows in parallel solution of partial differential equations." Springer-Verlag, ed. by P. Björstad and M. Luskin, 159-181.

Fischer, P. F., J. W. Lottes and S. G. Kerkemeier. http://nek5000.mcs.anl.gov

Fletcher, C. A. (1988). Computational Techniques for Fluid Dynamis. **Vol. I - II**. Springer-Verlag, Berlin.

Gerrard, J. H. (1978). "The Wakes of Cylindrical Bluff Bodies at Low Reynolds Number." Philosophical Transactions of the Royal Society of London. Series A, Mathematical and Physical Sciences, **288**(1354): 351-382.

Gopalkrishnan, R. (1993). "Vortex induced forces on oscillating bluff cylinders." Phd Thesis, Department of Ocean Engineering, MIT, Cambridge, MA, USA.

Gottlieb, D. and S. A. Orszag (1977). Numerical Analysis of Spectral Methods: Theory and Applications. SIAM-CBMS, Philadelphia.

Govardhan, R. and C. H. K. Williamson (2000). "Modes of vortex formation and frequency response of a freely vibrating cylinder." Journal of Fluid Mechanics, **420**: 85-130.

Govardhan, R. and C. H. K. Williamson (2001). "Mean and fluctuating velocity fields in the wake of a freely-vibrating cylinder." Journal of Fluids and Structures, **15**(3-4): 489-501.

Gresho, P. and R. Sani (1987). "On pressure boundary conditions for the incompressible Navier-Stokes equations." Int. Journal of Numerical Methods in Fluids, **7**: 1111 -1145.

Griffin, O. M. (1985). "Vortex-Induced Vibrations of marine cables and structures." NRL Memorandum Report, Naval Research Laboratory. Washington DC.

Griffin, O. M. and S. E. Ramberg (1974). "The vortex-street wakes of vibrating cylinders." Journal of Fluid Mechanics, **66**: 553-576.

Guermond, J. L. and J. Shen (2003). "A new class of truly consistent splitting schemes for incompressible flows." Journal of Computational Physics, **192**: 262–276.

Hama, F. R. (1957). "Three-dimensional vortex pattern behind a circular cylinder " J. Aeronaut. Sci., **24**: 156-159.

Henderson, R. D. (1995). "Details of the drag curve near the onset of vortex shedding." Physics of Fluids, **7**(9): 2102-2104.

Henderson, R. D. (1997). "Nonlinear dynamics and pattern formation in turbulent wake transition." Journal of Fluid Mechanics, **352**: 65-112.

Israeli, M., S. A. Orszag and M. O. Deville (1986). "Boundary Conditions for Incompressible Flows." Journal of Scientific Computing, **1**(1): 75–111.

ITTC (2008). "The specilast comitee on vortex-induced vibration comitee." Proceedings of the 25th ITTC II: 641-668.

Jauvtis, N. and C. H. K. Williamson (2003). "Vortex-induced vibration of a cylinder with two degrees of freedom." Journal of Fluids and Structures, **17**(7): 1035-1042.

Jauvtis, N. and C. H. K. Williamson (2004). "The effect of two degrees of freedom on vortex-induced vibration at low mass and damping." Journal of Fluid Mechanics, **509**: 23-62.

Jeon, D. and M. Gharib (2001). "On circular cylinders undergoing two-degree-of-freedom forced motions." Journal of Fluids and Structures, **15**(3-4): 533-541.

Kaiktsis, L., G. S. Triantafyllou and M. Özbas (2007). "Excitation, inertia, and drag forces on a cylinder vibrating transversely to a steady flow." Journal of Fluids and Structures, **23**(1): 1-21.

Karniadakis, G. E. (1989). "Spectral element simulations of laminar and turbulent flows in complex geometries." Applied Numerical Mathematics, **6**(1-2): 85-105.

Karniadakis, G. E., M. Israeli and S. A. Orszag (1991). "High-order splitting methods for the incompressible Navier-Stokes equations." Journal of Computational Physics, **97**(2): 414-443.

Karniadakis, G. E. and G. S. Triantafyllou (1992). "Three-dimensional dynamics and transition to turbulence in the wake of bluff objects." Journal of Fluid Mechanics, **238**: 1-30.

Karniadakis, G. E. and S. J. Sherwin (2005). Spectral/hp methods for computational fluid dynamics. Oxford University Press.

Kim, J. and P. Moin (1985). "Application of a fractional-step method to incompressible Navier-Stokes equations." Journal of Computational Physics, **59**: 308–323.

Kim, T. and J. Kim (2010). "Numerical analysis of the three-dimenional wake flow and acoystic field around a circular cylinder." Int. J. of Aeronautical & Space Sci., **11**(4): 319-325.

Lee, J. C., C. E. Frouzakis and K. Boulouchos (1996). "Numerical study of opposed-jet H-2/air diffusion flame -Vortex interactions " Comb. Sci. Techn., **158**: 365-388.

Maday, Y. and A. T. Patera (1989). "Spectral element methods for the incompressible Navier-Stokes equations." Annual Review of Fluid Mechanics, **24**: 167-204.

Maday, Y., A. T. Patera and E. M. Rønquist (1990). "An Operator-integration-factor splitting method for time-dependent problems: Application to incompressible fluid flow." Journal of Scientific Computing, **5**(4): 263-292.

Marcollo, H. and J. B. Hinwood (2006). "On shear flow single mode lock-in with both cross-flow and in-line lock-in mechanisms." Journal of Fluids and Structures, **22**(2): 197-211.

Mittal, S. and V. Kumar (1999). "Finite element study of vortex-induced cross-flow and in-line oscillations of a circular cylinder at low Reynolds numbers." International Journal for Numerical Methods in Fluids, **31**: 1087-1120.

Mittal, S. and V. Kumar (2001). "Flow-induced vibrations of a light circular cylinder at Reynolds numbers 10^3 to 10^4." Journal of Sound and Vibration, **245**(5): 923-946.

Moe, G. and Z. J. Wu (1990). "The lift force on a cylinder vibrating in a current." ASME Journal of Offshore Mechanics and Arctic Engineering, **112**: 297–303.

Morse, T. L. and C. H. K. Williamson (2006). "Employing controlled vibrations to predict fluid forces on a cylinder undergoing vortex-induced vibration." Journal of Fluids and Structures, **22**(6-7): 877-884.

Morse, T. L. and C. H. K. Williamson (2009). "Fluid forcing, wake modes, and transitions for a cylinder undergoing controlled oscillations." Journal of Fluids and Structures, **25**(4): 697-712.

Morton, C. R. (2010). "Experimental and Numerical Investigations of the Flow Development over Cylinders with Stepwise Discontinuities in Diameter." Master Thesis, University of Waterloo, Ontario, Canada.

Mukundan, H. (2008). "Vortex-Induced Vibration of marine risers: Motion and force reconstruction from field and experimental data." Phd Thesis, MIT, USA.

Norberg, C. (2003). "Fluctuating lift on a circular cylinder: review and new measurements." Journal of Fluid and Structures, **17**: 57-96.

Ongoren, A. and D. Rockwell (1988). "Flow structure from an oscillating cylinder. Part 2. Mode competition in the near wake." Journal of Fluid Mechanics, **191**: 225-245.

Orszag, S. A., M. Israeli and M. O. Deville (1986). " Boundary conditions for incompressible flows." Journal of Scientific Computing, **1**(1): 75-111.

Panton, R. L. (2005). Incompressible Flow. 3rd ed. Hoboken : John Wiley.

Patera, A. T. (1984). "A spectral element method of fluid dynamcs: Laminar flow in a channel expansion." Journal of Computational Physics, **54**: 468-488.

Perdikaris, P. G., L. Kaiktsis and G. S. Triantafyllou (2009). "Chaos in a cylinder wake due to forcing at the Strouhal frequency." Physics of Fluids, **21**(10).

Prandtl, L. (1928). "Motion of fluids with very little viscocity." N.A.C.A. Technical Memorandum No 452.

Protos, A., V. W. Goldschmidt and G. H. Toebes (1968). " Hydroelastic forces on bluff cylinders. ." ASME Journal of Basic Engineering, **90**: 378–386.

Provansal, M., C. Mathis and L. Boyer (1987). " Benard-von Karman instability: transient and forced regimes." Journal of Fluid Mechanics, **182**: 1-22.

Raghavan, K. (2007). "Energy extraction from a steady flow using Vortex Induced Vibration." PHD Thesis, University of Michigan.

Rogallo, R. S. and P. Moin (1984). "Numerical simulation of turbulent flows." Annu. Rev. Fluid Mech., **16**: 99-37.

Roshko, A. (1954). "On the development of turbulent wakes from vortex streets." N.A.C.A. Report. No. 1191.

Sarpkaya, T. (1977). "In-line and transverse forces on cylinders in oscillatory flow at high Reynolds numbers." Journal of Ship Research, **21**: 200-216.

Sarpkaya, T. (1978). "Fluid Forces on Oscillating cylinders." Journal of Waterway Port Coastal and Ocean Division ASCE. WW4, **104**(4): 275-290.

Sarpkaya, T. (1995). "Hydrodynamic damping, flow-induced oscillations, and biharmonic response " ASME Journal of Offshore Mechanics and Arctic Engineering, **117**: 232 - 238.

Sarpkaya, T. (2004). "A critical review of the intrinsic nature of vortex-induced vibrations." Journal of Fluids and Structures, **19**(4): 389-447.

Sarpkaya, T. and R. L. Shoaff (1979). "A discrete vortex analysis of flow about stationary and transversely oscillating circular cylinders." Technical Report NPS-69SL79011, Naval Postgraduate School. Monterey, CA, USA.

Stansby, P. K. (1976). "The locking-on if vortex shedding due to the cross-stream vibration of circular cylinders in uniform and shear flows." Journal of Fluid Mechanics, **74**: 641–665.

Techet, A. H. (2005). http://web.mit.edu/13.42/www/handouts/reading-VIV.pdf

Thompson, M., K. Hourigan and J. Sheridan (1996). "Three-dimensional instabilities in the wake of a circular cylinder." Experimental Thermal and Fluid Science, **12**(2): 190-196.

Thompson, M. C., T. Leweke and C. H. K. Williamson (2001). "The physical mechanism of transition in bluff body wakes." Journal of Fluids and Structures, **15**(3-4): 607-616.

Toebes, G. H. (1969). "The unsteady flow and wake near an oscillating cylinder." Journal of Basic Engineering, **91**: 493–502.

Tutar, M. and A. E. Holdo (2000). "Large eddy simulation of a smooth circular cylinder oscillating normal to a uniform flow." ASME Journal of Fluids Engineering, **122**: 694–702.

Van Dyke, M. (1982). An Album of Fluid Motions. Parabolic Press Inc. Stanford, CA.

Vandiver, J. K. (1983). "Drag coefficients of long flexible cylinders." Proc. Offshore Technology Conference, Paper No 4490.

Wieselberger, C. (1921). "New data on the law of hydro- and aerodynamic resistance." Physikalische Zeitschrift, **22**: 321-382.

Willden, R., R. McSherry and J. Graham (2008). "Prescribed cross-stream oscillations of a circular cylinder at laminar and early turbulent Reynolds numbers." Proceedings of the Fifth Bluff Bodies and Vortex-Induced Vibration Conference, Brazil.

Williamson, C. H. K. (1988). "The existence of two stages in the transition to three-dimenionality of a cylinder wake." Physics of Fluids, **31**(11): 3165-3168.

Williamson, C. H. K. (1989). "Oblique and parallel modes of vortex shedding in the wake of a circular cylinder at low Reynolds numbers." Journal of Fluid Mechanics, **206**: 579-627.

Williamson, C. H. K. (1992). "The natural and forced formation of spot-like 'vortex dislocations' in the transition of a wake." Journal of Fluid Mechanics, **243**: 393-441.

Williamson, C. H. K. (1996). "Vortex dynamics in the cylinder wake." Annu. Rev. Fluid Mech., **28**: 477-539.

Williamson, C. H. K. (1996a). "Three-dimensional wake transition." Journal of Fluid Mechanics, **328**: 345-407.

Williamson, C. H. K. and R. Govardhan (2004). "Vortex-induced vibrations." Annu. Rev. Fluid Mech., **36**: 413-455.

Williamson, C. H. K. and R. Govardhan (2008). "A brief review of recent results in vortex-induced vibrations." Journal of Wind Engineering and Industrial Aerodynamics, **96**(6-7): 713-735.

Williamson, C. H. K. and A. Roshko (1988). "Vortex formation in the wake of an oscillating cylinder." Journal of Fluids and Structures, **2**(4): 355-381.

Wu, J., J. Sheridan, J. Soria, and M. C. Welsh (1994). "An experimental investigation of streamwise vortices in the wake of a bluff body." Journal of Fluids and Structures, **8**(7): 621-635.

Yanenko, N. N. (1971). The method of fractional steps. Springer-Verlag.

Zdravkovich, M. M. (1997). Flow Around Circular Cylinders: Fundamentals. Oxford University Press.

Zdravkovich, M. M. (2003). Flow Around Circular Cylinders: Applications. Oxford University Press.

Zhang, H. Q., U. Fey, B. R. Noack, M. König and H. Eckelmann (1995). "On the transition of the cylinder wake." Physics of Fluids, **7**(4): 779-794.